YEARBOOK
2025

INSTITUTE OF TECHNICAL PHYSICS
AND MATERIALS SCIENCE
HUN-REN CENTRE FOR ENERGY RESEARCH
PART OF THE HUNGARIAN RESEARCH NETWORK

http://www.mfa.kfki.hu/

Published by the
Institute of Technical Physics and Materials Science
HUN-REN Centre for Energy Research
Part of the Hungarian Research Network

HUN-REN EK MFA Yearbook 2025

Director: Prof. Béla Pécz, member of HAS

Address: Konkoly-Thege Miklós út 29-33, H-1121 Budapest, Hungary
Postal: P.O.Box 49, H-1525 Budapest, Hungary
Phone: +36-1-392 2224
E-mail: info@mfa.kfki.hu
URL: http://www.mfa.kfki.hu/
Editor: Krisztina Szakolczai, Ph.D.
Published by: HUN-REN EK MFA, Budapest, Hungary, 2026.

TABLE OF CONTENTS

GENERAL INFORMATION 5
Director's foreword 6
Organizational structure 9
Key infrastructures 10
Excellent Research Infrastucture - Aberration Corrected Transmission Electron Microscope Laboratory 11
Excellent Research Infrastucture - Microsystems and Nanosensors Laboratories 12
Budget 13
Publications and citations 14
Prizes and Distinctions 15
Highlights of the year 18
SCIENTIFIC REPORTS 21
Nanostructures Department 22
Impact of ambient molecular contamination on scanning tunneling microscopy measurements of van der Waals materials 23
Stabilization of ultra-small magic angle graphene superlattices by molecular intercalation 25
Directional reflection asymmetry in hexagonal and rhombohedral graphite nanoribbons 27
Bias-free generation of solar hydrogen and high-value glycerol oxidation products by low-bandgap perovskite photoelectrodes 29
Strain-induced modulation of the local conductance in MoS2 layers on gold nanoparticles 31
Bioinspired semiconductor nanoarchitectures for environmentally friendly photocatalysis 33
Photonics Department 35
Validity of Young-Dupré equation for advancing and receding situations by the Capillary Bridge Probe method 37
A novel, photoassisted synthetic route to transform Cu2O nanooctahedra to Cu2S quantum-dot superstructures 39
Spatial modulation of Cu2O shell growth on gold nanoprisms 42
Electrochemical Methods and Ellipsometric Characterization of Gold Nanoparticle-Based Sensors 44
Investigation of in- and out-diffusion of Li-ions in electrochromic tungsten-molybdenum combinatorial oxide films by spectroscopic ellipsometry 46
Effects of global curvature and illumination conditions on magic-mirror imaging 48
Thin Film Physics Department 50
Composition-dependent structural and optical properties of combinatorially deposited, RF sputtered gallium oxynitride layers 52
The Common Sublattice Method quantifies local deformations in epilayers 54
Evaluation methods for XPS depth profiling; a review 57
Effect of non-spherical shape of dry powder aerosol drugs on their airway deposition distribution 58
Microcombinatorial Preparation and Characterisation of Multicomponent Thin Films 59
Combinatorially optimized sensorics of sputtered gradient gold nanoparticle layers 61
Dramatic interaction between the Au TEM grid and sample as well as supported MoNi/MgO catalysts 63
Structural study of (001) rutile-type GeO2 semiconductor on rutile (TiO2) 64
Effect of Nitrogen Content on Microstructure and Mechanical Properties of DC Magnetron Sputtered CrMnMoSiY(N) High Entropy Coatings 65
Biomineralization at the nano scale 67

Preparation and investigation of biopolymer composite materials containing calcium phosphate doped with Mg and Zn components 69
Synthesis and Characterization of Hydroxyapatite from Eggshells 71
Hungarian Chips Competence Centre (HCHiP) 72
Nanosensors Department 73
Neutron absorption in thin boron carbide layers 74
Controlled Nucleation of Metal Sulfide Layers via Sulfur-Based Surface Functionalisation: Enhanced Initial Growth of GaS_x Thin Films 76
Progress toward Kitaev transmon generation 82
Biomechanical investigation of soft tissue transection using MEMS force sensing 84
Microsystems Department 85
Wearable gas sensors for emergency and extreme conditions 90
3D MEMS force sensor for tissue recognition 93
Characterisation of materials for bioMEMS applications 95
Microfluidic methods for particle and cell manipulation and analysis 98
Small scale production and development of near infrared LEDs 102
Cell culture media analysis in Organ-on-Chip applications 103
Solid-state nanopores for extremely sensitive nanosensors 106
Nanobiosensorics Department 107
Kinetic monitoring of molecular interactions during surfactant-driven self-propelled droplet motion by high spatial resolution waveguide sensing 108
Temporal pH waveforms generated in an enzymatic reaction network in batch and cell-sized microcompartments 109
Robotic manipulations of single cells using a large-volume piezoelectric micropipette with nanoliter precision 110
In situ monitoring of cell adhesion kinetics using label-free optical biosensors: Evaluating anticancer potential and selectivity of natural compounds 112
Complex Systems Department 113
Inter-role reciprocity in evolutionary trust game on square lattices 114
Quantitative comparison of power grid reinforcements 116
Scale-free behavior of weight distributions of connectomes 118
Derivation of potential for group interactions in evolutionary games 119
REFERENCES 120
MFA'S FULL LIST OF PUBLICATION IN 2025 125
LIST OF FIGURES 135

GENERAL INFORMATION

Director's foreword

As Director of the Institute of Technical Physics and Materials Science (MFA), it is my pleasure to welcome you to this Yearbook. This volume continues our annual series and presents the most important scientific achievements and events of 2025.

The year 2025 marked a profound transformation of HUN-REN, resulting in the establishment of a renewed research network under a new legal framework.
That was based on a law accepted by the parliament at the very end of 2024, which said: "Act XCI. 2024. on HUN-REN, the Hungarian Research Network The National Assembly, to further strengthen the autonomy of scientific research as enshrined in the Fundamental Law of Hungary, to more efficiently organise and more effectively support research activities, to ensure the long-term sustainability of Hungarian scientists' research, and to ensure that Hungarian research is considered to be among the most excellent on the international stage and receives the recognition it deserves, shall adopt the following Act:…"
This law determined the following main objectives:

- **Long-term funding:** The operation of HUN-REN is secured through a **25-year framework agreement** with the Hungarian State, complemented by **six-year detailed funding agreements**.
- **Institutional structure:** The research centres operate as **organizational units with derived legal personality** within the HUN-REN organization.
- **Asset management:** HUN-REN is entitled to freely manage and utilize the assets transferred to it by the Hungarian State free of charge for the purpose of carrying out its public research responsibilities.

However, the Budapest-Capital Regional Court officially registered HUN-REN only on 29 October 2025.

The Centre introduced a new slogan, **"ONE HUN-REN,"** to express the unity of the research network. Interestingly, when pronounced in Hungarian, it also carries the additional meaning that *HUN-REN exists*. Unfortunately, this unity was broken when the four humanities research centres were separated from the network and transferred to Eötvös Loránd University (ELTE). As a result, the implementation of the Hungarian Academy of Sciences (MTA) General Assembly's resolution became virtually impossible. According to that resolution, the MTA would transfer ownership of the properties used by the research network to the state, which would then hand them over free of charge to HUN-REN.

A salary adjustment was urgently needed. Initially, a 50% salary increase had been promised, and the additional government funding eventually made it possible, however, only a 30% increase was implemented. At the same time, promises were made that salary increases of a similar magnitude would be carried out over the following two years. Such increases are indeed necessary, as the 2025 salary adjustment merely compensated for the inflation accumulated over the previous four to five years.

During the final two months of the year, we were confronted with the dispute surrounding the PIC registration numbers required for participation in EU-funded projects. In the end, we were able to submit new proposals using a new PIC number, but transferring the ongoing projects to the new registration proved difficult and consumed a considerable amount of time and effort.

Meanwhile, we witnessed a worrying decline in Hungary's investment in research and development. A few years ago, Hungary spent 1.6% of its GDP on R&D, whereas the latest available figures show only 1.31%. This was reflected in the significantly reduced number of domestic funding opportunities. Moreover, less than half of this expenditure was financed by the government. From our perspective, this represents a highly negative trend, especially since there is broad professional consensus that

Hungary's current level of investment in R&D remains well below what is needed to sustain international competitiveness.

Despite the stagnation of public R&D spending, previously awarded research grants allowed our Institute to continue its scientific activities without major disruption. MFA continued its publication award programme recognizing outstanding papers published by young researchers.
On 7 May, the Assembly of Academicians elected the new Full, Corresponding, External, and Honorary Members of the Hungarian Academy of Sciences (MTA) from a joint list of 136 nominees. Among those elected was our colleague **Dr. Levente Tapasztó**, who became a **Corresponding Member of the Hungarian Academy of Sciences**.

Another major success was achieved when our colleague **Dr. János Volk** successfully defended his Doctor of the Hungarian Academy of Sciences (DSc) dissertation, entitled **"Ordered Zinc Oxide Nanowires,"** on 4 April 2025. The dissertation was approved with unanimous support from the review committee.
Three of our PhD students—Péter Márton, Deshabrato Mukherjee and Anita Bányai—successfully defended their doctoral dissertations. We congratulate them and their supervisors on this important achievement. Gábor Piszter successfully completed his habilitation and was appointed Senior Research Fellow.

It was a pleasure to participate in the ceremony in the Parliament building when our colleague Ferenc Vonderviszt and our former colleague Péter Basa received the prestigious Dénes Gábor award.

I was also delighted to learn that **Dr. Csaba Balázsi**, Scientific Advisor at our Institute, received the **Mrityunjay Singh Bridge Building Award** of the **American Ceramic Society (ACerS)** in Daytona Beach.
This international distinction is presented to individuals who have made outstanding contributions to the advancement of technical ceramics, significantly expanded the field's knowledge base, and played a major role in promoting the visibility and recognition of ceramic science and engineering.

I was also pleased to see that **Dr. Csaba Balázsi**, Scientific Advisor at our Institute, received the **Senior Award of the Hungarian Materials Science Society (MAE)** this year.

Our post-doc colleague, **Dr. András Pálinkás** gained the Outstanding Young researcher award of the Hungarian Academy of Sciences. **Dr. Adél Rácz** received the young researcher award of Centre for Energy Research.

In 2025, the HUN-REN Centre once again presented the **Róbert Bárány Award** to outstanding young researchers under the age of 40 across three scientific fields. Among the nine awardees was our colleague **Dr. Tímea Török** from the NanoSensors Laboratory, recognized for her research on memristors as nanoscale building blocks for neuromorphic computing.

In 2025, the President of HUN-REN awarded the title of **Research Professor Emeritus** to Dr. **Gábor Kornél Battistig** of the **HUN-REN Centre for Energy Research**.

In the field of electron microscopy our colleague **Dr. János Lábár** received the Árpád Barna prize for his developed 4D-STEM method based on diffraction. **Erzsébet Dódony received the junior category award for her work on crystal structure determination based on electron diffraction.**

The highly prestigious **Lendület (Momentum) Research Grant** was awarded to our colleague **Dr. Róbert Horváth** for the second time.

Our researchers were also awarded four Advanced Grants and one Starting Grant through the NKKP programme of National Research, Development and Innovation Office (NKFIH).

Our HUN-REN central administration coordinated a large GINOP+ application to purchase new scientific instruments in which our institution participated requesting a new aberration-corrected TEM/STEM microscope, electron-beam lithography system, deep reactive ion etching equipment, etc. The application gained the support from our ministry, and we waited for the advertisement of the final Call promised by the beginning of 2026.

We are proud of the scientific achievements presented in this Yearbook and hope you will enjoy reading about the work of our colleagues.

Previous editions of the MFA Yearbook are available electronically at: http://www.mfa.kfki.hu/hu/yearbook.

Prof. Béla Pécz
Director

Organizational structure

Director: Prof. Béla Pécz

Scientific departments	
Thin Film Physics Department	Katalin BALÁZSI, Ph.D.
Complex Systems Department	Géza ÓDOR, D.Sc.
Photonics Department	Péter PETRIK, D.Sc.
Nanobiosensorics Department	Róbert HORVÁTH, Ph.D.
Microsystems Department	Péter FÜRJES, Ph.D.
Nanosensorics Department	János VOLK, Ph.D.
Nanostructures Department and "Lendület" group - 2D Materials	Levente TAPASZTÓ, D.Sc.
"Lendület" group - Topological Nanostructures	Péter NEMES-INCZE, Ph.D.

Directly supervised functions	
Head of Scientific Advisory Council	Levente TAPASZTÓ, D.Sc.
Scientific secretary, projects and PR	Krisztina SZAKOLCZAI, Ph.D.
Quality control, patents, MTMT, REAL admin	Andrea BOLGÁR
Technical support	Károly BODNÁR
Financial administration	Zsuzsanna KELEMEN
Innovation manager, patents	Valéria OSVÁTH
Technology transfer (IPR)	Antal GASPARICS, Ph.D.

Key infrastructures

Excellent Research Infrastructures

The Thin Film Physics Department is strong at national and even international level at transmission electron microscopy (TEM), what they use to determine relationships between the microstructure and other physical properties. Their main facility, the Aberration Corrected Transmission Electron Microscope Laboratory was selected as Excellent Research Infrastructure by the National Research and Innovation Office.

The Microsystems and Nanosensors Laboratories run a unique semiconductor manufacturing facility in Hungary comprising two clean labs (300 m2 + 160 m2 – Class 100-10000) with complete Si-CMOS technology line together with a mask shop, the only complete Si CMOS technology. The laboratory was also selected as Excellent Research Infrastructure by the National Research and Innovation Office.

Nondestructive characterization Laboratory:

The Institute of Technical Physics and Materials Science of the Centre for Energy has decades of experience in non-destructive testing certified according to the ISO 9001: 2009 quality assurance system.

Material characterization methods offered for external users and partners: Non-destructive optical and magnetic measurement of surface nanostructures and materials including: spectroscopy; magnetic material testing; biosensors; curvature of surfaces; surface contamination and quality; water pollution tests

Sample properties to characterize:

- layer thickness (0.5-1000 nm);
- optical refractive index (accuracy: ~ 0.001);
- homogeneity;
- quality of interfaces;
- porosity (e.g., voids content in the porous layer);
- surface nanoroughness;
- layer composition in some cases (e.g., Si nanoparticle content in silica);
- measurement of carbon phases;
- crystallinity (lattice disorder of single crystals, disintegration);
- brittleness and material properties of steel structures
- crystal and band structure of semiconductors

Other main facilities and equipments:

- Electron Microscopy, Auger and Scanning Probe Lab
- Thin film, Surface Physics and Structures
- Ion Implantation and Ion Beam Analysis
- Semiconductor Lasers and different LPE Techniques
- Porous silicon preparation and studies
- Carbon nanotubes, preparation and studies
- Ceramics, high pressure, high temperature press, refractory metals

Excellent Research Infrastucture - Aberration Corrected Transmission Electron Microscope Laboratory

Description of the RI:
New generation of aberration corrected electron microscope, the open laboratory of the Hungarian Materials Science. Sub-nanometer resolution in TEM imaging providing atomic arrangement and analytical (EDS) information on a few nanometer scale with the four EDS detectors built into the column. Elemental maps can be taken by EDS. Heating holder (with precise MEMS chip) and study of reactions inside the microscope. Helping the university teaching and partner in industrial development.

Activities and Services:
Research of thin films exploring the growth mechanism and properties. Materials science analysis using transmission electron microscopy (TEM). Sample preparation, atomic resolution images with a resolution below 0.1 nm in TEM mode thanks to the spherical aberration corrector built in. Several detectors in Scanning Transmission Electron Microscopy mode for example giving images in which the contrast is proportional with the (square) atomic number. Preparation of elemental maps taken by EDS detector based on characteristic X-Ray lines. Plan view and Cross sectional specimens, depth profiling. Determination of phases, failure analysis. Investigation of semiconductors, metals, insulators and alloys.

Specification:
FEI Titan THEMIS 200 200 kV aberration corrected TEM/STEM microscope with image corrector
STEM modes: BF, DF, HAADF images
4 SDD EDS detectors built into the column
Image corrector energy spread: 0.8EV, information limit: 90pm, STEM resolution 164pm
Specimen tilting in double tilt analytical holder: X direction ± 35o, Y direction ±30o.
Field emission gun
CETA 16M camera

Excellent Research Infrastucture - Microsystems and Nanosensors Laboratories

Description of the RI:
The main tasks of the Departments and the RI are the research and development of physical, chemical/biochemical sensors and integrated systems:

- Si Microtechnology with special emphasis on development of MEMS devices and related technologies, materials, structural and functional characterizations.
- Development and fabrication of microfluidic systems, their application in new fields of medical diagnostics and lab-on-a-chip systems – BioMEMS.
- Sensor development with special emphasis on autonomous sensor systems, physical, chemical, mechanical, opical and thermal microsensors – MEMS.
- Development of semiconductor nanodevices, the sythesis and charactirization of quasi-one-dimensional semiconducting nanostrucrures, their integratation into functional sensoric, optoelectronic and photovoltaic devices – NEMS.
- Development and small scale production of NIR LEDs of unique physical parameters

Activities and Services:
The Department runs two clean labs (300 m2 + 160 m2 – Class 100-10000) comprising a complete Si-CMOS processing line and a mask shop, unique facility in Hungary. The technology allows to manufacture layers, patterned structures and devices with line resolution of 1 μm by optical and down to ≈10 nm by e-beam lithography on 3” and 4” Si and glass wafers. Competences available as service for partners:

- High temperature annealing, diffusion and oxidation; Rapid Thermal Treatment;
- Low Pressure Chemical Vapour Deposition of poly-Si, SiO2 and Si3N4 layers;
- Low Temperature Chemical Vapour Deposition;
- Plasma Enhanced Atomic Layer Deposition;
- Physical Thin Film Depositions – Electron beam evaporation, DC and RF Sputtering;
- Ion implantation;
- Reactive Ion Etching, Deep Reactive Ion Etching;
- Photolithography with back-side alignment and Nanoimprinting;
- E-beam lithography;
- Nanopatterning, deposition and etching by Focused Ion-Beam;
- Wafer-bonding;
- Wet chemical treatments;
- Electro-chemical porous Si formation;
- Liquid Phase Epitaxy of III-V compound semiconductors;
- Mask design, laser pattern generator;
- Polymer (PDMS, SU8, Polyimide) structuring by photolithography and micro-molding techniques,
- Chip dicing, packaging especially for sensor applications;
- Materials and structural analysis & characterization:, SEM, FIB, EDX, Atomic Force Microscopy, Electrochemical Impedance Spectroscopy, Stylus Profiler;
- Electrical and functional modelling and characterization.

Budget

Both the domestic and the EU grants were facing funding challenges in 2025. Whilist the activity of the propsal preparation remained unchanged the income dropped due to unforseen effects. The reorganization of the HUN-REN network consumed a lot of energy from both the administrators and from project leaders. The partial transfer of rights and obligations made contrancts amendments necessary, therefore caused delayes in scientific work and payments. Grants and R&D&I payments are about half of the total budget of the institute, the total budget in 2025 was approx. 3,8M€.

Also woth mentioning, that:

- the National Research, Development and Innovation Office (NKFIH) is behind advance payments, which means that domestic R&D&I projects are effectively being financed retrospectively by our institute, which is a huge burden.
- the Hungarian Competence Center for HPC (HCHIP) has been launched, but it is not a research program. Awareness-building activities consume significant resources (researchers' time), although its long-term impact is expected to be positive.
- the value of R&D&I services offered to industry has been stagnant for years.
- the long-awaited wage increase took place in September, but even with this, average researcher salaries remained way below the Western European levels.
- there are only a few funding calls remaining from the EU's Horizon Europe program, it is approaching the end of its current cycle.

MFA budget 2003-2025 (million HUF)

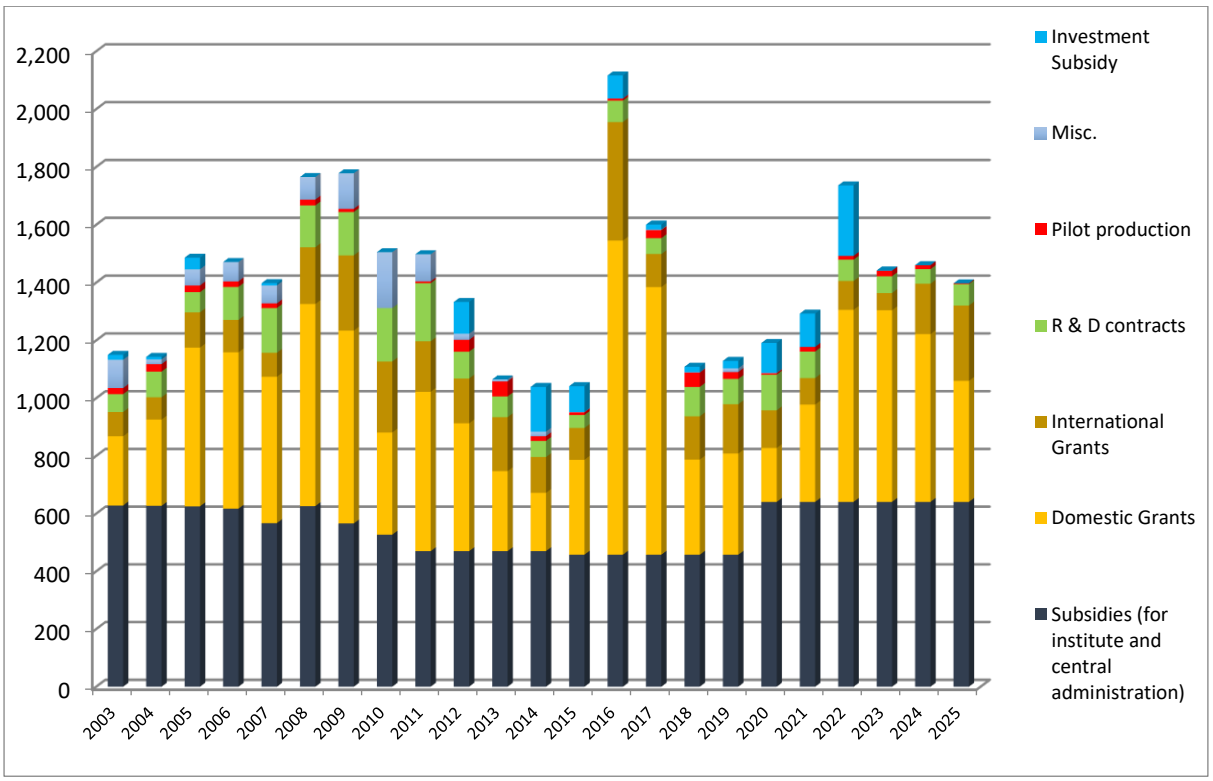

Publications and citations

According to the Thomson-Reuters ISI "Web of Knowledge", and MTMT2 databases, the Institute has an average publication activity of ca. 130 scientific papers in IF journals a year (link). Recently MFA researchers tend to publish in journals with higher IF and the number of citations are constantly increasing. The total IF was approx 820, the independent citations are increasing annually and are over 7800 in 2025.

The postdoc researchers are already under pressure to produce more papers in highly cited open access papers to be able to gain fundings from EU and domestic grants. This will increase with the new KPIs (key performance indicators) intorduced by the HUN-REN HQ this year.

MFA and its predecessor's publications and citations per year since 1998

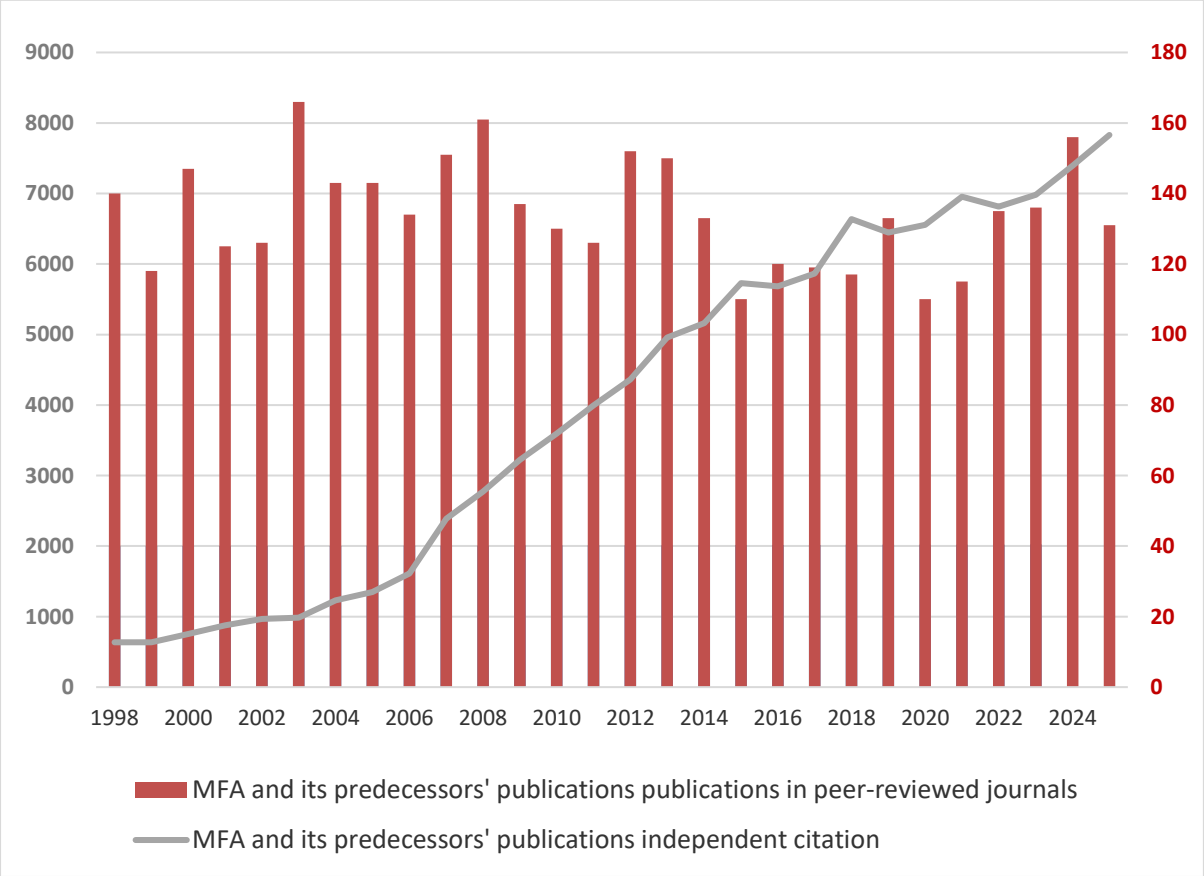

Prizes and Distinctions

	Levente TAPASZTÓ	Corresponding member of the Hungarian Academy of Sciences
	Ferenc VONDERVISZT	Dénes Gábor Award
	János VOLK	D.SC. Doctor of the Hungarian Academy of Sciences
	Csaba BALÁZSI	Mrityunjay Singh Bridge Building Award of ACERS
	András PÁLINKÁS	Young researcher award of the Hungarian Academy of Sciences
	János LÁBÁR	Árpád Barna Prize
	Erzsébet DODONY	Árpád Barna Prize for young researchers

	Tímea TÖRÖK	Róbert Bárány prize
	Gábor BATTISTIG	Professor emeritus of the HUN-REN Centre for Energy Research
	Adél RÁCZ	Young researcher award of the HUN-REN Centre for Energy Research
	Mátyás DABÓCZI	Postdoc researcher award of MFA
	Norbert NAGY	Postdoc researcher award of MFA
	Tímea TÖRÖK	Postdoc researcher award of MFA
	Zsombor SZOMOR	Young researcher award of MFA

György KÁLVIN — Young researcher award of MFA

Nicolett KANYÓ — Young researcher award of MFA

Ferenc BRAUN — Excellent research support award of MFA

Zsuzsanna KELEMEN — Excellent research support award of MFA

Highlights of the year

Dr. Ferenc Vonderviszt receives Dénes Gábor Award (From left to right: Dr. Miklós Bendzsel, president of NOVOTEL Foundation, Dr. Ferenc Vonderviszt biophysicist, Szabolcs Farkas president of SZTNH, source: https://sztnh.gov.hu/kezdooldal/hirek/atadtak-a-2025-os-gabor-denes-dijakat)

Dr. Csaba Balázsi receives the ACERS' "Mrityunjay Singh Bridge Building Award" at Daytona Beach

The **Hungarian Chip Competence Centre (HCHiP)** started its operation in 2025. HCHiP is the knowledge and innovation hub of the Hungarian semiconductor industry, aims to connect research, industry and education, facilitating the development and application of the latest chip technologies. As a member of the European Network of Chip Competence Centres (ACCCess), HCHiP supports Hungarian and European companies in strengthening their competitiveness and achieving technological independence. The consortium was formed from three partners have complementary competencies that can be coordinated in such a way that all the project goals can be achieved: Bay Zoltán Alkalmazott Kutatási Közhasznú Nonprofit Kft., Budapest University of Technology and Economics (BME), and HUN-REN Centre for Energy Research.

Key personnel of the HCHiP project on the kickoff meeting held in Budapest, November 2025.

The Ultrabalaton trail running competition was completed by 2 teams in 2025 again, this time 9 members of the Microsystems and Nanosensors Laboratory

SCIENTIFIC REPORTS

Nanostructures Department

Head: Dr. Levente TAPASZTÓ, D.Sc., research advisor

Research Staff:

Prof. László Péter Biró, Member Of the HAS
Zsolt Endre Horváth, D.Sc., Deputy Head of Laboratory
Mátyás Dabóczi, Ph.D.
Gergely Dobrik, Ph.D.
Krisztián Kertész, Ph.D.
Antal Adolf Koós, Ph.D.
Péter Kun, Ph.D.
Géza István Márk, Ph.D.
Péter Nemes-Incze, Ph.D.
Zoltán Osváth, Ph.D.
András Pálinkás, Ph.D.
Gábor Piszter, Ph.D.
Péter Süle, Ph.D.
Zoltán Tajkov, Ph.D.
Péter Vancsó, Ph.D.

Students:

Konrád Kandrai, Ph.D. Student
Soma Keszei, Ph.D. Student
Krisztián Márity, Ph.D. Student
Márton Szendrő, Ph.D. Student
György Kálvin, Ph.D. Student
Liza Lutter, M.Sc. student

The research activity of the Nanostructures Laboratory is based on the two-decade-long expertise in the synthesis, characterization and engineering of various nanostructures using scanning probe microscopy as the main experimental technique. Since more than a decade, our research efforts are focused on the investigation of two-dimensional materials. Besides graphene, in the last couple of years, novel 2D materials, mainly form the family of transition metal chalcogenides (TMC) have been intensely studied. Recently, we have further extended our activity with the investigation of layered topological insulator crystals. We have also successfully continued our research on bioinspired photonic nanoarchitectures.

Impact of ambient molecular contamination on scanning tunneling microscopy measurements of van der Waals materials

TKP2021-NKTA-05, Élvonal KKP 138144, Lendület LP2024-17, OTKA K 146156, EXCELLENCE 151372, 2022-1.2.5-TÉT-IPARI-KR-2022-00006

G. Kálvin, P. Vancsó, M. Szendrő, K. Kandrai, A. Pálinkás, L. Tapasztó, and P. Nemes-Incze

For more than a decade, the presence or absence of the phonon-induced gap in scanning tunneling microscopy of graphene and graphite has remained an unresolved inconsistency in the literature. While some STM experiments reproducibly revealed a pronounced suppression of tunneling conductance around the Fermi level, others, performed under nominally similar conditions, failed to detect this hallmark feature. Here, we identify and resolve the physical origin of this discrepancy by demonstrating that ambient molecular contamination [Ref.1.] is the decisive factor governing the visibility of the phonon gap in STM measurements [Ref.2.]. We show that exposure of graphite surfaces to ambient conditions leads to the formation of a self-assembled monolayer of normal alkanes, which profoundly modifies the tunneling junction. The presence of this alkane overlayer manifests itself experimentally in several ways. Atomic-resolution STM images acquired on contaminated surfaces exhibit enhanced noise and reduced contrast compared to ultrahigh-vacuum-cleaved samples.

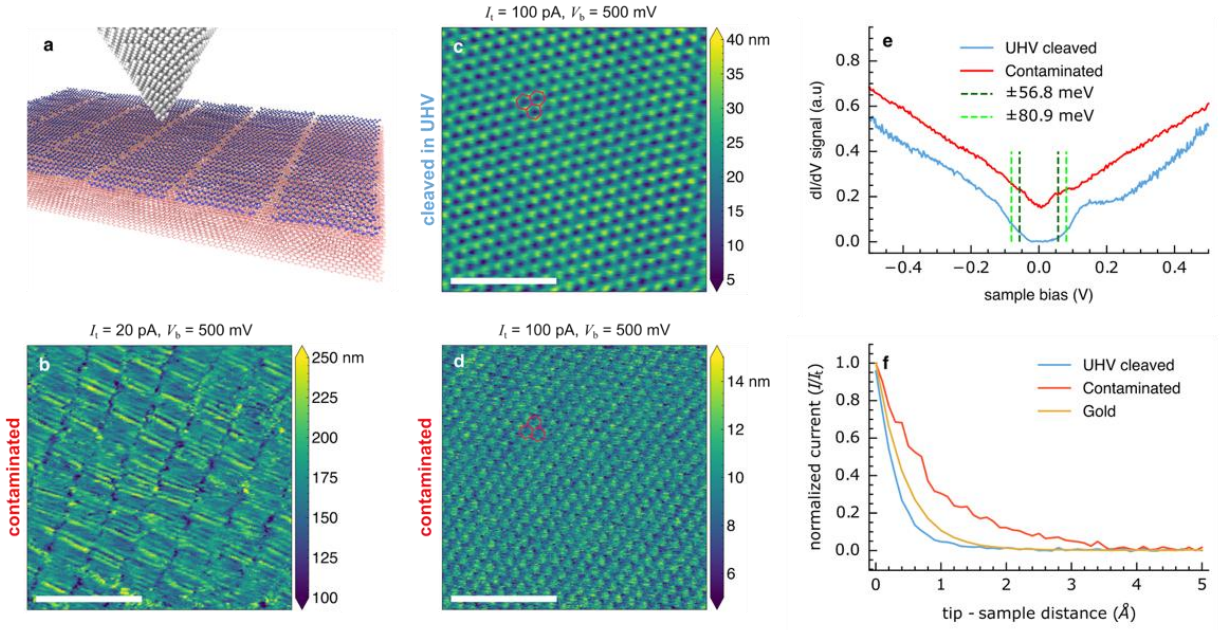

Figure 1. (a) Schematic image of the n-alkane self-assembled monolayer stemming from ambient air contamination. When measuring the surface by scanning tunnelling microscopy (STM) the tip can either scan above the layer or penetrate it. (b) STM image at the largest tip – sample separation showing the structure of the alkane overlayer. (c-d) Atomic resolution images of the contaminated surface (penetrating the alkane layer), show consistently larger current noise. (e) Comparison of the contaminated and clear graphite surface tunnelling conductance. The clean surface displays a clear phonon-gap. (f) Examples of I(z) curves on clean, contaminated graphite and gold samples, by measuring the tunnelling current as the tip is retracted. The contaminated samples systematically show an anomalously low decay rate of the tunnelling current.

Current–distance I(z) curves reveal an anomalously slow decay of the tunneling current, with decay constants reduced by factors of 1.5–5 relative to clean surfaces. Crucially, the same samples systematically lack the phonon-induced gap in their dI/dV spectra. These three observations: image noise, anomalous I(z) decay, and phonon-gap suppression, occur together and provide mutually consistent signatures of alkane contamination in the tunneling junction [Ref.2] (see Figure 1).

We demonstrate that the underlying mechanism is the appearance of an additional current pathway mediated by the alkane molecules. Although normal alkanes are wide-gap insulators, their conductance in a nanoscale junction is comparable to typical STM tunneling conductances. When the STM tip penetrates the molecular layer, one or more alkane chains can transiently bridge the tip and the graphite surface, forming a parallel transport channel analogous to a molecular break-junction configuration. As the tip is retracted, this molecular channel persists over several ångströms, producing a finite current even at tip-sample separations where pure vacuum tunneling would have already vanished. This break-junction-like transport channel both enhances current fluctuations and introduces an additional elastic tunneling contribution that fills in the phonon gap in the measured spectra

Our first-principles calculations show that the presence of an alkane overlayer can modify the intrinsic decay of graphite electronic wave functions into the vacuum, reducing the decay constant relative to the clean surface. In principle, this altered decay could be detected experimentally as a change in κ. In practice, however, the measurement of the intrinsic wave-function decay is overwhelmed by the dominance of the molecular transport channel. The current measured in I(z) spectroscopy above contaminated surfaces is no longer governed solely by vacuum tunneling but is dominated by alkane-mediated conduction, masking the genuine electronic decay of the graphite surface states. As a result, the experimentally extracted decay constants do not reflect the true wave-function attenuation but rather the effective transport properties of a mixed tunneling–molecular junction.

By establishing a direct and quantitative link between ambient alkane contamination, anomalous I(z) behavior, and phonon-gap suppression, our results resolve a long-standing experimental ambiguity in STM studies of layered carbon systems.

Stabilization of ultra-small magic angle graphene superlattices by molecular intercalation

Élvonal KKP 138144, 2022-1.2.5-TÉT-IPARI-KR-2022-00006

G. Dobrik, P. Kun, M. Szendrő, P. Vancsó, P. Nemes-Incze, L. Tapasztó

The correlated electronic states emerging in twisted bilayer graphene (TBG) at the first magic angle of 1.1° have been intensely investigated. This system offers particularly attractive features for studying strong correlations, since the electronic states are fully exposed, and the charge carrier density can be electrostatically tuned, enabling rapid mapping of correlated phase diagrams.

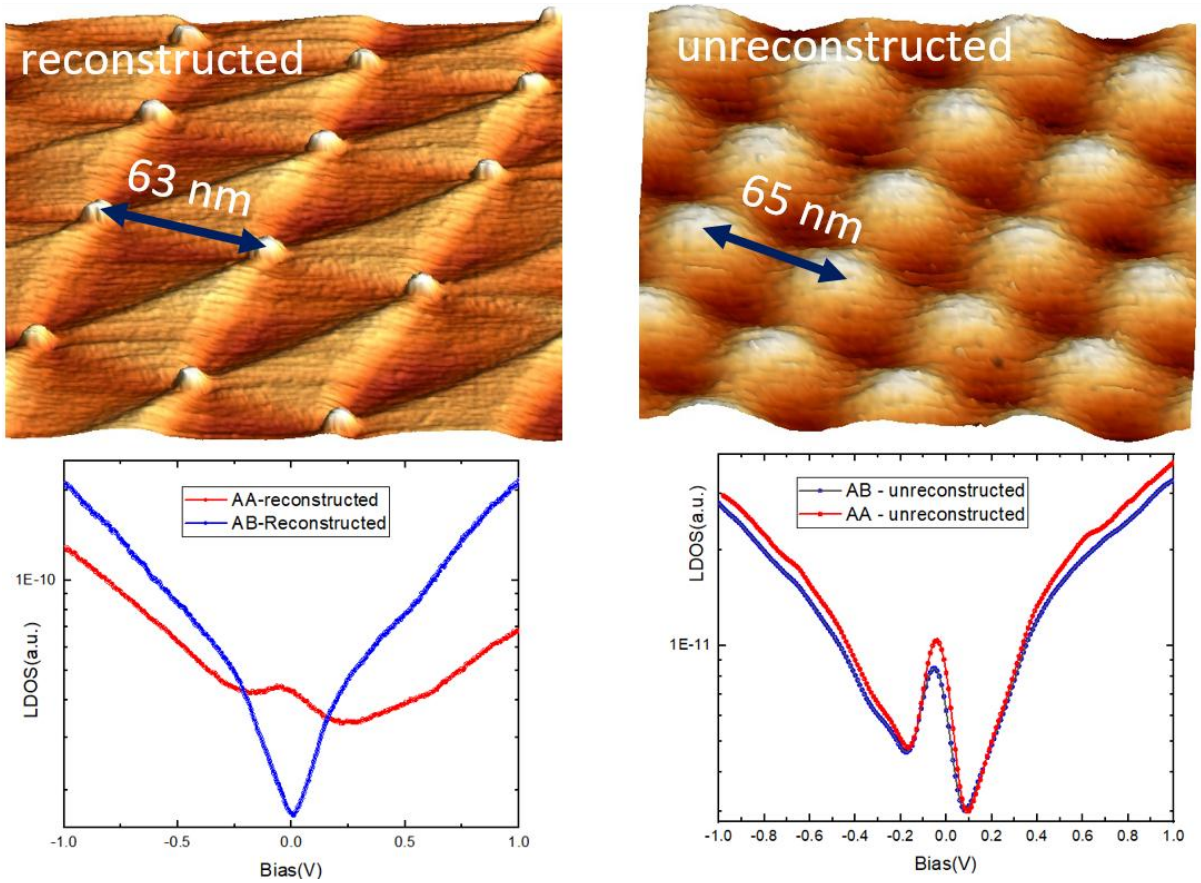

Figure 2. Topographic STM images of a) a reconstructed TBG superlattice of ~65 nm periodicity, corresponding to twist angle of ~0.21°, fabricated by the conventional tear-and-stack method and b) an unreconstructed giant (65 nm) TBG superlattice formed through the graphene auto-kirigami process. Tunneling spectra recorded on the bright (AA) and dark (AB/BA) regions of the reconstructed (c), and unreconstructed (d) 0.21° MATBG superlattices, the latter displaying sharper (FWHM ~ 90 meV) LDOS peak near the Fermi level on both AA and AB/BA regions, while a less intense and much broader (FWHM ~ 180 meV) peak ias observed only in the AA regions of the reconstructed superlattice.

The remarkable success of the Bistritzer–MacDonald continuum theory further predicts a hierarchy of smaller magic angles - near 0.5°, 0.4°, 0.24°, 0.21°, and beyond - which, however, have remained purely theoretical. Experimental studies revealed that moiré superlattices with twist angles below 1° become very fragile as the stacking configuration approaches the naturally favored AB alignment (0° twist), where large regions can be driven into perfect registry by minimal local lattice distortions. These reconstructions substantially broaden the flat bands, suppressing the correlation physics characteristic

of dispersionless states. Consequently, magic-angle superlattices of $\theta \leq 0.5°$ have long been considered too fragile - structurally and electronically - to be realized experimentally, despite the tantalizing prospect that accessing smaller magic angles, with progressively stronger correlations, could unlock a series of novel quantum phases.

Marginally twisted intercalated bilayer graphene samples have been prepared employing the graphene auto-kirigami process, combined with the deposition of a highly ordered alkane molecular layer on top of graphene. STM images have been acquired under UHV conditions, at room temperature, revealing a graphene superlattice, with a large periodicity of about 65 nm, corresponding to a twist angle of about 0.21º, closely matching the 5th predicted magic angle. In spite of the huge moiré unit cell (ultra-small twist angle), the intercalated superlattice displays extended bright (AA) regions at various bias voltages (Figure 2.b). For comparison the STM images of non-intercalated TBG samples with a similar (~ 0.21º) twist angle, fabricated by the conventional tear-and-stack method display the widely reported, strongly reconstructed moiré superlattice, with point-like AA regions (bright dots in Figure 2.a). According to detailed simulations, the molecular spacer layer intercalated between the graphene sheets, suppresses structural reconstructions while preserving sufficient interlayer tunneling for flat-band formation, in excellent agreement with our measurements. Remarkably, intercalation also delocalizes the flat-band wavefunctions across the whole moiré superlattice. This effect can be attributed to the shallowing of the moiré potential by intercalation, as well as the presence of disorder, which remarkably promotes the delocalization of the flat band wave functions, as predicted theoretically.

A major practical limitation of fabricating intercalated MATBG with the above discussed graphene auto-kirigami process is that the twist angle cannot be precisely controlled. Since the driving force of the auto-kirigami process is the vdW interaction, the twist angle is generally expected to be near 180º (0º), but the small deviations form 0 degree cannot be reliably controlled. Therefore, it is important to develop fabrication methods for intercalated graphene bilayers with more control over the twist angle, such as the widely used tear-and-stack method. The problem with the conventional tear-and-stack approach is that the forces exerted during the process are relatively high, squeezing the intercalant molecular layer into bubbles, and reestablishing the conventional interlayer distance. By proceeding as gentle as possible with this method, we were able to partially preserve the intercalated superlattices as shown in Figure 3.

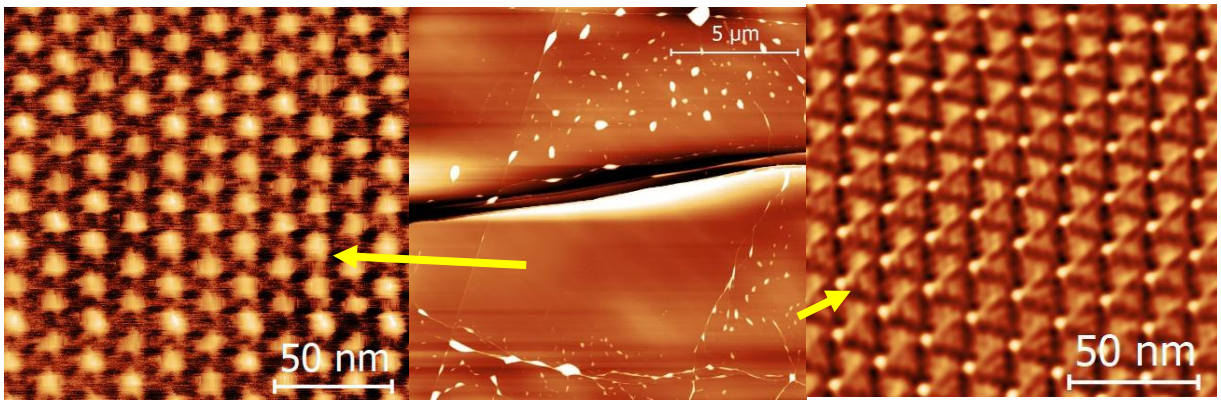

Figure 3. Center panel shows the AFM topography of a 0.7º twisted bilayer graphene sample prepared by the tear-and-stack method with alkane intercalant layer, displaying a large (5x5 μm^2) bubble-free area near the center of the image, next to areas showing the presence of bubbles. Conductive AFM images of the areas with bubbles (right) display a reconstructed superlattice of 20 nm periodicity. By contrast, the bubble-free area preserving the alkane intercalant layer, displays and unreconstructed 20 nm superlattice (left). We have also found that intercalated TBG superlattices are not only free of structural reconstructions but are also characterized by reduced twist-angle inhomogeneity, enabling the fabrication of uniform moiré superlattices on device-scale, a critical step toward reproducible twistronic devices.

Directional reflection asymmetry in hexagonal and rhombohedral graphite nanoribbons

TKP2021-NKTA-05, Élvonal KKP 138144, Lendület LP2024-17, OTKA K 146156, EXCELLENCE 151372, 2022-1.2.5-TÉT-IPARI-KR-2022-00006

K. Kandrai, A. Balogh (ELTE), G. Márk, D. Varga, Márton Szendrő, Z. Tajkov, K. Márity, P. Vancsó, L. Tapasztó, and P. Nemes-Incze

In a simple one-band medium, scattering from a defect obeys the principle of reciprocity: exchanging the source and detector yields the same response at the detector. However, if multiple bands are available, even with time-reversal symmetry and elastic scattering, this reciprocity can break, resulting in asymmetric reflection. Such non-reciprocal scattering has been demonstrated in photonic and phononic systems by introducing structural mirror asymmetry and employing mode-selective excitation. Here we demonstrate analogous behavior in a condensed matter systems of a rhombohedral-hexagonal graphite (RG–HG) junction separated by a domain soliton (see Figure 4.a) in a scanning tunneling microscopy experiment. In our experimental setup purely intravalley elastic scattering from the domain soliton leads to reflection asymmetry. As shown in Figure 4.d-i, the local tunneling conductance exhibits standing-wave modulation from intravalley scattering only within the hexagonal region, while the rhombohedral domains remain featureless, indicating absence of backscattering.

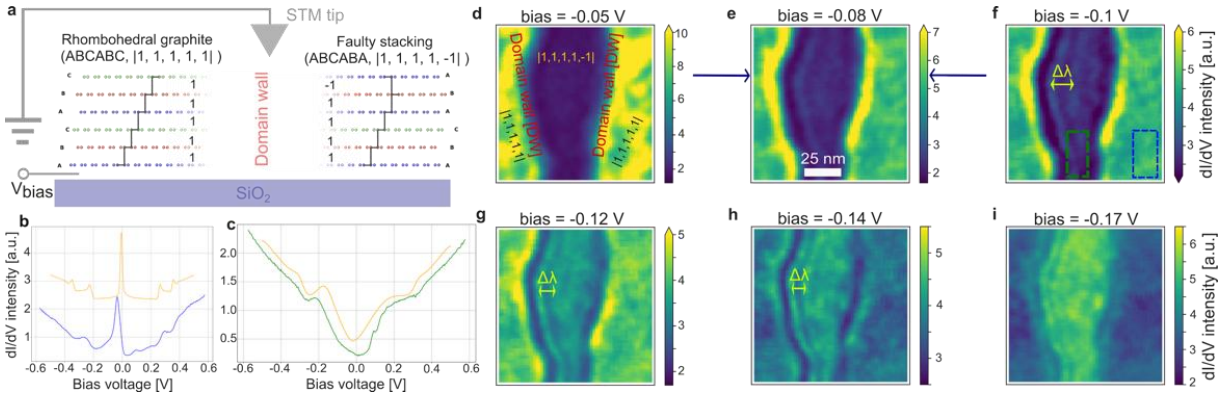

Figure 4. (a) Schematic illustration of the STM measurement on RG – hexagonal junctions. The hexagonal side of the sample is a 6-layer RG, with a hexagonal stacking fault at the top, denoted by the "-1" layer orientation of the top layer. (b, c) Measured and calculated LDOS of the RG and hexagonal side of the sample. The sample features hexagonal nanoribbon regions of a few 10 nm widths. One example is shown in panels (d - i), where we show the tunnelling conductance of the same area at various sample bias voltages. Ripples in the local tunnelling conductance can be observed in the hexagonal region bordered by two domain walls. The tunnelling conductance is a measure of the local density of states (LDOS) at the surface. The LDOS ripples shown by Δλ are only present in the middle hexagonal region.

Tight-binding calculations reproduce the intravalley interference patterns observed experimentally, supporting our interpretation (Figure 5.b). The observed reflection asymmetry originates from mode selection: the STM tip predominantly probes electronic states on the top surface, effectively isolating the top Dirac band in the hexagonal region and the top layer of the rhombohedral stack. Wave packet dynamics calculations confirm that this layer-specific probing, combined with the intrinsic layer polarization of the wavefunctions, gives rise to strong anisotropic scattering. Within the energy window corresponding to the RG band gap, the wave packet simulations show that the scattering amplitude from ABC to ABA exceeds that in the reverse direction by up to a factor of five.

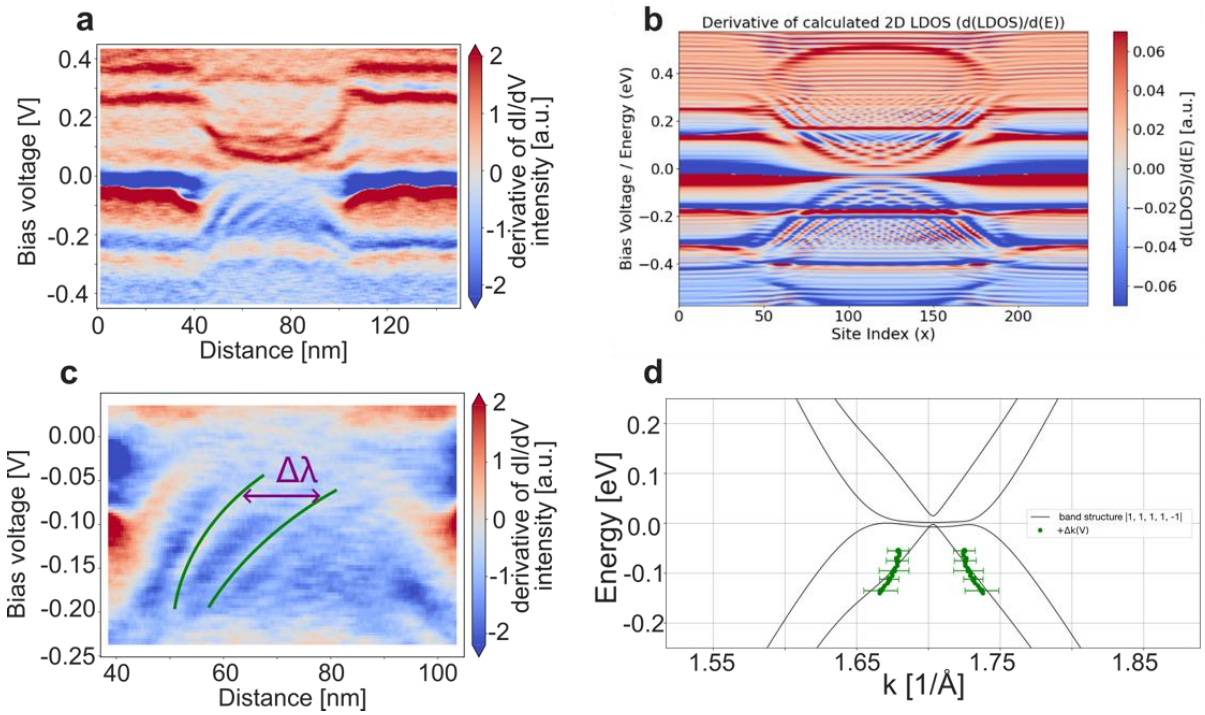

Figure 5. (a) dI/dV measurement across a RG – hexagonal – RG nanoribbon. The tunnelling conductance (dI/dV) is numerically differentiated along the bias voltage coordinate for better visibility of the intravalley scattering pattern. (b) Calculated local density of states (LDOS) of the top surface of the same nanoribbon geometry as in the measurement in (a). (c) Zoom into the dI/dV spectra in panel (b), highlighting the interference pattern arising in the hexagonal part of the sample. The scattering wavelength (Δλ) can be measured as the distance between peaks of the dI/dV signal across the sample surface. (d) From the bias voltage dependent Δλ values we can obtain the scattering wave vector (Δk), which we overlay onto the surface Dirac band of the hexagonal |1, 1, 1, 1, -1| structure.

We demonstrated unidirectional scattering in RG – HG junctions, where the mode selection occurs due to the STM tip probing only the top surface of the material. Such tailored charge injection is in principle feasible with van der Waals material contacts allowing for unidirectional electron wave steering capabilities for electron optics in a simple condensed matter system.

Bias-free generation of solar hydrogen and high-value glycerol oxidation products by low-bandgap perovskite photoelectrodes

HORIZON-MSCA-2022-PF-01 101103762 SOLARHYVALUE,
MTA NKM2025-4/2025, Élvonal KKP 138144

M. Daboczi, W.-J. Qiu, A. Koos, S. Keszei, L. Lutter, T. Ollar, J. S. Pap, C.-T. Lin, L. Tapaszto

Photoelectrochemical (PEC) water splitting by inexpensive photoelectrodes is a promising way of green hydrogen generation, which could become economically competitive if the reduction reaction of hydrogen evolution is coupled with oxidation of biomass waste into high-value chemicals. Perovskite photoelectrodes have great potential in revolutionising this field; however, their application is currently limited by their instability in aqueous environment and the use of typically large amounts of expensive precious metals catalysts, such as Pt.

This year, we have grown molybdenum disulfide (MoS2) on graphite sheets with thicknesses of 70 µm (G7) and 150 µm (G15) that are three orders of magnitude less expensive than the typically used highly oriented pyrolytic graphite (HOPG). Raman spectroscopy confirmed the presence of MoS2 as well as its multilayer (> 5) structure (Figure 6). The G15/MoS2 samples were applied as substrates for electrochemically depositing two atomic layer thick Pt (2L-Pt). These samples, despite their ultralow Pt loading, exhibited catalytic activity for the hydrogen evolution reaction in alkaline conditions comparable to that of commercial Pt/C deposited on G15 (Figure 6).

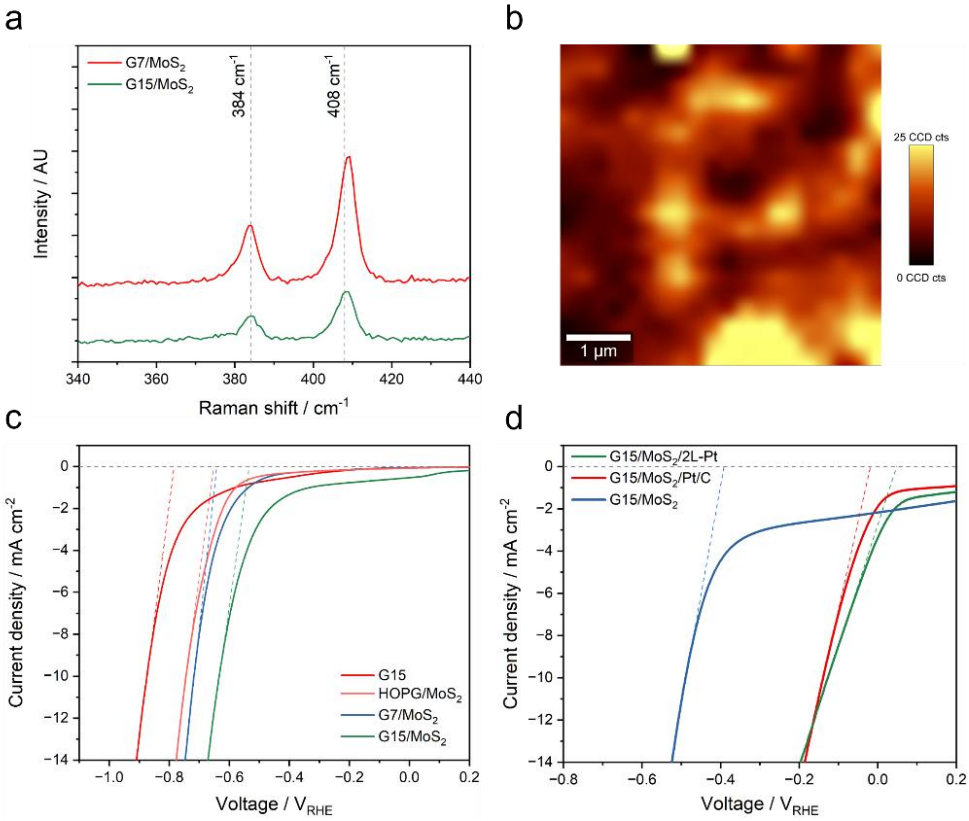

Figure 6. (a) Raman spectra of MoS_2 grown by CVD on G7 and G15 graphite layers. (b) Mapping of Raman peak intensity at 408 cm^{-1} for the G15/MoS_2 sample. (c) Current density–voltage scans of MoS_2 grown on different graphite substrates, recorded in an electrochemical cell in aqueous 0.5 M H_2SO_4 electrolyte. (d) Current density–voltage scans of G15/MoS_2 samples loaded by commercial Pt/C and ultralow amount of electrodeposited Pt (2L-Pt), recorded in aqueous 1 M NaOH electrolyte.

The developed G15/MoS2/2L-Pt catalytic sheet was integrated with a p–i–n type tin-lead perovskite photovoltaic device (bandgap of ~1.3 eV) by spraying a non-continuous adhesive layer at the back of the graphite sheet, followed by manual placement onto the top metal electrode of the solar cell to form an Ohmic contact. The photocathodes were prepared with different device designs, in which the active area was reduced to minimise losses due to low shunt resistance (Figure 7). The shunt resistance (defined here as the resistance between the top and bottom contact layers) was observed more often to drop after applying the graphite sheet in devices with larger active areas, highlighting both the importance and challenge of forming a uniform, pinhole-free photoactive layer. The champion devices reached stable photocurrent density of ~30 mA cm-2 under 1 sun illumination and a photocurrent onset potential as high as +0.8 V versus reversible hydrogen electrode (VRHE) in a three-electrode PEC setup.

The high fill factor and sufficient photovoltage of the photocathodes allowed for achieving photocurrent density of ~30 mA cm-2 even without any external bias, in a two-electrode PEC setup (Figure 7). During this bias-free operation solar hydrogen was generated at the surface of the photocathode, while glycerol was oxidised into high-value chemicals on the anode.

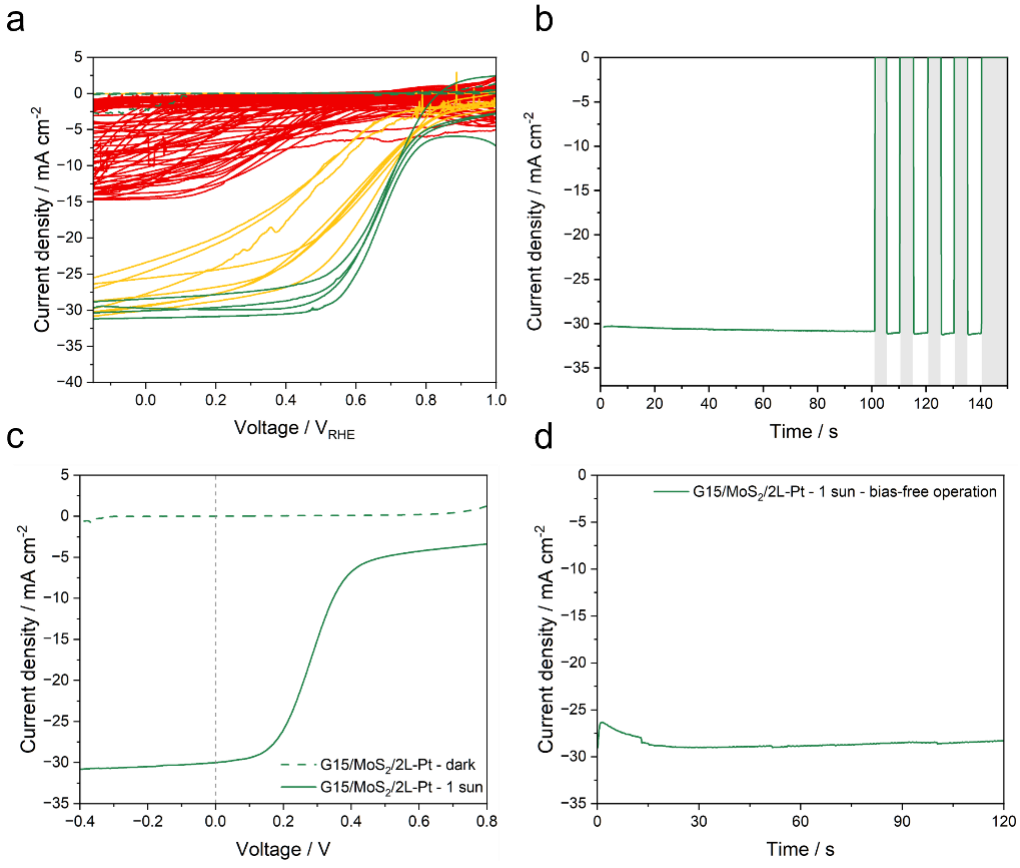

Figure 7. (a) Current density–voltage scans recorded in three-electrode PEC setup for perovskite photocathodes with device design changing from larger (red) towards optimised, smaller active area (yellow and green). (b) Chronoamperometric measurement of a perovskite photocathode at 0 V_{RHE} applied. Shaded areas indicate switching off illumination. (c) Current density–voltage scans recorded in two-electrode PEC setup for a perovskite photocathode. (d) Bias-free operation of the perovskite photocathode for simultaneous hydrogen evolution and glycerol oxidation. All measurements were performed in dark (dashed lines) or under 1 sun illumination (solid lines) in aqueous 2 M NaOH electrolyte containing 20 wt% glycerol.

Strain-induced modulation of the local conductance in MoS2 layers on gold nanoparticles

OTKA K 134258

Z. Osváth, A. Pálinkás, Gy. Molnár, P. Kun, A. A. Koós

This study investigates the strain modulation of local conductance in MoS2 layers induced by underlying Au NPs. By exfoliating MoS2 onto thin gold films and subsequently annealing, we create strained mono- and multilayer MoS2 structures. This process transforms the gold film into nanoparticles. To investigate the effect of strain on the local conductance of the MoS2 monolayers, we performed tunneling atomic force microscopy (TUNA) measurements. The topography of the study area is shown in Figure 8.a. Here, the larger part of the image shows gold nanostructures covered with monolayer MoS2, except for the left edge of the image, which shows a few-layer MoS2.

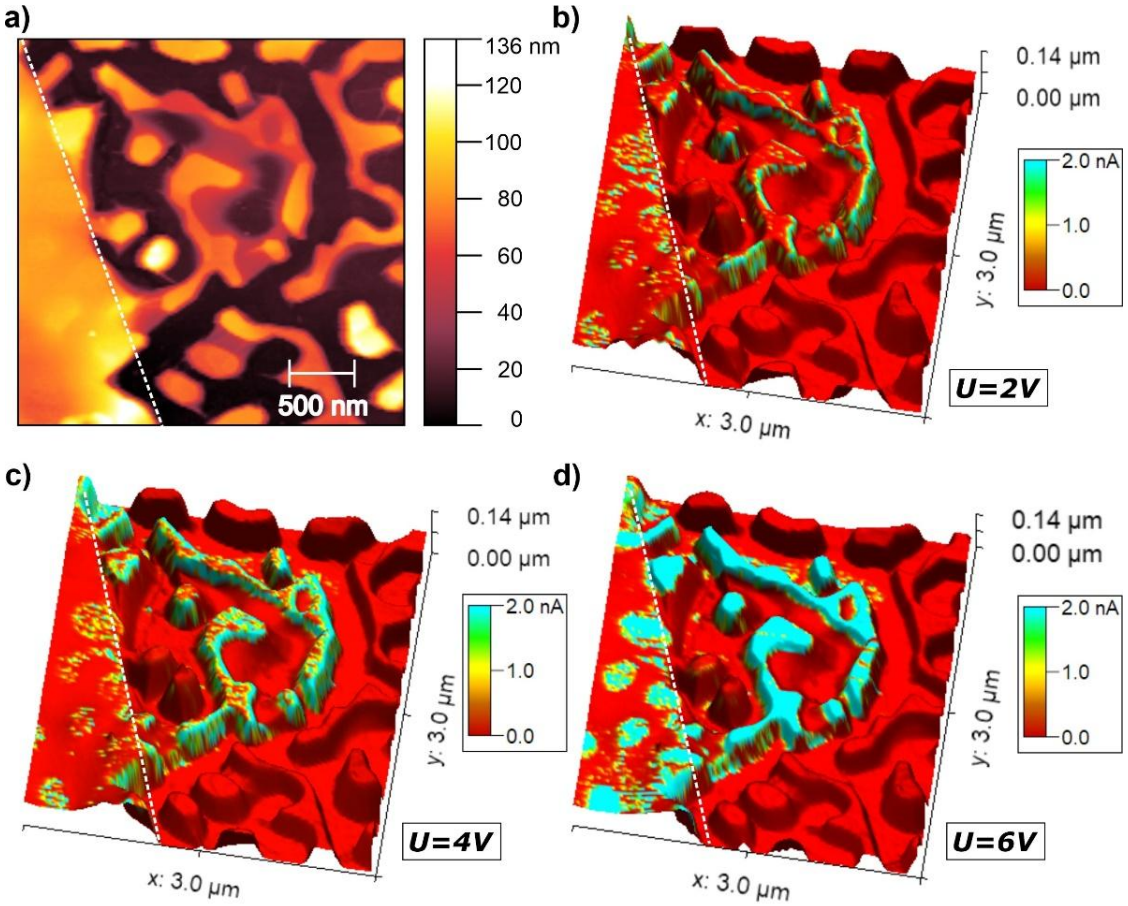

*Figure 8. (a) TUNA AFM topography and **(b)**–**(d)** tunneling current images of monolayer MoS_2 covering Au NPs. The current maps overlap with the topographic images. The dashed white line marks the few-layer/monolayer MoS_2 boundary. The tunneling current maps were measured at bias voltages (U) of 2 V (b), 4 V (c) and 6 V (d).*

The few-layer/monolayer MoS2 boundary is indicated by the dashed white line Figure 8.b–d show composite images of the tunneling current maps measured at different bias voltages (U), superimposed on the topographic image in Figure 8.a. Note that at U = 2 V (Figure 8), only some of the bent MoS2 monolayer parts display nonzero conductance. Increasing the bias voltage to 4 V (Figure 8.c) a larger region becomes conductive, and this tunneling conductance is further enhanced at U = 6 V (Figure 8.d).

It is important to note that at these higher voltages, finite conductance is measured not only on the bent parts, but also on the MoS2 parts which are directly supported by gold nanostructures. This indicates significant charge transfer from the Au NPs.

To exclude the electronic interaction with the gold, multilayer MoS2 flakes were prepared on top of Au NPs. In this case the TUNA measurements probe only the conductance of the topmost layer(s), which are not sensitive to the doping from the underlying Au NPs. alább shows a multilayer MoS2 flake on top of Au NPs.

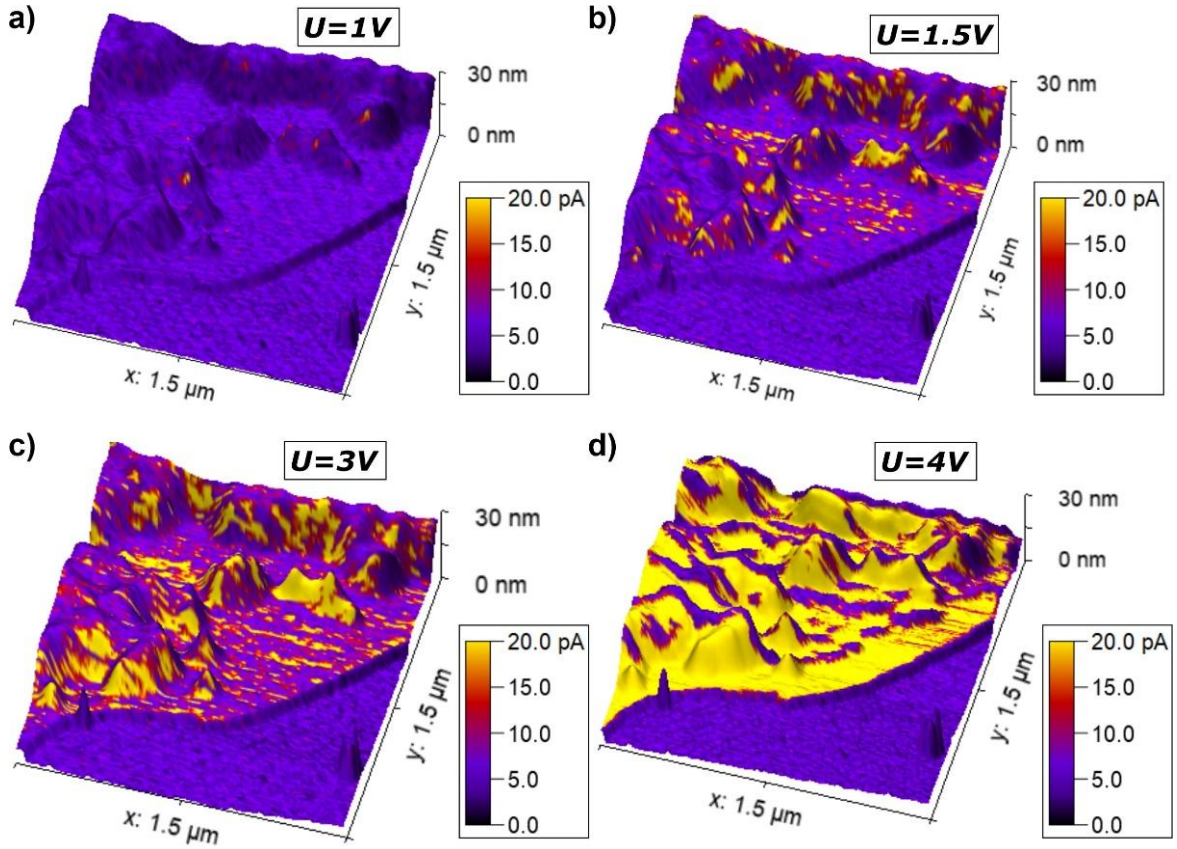

*Figure 9. TUNA AFM tunneling current maps (overlapped with the topography) measured on a multilayer MoS_2, using bias voltages (U) of 1 V (**a**), 1.5 V (**b**), 3 V (**c**), and 4 V (**d**).*

The tunneling current maps are superimposed on the topography, similarly to those in Figure 8.b–d. Using a bias voltage of U=1 V, nonzero conductance is detected only in a few specific points (Figure 9.a). Larger conducting regions are measured at U=1.5 V (Figure 9.b). These conducting domains further expand as the bias is increased to U=3 V (Figure 9.c), and at U=4 V the entire MoS2 flake is conducting (Figure 9.d). The purple stripes observed in Figure 9.d are attributed to non-conducting hydrocarbon contamination trapped from air. [Ref.3.]

Bioinspired semiconductor nanoarchitectures for environmentally friendly photocatalysis

OTKA PD 142985

K. Kertész, G. Piszter, G. Nagy, J. S. Pap, and L. P. Biró

Industrial pollutants in surface waters represent a growing environmental threat. An economical and environmentally sustainable strategy for their degradation is the utilization of virtually unlimited solar energy. Building on our experience with biotemplated photocatalysts based on butterfly wing scale nanoarchitectures, we developed novel bioinspired nanocomposites from non-toxic semiconductor materials with a scalable preparation method which makes them suitable for future industrial implementation.

Sample preparation began with an ethyl alcohol solution of zinc nitrate hexahydrate (Zn(NO3)2·6H2O), which was drop-cast onto a heated textured-glass substrate. Rapid solvent evaporation produced a sponge-like, porous zinc nitrate layer on the glass surface. The fully dried samples were then heat-treated in a tube furnace at 400 °C, resulting in complete structural transformation. X-ray diffraction (XRD) measurements confirmed the formation of ZnO with a wurtzite crystal structure, similar to ZnO thin films previously deposited on butterfly wing biotemplates by atomic layer deposition and known for their excellent photocatalytic activity.

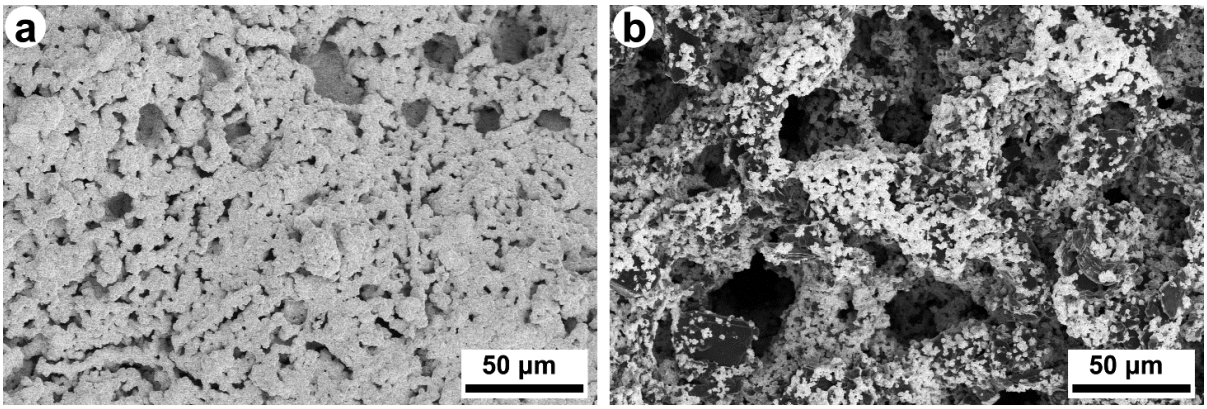

Figure 10. Scanning electron microscopy images of bioinspired ZnO nanostructures: (a) unmodified, pure ZnO; (b) ZnO-based sample doped with 10 wt% graphite nanoparticles.

A major advantage of this liquid-phase deposition method is its simplicity and suitability for coating large surface areas without the need for biological templates. The resulting structures, composed entirely of ZnO, exhibited a porous morphology resembling butterfly wing nanoarchitectures and a large catalytically active surface area. In addition, tuning the semiconductor band structure is straightforward, as dopants can be incorporated directly into the ZnO matrix by introducing them into the precursor solution or deposited onto its surface after annealing.

We investigated the optical and structural properties of the resulting bioinspired samples, as well as their photocatalytic performance, following the incorporation of various dopants (gold, graphite, MoS2, and g-C3N4 nanoparticles). Figure 10 presents scanning electron microscope images of the unmodified, pure ZnO and graphite nanoparticle-doped samples. Their nanostructures were morphologically very similar; however, their catalytic performance was found to be significantly different.

The photocatalytic performance of the samples was evaluated by the degradation of an aqueous solution of methyl orange dye under two hours of visible light irradiation. The pure ZnO structures were doped with four types of nanoparticles in three different concentrations (5, 10, and 15 wt%), and three independent measurements were performed for each sample. The photocatalytic reaction rate was found to depend on both the material quality and the additive concentration (Figure 11).

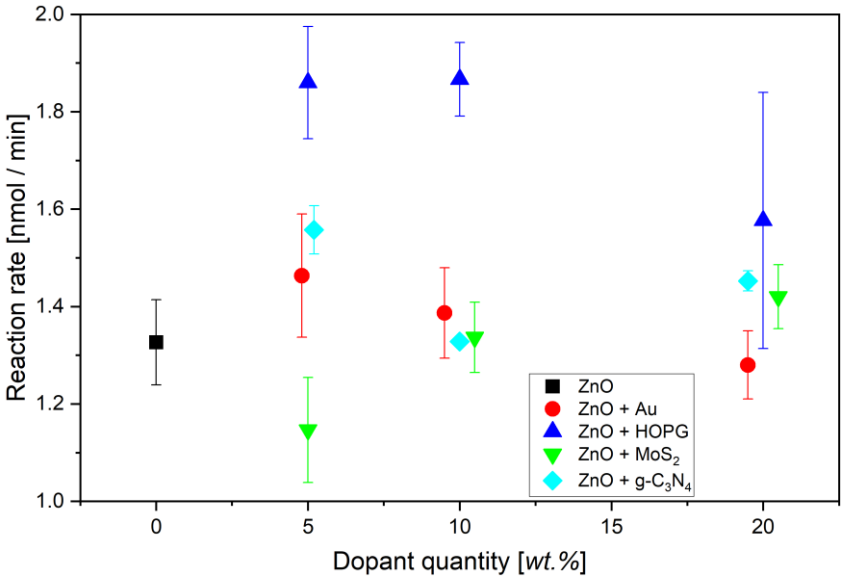

Figure 11. Photocatalytic performance of bioinspired ZnO nanostructures. The photodegradation rate of methyl orange dye was measured as a function of different additives and their concentrations.

Among the additives investigated, 10 wt% graphite nanoparticles proved to be the most effective in enhancing the photocatalytic reaction rate, closely followed by the 5 wt% sample. Their volumetric incorporation may increase dye adsorption at the surface of the nanocomposite and absorption efficiency of the incident light, resulting in markedly improved photocatalytic performance compared to the undoped sample and those containing other additives.

The results above demonstrate that nanocomposites inspired by butterfly wing photonic nanoarchitectures have significant potential in photocatalytic water purification. Although these bioinspired structures do not exactly replicate biological nanoarchitectures, they retain their advantageous properties in a form suitable for both the intended applications and also industrial-scale production.

In summary, our experimental work has progressed through the years from the detailed investigation of the structural and optical properties of photonic nanoarchitectures in butterfly wings to their application in water purification as functional biotemplates of semiconductor thin films, ultimately leading to the fabrication of bioinspired artificial structures presented in this work.

Photonics Department

Head: Dr. Peter PETRIK, D.Sc., scientific advisor

Research Staff:

Miklós Fried, D.Sc., Head of Ellipsometry Laboratory
András Deák, Ph.D., Head of Chemical Nanostructures Laboratory
Antal Gasparics, Ph.D.
Péter Márton, Ph.D.
Zoltán Lábadi, Ph.D.
Norbert Nagy, Ph.D.
Boglárka Nyerges
Ferenc Riesz, C.Sc.
Dániel Zámbó, Ph.D.
Géza Szántó, Ph.D.
Miklós Serényi, D.Sc., retired
György Kádár, D.Sc., Prof. Emeritus
Tivadar Lohner, D.Sc., Prof. Emeritus
János Makai, C.Sc., retired
András Hámori, dr. Univ., retired
György Juhász, dr. Univ., retired

Students:

Zynoda Ganieva, Ph.D. student
Noor Taha Ismael, Ph.D. student
Noémi Jakab,
Dávid Kovács, Ph.D. student
Deshabrato Mukherjee, Ph.D.
Berhane Nugusse, Ph.D. student
Máté Podráczki,
Shayesteh Raeisi, Ph.D. student
Alekszej Romanenko, Ph.D. student
Máté Stift, Ph.D. student
Chao Zeng, Ph.D. student

The Photonics Department develops unique methods and tools for non-destructive optical and magnetic measurement of surface nanostructures and materials (spectroscopy; magnetic material testing; biosensors; surface curvature measurement; surface testing; water contamination). One of the most important tasks of the Department is patenting and application of the methods in international projects with partners representing the industry and the high technology.

Key achievements of the Photonics Department in 2025 (detailed summaries of the research results can be found in the following project descriptions):

- creation of multicomponent, multimetallic nanoparticles for optoelectronic, photo- and electrocatalytic applications
- investigation of the formation and properties of metal-semiconductor and copper-oxide-shell nanostructures (formation of Cu2S quantum dot superstructures and their catalytic properties)
- new experimental and measurement results in the field of solid-liquid adhesion work measurement techniques, including on industrial samples (e.g. specially treated wheel rims)
- further development of the evaluation of Makyoh topography measurements: the effects of global curvature and illumination
- development of an in-situ investigation method for studying the electrochromic properties of combinatorial WO3/MoO3 layers
- combinatorial deposition of metal oxides for electrochromic applications
- development of sputtering processes for the preparation of gallium oxide and aluminum oxynitride layers

- characterization of sensor-targeted layers by simultaneous ellipsometric and electrochemical methods
- microscopic ellipsometer patent arising from a proof-of-concept grant
- development of materials applicable in the nuclear field
- patent procedure in progress for a method for determining thin-film phase diagrams
- formation of combinatorial plasmonic nanoparticles and their sensing properties

Validity of Young-Dupré equation for advancing and receding situations by the Capillary Bridge Probe method

N. Nagy

The need for the determination of solid-liquid adhesion work is as old as Dupré's definition of the reversible work of adhesion. In addition to its scientific importance, this quantity is a critical factor affecting product quality and performance in many industrial fields. In general, it plays crucial role if the liquid should completely cover a solid surface (e.g. coatings, paints, inks, lubricants, adhesives, pesticides) or, on the contrary, the liquid should not remain on the surface at all (liquid repellency, anti-icing, etc.).

Previously, a novel method was introduced to determine the value of adhesion work on flat surfaces directly, without the need of any model assumptions, and independently from uncertainties of contact angles. The method presented enables us to determine the adhesion work separately both for advancing and receding situations.

During a measurement cycle of capillary bridge probe, the capillary force is measured as a function of the change of bridge length that is as a function of the vertical displacement of the cylinder.

This work is only spent on changing the interfacial areas, if gravitational force is negligible. During approach and retraction, both the area of the liquid-vapor interface (A) and that of the solid-liquid interface (B) change. Consequently, the energy balance can be written as

$$-\int \vec{F} d\vec{z} = \Delta A \cdot \gamma_{LV} + \Delta B \cdot (\gamma_{SL} - \gamma_{SV}) \quad (1)$$

where $\overrightarrow{F}$ is the measured capillary force, $\vec{z}$ is the displacement of the cylinder, ΔA is the change of interfacial area between the liquid and vapor phase, and ΔB is the area change between the solid and the liquid, see Figure 12. (The value of ΔA and ΔB are also dependent on the start and end points of the interval (z-range), over which the integration is performed.)

After rearranging Equation (1), the difference term in the bracket can be expressed as:

$$(\gamma_{SL} - \gamma_{SV}) = -\frac{\int \overrightarrow{F}\, d\vec{z} + \Delta A \cdot \gamma_{LV}}{\Delta B}. \quad (2)$$

One can substitute this experimentally otherwise unattainable term into the definition of adhesion work:

$$W_a \equiv \gamma_{LV} - (\gamma_{SL} - \gamma_{SV}) \quad (3)$$

Furthermore, considering that the net force and the displacement have only z-component, the vector notation can be omitted. This resulting formula gives the value of the solid-liquid adhesion work without the need of including any contact angle in the equation:

$$W_a = \gamma_{LV} + \frac{\int F\, dz + \Delta A \cdot \gamma_{LV}}{\Delta B}. \quad (4)$$

Integration between the start and end points of approach and retraction gives the mechanical work done in the advancing and receding phases, respectively. The change of interfacial areas can be determined by simple image analysis in cylindrically symmetric case. Therefore, the solid-liquid adhesion work can be calculated according to Equation (4) for both the advancing and receding contact lines.

It is an interesting question what is the relation between the directly measured adhesion work values and the values calculated from the Young-Dupré equation? In other words: is the Young-Dupré equation valid separately for advancing and receding situations?

In Figure 12, the directly measured adhesion work values were plotted. The blue and red points represent the work of adhesion measured in the advancing and receding phase, respectively. The green points were measured in readvancing situation. This readvancing effect can be observed in case of perfect wetting: the receding contact line starts to advance again during the retraction of the cylinder. (The readvancing contact line already finds wetted surface in front of it; hence the measured contact angle is lower than in the receding situation, its value is typically ≤1°.) The corresponding vertical error

bars show the standard deviation of the directly measured adhesion work values determined according to the above-described procedure. The adhesion work values were plotted as a function of contact angle, of which values were measured during the same capillary bridge probe measurement and obtained by analytic evaluation as described previously. The horizontal error bars show their standard deviation.

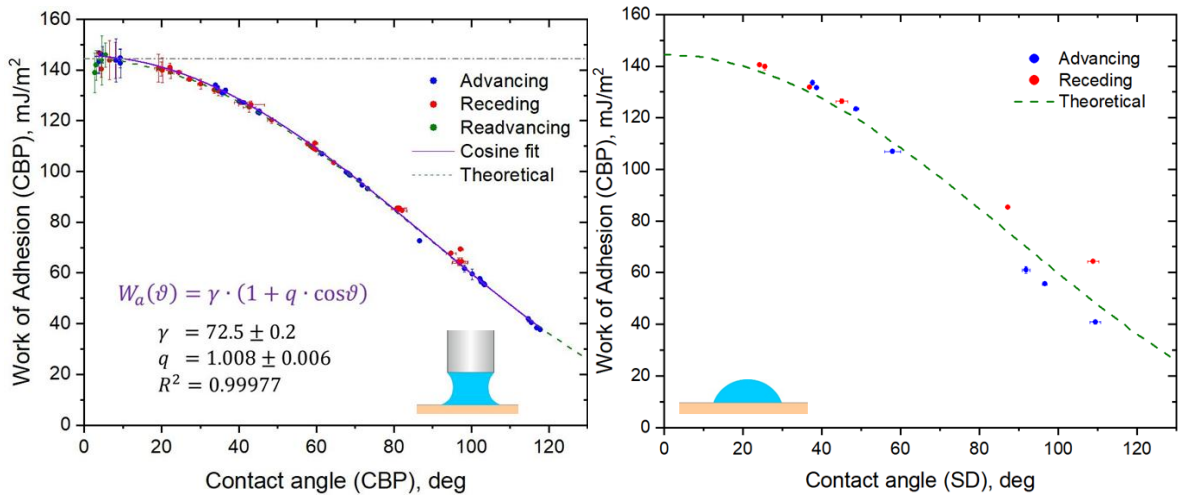

Figure 12. (left) Directly measured adhesion work values as a function of contact angles determined during the same capillary bridge probe (CBP) measurement. The inset shows the result of the fit of a general cosine function to all measurement points. The fitted purple curve is in excellent agreement with the theoretical dashed green curve corresponding to the Young–Dupré equation. For this validation, metal, semiconductor, dielectric, and polymer surfaces were measured in clean, contaminated, acid-, and plasma-treated condition using ultrapure water as test liquid. (right) Work of adhesion values measured by capillary bridge probe (CBP) as a function of water contact angles determined by the sessile drop (SD) method. The purple dashed line represents the theoretical prediction of the Young–Dupré equation.

In conclusion, accurately measured advancing and receding contact angles can be used to calculate the adhesion work for the two different situations. It is worth to note that the calculation of adhesion work from the Young–Dupré equation relies on the precise measurement of the contact angle. When for instance, the directly measured adhesion work is plotted against the sessile drop contact angles, the correlation is of much lower quality (Figure 12 (right)). Furthermore, in accordance with the previous consequence, this novel direct method provides an additional advantage: if the receding contact angle is not a stationary definite value, an effective receding contact angle can be calculated from the measured adhesion work using the Young–Dupré equation. [Ref.4.], [Ref.5.], [Ref.6.].

A novel, photoassisted synthetic route to transform Cu2O nanooctahedra to Cu2S quantum-dot superstructures

OTKA FK 142148; TKP2021-NKTA-05

D. Kovács, G. Z. Radnóczi, Zs. E. Horváth, K. Frey, A. Sulyok, Z. Fogarassy, J. S. Pap, A. Deák, D. Zámbó

The family of copper-sulfides includes numerous materials, which are relevant in minerology as well as in nanoscience and possess various stoichiometries (hence, they can be denoted as Cu2-xS, where the $0<x<1$). For well-defined nanocrystals or nanoparticle-based materials, the structure, composition and stoichiometry have a profound impact on the optical and electrochemical properties. The main challenge in synthesizing copper chalcogenides is closely connected to the ability of natural oxidation and sulfidation of chalcophile metals such as Cu or Ag. This technically means that copper sulfides and oxides tend to oxidize and sulfidize at ambient conditions, respectively.

In the recent years we have developed a reliable strategy for the synthesis of Cu2O nanooctahedra showing excellent morphological stability, tunable optical and enhanced catalytic activity. However, even in optimized storage conditions (dark, 4°C, ethanol as solvent), the particles' composition and morphology slightly changed after 8 months of storage. We have shown that the particles undergo partial natural sulfidation which phenomenon can be linked to the presence of thiolated molecules and inorganic sulfur compounds in the atmosphere. This natural process motivated us to develop a novel strategy of the transformation of Cu2O nanooctahedra to copper sulfide particles by using a small-chain thiolated alcohol (β-mercaptoethanol, BME) to initiate the oxide-sulfide transition wet-chemically. [Ref.7.] The schematics in Figure 13 shows the steps of the synthesis.

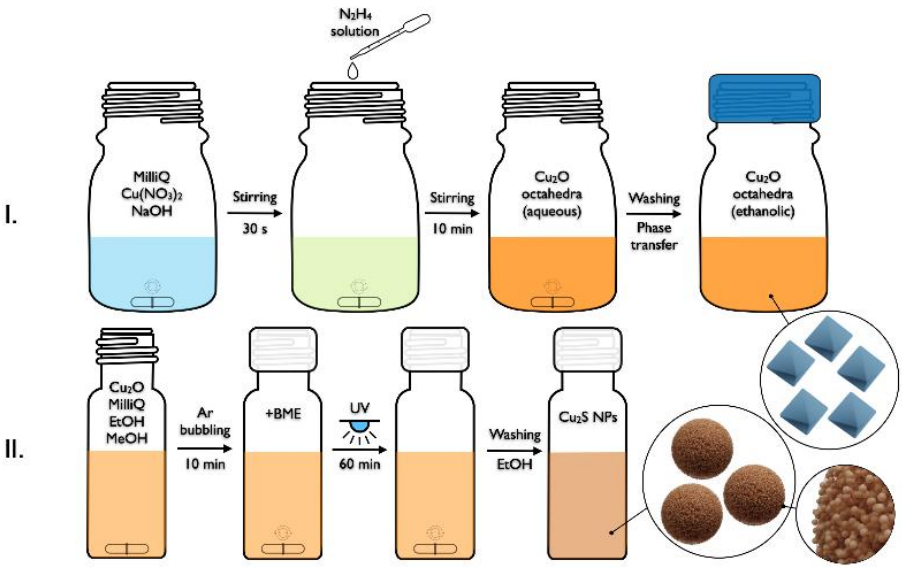

Figure 13. Schematics on the synthesis of Cu2O nanooctahedra and their photoassisted chemical transformation to Cu2S quantum-dot superstructures. [1]

The presence of mercaptoethanol itself does not generate well-defined copper sulfide species due to the oxidation and sulfidation occurring simultaneously at ambient conditions. This results in partially sulfidize particles and overoxidized (CuO) fibers in the solution. This oxidation pathway can be successfully eliminated by applying inert atmosphere (Ar) and UV-light illumination enabling the

reliable synthesis of colloidally stable, spherical copper sulfide particles. The optical properties change stepwise upon increasing the amount of added BME showing a shifting peak position from ca. 550 nm to 400 nm and a broadening (Figure 14.a). Interestingly, the TEM investigations reveal the presence of small (4-5 nm) quantum dots building up the larger copper sulfide particles. Moreover, the dots are separated by an amorphous organic thin layer. Elemental mapping confirmed that the ca. 250 nm in diameter spheres consist of Cu and S, and the low amount of O is present (Figure 14.b). However, this oxygen content cannot be further suppressed, which implies the existence of a stable copper sulfide phase and another oxygen-containing species.

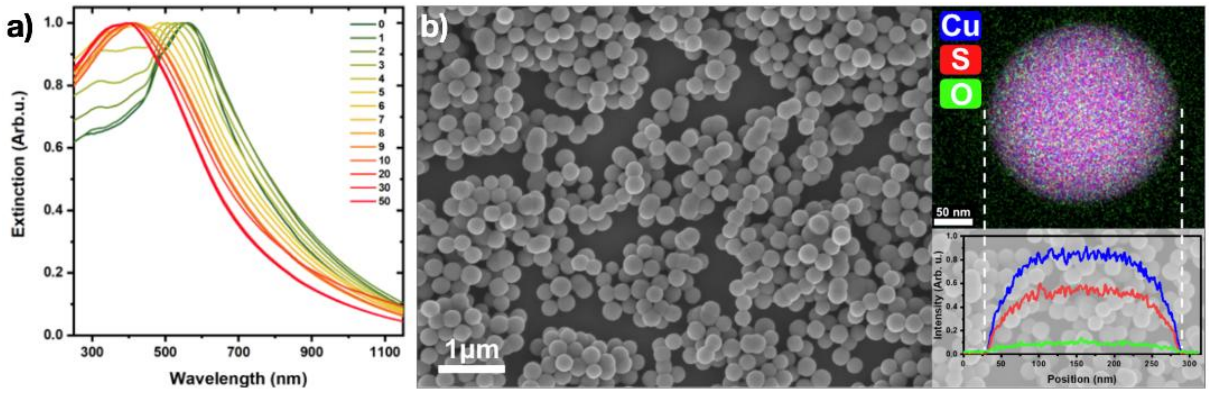

Figure 14. Evolution of the extinction spectrum upon increasing the concentration of BME (a). SEM image and TEM elemental map of the Cu2S particles (b). [Ref.7]

Performing advanced TEM sample preparation method and SAED, the precise stoichiometry and phase of the nanospheres could be identified (Figure 15.a-c). The sulfidized particles are superstructures consisting of small Cu2S quantum dots, which are separated by a thin layer of organic thiol. Furthermore, these spherical particles can be decorated with small Au nanograins to achieve a semiconductor-metal multicomponent nanosystem, where the photogenerated carriers can be spatially separated. Macroscopic electrodes from the Cu2S and Cu2S/Au particles can be prepared on a conductive substrate, thus, the electrochemical properties of the model systems were also investigated. Open circuit potentiometry (Figure 15.d) revealed that all synthesized nanoparticle electrodes show p-type nature, and the presence of Au suggests an enhanced charge carrier separation. Under chopped light illumination, the electrodes generate cathodic current which reaches the maximum value of 50 µAcm-2 for the Cu2S@Au platform (Figure 15.e). After negative polarization, the particles at the surface of the ITO remain morphologically stable (Figure 15.f) which suggest their potential use in (photo)electrochemical processes. [Ref.7.]

Regarding the formation mechanism of the Cu2S quantum-dot superstructures, the following pathway can be proposed (Figure 16): reactive sulfur species (RSS) are formed from the organic thiol upon high-energy UV illumination facilitating first the homolytic cleavage of the S-H bond or the disulfide (S-S) bond. These (most probably thiyl) radicals can interact with the surface Cu centers of the copper oxide nanoparticles initiating a gradual anion (from O to S) in the sublattice. Simultaneously, UV light generates charge carriers in the Cu2O itself, from which the electrons can reduce the surface-bound organocopper species to provide sulfur for the ion exchange reaction. This work sheds light on the complex formation mechanism, the optimal conditions and the optical, structural and electrochemical properties of novel Cu2S superstructures prepared from Cu2O sacrificial template. [Ref.7.].

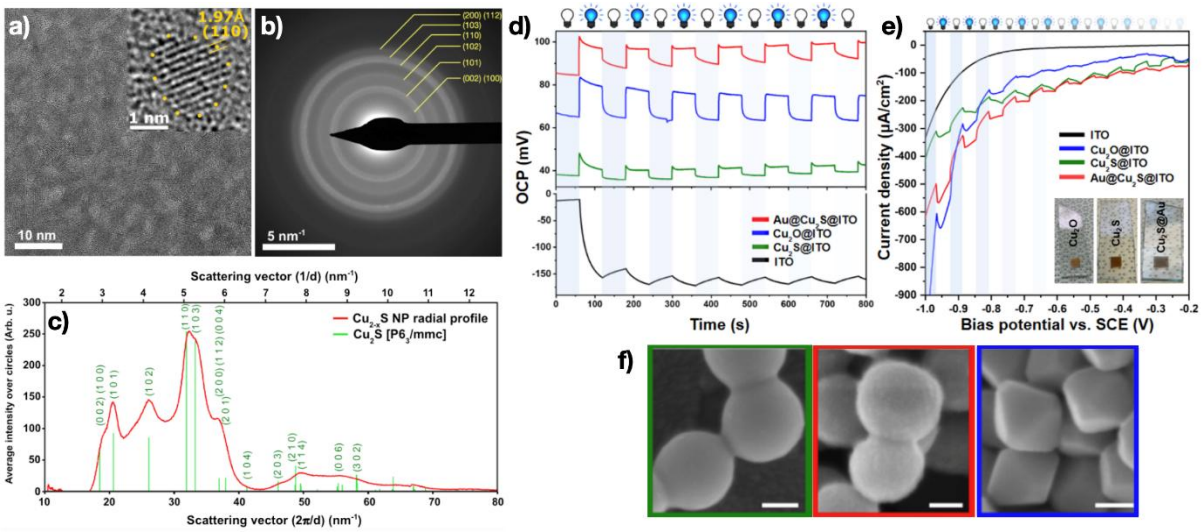

Figure 15. Phase identification (a-e) and electrochemical investigations (d-f) on the synthesized nanoparticles. [Ref.7]

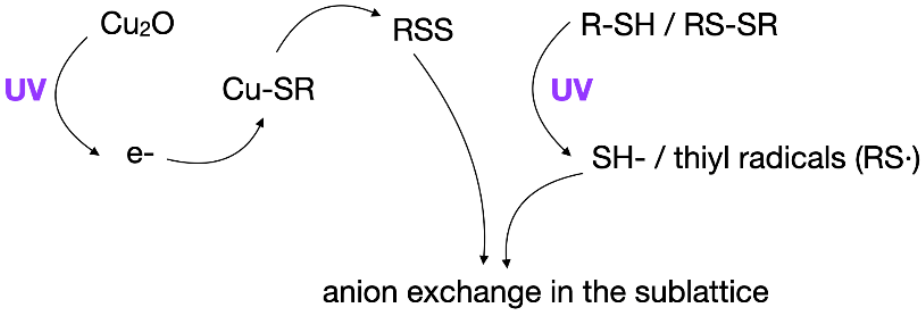

Figure 16. Proposed mechanism of the Cu2O-Cu2S photoassisted transformation process.

Acknowledgement: D.K. acknowledges the support of Pro Progressio and the József Varga Foundation. Project no. TKP2021-NKTA-05 has been implemented with the support provided by the Ministry of Innovation and Technology of Hungary from the National Research, Development, and Innovation Fund (NRDI), financed under the TKP2021 funding scheme. The work was financially supported by the NRDI Fund of Hungary under the grant OTKA FK 142148.

The work has been selected as the „Paper of the month" by the Section of Chemical Sciences of the Hungarian Academy of Sciences in September, 2025: https://mta.hu/vii-osztaly-a-honap-publikacioja/2025-szeptemberi-kiemelt-publikaciok-114720

Spatial modulation of Cu2O shell growth on gold nanoprisms

OTKA FK 142148, TKP2021-NKTA-05

Z. Ganieva, D. Kovács, Z. Osváth, D. Zámbó, and A. Deák

Environmentally friendly and earth abundant metal oxide semiconductors are intensively studied for optoelectronic and catalytic applications, but they suffer from low charge carrier mobilities, that represents a major obstacle for their large-scale use. Nanoscale metal/metal-oxide nanoparticles might help in this regard, as at this scale recombination processes might be suppressed and a more efficient separation of the charge carriers generated in the semiconductor domain could be achieved. [Ref.8.]. Another advantage in such hybrid systems might come from the possibility to harvest hot carriers from the metal. Theoretically, the hot carriers generated in the plasmonic metal nanoparticles have to overcome only the Schottky barrier formed at the metal/oxide semiconductor interface, hence charge injection into the semiconductor and contribute to the efficiency of optoelectronic processes at the semiconductor. In this regard, partial core/shell structures are especially appealing, as they allow the simultaneous access both the metal and semiconductor domains. Cu_2O is a p-type semiconductor with its optical band-gap located in the visible wavelength range and has an excellent combability with gold, allowing the wet-chemical growth of a Cu_2O shell around gold nanoprisms [Ref.9.].

In this work we used the controlled spatial modulation of the gold nanoprisms' surface energy to partially prevent Cu_2O deposition on gold nanoprisms [Ref.10]. The approach relies on the inhomogeneous accumulation of a thiol molecule (5-amino-2-mercaptobenzimidazole - AMBI) on the prisms' surface during a surface modification reaction prior to Cu_2O deposition. AMBI is known to effectively block the deposition of Cu_2O on gold nanoparticles, provided it is present at a sufficient high packing density at the interface. Under appropriate conditions in terms of reaction temperature and AMBI concentration, submonolayer coverage of the prisms can be achieved, showing the presence of some high-density molecular patches (Figure 17). Already at concentrations that show a patchy AMBI adsorption at the nanoprisms' flat faces (Figure 17.b), almost complete coverage of the side and tip regions can be anticipated due to the higher energy binding sites in these regions, which can be exploited the reduce the Cu_2O deposition in these particle regions during the wet-chemical growth of the shell.

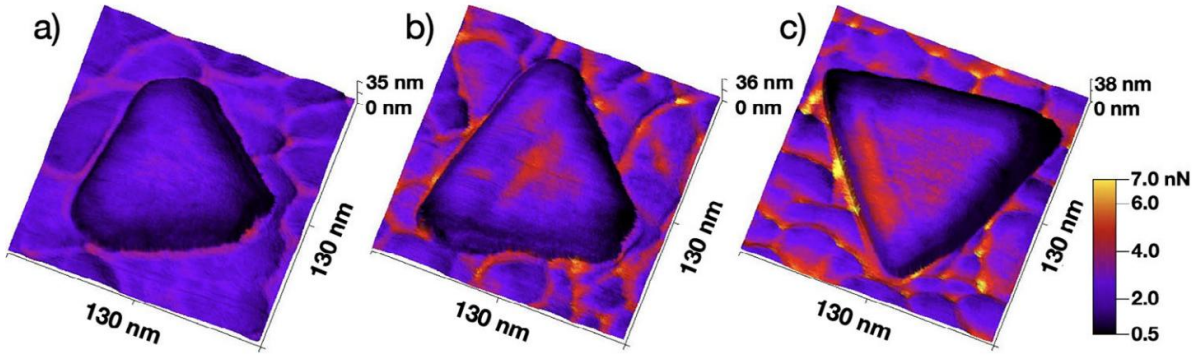

Figure 17. Scanning probe microscopy derived topography of the indium tin oxide supported nanoprisms overlain with the adhesion force maps: no AMBI treatment a) and surface modification at 1 μm b), and 190.5 μm AMBI c). [Ref.10.]

This was confirmed by investigating the evolution of the Cu_2O shell growth over the reaction time, quenching the process at different time instances and investigating the particle morphology ex-situ by transmission electron microscopy (Figure 18). If AMBI is absent, Cu_2O forms a neat shell around the gold nanoprisms in a shape conform manner (top row). When the gold nanoprisms are pretreated with AMBI under optimised conditions, however, strong structural inhomogeneity of the shell develops. The number of nucleation sites is strongly reduced, which is especially clear in the early phase of the shell growth. It must be stressed that the few Cu_2O domains on the prism surface in the presence of AMBI in the beginning phase (15 s) agreed well with the scanning probe microscopy derived adhesion map pattern. Nevertheless, the observed Moiré pattern for these few dots indicates that the excellent compatibility between the gold and Cu_2O is preserved at the nucleation sites. At later growth stages the initial Cu_2O domains grow larger and fuse together. It seems, however, that the combination of AMBI coverage and the surface curvature at the prism tips effectively prevents the growing and fusing Cu_2O domains to engulf the prism tips, leaving then exposed even after the competition of the growth process.

The prepared structure ensures the simultaneous access of both the metal and semiconductor domains and hence can be of interest for optoelectronic and catalytic use. Additionally, the high optical near field at the prism tips that develop upon exciting localised plasmons at the prisms can also be utilised.

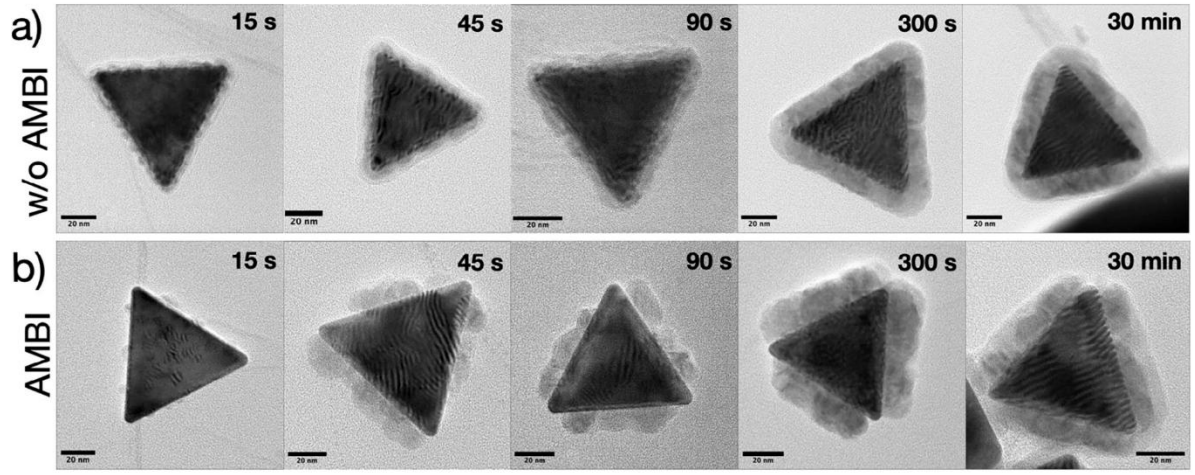

Figure 18. TEM images of the Cu2O/Au nanoparticles prepared without (upper row) and in the presence of AMBI (lower row). [Ref.10.]

Electrochemical Methods and Ellipsometric Characterization of Gold Nanoparticle-Based Sensors

OTKA K 146181

M. K. Stift, A. Bonyár, Z. Lábadi, É. Tóth, H. Jankovics, F. Vonderviszt, P. Petrik

Heavy-metal ions in drinking water can lead to serious health risks even at low concentrations, and rapid, on-site monitoring remains a major challenge. Our aim is to develop a portable electrochemical sensor concept that combines selective biomolecular recognition with fast and objective readout, while making sure that it can be used without skilled labor [Ref.11.].

Our sensing interface is built from an electrochemically deposited gold nanoparticle (AuNP) layer formed on an Au-evaporated silicon substrate and a layer of genetically engineered flagellin filaments immobilized on the nanostructured surface. This approach is based on prior work at the Photonics Laboratory demonstrating that bioengineered flagellar nanotubes can be immobilized on gold surfaces and used to create selective sensing layers for Ni(II) detection [Ref.11.], [Ref.12.]. Figure 19 shows the Au-evaporated 15 x 15 mm silicon substrate before electrochemical treatment.

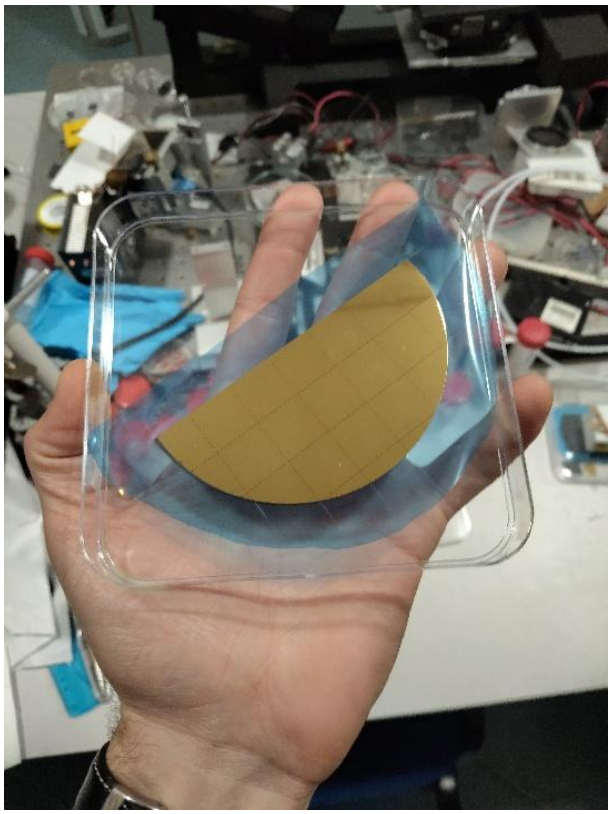

Figure 19. Au-evaporated silicon substrate (15 x 15 mm) before the electrochemical deposition treatments.

AuNP growth and specific protein immobilization were performed in a three-electrode electrochemical cell using different amperometry methods such as preparative cyclic voltammetry and chronoamperometry. Cyclic voltammetry provides a convenient way to track redox changes and characterize the response of the sensor through certain anodic and cathodic peaks [Ref.13.], [Ref.14.].

Throughout the deposition steps, in-situ spectroscopic ellipsometry was used as a non-invasive optical monitoring method to follow the changes on the surface during the electrochemical processes. So to conclude, our approach was a combined electrochemical-optical workflow.

Figure 20 shows a SEM image after AuNP deposition and subsequent protein immobilization. It illustrates an adequate nanostructured gold surface; together with electrochemical measurements in Ni(II)-containing solutions, the results support the feasibility of semi-quantitative Ni detection and motivate further selectivity studies with additional heavy-metal ions. [Ref.11.]

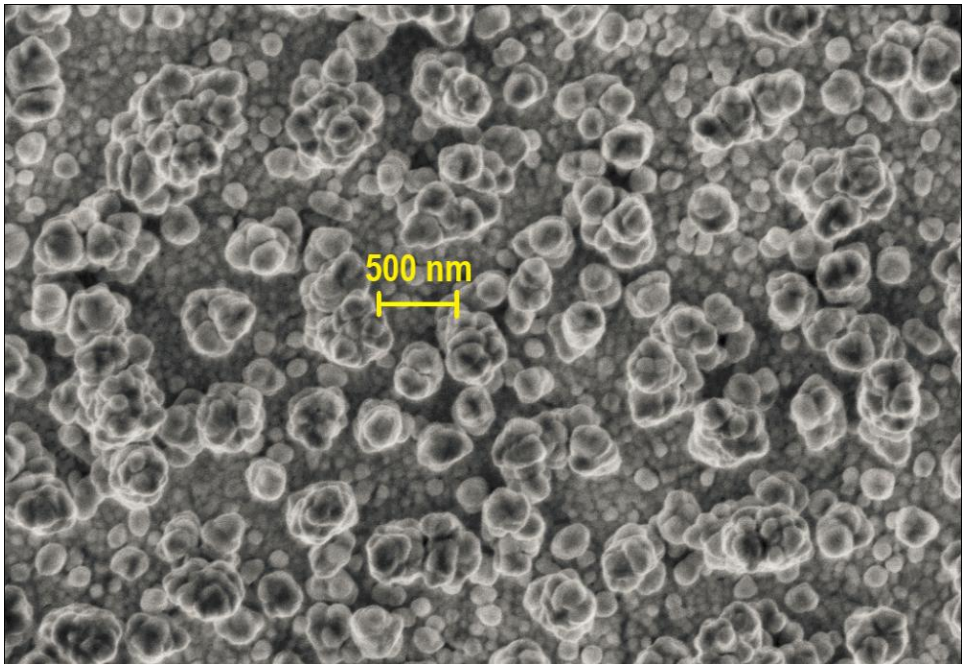

Figure 20. SEM image of the surface after electrochemical AuNP deposition and immobilization of engineered protein filaments.

Investigation of in- and out-diffusion of Li-ions in electrochromic tungsten-molybdenum combinatorial oxide films by spectroscopic ellipsometry

OTKA K 143216, OTKA K 146181

Z. Lábadi, P. Petrik and M. Fried

Reactive (Ar-O_2 plasma) magnetron sputtered WO_3-MoO_3 mixed oxide electrochromic layers [Ref.16] were deposited onto a 4' [100] silicon wafer. The layer was composition graded (i.e. WO_3 content changed in the 0-100% range alongside the wafer diameter).

We determined and mapped the composition and optical parameters. Measurements were done in a liquid electrochemical cell using Spectroscopic Ellipsometry (SE). Electrochemical measurements were performed in 1M lithium perchlorate (LiClO4) / propylene carbonate electrolyte.

Different optical models, such as the Bruggeman Effective Medium Approximation (BEMA) or the 2-Tauc–Lorentz multiple oscillator model (2T–L), were used to obtain the thickness and composition maps of the sample. Scanning Electron Microscopy (SEM) with Energy-Dispersive X-ray Spectroscopy (EDS) has been used to check the SE results. The performance of diverse optical models has been compared. We showed that in the case of molecular-level mixed layers, 2T–L is better than EMA. [Ref.15.] Figure 21 shows the experimental arrangement for the combined SE and electrochemical measurement.

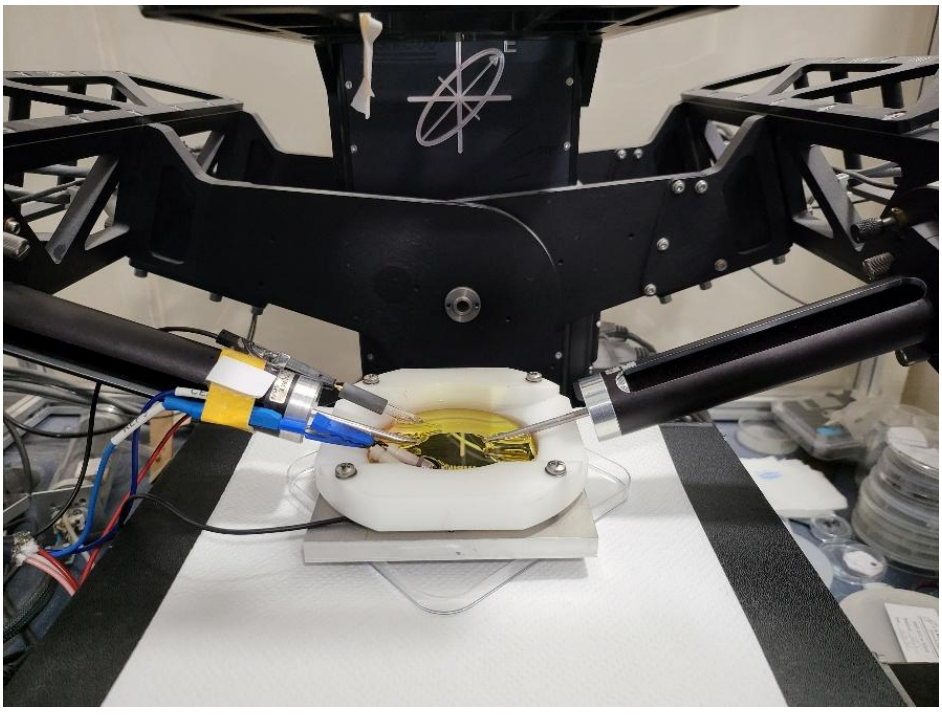

Figure 21. Experimental arrangement for in-situ SE measurements in the electrochemical liquid cell.

Electrochromic coloration efficiency (CE) as a function of composition (Figure 22) was established on independent transparent samples [Ref.17] (Coloration Efficiency measures the amount of optical change per unit of charge injected into the material. Higher CE indicates more efficient use of energy and can lead to lower power consumption in devices.)

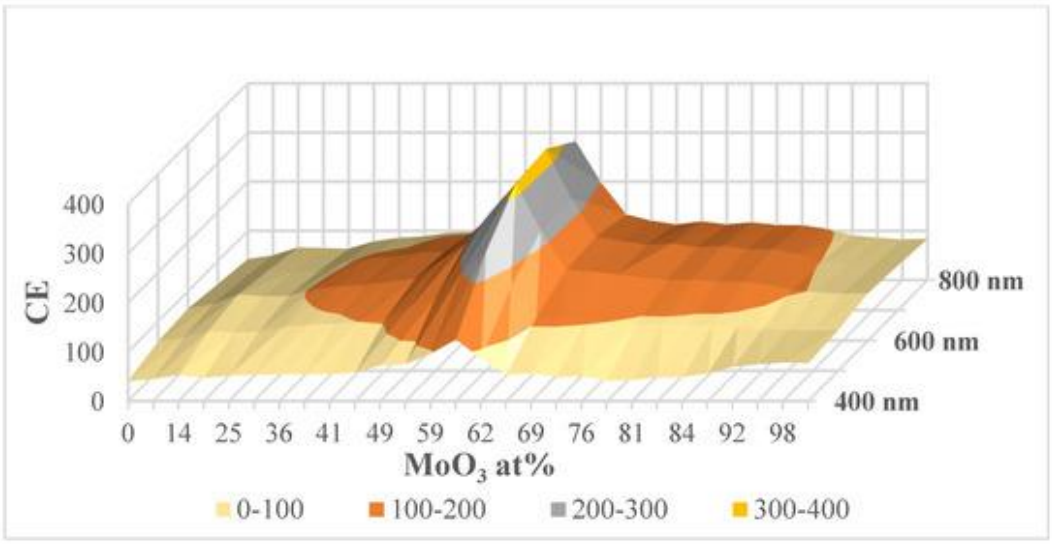

Figure 22. Calculated CE data as a function of MoO3 fraction—3D graphical representation.

After determining the thickness and composition maps the sample was forced through electrochemical reduction and oxidation cycles. Controlled current was applied through the cell setting up reversible electrochemical cycles of coloration and bleaching [Ref.16.]. SE measurements were recorded in the central position in-situ, real-time and full mapping after the last coloration cycle. Ellipsometric spectra were evaluated using a multi-layer, multi-parameter optical model. Components of complex refractive indices were attributed to the in- and outdiffusion of Li into the oxide layer.

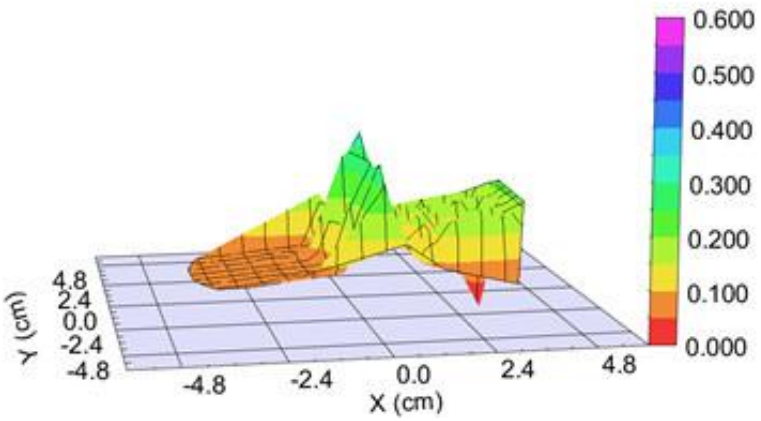

Figure 23. Amplitude of the k (extinction) parameter as a function of the position.

Optical model (used for dry mapping after electrochromic experiment) consisted of the following layers: Air - Surface roughness - Cauchy disp. (mixed layer + Li) - intermixed – Gold substrate.

Figure 23 shows the measured k parameter map. The k Amplitude (extinction) parameter can be considered as a good indicator of Coloration Efficiency. The maximum k value shows that the optimal composition is at 75 % MoO3 – 25 % WO3 composition. Changes in the k parameter in the top layer are proper indicators of the in- and out-diffusion of Li-atoms. Increasing Li concentration causes higher k values. The coloration process therefore can be in situ monitored by SE combined with appropriate optical model.

Effects of global curvature and illumination conditions on magic-mirror imaging

OTKA K 146181

F. Riesz

Magic mirrors (in Japanese, Makyoh) are bronze mirrors with a backside relief pattern, originating from ancient China and Japan. If a light beam falls on the mirror surface, an image is projected on a distant wall that resembles the back pattern as if the mirror was transparent [Ref.17.]. These mirrors fascinated laymen and scholars alike during centuries, and since the 19th century, when Western scholars became aware of these mirrors, they have been actively studied. It was clarified that a nearly invisible surface relief is formed on the polished front face during manufacturing by mechanical means of the back relief. The image is then created by the local deflection of the reflected rays by this front relief; more precisely, the image intensity at a screen point is related to the local curvatures of the corresponding mirror surface element. The principle's fruitful modern application is 'Makyoh topography', used mostly for the visualisation of surface defects of semiconductor wafers.

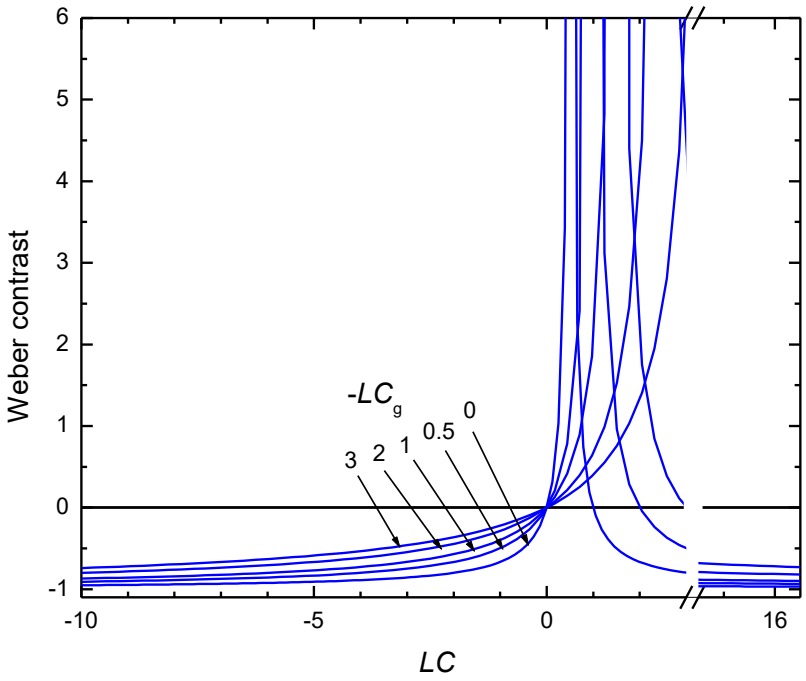

Figure 24. Dependence of the image contrast on local and global curvatures

Most ancient magic mirrors possess a global convexity, semiconductor wafers may also be curved or warped, thus the effect of global curvature is worthy of attention. It has been shown earlier using a geometrical optical analysis [Ref.18.] that a C_g global curvature (in addition to the trivial effects of image magnification and intensity reduction) can be considered by introducing an effective screen distance L_{eff} given as the reciprocal addition of the physical screen distance L and -1/(2C_g). That is, a uniformly curved mirror with a surface relief behaves as a flat mirror with the surface relief "cascaded" with a curved mirror without a relief. The contrast relations can also be analysed using elemental models [Ref.19.]. Even though the models are simple, there are several ways to visualise the results, each emphasising different aspects of the phenomenon. Figure 24 shows a possible way: one-dimensionally curved surface elements are considered on a spherically curved mean surface, and the Weber contrast values of these elements are plotted against the curvature normalised with L for various global

curvatures, that is, each point in a curve represents a given position of the mirror. The main conclusions are that the global convex curvature decreases contrast and decreases the sensitivity of the contrast to screen distance.

Original magic mirrors are meant to be illuminated by the Sun, that is, a collimated source. For modern demonstrations, exhibitions, as well as sometimes in semiconductor topography, the more convenient point source is used. This is optically equivalent to the introduction of a global convex curvature with radius twice the source distance (Figure 25). This leads to the appearance of the curvature effects outlined above even for a flat mirror: the reciprocal addition rule renders the sensitivity of the image pattern to screen distance reduced (a phenomenon often observed in magic mirrors), leading to an upper limit of the effective screen distance, thus, limited sensitivity in the topography application.

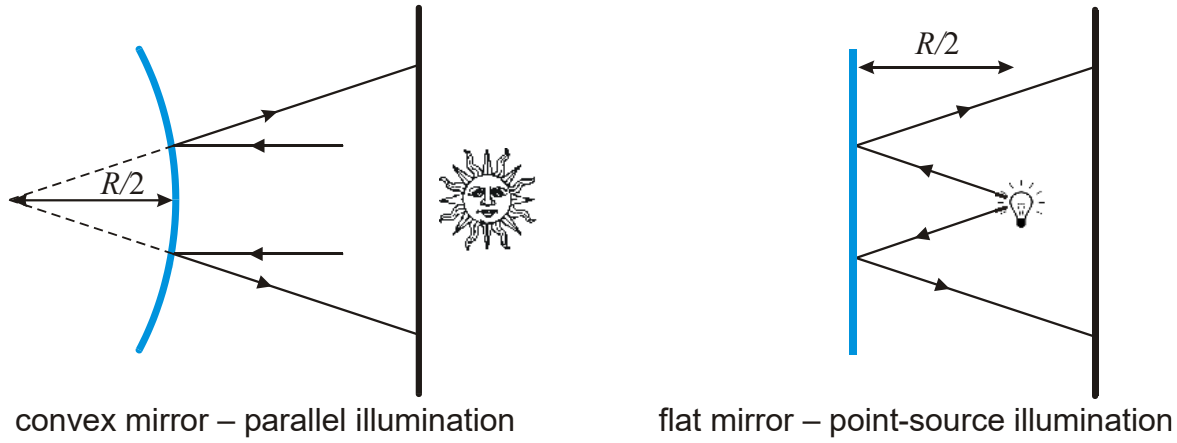

Figure 25. Optical equivalence of a globally convex mirror and a flat mirror with point-source illumination

Thin Film Physics Department

Head: Dr. Katalin BALÁZSI, Ph.D., senior scientist

Research Staff

Alaa Almansoori, Ph.D.
Csaba Balázsi, D.Sc.
Ildikó Cora, Ph.D.
Zsolt Czigány, D.Sc.
Zsolt Fogarassy, Ph.D.
Klára Hajagos-Nagy, Ph.D. (Maternity Leave)
Mónika Furkó, Ph.D.
Tamás Kolonits, Ph.D.
Viktória Kovácsné-Kis, Ph.D.
Olga Krafcsik, Ph.D. (50%)
Béla Pécz, D.Sc., Deputy General Director of HUN-REN EK, MFA Director
György Zoltán Radnóczi, Ph.D.
Adél Rácz, Ph.D.
György Sáfrán, D.Sc.
Attila Sulyok, Ph.D.
Péter B. Barna, D.Sc., Prof. Emeritus
Miklós Menyhárd, D.Sc., Prof. Emeritus
György Radnóczi, D.Sc., Prof. Emeritus
János Lábár, D.Sc, Prof. Emeritus

Ph.D. Students

Dániel Olasz
Erzsébet Dódony
Maroua H. Kaou
Wasan Alkaron (Hungaricum Stipendium)
Boglárka Ódor Almássy

Technical Staff

Andrea Jakab-Fenyvesiné
Andor Kovács
Balázs Erki
Valéria Osváth
Noémi Szász
Viktor Varga

The scientific results of the Thin Film Physics Department are related to thin film, technical and bioceramic fields. The main research topics are in line with modern trends of material science with respect to a 65-year long history of the department.

The development of the 2D semiconductor, multicomponent, semiconductor thin films and technical ceramics were the important base research fields supported by several international basic scientific projects and collaborations in 2025.

The Department's unique strength, both nationally and internationally, lies in the structural investigation of various materials using transmission electron microscopy (TEM). Through TEM analyses, the relationship between microstructure and the resulting material properties was systematically demonstrated. These research activities were strongly supported by methodological developments based on electron diffraction techniques.

In 2025, the Department published 50 scientific papers in peer-reviewed journals, including D1- and Q1-ranked publications, with a cumulative impact factor of 260. Members of the research group delivered invited lectures and contributed oral presentations at numerous national and international conferences. During the last two years, the group received approximately 4,300 independent citations.

Researchers of the group also contributed extensively to higher education by teaching semester-long university courses and conducting laboratory practices at Eötvös Loránd University, Budapest

University of Technology and Economics, University of Pannonia, and Óbuda University. In addition, five PhD students were supervised by members of the group.

Members of the Thin Film Physics Department also played an active role in organizing several national and international scientific conferences, thereby contributing significantly to the advancement and dissemination of scientific knowledge within the field:

- 49th International Conference and Expo on Advanced Ceramics and Composites (ICACC2024) USA – Balázsi Csaba, Balázsi Katalin (symposium lead org.)) Daytona Beach, USA 2025 January 26-31
- IXth Conference of the European Ceramic Society, August 31 to September 4, 2025, International Congress Center in Dresden, Germany (EU), Balázsi Csaba, Balázsi Katalin (scientific committee members)
- The Ninth International Symposium on Dielectric Materials and Applications (ISyDMA'9), Faculty of Sciences Semlalia, Cadi Ayyad University and The Executive Committee of ISyDMA, 7–9 May 2025, Marrakech, Morocco Balázsi Csaba, Balázsi Katalin (scientific committee members)
- Global Forum on ADVANCED MATERIALS AND TECHNOLOGIES FOR SUSTAINABLE DEVELOPMENT (GFMAT-3) Sheraton San Diego, 2026.05.31-06.05 (USA) – Katalin Balázsi (symposium lead organizer)
- Annual conference of the Hungarian Microscopic Society 2025 (MMT) Siófok 2025 May – Pécz Béla, Lábár János Radnóczi Gy. Zoltán
- Multinational Congress on Microscopy, Portoroz, Slovenia, 2025. september 7-12, “Magnetic, ferroelectric, and spintronic materials” symposium leader Viktória Kovácsné Kis

Social activity of the group is landmarked by nearly 20 memberships in different committees of the Hungarian Academy of Sciences and in boards of international societies such as the European and American Ceramic Society, the International Ceramic Society and the International Union for Vacuum Science.

Composition-dependent structural and optical properties of combinatorially deposited, RF sputtered gallium oxynitride layers

TKP2021-NKTA-05

M. Gajdics, I. Cora, T. Kolonits, Gy. Sáfrán, E. Szilágyi, Zs. Zolnai and B. Pécz

Recently, Ga-based semiconductor thin films have gained increasing interest in the field of electronics and optoelectronics. GaN is commonly used in blue LEDs and in high-electron mobility transistors, while Ga2O3 can be utilized in rectifiers and solar-blind UV photodetectors. In comparison, gallium oxynitrides are in a less developed state. Nevertheless, gallium oxynitrides present promising optical and electronic properties for the use in various electronic and optoelectronic applications. The possibility to tune these properties through the control of the elemental composition of Ga-O-N is an important aspect of these materials. Previous works only studied gallium oxynitrides with specific compositions and the relationship between optical properties and elemental composition is still not fully explored.

In this work we used a combinatorial method to deposit a gallium oxynitride film with continuous composition gradient within the sample. This approach enabled us to map the optical and structural properties of the sample as a function of composition and accelerated the exploration of composition-property relationships. The combinatorial films were deposited using reactive radio-frequency (RF) sputtering where the nitrogen partial pressure was kept constant, while the oxygen flow rate (and hence the partial pressure) varied using a gas flow controller. The sputtering gas mixture also contained Ar and different N2/Ar partial pressure ratios were tested to cover as wide composition range as possible. The composition of the films was determined by Energy Dispersive X-ray Spectroscopy and Elastic Recoil Detection Analysis. The optical properties of the samples were investigated by Spectroscopic Ellipsometry both in reflection and in transmission mode. Structural characterization was performed by X-ray Diffraction and Transmission Electron Microscopy.

As the oxygen flow rate decreased in the vacuum chamber, the oxygen content of the samples decreased and simultaneously the refractive index increased. Refractive indices ranging from the index of Ga2O3 to the index of GaN were measured. The optical transmission of the film also changed as the oxygen content decreased, namely, the absorption edge shifted to higher wavelengths and the transmittance in the visible region decreased. The optical bandgap of the material decreased from that of Ga2O3 to that of GaN with decreasing oxygen flow rate. These results show that by controlling the deposition parameters the elemental composition and the optical properties of the samples can be tuned. Combinatorial samples with different N2/Ar partial pressure ratios were prepared and the compositional variation, the refractive index and the optical bandgap are plotted in the ternary diagrams of Figure 26.a-b-c respectively. From Figure 26.b-c it is clear the same refractive index/optical gap can occur for multiple different compositions (see dotted lines in Figure 26.b. To further characterize the relationship between these properties, it is useful to find a parameter that is invariant for the compositions with the same optical property. This parameter is determined to be S=(Ga-0.76O-0.24N)/(Ga+O+N), where Ga, O and N are the concentrations of the corresponding elements. If the refractive index data is plotted as a function of this S parameter (Figure 26.d), the curves corresponding to the different combinatorial samples shift relatively close together, indicating that the dependence of the refractive index on the composition of the sample can be reasonably described by this parameter. The only exceptions are at low and high values of the parameter, where a divergence of the curves can be seen.

The structural characterization of the combinatorial films revealed that the layers are amorphous at high oxygen contents and as the oxygen content decreases the structure changes to polycrystalline. The crystalline phase was identified as the wurtzite-type phase of GaN. The growth pattern also changes

with the oxygen flow rate, i.e. at first tiny nanocrystals were observed and as the oxygen content further decreased columnar grains started to appear. The change in the grain structure correlated well with the change of the oxygen concentration in the film.

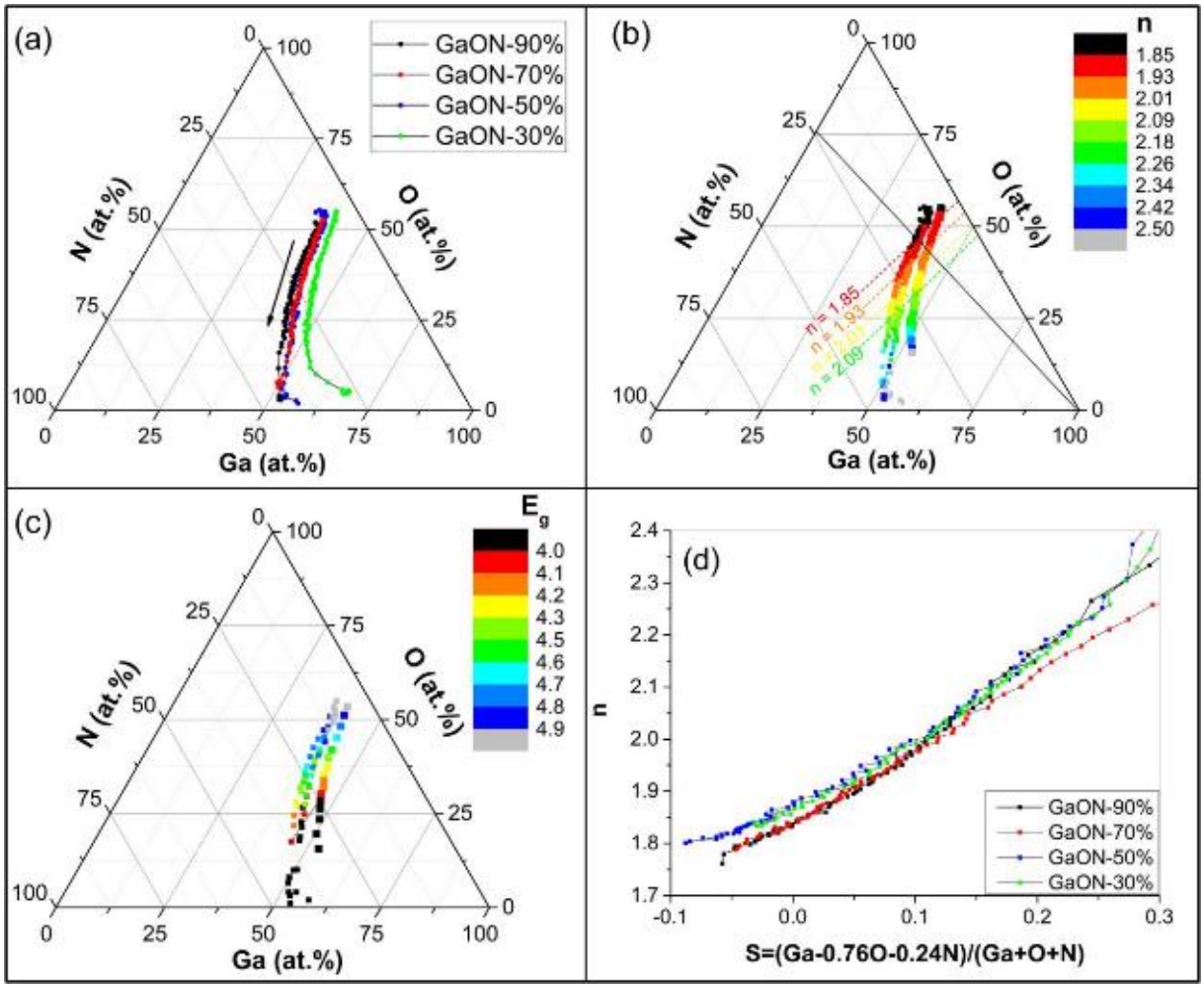

Figure 26. Ternary diagrams showing (a) the compositional variation, (b) refractive index (at 632.8 nm) and (c) optical gap of the four combinatorial samples with different N_2/Ar partial pressure ratios. The arrow in (a) represents decreasing oxygen flow rate during deposition, i.e. the direction from 0 mm to 20 mm. The dotted lines in (b) are the "iso refractive index" lines, while the black line is perpendicular to them. The (d) refractive index plotted as a function of the S parameter.

In conclusion, it was demonstrated that the optical and structural properties of the gallium oxynitride film can be tuned by controlling the composition, and the relationship between the refractive index and the composition was determined.

The Common Sublattice Method quantifies local deformations in epilayers

J. L. Lábár, I. Cora, B. Pécz,
Alexander Azarov (University of Oslo) and Andrej Kuznetsov (University of Oslo)

Measurement of strain in epitaxial layers frequently faces the problem of localizing "perfectly" unstrained regions to use as a reference for the whole structure. Here, we present a method developed for deducing such references in the unstrained substrate (with one crystal structure) to determine the local lattice deformations in the layer (with another crystal structure). The method works if there is a common sublattice in the layer and the substrate, so that the deviations from it may be used to interrelate the experimentally recorded data. Such sublattice always exists in an epitaxial layer on a substrate system. The precision of the method is ~0.5% in strain values.

The common sublattice method (CSM) is based on the measurement of electron diffraction patterns from thin lamellae using a transmission electron microscope (TEM) operated in microprobe scanning mode (μP-STEM). It is based on the output of a four-dimensional (4D) electron diffraction (ED) dataset processed by the 4D-ED method.

The common sublattice is defined in reciprocal space. Let δ_1 and δ_2 two predefined small numbers while $\underline{\mathbf{a}}_1^*$ and $\underline{\mathbf{b}}_1^*$ the base vectors of lattice$_1$ and $\underline{\mathbf{a}}_2^*$ and $\underline{\mathbf{b}}_2^*$ the base vectors of lattice$_2$. If there exists a pair of reciprocal vectors $\underline{\mathbf{a}}^*$ and $\underline{\mathbf{b}}^*$ that all the reciprocal vectors ($\underline{\mathbf{g}}_1$) of lattice$_1$ in the 2D observed reciprocal space plane (i.e. the diffraction pattern measured from the given zone axis orientation) are close to $n_1\cdot\underline{\mathbf{a}}^* + m_1\cdot\underline{\mathbf{b}}^*$ (i.e. $|n_1\cdot\underline{\mathbf{a}}^*+m_1\cdot\underline{\mathbf{b}}^*-\underline{\mathbf{g}}_1|<\delta_1$) and $n_2\cdot\underline{\mathbf{a}}^* + m_2\cdot\underline{\mathbf{b}}^*$ is close to all the reciprocal vectors ($\underline{\mathbf{g}}_2$) of lattice$_2$ (i.e. $|n_2\cdot\underline{\mathbf{a}}^*+m_2\cdot\underline{\mathbf{b}}^*-\underline{\mathbf{g}}_2|<\delta_2$) than linear combinations of $\underline{\mathbf{a}}^*$ and $\underline{\mathbf{b}}^*$ with integer multipliers define the common sublattice. Small deviations (δ_1 and δ_2) are treated by the separate lattice fitting to each pattern irrespective of the fact that the small deviation was caused by changes in the lengths of the base vectors or in the angle between them or both. The d-values are always measured from the fitted lattice.

Relative lattice distortion (strain) is determined from the d-values in the layer (d_l) and the reference area (d_{ref}).

$$\varepsilon = \frac{d_l - d_{ref}}{d_{ref}} = \frac{g_{ref} - g_l}{g_l}$$

where $g=1/d$ in accordance with convention in electron diffraction.

Our CSM method extends strain measurements in epitaxial layers from the simple case of a cubic layer on a cubic substrate to the general case of a substrate with one crystal structure and a layer on it from another crystal structure. In our method, we calibrate the system by measuring an unstrained reference in the substrate, and the strain in the layer is given relative to the unstrained lattice of the layer based on an interrelation of the two structures. The benefit of the new method over the GPA method is that the new method is insensitive to either the variations of local thickness of the sample or minor variations of bending of the lamella or experimental parameters like camera length and convergence angle. Another huge advantage is that a much larger area can be measured in the TEM as compared to HRTEM based methods like GPA. The proof-of-concept is obtained using samples of cubic γ-Ga_2O_3 layers on a monoclinic β-Ga_2O_3 substrate. Our measurements reveal anisotropic lateral strain resulting from the anisotropic lateral mismatch between the cubic γ-Ga2O3 layer and the monoclinic β-Ga2O3 substrate. The layer was created by Ni-ion irradiation of the monoclinic substrate. Two TEM lamellae were cut from each of differently heat-treated samples. An as-implanted sample from both [110] and [100] orientations and samples heat treated at 300°C and 700°C, respectively, from [110] orientations of the γ-phase. Figure 27 shows the measured local lattice deformations together with the changes in

crystal structure (Model). Strain is obtained by subtracting Model from the measured lattice deformation as shown in Figure 27.

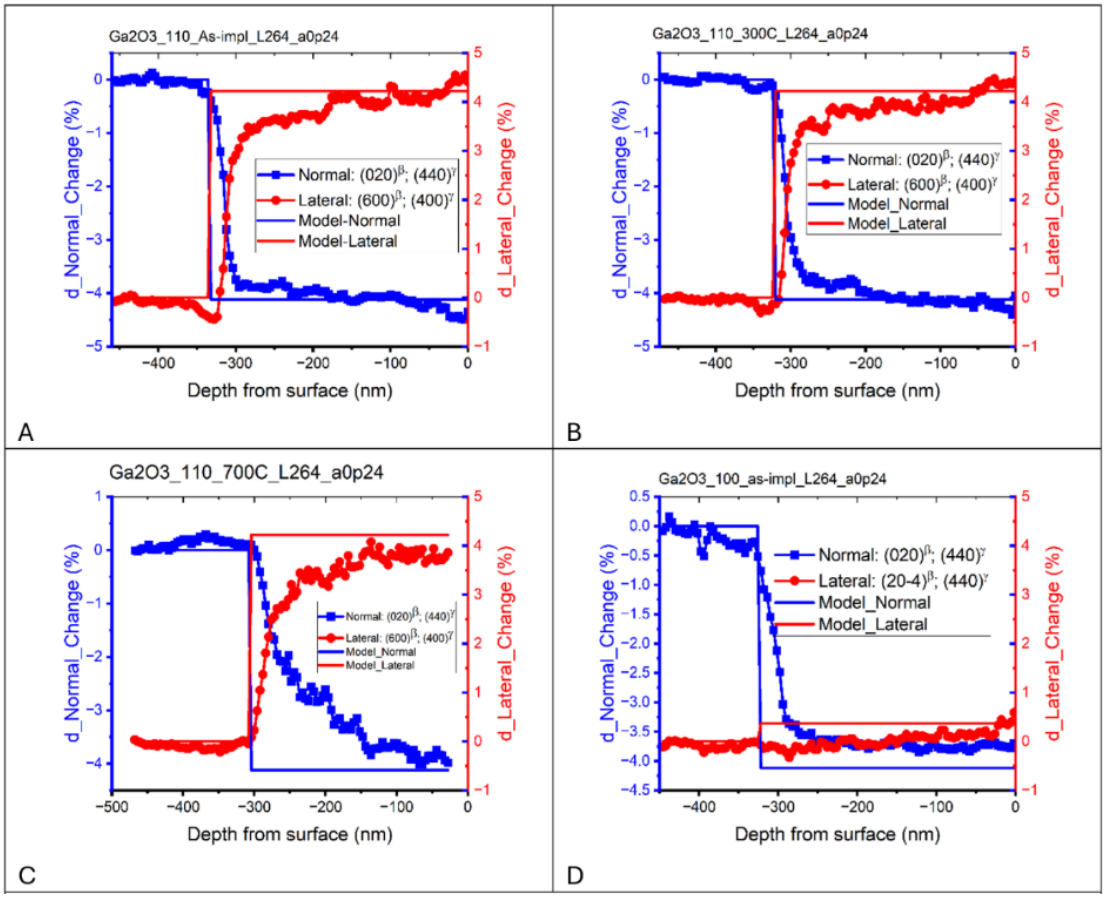

Figure 27. Depth distribution of measured changes in d-values together with changes in d-values of the Model. Blue=Normal component. Red=Lateral component. (α=0.24 mrad and L=264 mm). (a) as-impl [110]$^{\gamma}$; (b) 300C [110]$^{\gamma}$; (c) 700C [110]$^{\gamma}$; (d) as-impl [001]$^{\gamma}$. Deviations of the measured values (symbols) from the Model (lines) indicate presence of strain. Notice that the orientations are orthogonal in (a) and (d).

In Figure 28 (as-implanted sample in [110]$^{\gamma}$ orientation) black squares show averaged in-plane (lateral) and out-of-plane (normal) strain component across the layer including the substrate β-Ga_2O_3 and the transformed γ-Ga_2O_3 layer. Three main parts of the strain curves can be differentiated, that we discuss in detail: 1) the β→γ transformation front, 2) ca. 35 nm wide range after the transformation front (interface region), where the slope of the strain curves is high, 3) range up to the top of the layer (far from interface region) where the slope of the strain curves is low. The implantation depth, where the strain curve shows sharp jump/step is measured to be 320 nm (+-10). At the transformation front the top of the β substrate probably shows a little bit compression strain, while γ shows 3.75 % out-of-plane tensile strain and -4 % in-plane compression strain. After the β/γ transformation front within ca. 35 nm most of the strain is relaxed and reaches +0.4 % in normal direction (tensile strain), measurement sets) is shown to provide trend-lines in the individual regions. If we disregard the observed trend in either the substrate region or in the far from interface region and interpret any variation of data as if it were statistical scattering of data, we obtain a conservative overestimation of standard deviation (precision).

Annealing of the sample at 300°C only caused slight changes in the strain curve. The most striking difference compared to the non-annealed sample is the depth of the γ Ga_2O_3 layer, which is ca. 10 nm less, i.e. the thickness of the γ layer has been decreased to ~310 nm. This indicates that (back)transformation from γ→β has started at the interface front. Meanwhile the compression strain

measured in the top of the β substrate in the as-implanted sample disappeared/relaxed. Parallel to this the compression in-plane and tensile out-of-plane strain seems to slightly increase but the change is within the error of the measurement. After the transformation front with ca. 35 nm the slope of curve is very similar to the strain curves measured from the as-implanted sample. Energy dispersive x-ray spectrum (EDS) depth distributions showed the same Ni distribution in all three samples.

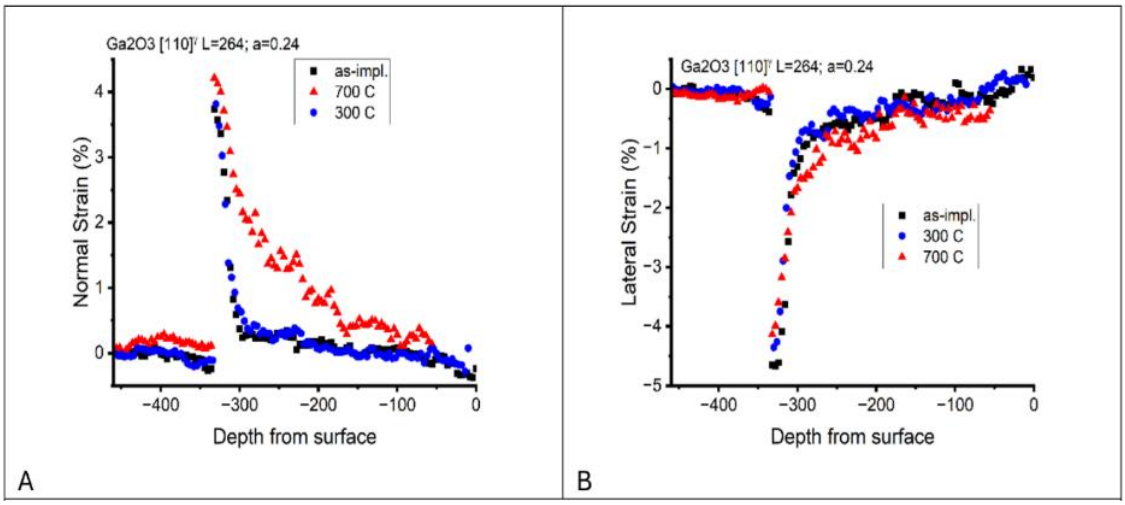

Figure 28. Variation of depth distribution of strain in samples with different heat treatment. (α=0.24 mrad and L=264 mm. Beam direction=sample orientation [110]$^{\gamma}$). Black square=as implanted. Blue circle=heat treated at 300 C. Red triangle=heat treated at 700 C. (a) Normal strain (in direction of (020)$^{\beta}$//(440)$^{\gamma}$). (b) Lateral strain (in direction of (600)$^{\beta}$//(400)$^{\gamma}$). Three spatial sections are identified: Substrate region (from -460 nm to -328 nm), interface region (from -324 nm to -292 nm) and far from interface (close to surface) region (from -288 nm to 0 nm). Strain is close to zero at the substrate region, as expected. Steep change is observed in the interface region. Strain curves for the as-impl and the 300 C samples coincide within the statistical scatter, while the 700 C sample shows a much slower variation of strain in the far from interface region.

Annealing of the sample at 700°C caused more significant changes. At this annealing temperature γ transforms back to β not only at the interface but inside the γ layer as well, as we documented this in individual ED patterns. Therefore, the slope of the strain curve after the transformation front shows more tensile out of plane and compressive in-plane strain component with slower decrease toward the surface caused by the coexistence of both polymorphs. This also implies the increasing relative amount of β closer to the interface. The maximal measured strain values of the layer at the interface are +4 % tensile out-of-plane strain and -4 % compression in-plane strain. As a continuation of the tendency/trend the transformation front γ→β shifts toward into the layer that results in a decreased thickness (304 nm+-10 nm) of the layer containing γ phase.

The common sublattice method deduces references in the unstrained substrate (with one crystal structure) to determine the local lattice deformations in the layer (of another crystal structure). The method works if there is a common sublattice in the layer and the substrate (what is fulfilled in all epitaxial configurations), so that the deviations from it may be used to interrelate the experimentally recorded data. The new method overcomes several severe limitations of the geometrical phase analysis method, e.g. of having a limited field of view and requirements to resolve the lattice image which may be challenged by the camera size for large areas to examine. Furthermore, our method is insensitive to lamella thickness variations. Measurements on lamellae cut from orthogonal crystal orientations revealed non-isotropic lateral strain in Ga_2O_3 layers. The reliability was further proven by collecting data with different camera length, convergence angle conditions, and variable lamellae thicknesses. Consistency of the results shows the usefulness of the method. [Ref.20.]

Evaluation methods for XPS depth profiling; a review

A.S. Racz, M. Menyhard

X-ray photoelectron spectroscopy (XPS) is a widespread method in modern material science to study widely varied functional materials (metals, polymers, semiconductors). In most of these applications there is a need of the detailed knowledge of the surface and surface close chemistry. XPS with its excellent chemical sensitivity can directly be applied to the analysis of the surface layer in the range of some nms. It is known that its depth resolution is poor because of its relatively high information depth (5-10 nm). Several methods have been developed to solve this problem. Additional problem arises, when thicker regions are to be analysed. In this case it should be combined with various depth profiling techniques, which introduce alterations like mixing, preferential sputtering, roughening etc. In this case one should consider both problems high information depth and altered sample during the evaluation of the measured spectra. In this review we present the advantages and disadvantages of the techniques available for tackling these issues focusing mainly on ion etching techniques, monoatomic and cluster argon sputtering, available. We also discuss modern methods like high energy XPS (HAXPES) and femtosecond laser ablation (fs-LA). Evaluation problems are discussed through case studies aiming to provide a guide for choosing between the different methods, highlighting pitfalls and proposing solutions. The different XPS depth profiling methods are summarized in Table 1. [Ref.21.].

Substance	Method	Advantage	Disadvantage
organics, polymers	GCIB	preserve of chemical bonds	morphology development
thin layers up to 10 nm	No sputter removal ARXPS Tougaard method	preserve of chemical bonds, band structure etc.	thickness limitation, special evaluation methods
buried interfaces	Sputter removal of cover layer until the altered layer reaches the interface: XPS HAXPES	preserve of chemical bonds, band structure etc.	HAXPES: X-ray sensitivity, complex experimental setup, issues with sensitivity factors
layers thicker than 10 nm	monoatomic argon	high sputtering rate, well developed evaluation techniques	argon implantation, preferential sputtering, morphology development, chemical bond alteration
layers thicker than 10 nm containing inorganic compounds	Monoatomic ion + GCIB	might optimize the damage reasonable sputtering rate	complex experiment no sufficient understanding of GCIB effects
sensitive inorganics	GCIB	preserve of chemical bonds	low sputtering rate preferential sputtering, morphology development
thick inorganics	fs laser ablation	preserve of chemical bond high sputtering rate	new technique, little experiences, not for thin layers

Table 1. Tips for XPS based analyses for various types of samples.

Effect of non-spherical shape of dry powder aerosol drugs on their airway deposition distribution

T. Kolonits, Sz. Kugler (EKBI), P. Füri (EKBI), A. Nagy (Wigner FKI), Á. Farkas (EKBI)

During the research, 5 commercially available aerosol drugs were investigated, in aspect that in which part of the airways, and in what size and shape distribution do they deposit. These drugs are currently used in the therapy of chronic obstructive pulmonary disease (COPD) and/or asthma as short- or long-acting bronchodilators and anti-inflammatory cortico-steroids. The commercial names of the drugs are: Bretaris® Genuair®, Buventol® Easyhaler®, Trelegy® Ellipta®, Ultibro® Breezhaler® and Symbicort® Turbuhaler®.

The lung was emulated with a so-called cascade impactor, to which the inhalers were connected with 3D printed adapters. Scanning electron microscope was used to quantify the size and shape ("non-sphericity") of the particles. The latter is important because in medical R&D flow simulations, drug particles are considered as spherical. Comparing our measurement data with numerical models, we found that although the particles visibly deviate from the spherical shape, neglecting the irregular shape does not lead to a major distortion of the simulation results. There is one exception: in the case of one drug (Trelegy® Ellipta®), we have observed small, elongated fibers. These fibers already showed significantly different behavior than spherical particles, which is manifested in a significant increase in their deposition in the terminal bronchioles, immediately before the respiratory bronchioles [Ref.22.].

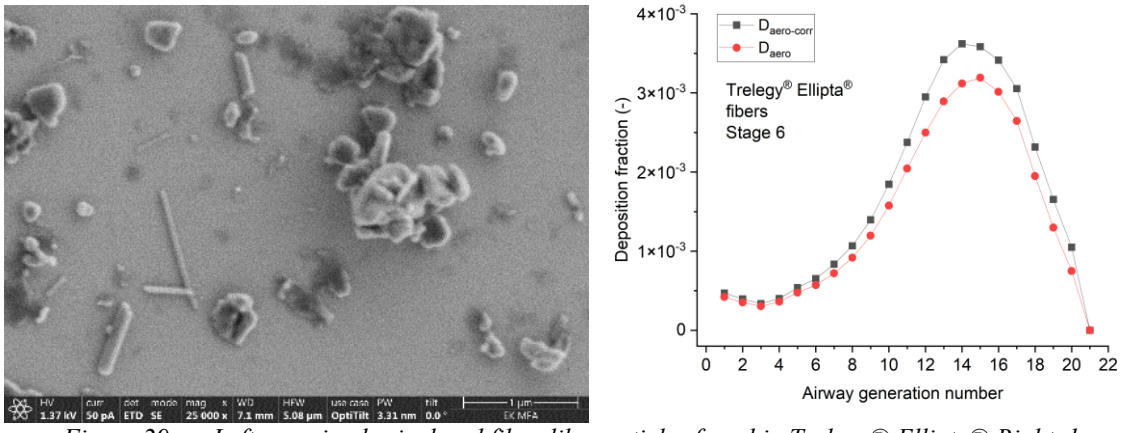

Figure 29. Left: quasi-spherical and fiber-like particles found in Trelegy® Ellipta® Right: bronchial deposition fractions of the fibres with and without considering the diameter correction with the shape factor.

Microcombinatorial Preparation and Characterisation of Multicomponent Thin Films

OTKA K 143216

Gy. Sáfrán, M. Serényi, D. Olasz, E. Dódony, T. Kolonits, I. Cora, V. Kovácsné Kis, N. Szász, A. Jakab, A. Kovács, P. Petrik, M. Fried, Zs. Zolnai

The mid-term performance of our project was rated excellent by the OTKA Committee in 2024. In 2025, we continued and further developed the single-sample-based microcombinatorial method that had been elaborated for a comprehensive investigation of the composition-dependent properties of binary and ternary thin films. The results have led to several scientific publications [Ref.23.]-[Ref.29.].

1. Development of a simplified combinatorial thin film growth and characterization technique

With the participation of Gergő Dobrik, Noémi Szász, Peter Petrik and Levente Illés, we are developing a simplified combinatorial thin film deposition and characterization technique that enables the efficient combinatorial preparation and investigation of 3–4 component thin film systems. A patent application based on this technical solution is planned for submission in 2026.

2. Microcombinatorics combined with variable pulsed gas inlet (GPC)

By combining microcombinatorics with variable pulsed gas inlet (GPC) using new Bronkhorst mass flow controllers, cathode poisoning during reactive sputtering can be avoided, thereby eliminating abrupt changes in the sputtering regime and in film properties.

This method was applied to the combinatorial growth of RF-sputtered ternary thin film systems, namely various (Si–Ga–Al) -oxynitrides, and to the investigation of their optical and structural properties, in collaboration with researchers Miklós Serényi and Marcell Gajdics, and PhD student Dániel Olasz.

3. Cooperative Doctoral Program (KDP) – PhD work of Dániel Olasz

Within the framework of the Cooperative Doctoral Program (KDP) associated to the OTKA project, PhD student Dániel Olasz is conducting research entitled “Composition-dependent structural and mechanical properties of binary thin films” in collaboration with university supervisor N. Q. Chinh (ELTE).

The student prepared Al–Cu, Y–Ti–O and Al–O–N thin films with compositions varying over the entire concentration range. Transmission electron microscopy (TEM), ellipsometry, and nanoindentation measurements were performed to characterize their structural morphological, and material properties ie. hardness, deformation mechanisms, optical refractive index, amorphous and crystalline phases and their composition.

The publication on the Al–Cu system appeared in January 2026. The first version of the PhD dissertation has been completed, and the defense is planned for 2026.

4. PhD work of Erzsébet Dodony – Me-silicide thin films

Also methodologically connected to the present OTKA project is the PhD work of Erzsébet Dodony entitled “Formation of Me-silicide thin films.” The candidate has completed her PhD dissertation and successfully passed the internal (pre-defense) examination. The thesis has been officially submitted to the ELTE Doctoral School of Physics, and the public defense is expected in 2026.

5. Application of microcombinatorial TEM in catalysis research – methane pyrolysis at the nanoscale

The principal investigators of the internal EK project entitled “Application of microcombinatorial TEM in catalysis research; methane pyrolysis at the nanoscale.” are Anita Horváth, EKBI and György Sáfrán, MFA.

Combinatorial Mo–Ni nanocrystalline bimetallic catalysts with composition varying continuously within a single sample were investigated by TEM and EDS to determine their composition, structural, and morphological properties. This method enables efficient optimization of bimetallic catalyst composition to maximize catalytic activity and lifetime.

We demonstrated that at high temperatures (600–900 °C) the Au TEM grid is unstable; Au diffusion occurs, and the presence of gold has a degrading effect on methane decomposition catalysis. A peer-reviewed publication has resulted from this work.

6. Development and optimization of gold nanocrystal biosensors

In collaboration with the Photonics Laboratory led by Péter Petrik, we contributed to the development of gold nanocrystal biosensors based on the influence of plasmonic effects evoked by various applied molecules. The particles morphology and size distribution was combinatorially optimized by preparing and annealing graded-thickness thin films, followed by TEM and ellipsometric characterization and testing with water ethanol and RAMAN MBA reporter molecules

7. Ellipsometric phase mapping of combinatorial thin film systems

Together with the Photonics Laboratory led by Péter Petrik, we worked on a patentable method and technical solution for comprehensive composition- and temperature-dependent ellipsometric characterization and phase mapping of two-componwent combinatorial thin film systems. Related patent application is under preparation. Submission is expected in 2026.

Combinatorially optimized sensorics of sputtered gradient gold nanoparticle layers

OTKA K 143216, KDP-2021 scholarship

D. Mukherjee, K. Kertész, Zs. Zolnai, Z. Kovács, A. Deák, A. Pálinkás, Z. Osváth, D. Olasz, A. Romanenko, M. Fried, S. Burger, Gy. Sáfrán, P. Petrik

Within our institution, within the framework of cooperation between two laboratories (Thin-film physics and Photonics), Au nanoparticles with gradually changing properties were produced on fused silicon dioxide using DC magnetron sputtering and annealing in order to find the range in the sample that provides the best response, i.e., to optimize the plasmonic sensing of molecules. The combinatorial gradient approach [Ref.30.] resulted in a linear change in the effective thickness of the deposited Au on the substrate.

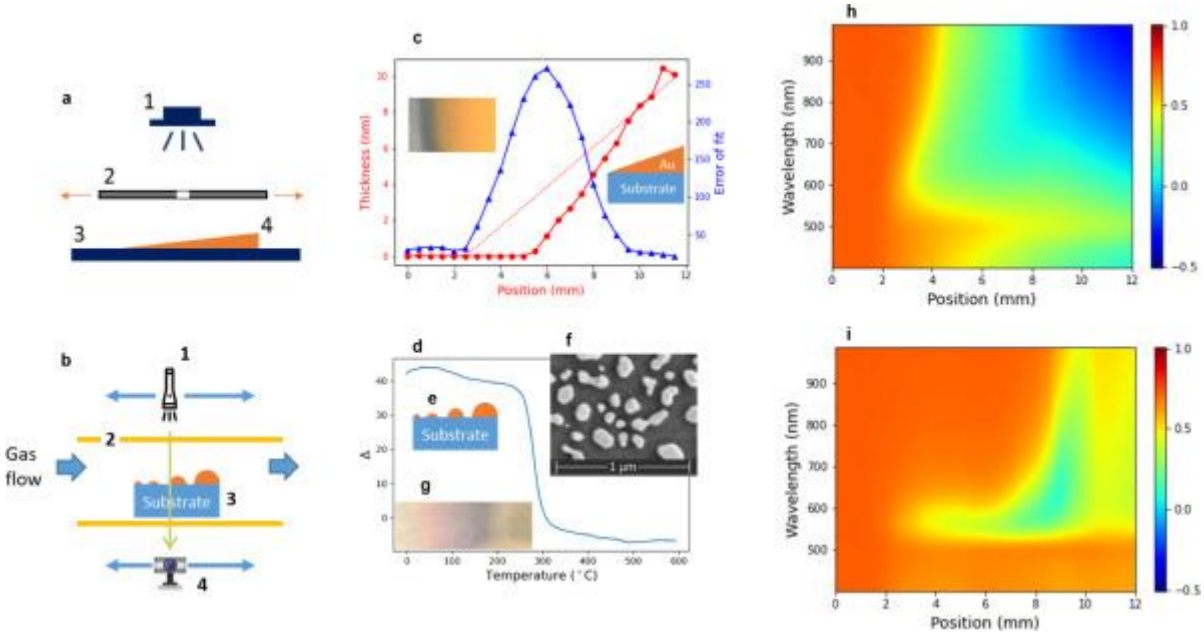

Figure 30. (a) Set-up for micro-combinatorial deposition (1) magnetron sputtering source, (2) moving slit, (3) substrate, and (4) graded-thickness gold layer. (b) Optical transmission cell with (1) light source, (2) glass chamber, (3) substrate with annealed nanoparticles and (4) spectrometer. (c) Thickness vs. position (red circles), effective thickness (also called 'mass thickness' corresponding to the deposited amount of material (dotted line), and error of fit for the as-deposited graded Au sample 'B' measured by spectroscopic ellipsometry (SE). (d) Change of measured thickness by SE as a function of temperature during annealing at the position at 8 mm on sample 'B.' (e) Schematic, (f) scanning electron micrograph (at a position of 8 mm), and (g) optical image of the sample after annealing. (h) and (i) show m33 spectra on sample 'B' over the range of positions from 0 to 12 mm for the as-deposited and 300 °C annealed state, respectively.

Scanning optical spectroscopies [Ref.31.] were used to characterize the optical and sensing properties for water, ethanol and MBA reporter molecules, as a function of equivalent deposited thickness d_i. The best gas sensing positions along the sample were found for d_i values of 2–4 nm, explained by the high surface density of gold particles and the high ratio of covered area in this region. The covalently bonded Raman reporter MBA molecules can most sensitively be detected at the highest plasmon peak region of $d_i \approx 7$ nm when using ellipsometry. However, the most sensitive region for the Raman measurement of the MBA molecules is at $d_i \approx 1.6$ nm. The formation and sensing performance

of the layers were modeled and explained using finite element calculations. We have shown that our combinatorial sputtering method for arbitrary thickness and composition profiles can accurately and quickly locate optimal sensing parameters [Ref.32.]. It supports the discussion of theoretical and experimental considerations due to the large amount of data generated by quick optical scanning. The present results also show that our approach is suitable for the high throughput testing of new materials and structures and for creating experimental databases for theoretical analysis and machine learning.

Acknowledgements
This publication was supported by the Cooperative Doctoral Programme of the Ministry of Innovation and Technology, KDP-2021, Doctoral Student Scholarship Programme, funded by the National Research, Development and Innovation Fund. The research was also supported by the OTKA grants 146181, K-143216, K-134258 and PD-146479.

Dramatic interaction between the Au TEM grid and sample as well as supported MoNi/MgO catalysts

Application of Micro-Combinatorial TEM in Catalysis Research (EK internal project)

A. Horváth, M. Németh, A. Beck, D. Olasz, M. Serényi, Gy. Sáfrán

The decomposition of methane in an inert atmosphere—also known as methane pyrolysis—produces CO_2-free "turquoise" hydrogen and solid carbon. The MgO-supported bimetallic molybdenum–nickel (MoNi) catalyst exhibits promising synergistic effects in this reaction. Our objective was to efficiently investigate how variations in the Mo/Ni ratio influence catalytic performance, with particular emphasis on carbon deposition. A novel micro-combinatorial TEM technique was successfully applied, in which magnetron sputtering was used to generate Mo–Ni nanoparticles with a continuous compositional gradient on a SiOx-coated gold TEM grid, presumed to remain stable even at high temperatures [Ref.33.]. Post-treatment of the model catalyst sample at 800 °C in diluted hydrogen resulted in uniform particles with varying compositions.

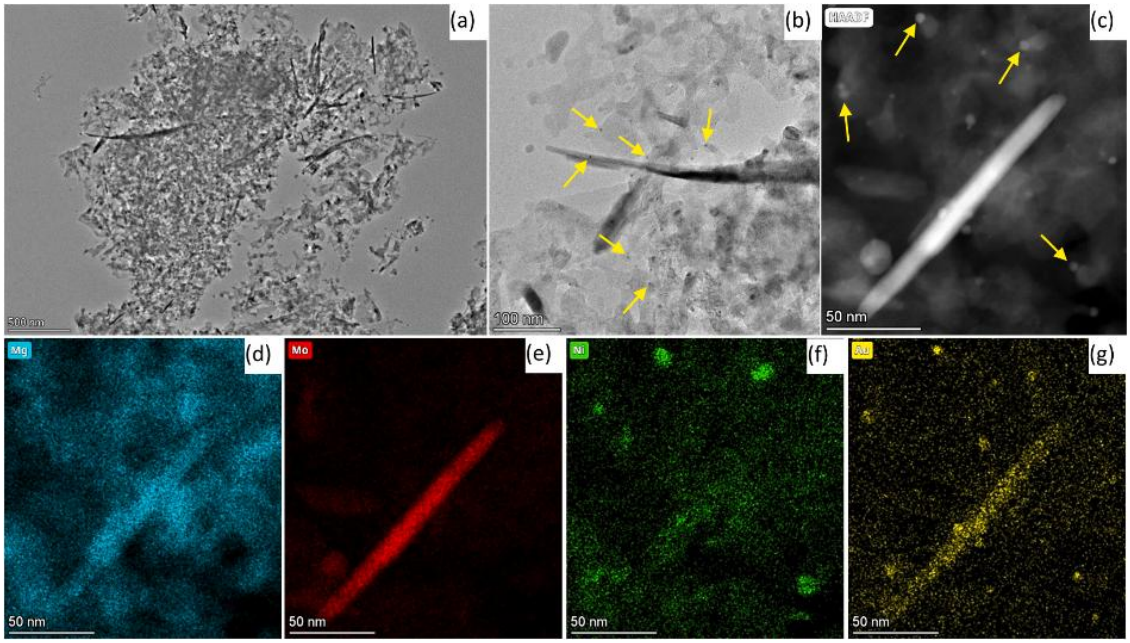

Figure 31. TEM micrographs of the supported MoNi/MgO powder catalyst deposited on a C/Au grid and subjected to reduction and reaction treatment at 800 °C: a) TEM overview image; b) high-magnification image, with dark-contrast Au particles indicated by arrows; c) selected area for further STEM–EDS analysis, Au particles marked by arrows; d) STEM–EDS Mg map; e) Mo map; f) Ni map; g) Au map of the same area.

However, methane treatment experiments revealed a significant limitation: at high temperatures, the gold and SiOx components of the TEM grid interacted with the catalyst, leading to partial segregation and oxidation of Mo and Ni, thereby inhibiting carbon formation. A model MoNi sample sputtered onto an MgO-coated carbon membrane supported on a gold TEM grid exhibited similar gold-induced effects—mixed metal oxides formed, but no carbon. Interestingly, when a MoNi/MgO powder catalyst was placed onto the gold grid, no carbon formation occurred either. In contrast, in control experiments conducted without the gold grid—as expected—carbon nanotubes were formed. These results highlight the critical influence of the TEM grid material on catalytic behavior and suggest that gold may actively suppress coke formation. This could be valuable in reactions where the inhibition of coking is desirable.

Structural study of (001) rutile-type GeO2 semiconductor on rutile (TiO2)

MTA NKM2023-15/2023

I. Cora, B. Pécz (HUN-REN CER)
P. Mazzolini, M. Bosi, G. Cicconi, F. Mezzadri (IMEM CNR, Uni. of Parma)
A. Ugolotti, Leo Miglio (Uni. of Milano)

The ultra-wide bandgap semiconductor rutile germanium oxide (r-GeO2, Eg ≈ 4.6 eV) is gaining momentum in the quest for novel materials for power electronics. In this work, we experimentally and theoretically investigate the physical mechanisms behind the nucleation and growth of epitaxial (001) r-GeO2 on isostructural r-TiO_2 substrates via metalorganic vapor phase epitaxy (MOVPE) using isobutylgermane and O_2 precursors. In the identified deposition window, the thin film growth seems to be affected by partial GeO suboxide desorption, and we observe that the layers are always composed of r-GeO_2 islands embedded and/or surrounded by amorphous material. Ge/Ti interdiffusion at the epilayer-substrate interface is found at the base of each r-GeO_2 island; combining experimental analysis and multiscale theoretical simulations we discuss how such a process is fundamental to achieve partial strain mitigation allowing for the nucleation of epitaxial r-GeO_2 and suggest in this regard a limiting threshold to avoid the formation of amorphous material. Moreover, we shed light on the formation of different facets in r-GeO_2 at early stages of growth and after merging of islands. [Ref.34.]

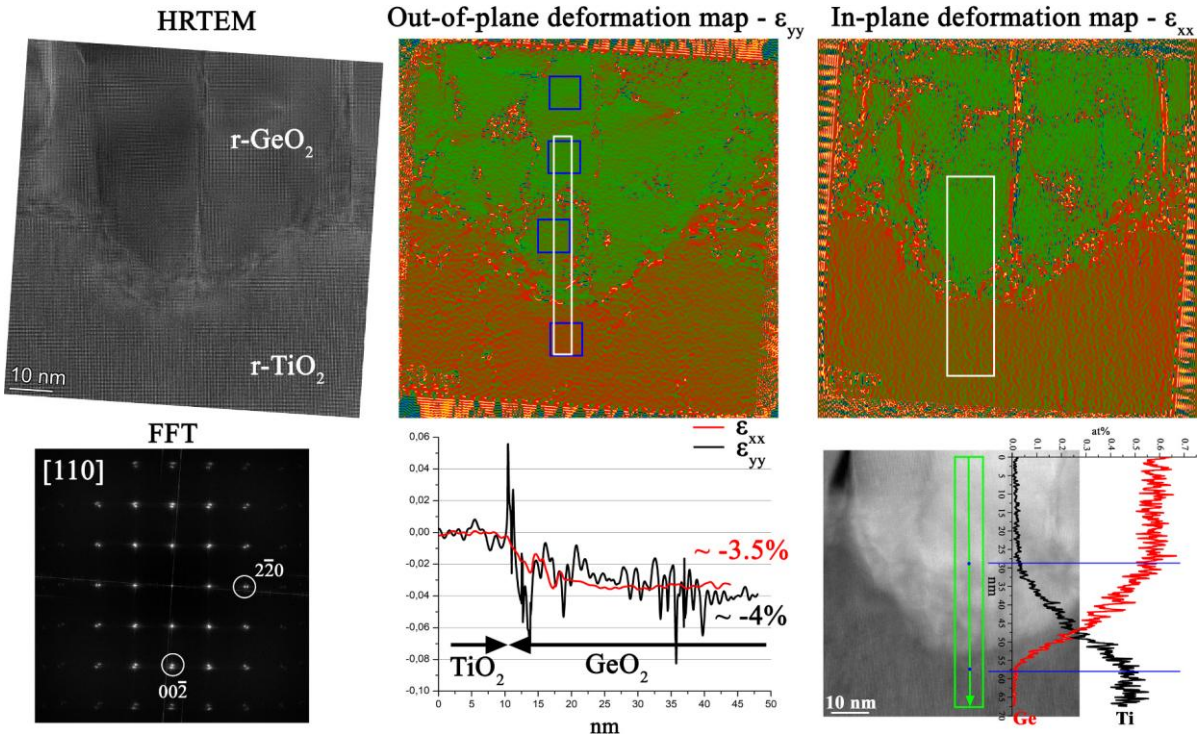

Figure 32. Geometric phase analysis (GPA) was performed from HRTEM images of the intermixing region, obtaining ε_{xx}, ε_{yy} deformation maps. The HRTEM image with the corresponding FFT, ε strain/deformation maps and integrated EDS line-profiles of Ti and Ge signed on the HAADF image in [110] projection (sample #212). ε_{xx} and ε_{yy} strain/deformation maps were calculated using periodicities signed on the FFT. TiO_2 was selected as the reference. The integrated and averaged deformation values inside the white rectangles are presented below the maps. The average out-of-plane deformation values calculated inside the blue rectangles are the following; r-TiO_2: ε_{yy} =0.0004(50), and r-GeO_2: ε_{yy} =-0.027(14) in the mixing area at the interface, ε_{yy} =-0.040(7) and ε_{yy} =-0.040(7) above. ε_{xx} =-0.035(10) is more homogeneous in the root part of the r-GeO_2 crystal and above.

Effect of Nitrogen Content on Microstructure and Mechanical Properties of DC Magnetron Sputtered CrMnMoSiY(N) High Entropy Coatings

L. Vrána, T. Stasiak, M. Fekete, V. Buršíková, Zs. Czigány, K. Balázsi, P. Souček

This study investigates Cr-Mn-Mo-Si-Y-(N) high-entropy alloy and high-entropy nitride coatings, with a focus on their structural, compositional, and mechanical properties [Ref.35]. These coatings were developed using reactive DC magnetron sputtering in an Ar/N_2 atmosphere, combining strong and weak nitride-forming elements with significant differences in atomic radii. The nitrogen content in the coatings was found to saturate below 45 atomic percent (at.%), stabilized by nitrogen vacancies. Bias applied during deposition did not influence the chemical composition or microstructure. Increasing the N_2 flow rate led to a reduction in the deposition rate due to target poisoning while also increasing the nitrogen content until saturation was reached. Microstructural analysis revealed that coatings deposited at room temperature formed an amorphous structure, while formation of nanocrystals occurred at a substrate temperature of 580 °C in coatings containing more than 40 at.% nitrogen. The coatings exhibited a distinctive structure with alternating Cr-Mo-rich and Si-Mn-rich nanolayers (Figure 33). These layers showed significant compositional variability, with Cr and Si demonstrating the greatest changes. Cr-Mo-rich layers contained FCC nanocrystallites, whereas Si-Mn-rich layers remained amorphous due to the weak nitride-forming properties of Mn and the lattice distortion introduced by Si and Y.

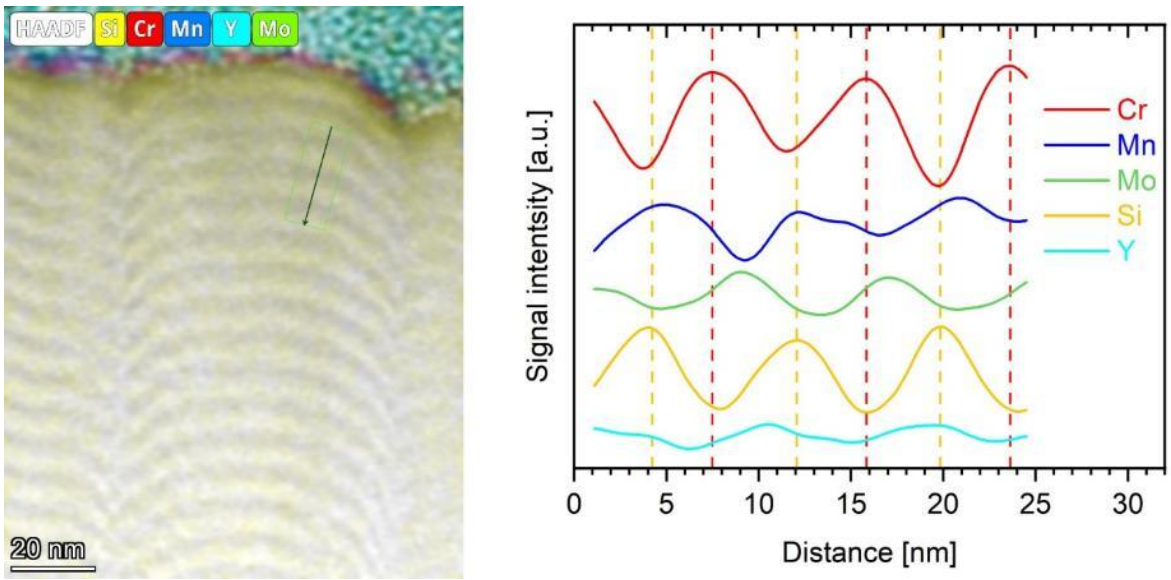

Figure 33. Line profile in the EDS elemental map indicating the concentration correlation of Cr with Mo and Si with Mn.

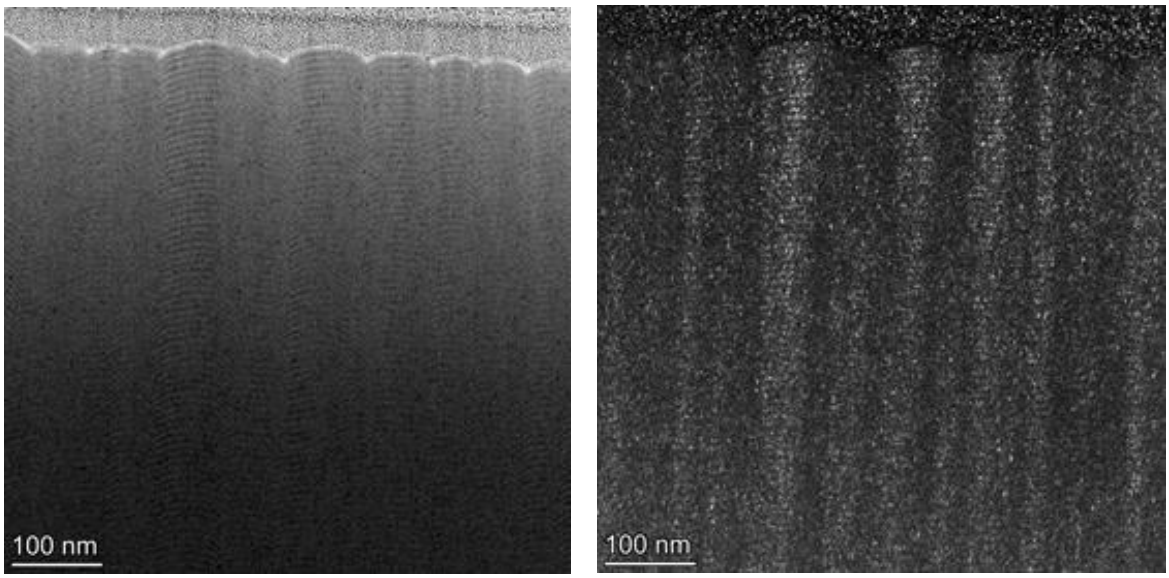

Figure 34. Bright and dark field images of the Cr-Mn-Mo-Si-Y-(N) high entropy nitride coating deposited at 580C and 100V bias. The bright contrast in the DF image indicates the location of the crystalline fcc phase.

The evidence for the alternation of amorphous and crystalline phases are the bright field (BF) and dark field (DF) image pairs: the crystalline layers are a bit darker in BF images, and these layers contain some distinct bright spots (crystallites) in DF images (Figure 34). High-resolution TEM images also confirmed this nanostructure. The mechanical properties of the coatings improved significantly with nitrogen incorporation and a substrate temperature of 580 °C. At these conditions, the coatings achieved a peak hardness of 15.5 GPa and a reduced modulus of 195.1 GPa. Elastic deformation parameters (H/E) and plastic deformation parameters (H^3/E^2) reached values of 0.09 and 0.12 GPa, respectively, indicating enhanced durability and resistance to mechanical deformation. The study also highlighted the influence of deposition geometry, substrate rotation, and elemental targets in forming the alternating nanolayer structure. The phase separation observed between Cr-Mo-rich and Si-Mn-rich layers suggests a potential chemical separation mechanism, warranting further investigation. Nitrogen incorporation and a substrate temperature of 580 °C emerged as key factors driving the improved structural and mechanical performance of the coatings. These findings provide valuable insights into the development of high-entropy nitride coatings, positioning them as promising candidates for advanced material applications.

Biomineralization at the nano scale

OTKA K 125100

V. Kovácsné Kis, Zs. Kovács (ELTE), M. Hegedűs (ELTE), N. Rózsa (Semmelweis University), É. Mlinkó (Semmelweis University), Z. Szekanecz (University of Debrecen), L. Illés, N. Szász, L. Vásárhelyi (University of Szeged), Á. Kukovecz (University of Szeged), H. Schwarcz (McMaster University), N. Nassif (CNRS LCMCP)

In 2025, we published two important papers in the field of Ca-phosphate biomineralization, both were preceded by couple of years of research.

Bone apatite crystal structure [Ref.36.]. While detailed multiscale models explain the complex hierarchical structure of bone, there has been an unresolved paradox between bone apatite nanomorphology dominated by large (010) facets and apatite hexagonal crystal structure. Crystal structure studies of bone apatite are difficult due to intimate structural intergrowth with organic matrix and small crystal size, (2-6 nm thickness along b and 30-40 nm width). Our high resolution TEM (HRTEM) analysis (Figure 35) of isolated individual mineral platelets (MPs) show that the MPs are polycrystalline, composed of crystallites whose **c**-axes are mostly co-aligned with few degrees of misorientation forming mesocrystalline assemblies. Based on Fast Fourier Transform analysis of HRTEM images of nanocrystals we propose monoclinic structure with a(mon)=a(hex), b(mon)=2a(hex), c(mon)=c(hex). Monoclinic model resolves the paradox and explains nanomorphology in terms of crystal structure. Moreover, it allows the development of non-equivalent (010) factes with different composition, polarity and atomic arrangement. As a consequence, the orientation of the (010) crystal surface relative to collagen becomes biologically significant, which was presumed in previous studies [Ref.37.].

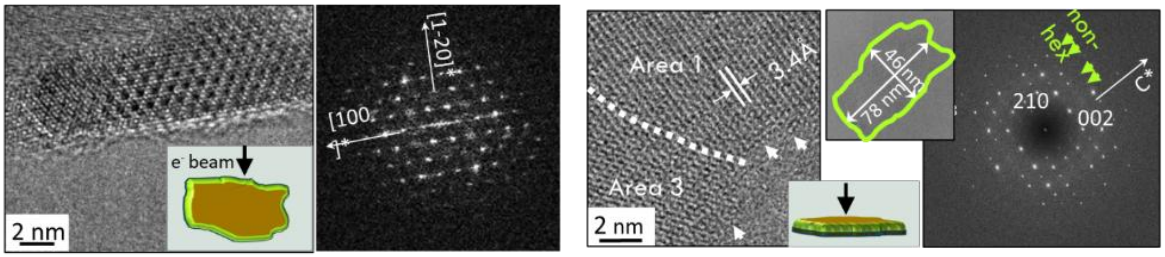

Figure 35. Edge view (left) and plane view (right) HRTEM of individual bone mineral platelets with their corresponding FFTs. Features deviating from hexagonal symmetry are indicated in the plane-view FFT.

Monoclinic crystal structure of bone apatite was verified inside bone tissue, using cryo-Ar milled thin sections as well. We also show that the same monoclinic structure appears in plate-like crystals of biomimetic apatite used successfully for bone regeneration [Ref.38.]

Ribbon-like hypomineralization in human enamel [Ref.39.]. Molar-incisor hypomineralization (MIH) is a developmental enamel disorder with up to 14 % prevalence, characterized by reduced mineral content, hypersensitivity, and post-eruptive enamel breakdown. As the causes of this disorder remain unclear to date, MIH, including the optimization of treatment strategies, is an area of intensive investigation. We have reported a new form of hypomineralization with uncommon appearance in dental practice for the first time. We have compared structural and chemical alterations in teeth exhibiting this ribbon-like hypomineralization (RLH) to the characteristics of sound and MIH-affected teeth.

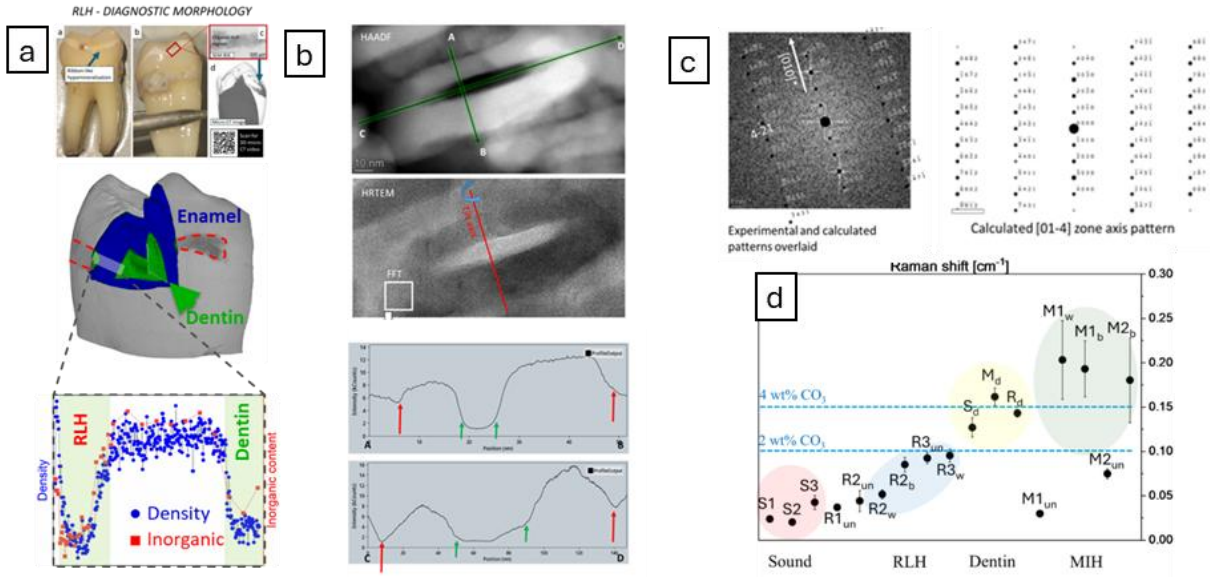

Figure 36. (a) Diagnostic appearance of RLH enamel and density change shown by micro-CT. b) HAADF and HRTEM of hollow nanocrystals characteristic of RLH enamel. (c) Simulated SAED shows that asymmetric contrast gradient around the core of the crystals, observed on HAADF is due to small tilt. (d) Raman spectral parameters of RLH enamel allow clear distinction from MIH enamel.

Microporosity, mineral density and characteristic 3D macroscopic shape of the RLH affected volumes were captured by micro-CT analysis. On the submicron-scale (Figure 36), nanoporosity, unusual nanocrystal morphologies and reduced size of apatite nanocrystals have been revealed. These RLH specific features are coupled with a particular chemical fingerprint in Raman spectroscopy, which allows its clear separation from MIH affected and sound enamel. Based on these nanostructural features we conclude different failure mechanisms in the biochemical control during crystallization of the RLH and MIH enamel.

Acknowledgement: Funding of this study was provided by the National Research, Development and Innovation Fund Office, Hungary (grant number 125100, V.K.K.). Some aspects of hypomineralized enamel research was funded by ÚNKP-23-3 New National Excellence Program of the Ministry for Culture and Innovation of Hungary (M.H.).

Preparation and investigation of biopolymer composite materials containing calcium phosphate doped with Mg and Zn components

OTKA FK 146141

M. Furkó

A novel method for producing porous biopolymer composite scaffolds doped with bioactive Mg- and Zn-containing calcium phosphate (mCaP) was developed.

Two polymers were used as matrices: a natural polymer, cellulose acetate (CA), and a synthetic polymer, polycaprolactone (PCL). The biomineralized calcium phosphate particles were synthesized via wet chemical precipitation, followed by the addition of organic biominerals, such as magnesium gluconate and zinc gluconate, to enhance the bioactivity of the pure CaP phase. The morphological and chemical characteristics of the two composite types were evaluated, as well as the impact of biomineralization on the particle structure of pure CaP. The precipitated mCaP primarily consisted of nanocrystalline apatite, and the addition of organic trace elements significantly influenced morphology by reducing particle size. FE-SEM EDS confirmed the successful incorporation of mCaP particles into both the CA and PCL polymer matrices. Short-term immersion tests revealed slow degradation rates for both composites, with moderate and gradual ionic dissolution observed via ICP-OES measurements. The PCL-based composite exhibited minimal weight loss during immersion, decreasing by only 0.5%, while the CA-based composite showed an initial slight weight gain before gradually decreasing over time. The morphology of the composites is shown in in Figure 37.

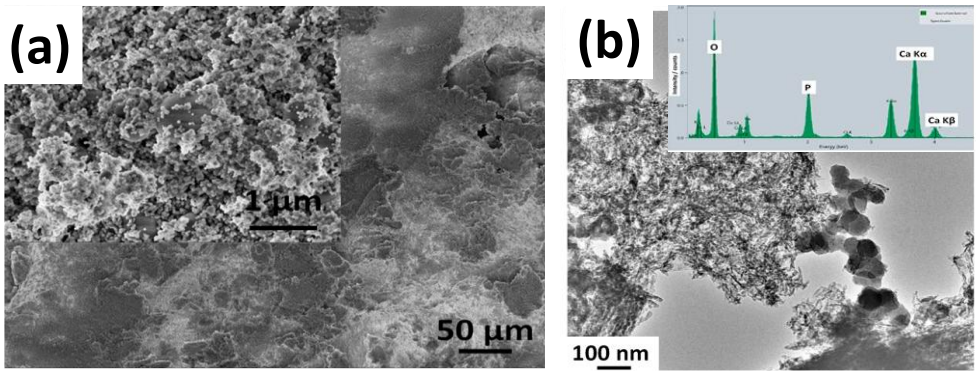

Figure 37. Scanning electron microscope image (a) low-magnification TEM image (b), and the corresponding EDS of PCL-mCaP composite.

The changes in both morphology and weight of the composites were monitored over a short-term (two weeks) immersion period to assess the biodegradability of the composite samples and to gain insights into the morphological changes caused by the soaking procedure in general. In addition, we measured the concentrations of the dissolved calcium, magnesium, zinc, and phosphorus ions by ICP-OES at different time intervals. Figure 38 illustrates the morphology of CA-mCP and the PCL-mCP samples as prepared and after two weeks of immersion in saline solution.

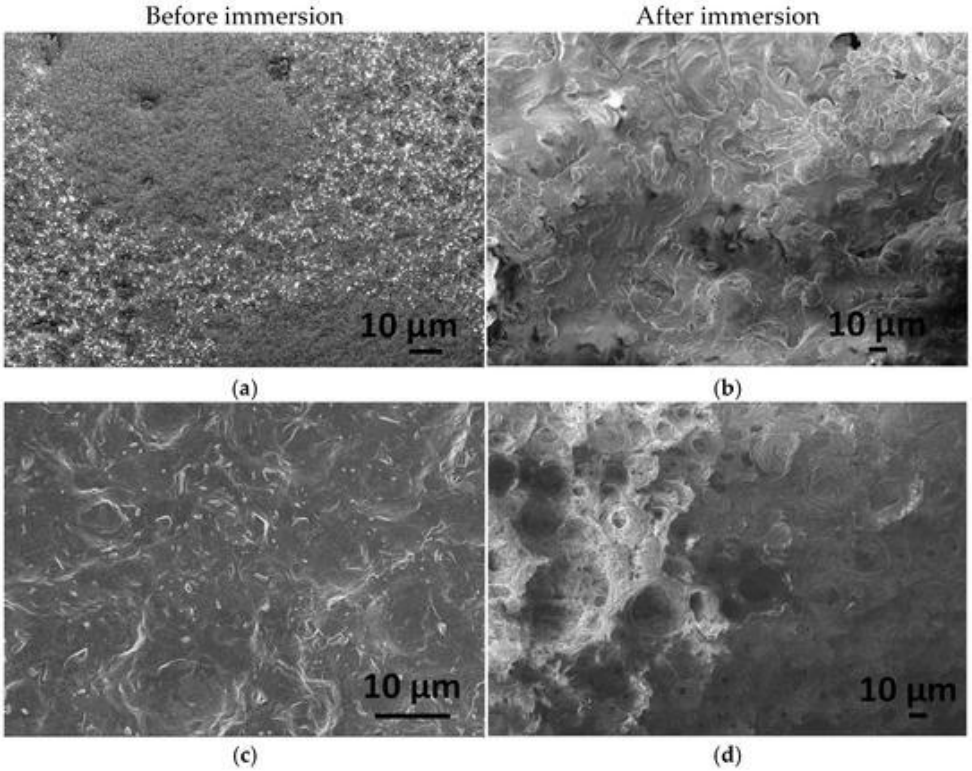

Figure 38. FE-SEM images on CA-mCP (a) and PCL-mCP (c) composites, as well as CA-mCP (b) and PCL-mCP (d) composites, after two weeks of immersion in saline solution.

Synthesis and Characterization of Hydroxyapatite from Eggshells

B. Almássy, K. Balázsi and Cs. Balázsi

The objective of the PhD research of Boglarka Almassy (Obuda University) is to develop a novel and efficient synthesis route for hydroxyapatite (HAp) from eggshells. The work aims to systematically optimize all controllable synthesis parameters in order to replicate the structure and properties of natural bone, producing a highly biocompatible and bioactive material for bone tissue engineering applications.

The pure hydroxyapatite (HAp) was successfully produced by using eggshells as a calcium precursor. The calcined eggshells were reacted with diammonium hydrogen phosphate in a mechanochemical method using attritor milling. Half of the synthetized samples were subjected to a second calcination process. The structures of the samples were investigated by scanning electron microscopy, X-ray diffraction, and Fourier transform infrared spectroscopy. As-milled samples had pure, nanosized HAp particles, while the secondarily calcinated samples exhibited larger, well-defined, porous, closely resemble natural HAp structures. This sintered sample has high potential for bone tissue engineering applications due to its morphology and structure.

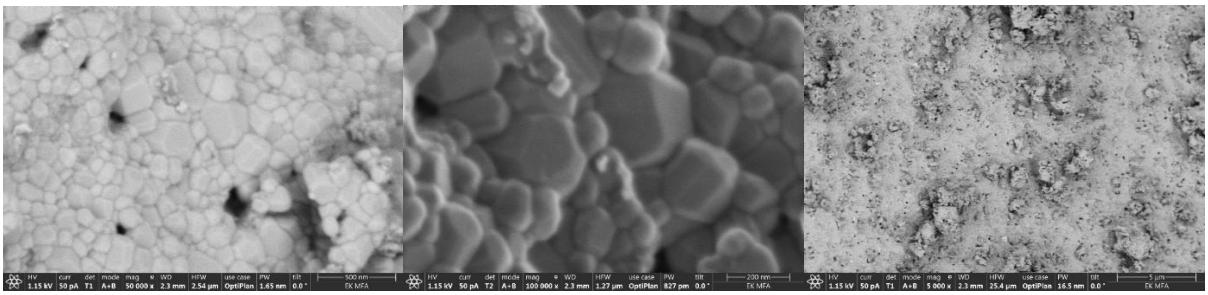

Figure 39. SEM micrographs of the HAp sample obtained at different magnifications. The high magnification images reveal well-defined crystalline particles with faceted surfaces. Pores can be observed between the agglomerated particles, while the lower magnification image provides an overview of the porous architecture of the material. The presence of an interconnected pore network is important for bone-related applications. It can support tissue ingrowth and osseointegration.

Hungarian Chips Competence Centre (HCHiP)

101217997 — HCHiP — DIGITAL-Chips-2024-SG-CCC-1, 2025-1.3.4-KDT_HCHIP-2025-00001

K. Balázsi, P. Fürjes, C. Balázsi, J. Volk

The Hungarian Chips Competence Centre (HCHiP) was established in line with the objectives of the European Chips Act to strengthen Hungary's role in the semiconductor ecosystem (Figure 40). The Centre is implemented in cooperation with three key domestic institutions – Bay Zoltán Applied Nonprofit Ltd., as the consortium leader, Budapest University of Technology and Economics and HUN-REN Centre for Energy Research as consortium members. The competence centre, which operates from March 2025, aims to make state-of-the-art technologies, educational opportunities and research infrastructure available to domestic companies, especially small and medium-sized enterprises (SMEs). HCHiP provides access to design and manufacturing platforms, pilot production lines and European research networks through the network of chip competence centres (aCCCess - www.acccess.eu), while supporting technology transfer, innovation and professional training.

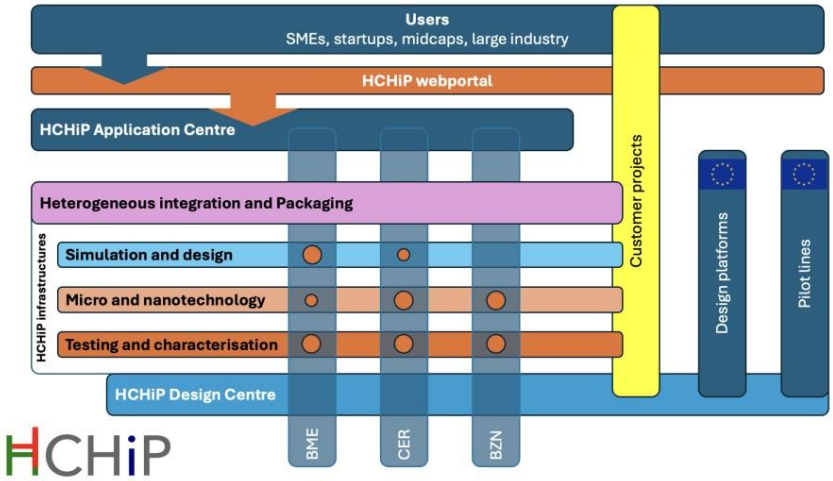

Figure 40. Structure of HCHiP competence centre (www.hchip.eu)

The main objective of WP4 led by HUN-REN EK is to create the technological framework that enables the connection of the infrastructures and their interoperability.

- Define and create a fully interoperable connected infrastructure capable to extensively and efficiently support the pilot development of the users of the Chips Competence Centre.
- Demonstrate the technological connectivity and interoperability within the Competence Centre through a selected development case study.
- Identify the external technological gateways to industrial service providers and other EU CCs to reach EU compatibility.

The HUN-REN EK undertakes tasks in the fields of research, technological development, prototyping services and education, and leads the "Development of Infrastructure Interoperability" work package in the project. The main competencies of the research center are micro- and nanotechnology solutions, chip packaging and integration techniques; thin films, complex material systems, ceramic substrates and their manufacturing technologies; and the development and application of state-of-the-art material testing techniques. The cleanroom infrastructure, featuring available micro- and nanomechanical technologies, is suitable for 3D machining of 4" diameter semiconductor / glass / polymer substrates, development and electro-mechanical integration of mechanical, chemical and biosensors, optoelectronic devices. Our specialists are able to successfully support chip development and manufacturing processes in the modeling, design, prototyping and functional validation stages.

Nanosensors Department

Head: Dr. János Volk, Ph.D., Senior Research Fellow

Research Staff:
Zsófia Baji, Ph.D.
Szabolcs Csonka, Ph.D. (20%)
Olivér Kürtössy, Ph.D.
György Molnár, D.Sc.
Nguyen Quoc Khánh, Ph.D.
Péter Lajos Neumann, Ph.D. (50%)
László Pósa, Ph.D.
Tímea Nóra Török, Ph.D.
Zsolt Zolnai, Ph.D.

Ph.D. Students / Diploma Workers:
László Kelemen, M.Sc. student
János Márk Bozorádi, Ph.D. student (50%)
Bertalan Németh, B.Sc. student
Hanna Stephan, M.Sc. student
Máté Sütő, Ph.D. student (50%)
Bence Vasas, Ph.D. student (40%)
Tamás Zeffer, Ph.D. student (50%)

Engineers:
Ferenc Braun, engineer
Levente Illés, engineer
Dávid Kóti, MSc physicist
Attila Nagy, technician
Zoltán Kovács, microscope-specialist

The Nanosensors Lab aims to develop practical sensors based on new principles of operation by exploiting the results of basic research. To this end, the group makes use of unique experimental infrastructure and the diverse expertise of its research and engineering team. The Nanosensors Research Group, in collaboration with the Microsystems Laboratory (MRL), maintains two semiconductor cleanrooms (nanofabrication and Si MEMS), as well as several auxiliary laboratories, within the Micro- and Nanotechnology Research Laboratory. This research infrastructure has recently been awarded the *Excellent Research Infrastructure* distinction by the National Research, Development and Innovation Office (NKFIH).

In the following, 5 selected examples are presented from a broader range of ongoing research activities, covering (i) the characterization of functional thin films (1–2); (ii) neuromorphic oscillators (3); (iii) quantum electronics (4); and (iv) application-specific embedded systems (5). These research activities are conducted mainly within the framework of four domestic projects (TKP2021-NVA-03: Environmental Monitoring Sensors for Emergency and Extreme Conditions; OTKA K: Investigation of Luminescence and Ionization Energy Deposition Processes in Microstructured Semiconductors Based on Neutral and Charged Particle Conversion Phenomena; OTKA FK: Atomic Layer Deposition and Applications of Functional Sulfide Nanolayers; OTKA K: Development of Nanometer-Scale Resistive Switching Memory Devices), one EU research project (Horizon 2020 EIC: Quantum Bits with Kitaev Transmons), and one mobility program (EU-RISE: Integrated Nanocomposites for Thermal and Kinetic Energy Harvesting). In addition, the Nanosensors Laboratory has provided electron microscopy and nanofabrication services to several industrial partners (Semilab, LightTech, Bosch, Puli Space Technologies), supported the nanofabrication infrastructure of the Quantum Information National Laboratory (QNL), and has been actively involved in university education at the Budapest University of Technology and Economics and Óbuda University.

Neutron absorption in thin boron carbide layers

OTKA K 143263, TKP2021-NVA-03

Z. Zolnai, Z. Kis (HUN-REN EK Nuclear Analysis and Radiography Department),
N. Q. Khánh, Z. Kovács, G. Battistig,
L. Szentmiklósi (HUN-REN EK Nuclear Analysis and Radiography Department), and J. Volk

Boron-based neutron absorbers offer a promising alternative to their competitors, e.g. ^{6}Li-based ones. The benefits to use boron are as follows: (i) ca. four times higher capture cross-section of ^{10}B for thermal (cold) neutrons as compared to that of ^{6}Li. (ii) less kinetic energy of 2.79 MeV in the ^{10}B(n,α)^{7}Li neutron capture reaction is distributed on the reaction products as compared to the ^{6}Li(n,α)^{3}H neutron absorption process with a higher energy release of 4.78 MeV. Consequently, there are shorter stopping ranges of the reaction products in the neutron absorber and in the coupled scintillator layer for ^{10}B as compared to ^{6}Li. (iii) Such features enable reduced neutron absorber thickness and more confined light production volume for scintillation-type isotopically enriched ^{10}B-based neutron detector structures.

A favorable boron containing neutron absorber material is boron carbide [Ref.40], with unique physical properties beneficial for a wide range of applications. The high melting point and thermal stability enable its use as refractory material. It can also be applied as abrasive powder and coating; as well as in ballistic performance due to its low density and high hardness. Usually, the composition of boron carbide layers prepared by different technologies varies in the range B_4C – $B_{10}C$.

In nuclear science applications, a simple construction for neutron detection may be a thin boron carbide neutron absorber layer on top of an efficient scintillator substrate. In this case, 1.47-MeV α and 0.84-MeV Li^{+} particles, emitted in the ^{10}B(n,α)^{7}Li reaction induce ion induced light emission, i.e., ionoluminescence (IL) in the scintillator. A promising scintillator material is e.g. Al_2O_3, with intense IL light emission and high radiation resistance [Ref.41.]. Left panel in Figure 41 shows schematics of a $^{10}B_5C/Al_2O_3$ scintillation-based planar neutron detector structure.

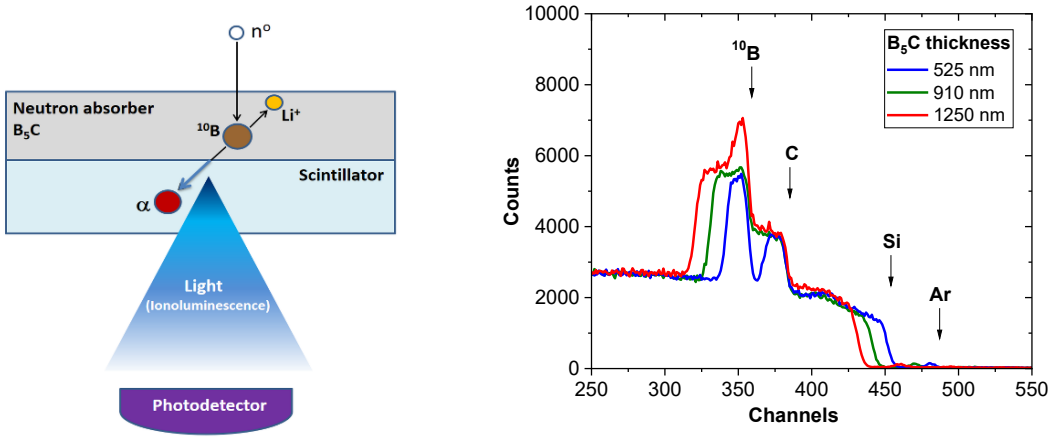

Figure 41. Left: Schematics of a scintillation-based planar neutron detector structure. Right: 1.6 MeV proton-EBS spectra of 10B5C layers with varying thickness deposited on Si substrate. Arrows represent spectral edge positions for different components.

In this case, geometrical optimization based on well described energy conversion processes in the system results in effective neutron capture and detection. We deposited isotopically enriched $^{10}B_5C$ layers (boron-rich boron carbide) on Si substrates by pulsed DC-sputtering. Right panel in Figure 41 shows 1.6 MeV proton-EBS (Elastic BackScattering) spectra of our $^{10}B_5C$ layers with varying thickness

deposited on Si. ^{10}B/C atomic ratios and boron carbide layer thicknesses were determined from the proton-EBS spectra with good accuracy.

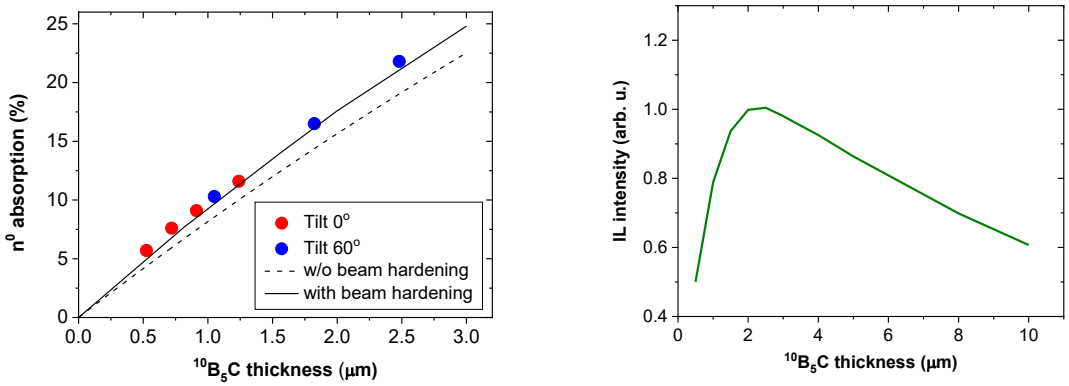

Figure 42. Left: Neutron absorption as a function of $^{10}B_5C$ layer thickness. Dots represent experimental data recorded at 0° and 60° sample tilt angle, while the solid (dotted) line shows calculated values with (without) taking into account beam hardening for neutrons. Right: Calculated normalized light (ionoluminescence, IL) yield of the scintillator vs. $^{10}B_5C$ layer thickness for a planar neutron detector structure shown in Figure 41.

Neutron absorption experiments on the $^{10}B_5C$ layers were performed with a poly-energetic cold neutron beam at the NORMA station of the Budapest Neutron Centre (BNC) [Ref.42-43]. Left panel in Figure 42 shows neutron absorption as a function of deposited $^{10}B_5C$ layer thickness. NORMA measurements were performed at two different sample tilt angles of 0° and 60° with respect to the neutron beam. There is a good agreement between measured and calculated absorption values when the $^{10}B_5C$ layer induced beam hardening (change of the neutron energy spectrum after crossing through an absorbent layer) for the poly-energetic neutron beam is taken into account, see the black solid line in Figure 42.

Right panel in Figure 42 shows the calculated normalized light yield (ionoluminescence (IL) intensity) of the scintillator as a function of deposited $^{10}B_5C$ layer thickness, for a $^{10}B_5C/Al_2O_3$ planar neutron detector structure. Interplay between neutron absorption in the $^{10}B_5C$ layer and the IL emitted by the α and Li^+ ions due to their electronic stopping in Al_2O_3 results in a maximum IL yield for a $^{10}B_5C$ layer thickness of ca. 2.5 μm, see the green line in Figure 42.

Our experiments with thin $^{10}B_5C$ layers as neutron absorbers show that effective neutron capture and energy conversion into ionoluminescence light intensity can be achieved already at a small boron carbide layer thickness of 2.5 μm and simple planar detector geometry.

Controlled Nucleation of Metal Sulfide Layers via Sulfur-Based Surface Functionalisation: Enhanced Initial Growth of GaS_x Thin Films

OTKA FK 139075, 2024-1.2.2-ERA_NET-2025-00025, TKP2021-NKTA-05, Bolyai Scholarship

Zs. Baji, Z. Kovács, Z. Szabó, O. Hakkel, A. Sulyok, Zs. Fogarassy, Zs. Bérces, J. Volk

Atomic layer deposition (ALD) allows nanometre-precision control of film thickness, chemical composition, and conformality. Transition-metal chalcogenides and related sulfides have attracted considerable interest. One persistent problem with sulfide ALD is the poor nucleation on SiO_2. Untreated Si-oxide surfaces contain an insufficient number of OH sites, which leads to island formation, and non-uniform early-stage growth. Additionally, sulfides adhere poorly to oxygen-terminated surfaces, and tend to agglomerate.

This work demonstrates that surface chemistry critically determines sulfide ALD nucleation behaviour. Replacing surface -OH groups with sulfur-containing sites provides more chemically compatible nucleation sites for metal-sulfide ALD. GaS_x ALD serves as a model system to illustrate how surface chemistry governs nucleation, coalescence dynamics, and island morphology.

The GaS_x films were grown at 200 °C in a Picosun R-200 reactor using $Ga_2(NMe_2)_6$ (heated to 135 °C) and H_2S. The as-grown films were amorphous, smooth (RMS ~0.4 nm), and optically transparent. XPS confirmed uniform Ga:S ≈ 1:1 composition throughout the depth, with negligible oxidation. The optical band gap (~4 eV) is consistent with amorphous GaS_x.

The nucleation behaviour on different SiO_2 surfaces was examined, and it was found that an island-like growth occurs on native oxide, CVD and thermal oxide surfaces on Si. According to the XPS measurements, GaS layers grown on thermal oxide exhibited a 30% higher nucleation density than those on native oxide, and CVD oxide had a 90% higher surface coverage, suggesting that the chemical and structural characteristics of the oxide layer play a significant role.

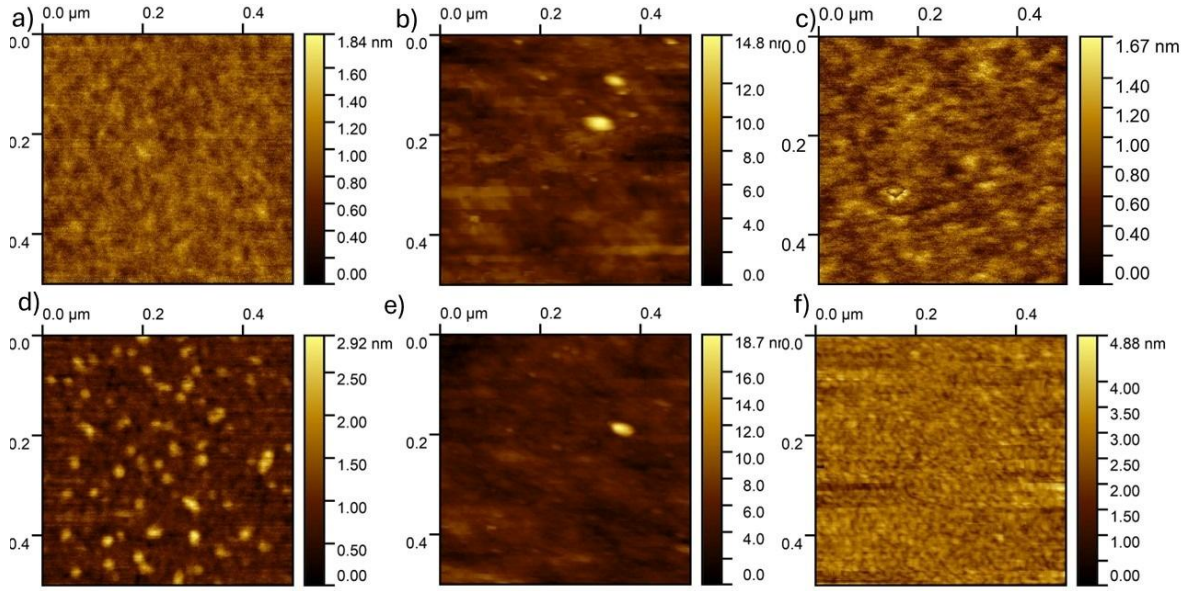

Figure 43. The surfaces of the different oxides: (a) native Si-oxide, (b) CVD oxide and (c) thermal oxide; and their morphologies after 15 deposition cycles: (d) deposition on native oxide, (e) deposition on CVD oxide, and (f) deposition on thermal oxide.

Nucleation of ALD layers is often enhanced by increasing the -OH coverage with a chemical pretreatment. This was attempted with a Piranha treatment, which enhanced the chemisorption of the gallium precursor, thus these samples showed higher island densities and partial coalescence after only 5 cycles. However, agglomeration remained an issue: sulfides preferentially bond to themselves rather than to –OH, causing clustering and slow lateral growth, thus, hydroxylation improves nucleation quantity but not chemical compatibility.

The novelty of the present works lies in the approach of modifying the surface with sulfide-containing anchoring species. The applied three different surface functionalization approaches investigated in this study are shown in Figure 44.

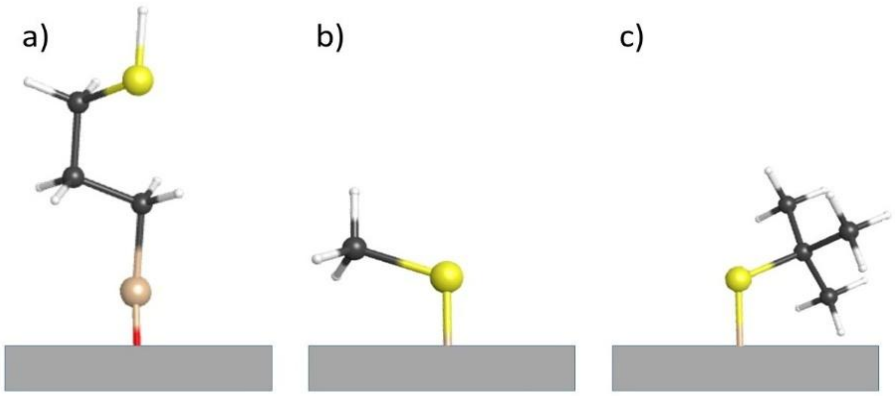

Figure 44. Schematic illustration of the three surface functionalisation approaches applied to silicon oxide substrates prior to GaS_x deposition: (a) silane-based thiolation using mercaptopropyl-trimethoxysilane, yielding an organic spacer layer terminated with –SH groups; (b) gas-phase treatment with DMDS (c) or DTBDS producing sulphur-containing surface species The grey line represents the native Si-oxide surface covered by surface hydroxyl groups.

Mercaptopropyl-trimethoxysilane introduces surface $–(CH_2)_3–SH$ groups. While XPS confirmed successful thiol adsorption, AFM showed increased roughness and non-ideal morphology. The presence of an organic spacer layer introduced steric effects and heterogeneous surface energies. GaS_x coverage improved but did not reach the quality needed for uniform sulfide nucleation.

Gas-phase dialkyl disulfides treatments offer a cleaner and easier sulfur-functionalisation pathway. Dimethyl disulfide (DMDS) and di-tert-butyl disulfide (DTBDS) are sulfur containing ALD precursors that can be in-situ used in the ALD reactor by pulsing them onto the substrate surface prior to deposition. DMDS dissociatively chemisorbs, yielding $CH_3S–$ surface groups. This resulted in the highest nucleation density among single-step treatments with a uniform and fine island distribution. XPS showed ~2.6× higher Ga content after 20 cycles, and a near-continuous coverage was measured with AFM after 15–20 cycles. DTBDS treatment yielded an improved nucleation relative to untreated Si but was less effective than DMDS due to steric hindrance from bulky tert-butyl groups, limiting the density of accessible sulfur sites.

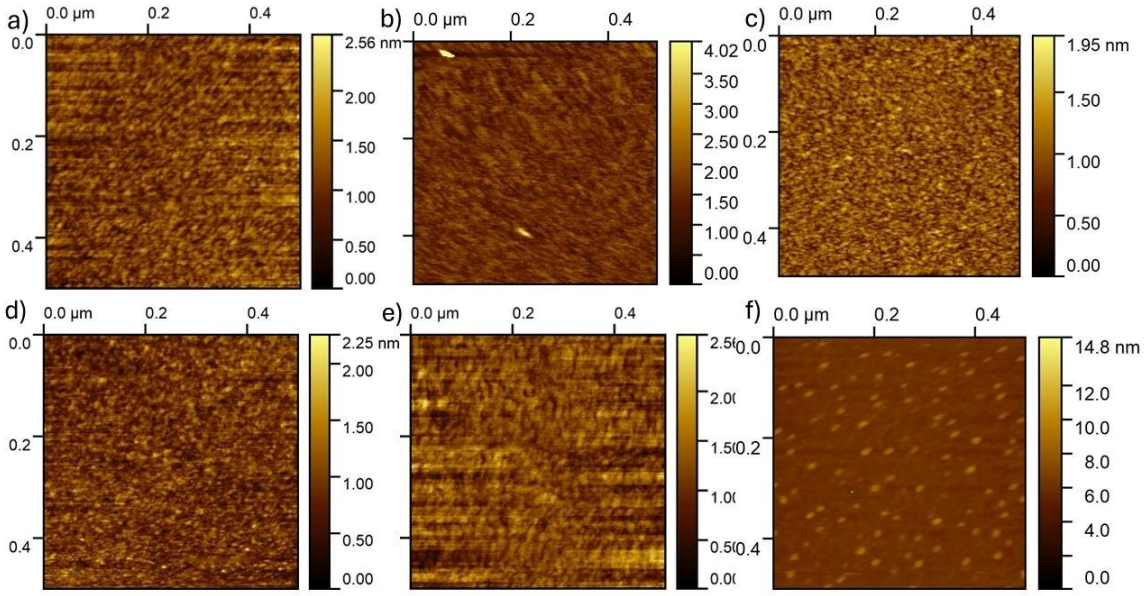

Figure 45. AFM micrographs of (a) 5 cycles of GaSx on native oxide covered Si, (b) the same with piranha pretreatment, (c) DMDS pretreatment, (d) di-tert-butyl-disulfide pretreatment, (e) piranha+dmds pretreatment, and (f) thiolation with mercaptopropyl-trimethoxysilane

Our findings establish sulfur-based surface functionalisation as a powerful and general strategy to improve nucleation in sulfide ALD for GaS, VS_x, ZnS, and potentially TMDC systems. [Ref.44.]

Ultrafast oscillators made of nanoscale VO2 memristors for neuromorphic electronics

OTKA K 143282

Zs. Pollner (BME), T. N. Török (BME), L. Pósa, M. Csontos, S. W. Schmid (BME), H. Kim, A. Piqué, J. Volk, and A. Halbritter (BME)

Oscillatory neural networks (ONNs) have emerged as a promising solution to overcome the von Neumann bottleneck in data processing, which limits the speed and efficiency of traditional computing architectures. ONNs leverage the inherent oscillatory properties of volatile memristors to perform computations in a parallel and energy-efficient manner, offering a significant advantage over conventional systems [Ref.45.]. In particular, the performance of ONNs is directly influenced by the frequency of oscillations; higher oscillation frequencies enable faster and more energy-efficient computations, thereby reducing the overall computing time and energy consumption. Vanadium dioxide (VO_2) memristors have garnered significant interest in the field of neuromorphic computing due to their unique property of undergoing an insulator-to-metal transition (IMT) near at T=67°C [Ref.46.], [Ref.47.]. This characteristic enables them to function as dynamic memory elements with applications in ONNs [Ref.48.].

A traditional VO_2 oscillator circuit (see Figure 46.a) consists of a serial resistor, the memristor and a parallel capacitance. The primary function of the series resistor in this circuit is to establish a voltage divider, thereby ensuring that when the memristor is in its high resistance state, it undergoes a high voltage, so an electronically induced insulator-to-metal transition happens. However, in its low resistance state, the memristor is subjected to a reduced voltage, which induces it to switch off immediately. The capacitance in the circuit is the main decisive factor of the oscillation frequency. One can measure the voltage drop on the memristor (Figure 46.c), blue trace) and the current passing through the memristor (Figure 46.c), black trace) and easily determine the frequency. Our goal was to design a circuit which can exceed the previously reported highest 10 MHz oscillation frequency [Ref.49.]. With our simplified oscillator circuit (Figure 46.b) it is possible to reach ultra-fast 167 MHz oscillations as shown in Figure 46.d. In this circuit we measure only the flowing current to reduce measurement system impact on the circuit.

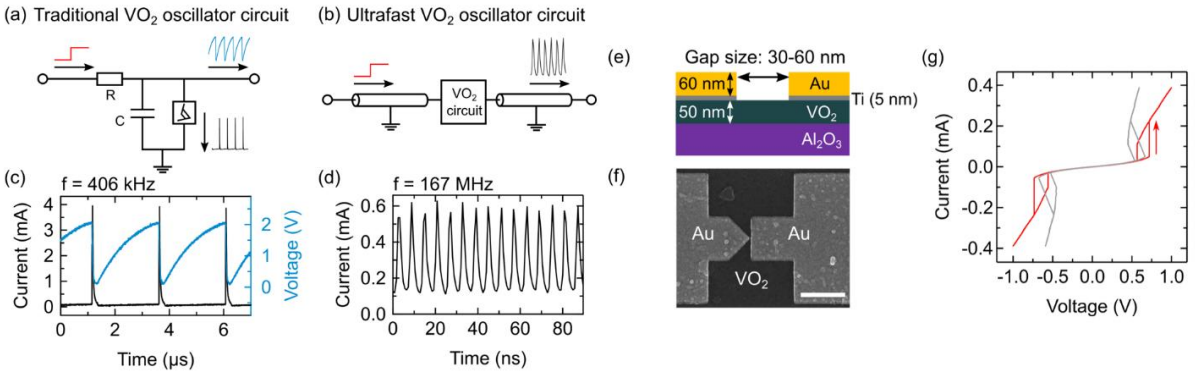

Figure 46. Device characteristics and comparison of high and low frequency oscillations. (a) Low frequency oscillator setup. (b) High frequency oscillation setup. (c) Low frequency oscillation waveforms showing the measured current (black) and voltage drop on the memristor (blue). (d) Measured current waveform of the highest frequency oscillation with 167 MHz. (e) Schematic of the memristor device highlighting the small device size. (f) Scanning electron micrograph of a representative VO2 memristor, scale bar: 1 µm. (g) Low frequency I(V) graph of a VO2 device as a function of driving voltage (red) and as a function of the bias voltage measured on the memristor (grey).

This noteworthy frequency advancement was made possible by the creation of a simplified and optimized electrical circuit, coupled with the use of memristors featuring small active domain sizes of ~30 nm. The schematic vertical cross-section of our planar, ≈30 nm gap size devices is shown in Figure 46.e. For the high frequency experiments, the use of a doped Si substrate would be disadvantageous due to the high stray capacitance towards the substrate, so a well insulating Al_2O_3 substrate was applied. The 50 nm thick epitaxial VO_2 layer was deposited on the substrate by pulsed laser deposition method according to [Ref.50.]. The 60 nm thick gold top electrodes were patterned by standard electron beam lithography also using a5 nm Ti adhesive layer underneath.

A key feature of the structure is the asymmetric lateral geometry (Figure 46.f): a rectangular electrode on one side faces a V-shaped electrode on the other side. This geometry enables the production of ultrasmall (≈30 nm) gap sizes and the confinement of the active region in an ultranarrow, nanoscale spot [Ref.51.]. This confined geometry is considered crucial for the ultrafast operation, as well as for achieving sufficiently low switching threshold voltages at room temperature [Ref.52.]. The electrical switching is represented by the *I(V)* curves of our devices in Figure 46.g where the red trace shows the measured current as a function of the V_{drive} *drive voltage* applied to the VO_2 memristor and the R_S = 1050 Ω resistor in series, whereas the grey graph is the function of the $V_{bias}=V_{drive}-I\cdot R_S$ voltage drop on the memristor.

Figure 47.a depicts the circuit diagram of the ultrafast oscillator measurements. Note, that at both ends, impedance matched output/input of the function generator/oscilloscope were used. The signals were transmitted via coaxial cables to a coplanar waveguide PCB, where an SMD resistor *R* was connected to the memristor. This sample holder has $C < 2$ fF capacitance, which does not affect the oscillations in the ~ 100 MHz regime. Compared to the traditional oscillator circuit (see Figure 46.a), the key difference is that capacitance is omitted from the circuit, and two factors can limit the oscillation speed in such circuits: (i) the finite times required for the operation of the memristor, the inner set/reset timescales of the device, and (ii) the *d* distance between the resistor and the memristor, which introduces a finite voltage build-up time in the circuit.

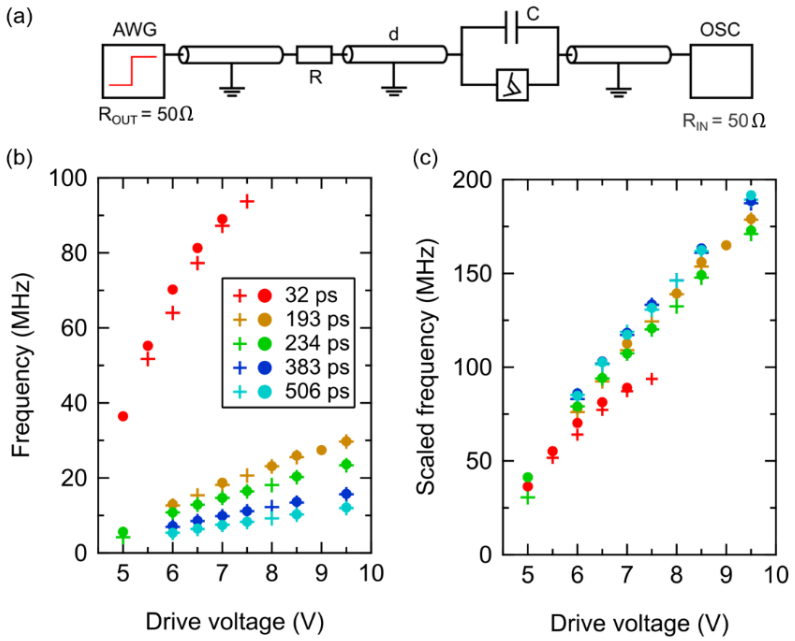

Figure 47. In-depth experimental results concerning distance limitation. (a) Circuit schematics used for achieving ultrafast oscillations, and to study distance limitation. (b) Drive voltage and distance dependence of the achieved oscillation frequency. Different colors show different memristor-serial resistance cable lengths, as shown in the legend. (c) Cable length scaling of the oscillation frequency.

The *d* distance is in the ~mm regime in our case, corresponding to signal propagation times of tens of picoseconds. To understand how the frequency of ~100 MHz oscillators (~ns period time) is limited by delay times of tens of picoseconds we need to incorporate signal propagation times while investigating our high frequency circuit. First, for simplicity, and because of negligible parallel capacitance ($C < 2$ fF) of our memristor, we treat the memristor in its ON/OFF states as a simple resistive element. Its behavior at high frequencies can be easily described by transmission and reflection originating from current continuity and Ohm's law. Those imply that on a resistor, part of the electrical signal is reflected and part of it is transmitted. So, as voltage is turned on, a wavepocket will come and get partially reflected from the serial resistor and a part will be transmitted. The same process happens at the memristor. As time goes on, due to the reflections, voltage drops will build up on the memristor and the serial resistance. In the time $\rightarrow \infty$ limiting case, the ratio of the voltages across the memristor and the resistor would be the same as the ratio of the voltage drops expected in the DC scenario.

To study the distance dependence of the oscillation frequency, we varied the d distance between the memristor and the resistor, and tuned the driving voltage amplitude to different values, as seen in Figure 47.b. We re-scaled the oscillation frequencies with the time delays according to the equation $f_{\mathrm{Scaled}} = f_{\mathrm{LongDistance}} \cdot (\Delta t_{\mathrm{LongDistance}} / \Delta t_{\mathrm{ShortDistance}})$. In Figure 47.c the scaled frequencies are plotted with respect to the drive voltage which show great match with each other for the four longest distances (delay times). However, in the scenario of the minimal time delay of $t_{\mathrm{Delay}} = 32$ ps (red datapoints in Figure 47.c, the frequency deviates from the perfect scaling. This deviation is caused by the inner set/reset times of the memristor, which start to play a role at the investigated time domain.

In conclusion, we demonstrated a high frequency VO_2 oscillator consisting of a serial resistor and a memristor only. Our planar antisymmetric geometry samples can reach 167 MHz and reproducibly reach the 100 MHz frequency regime. We conducted measurements varying the time delay between the resistor and memristor which demonstrate, that in the case of the shortest delay, the inner switching times of the device start to limit the oscillation frequency. Further details can be found in our recent work [Ref.53.].

Progress toward Kitaev transmon generation

HORIZON-EIC-2022-PATHFINDERCHALLENGES-01-06-101115315 (QuKIT)

M. Sütő[1], O. Kürtössy[1], B. Vasas[1], D. Kóti[1], Z. Kovács, and Sz. Csonka[1]
[1]In collaboration with the Department of Physics, BME, Budapest, Hungary
BME staff: M. Berke, Z. Scherübl, P. Makk

Quantum computing promises much faster calculations than today's computers but building reliable quantum devices is still challenging because quantum bits (qubits) are very sensitive to their environment. In the QuKIT collaboration, we aim to develop a new type of robust qubit by combining a Kitaev chain with a transmon qubit (Figure 48.a). A Kitaev chain is a special superconducting structure that can protect quantum information from small disturbances, a property known as topological protection. In simple terms, this means the qubit becomes more resistant to noise and errors. The transmon qubit is a well-established platform that allows precise control and reliable readout of the qubit state. The device is based on a InAs/InGaAs heterostructure, covered by a superconducting aluminum film (Figure 48.b). Our work focuses on two goals: testing whether this aluminum layer can be used to build high-quality transmon qubits, and fabricating and measuring a minimal Kitaev chain device.

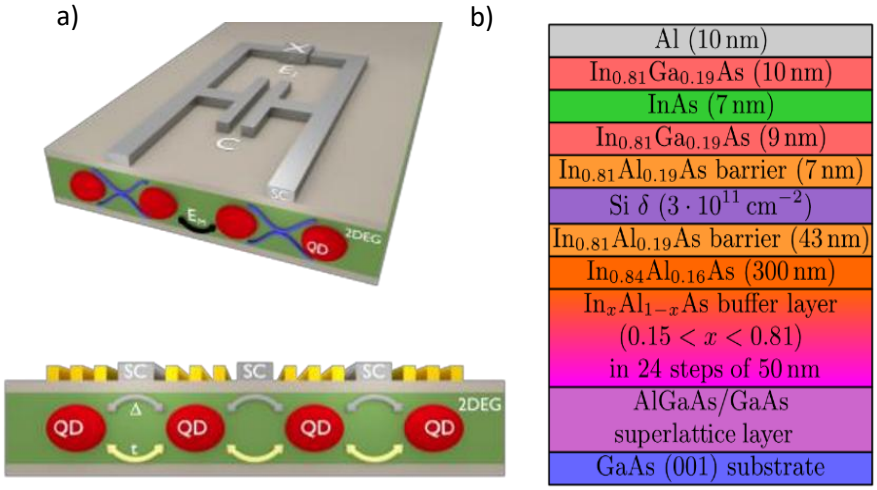

Figure 48. (a) Schematics of the novel Andreev qubit formed by coupling a traditional transmon to a minimal Kitaev chain (source: QUKIT Proposal Part B). (b) Our platform for the realization of the Kitaev qubit: near-surface InAs 2DEG contacted by an epitaxial Al layer.

In earlier work [Ref.54.], we investigated a Josephson junction based on a two-dimensional electron gas with epitaxial aluminum contacts, integrated into an rf SQUID inductively coupled to a superconducting microwave resonator. In this configuration, the junction behaves as a flux-tunable inductance, allowing its properties to be extracted from shifts in the resonator frequency. The technique enables characterization of the junction's supercurrent and average transmission, establishing a reliable platform for studying hybrid devices.

Building on this platform, we designed and fabricated a device consisting of two superconducting loops, each containing a Josephson junction and coupled to the same resonator, to explore the predicted hybridization of Andreev bound states into an "Andreev molecule". The phase across each junction can be controlled independently using magnetic fields or on-chip control lines. The first generation of devices has been successfully fabricated and measured at millikelvin temperatures. The data already show nontrivial behavior indicative of mutual coupling between the junctions. Ongoing measurements and analysis aim to quantify the strength and nature of this coupling.

To realize half of a minimal Kitaev chain, two quantum dots separated by a narrow superconducting segment are required (Figure 50.a). In this architecture, the superconducting channel serves as a source of Cooper pairs, which are subsequently split into the two quantum dots. As a first step toward this goal, we fabricated a gate-defined quantum dot device using multiple layers of electrodes. The first gate layer confines the two-dimensional electron gas (2DEG) into a quasi-one-dimensional channel, while a second layer of thin finger gates is used to define and control the quantum dots. Measurements on this device demonstrate the formation of single quantum dots, as evidenced by the observation of Coulomb diamonds in the transport measurements (Figure 50.b). However, the dots are not sufficiently stable for reliable operation. Based on these results, we are currently designing and fabricating a more stable double quantum dot device, in which the dots will be separated by a superconducting element to enable controlled Cooper-pair splitting and further progress toward the minimal Kitaev chain implementation.

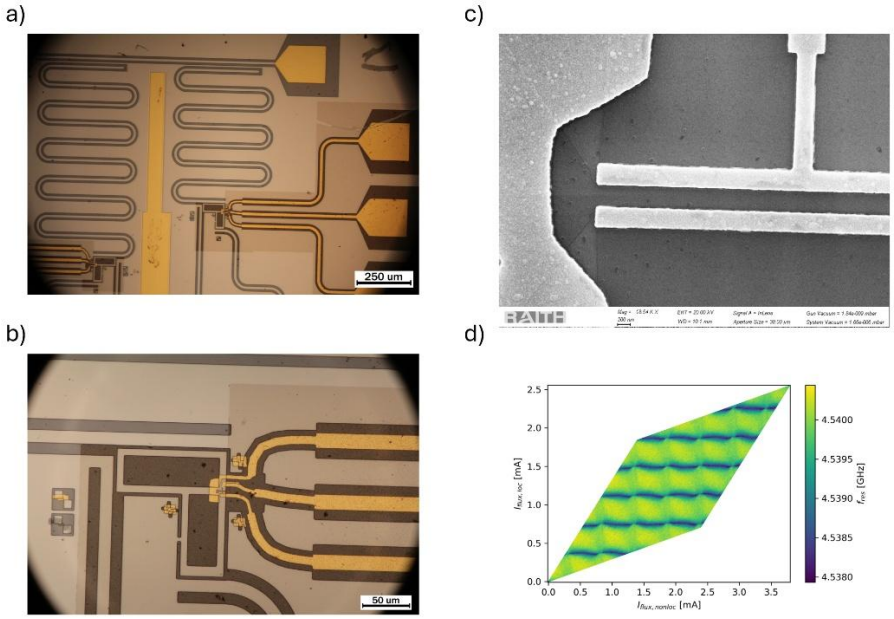

Figure 49. (a–b) Optical micrographs of a λ/4 coplanar waveguide resonator patterned from the epitaxial Al layer and the inductively coupled double-loop structure. (c) Scanning electron micrograph of the double Josephson junction device. Electrostatic gate electrodes are used to tune the charge carrier density in the junctions. (d) Resonance frequency of the resonator as a function of the magnetic flux applied to the two superconducting loops. The crossing of resonance-frequency dips indicates a nontrivial, mutually dependent response of the two loops.

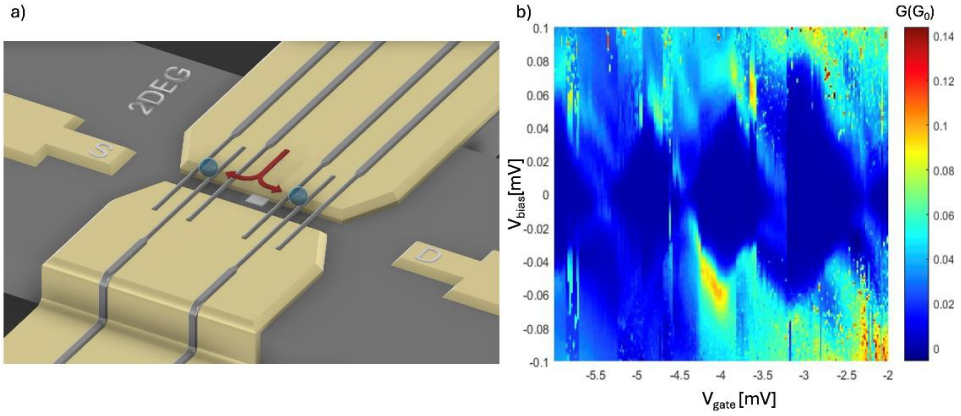

Figure 50. (a) Cooper-pair splitting device. The trapezoidal electrodes deplete the electrons in the 2DEG, forming a quasi-one-dimensional channel. Beneath this channel lies the end of the superconducting aluminum contact, which acts as the Cooper-pair source. Finger gates deposited on top define and control the quantum dots. (b) Single quantum dot measurement. Coulomb diamonds are visible in the transport data; however, the device exhibits instability during operation.

Biomechanical investigation of soft tissue transection using MEMS force sensing

J. M. Bozorádi, P. Révész, F. Braun, L. Illés, A. Nagy, J. Volk

Biomechanical characterization of biological tissues is an increasingly important field at the intersection of medical and engineering sciences. Depending on the clinical relevance, investigations may focus on the elasticity, thickness, or mechanical response of various tissue types. However, in-vivo characterization remains challenging, particularly in the case of delicate anatomical structures.

In collaboration with the Department of Otorhinolaryngology at the University of Pécs, our work focused on the biomechanical investigation of the chorda tympani nerve (CTN), which is frequently exposed during middle-ear surgery. Accidental injury of the nerve may lead to altered taste sensation and dry mouth, affecting a considerable fraction of patients after surgery. Despite its clinical importance, the force required to transect the CTN has not previously been quantified.

To address this challenge, we developed a compact handheld measurement tool based on a MEMS force sensor assembly (Figure 51). The system enables controlled in-situ force measurements on human cadaveric samples while reproducing realistic surgical conditions. The disposable sensor head consists of a miniature, in-house developed 3D MEMS force sensors mounted on flexible printed circuit boards, while the handheld unit contains the readout electronics and wireless data acquisition system.

Following ethical approval at the University of Pécs, measurements were carried out on fresh human cadaveric samples. The developed platform enabled the successful recording of transection events and provided the first experimental estimates of the force range associated with CTN injury. Further details and comprehensive experimental results are provided in a manuscript currently under review for publication [Ref.55.][Ref.55.]

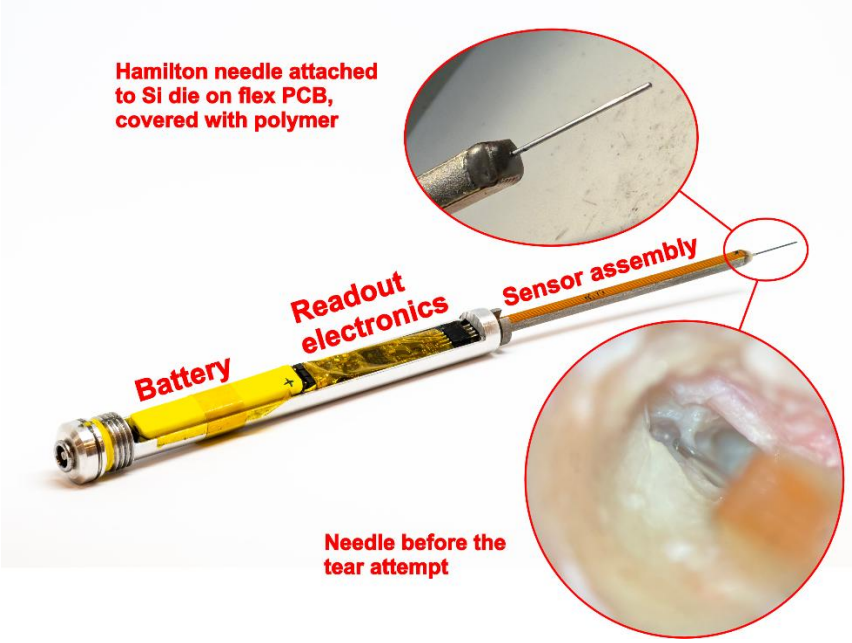

Figure 51. Handheld tissue tester with the sensor assembly before transection of the chorda tympani nerve.

Microsystems Department

Head: Dr. Péter FÜRJES, Ph.D., senior research fellow

Research Staff:
István Bársony, member of HAS
Orsolya Bálint-Hakkel, Ph.D.
Anita Bányai, Ph.D.
Barbara Beiler, Ph.D.
Ferenc Bíró, Ph.D.
Csaba Dücső, Ph.D.
András Füredi, Ph.D.,
Péter Fürjes, Ph.D.
Zoltán Szabó, Ph.D.
Zsófia Sztyéhlikné Bérces, Ph.D.

Engineers / technicians:
Gabriella Bíró, technician
Tibor Csarnai, electrical engineer
Magda Erős, technician
Róbert Hodován,
mechatronic engineer
István Laczkovics, technician
Csaba Lázár, electrical engineer
Margit Pajer, technician

PhD Students:
Lilia Bató (ÓE Univ. Óbuda)
Dóra Bereczki (ÓE Univ. Óbuda)
János Márk Bozorádi (ÓE Univ. Óbuda)
Zsombor Szomor (ÓE Univ. Óbuda)

The main goal of the Microsystems Laboratory is to research and develop integrated sensors and sensor systems, MEMS and BioMEMS devices fabricated by silicon or polymer micro- and nanomachining technology.

The activity covers the characterisation of novel functional materials, development of sensing principles, technology solutions and application-specific microsystems. The utilisation of micro- and nanomachining technology enables the miniaturisation of sensing and analytical systems and integration of various functions of sample preparation, sensing, readout, actuation or communication.

The laboratory is focusing on the development of mechanical, physical, chemical (and biochemical) sensors, functional micro- and nanofluidic devices, implantable microsystems and infrared LED. Our medium-term goal is to broaden the spectra of perspective research topics of MEMS systems and to develop a systematic organisation by forming a dynamic and growing research groups in the Microsystems Laboratory. Considering the financial environment our research directions fit to the European and Hungarian strategic roadmaps and directives (S3 - National Smart Specialisation Strategy) by the following research topics:

Health	*BioMEMS, microfluidic, Lab-on-a-Chip (LoC), Organ-on-a-Chip (OoC) systems, Point-of-Care (POC) diagnostics, therapeutic drug monitoring (TDM), personal medicine, implantable, wearable devices, continuous monitoring,*
Cutting-edge technologies	*human-machine interaction and cooperation – sensors for robotics, driving safety sensors, AI based signal and data processing,* *biosensors, space technologies (microfluidics and diagnostics for space applications),* *advanced materials and manufacturing technologies: novel materials, nanotechnologies,* *3D manufacturing,*
Energy, climate	*sensors for energy industry, characterisation photovoltaic systems,* *gas sensors (smart home, smart clothes), low consumption electronics,*
Agrifood	*food and environment safety sensors (water monitoring), optical (UV-VIS, infrared, Raman) spectroscopy*

Infrastructure and technological competencies

The Laboratory operates a unique infrastructure in Hungary; therefore, its sustainable operation and development is a strategic goal. The infrastructure is open for academic and industrial partners to fabricate (and to characterise) complex, purpose-designed microsystems, nanocircuits, as well as Lab-on-a-Chip devices and to develop their technology solutions.

The high-tech microtechnology related fabrication and characterisation systems work in a class 10 cleanroom facility. The laboratory is dedicated for 3D processing of 4" Si / glass / polymer substrates with maximal resolution of 1μm, together with lithographic mask manufacturing. Electron beam lithography and focused ion beam (FIB) milling are also available with resolution of 20nm. Multi-domain Finite-Element Modelling (FEM), and process simulation also support the structural design and development. Wide spectra of characterisation techniques are also available: optical (fluorescent) and electron microscopy (SEM and EDS), atomic force microscopy (AFM), profilometry, optical and electrical measurements, electrochemical impedance spectroscopy, microfluidic characterisation, mechanical vibration and climate test chambers, UV-Vis / IR / FTIR / FLUORESCENT / RAMAN spectroscopy, etc.

Available micromachining techniques:

- Patterning – mask design, laser pattern generator, photolithography, (double side) alignment, electron beam lithography (E-Beam), Focused Ion Beam processing – FIB milling, nanoimprinting
- Structured polymer layers – PMMA, PI, SU8 patterning, micromoulding, soft lithography – PDMS, hot embossing technique for polymers
- Wet chemistry – chemical wafer cleaning, isotropic and anisotropic etching techniques
- Dry chemistry – deep reactive ion etching, plasma etching techniques (DRIE, RIE)
- High temperature processes – thermal oxidation, annealing, rapid thermal annealing (RTA)
- Physical thin film depositions – Thermal and electron beam evaporation, DC and RF sputtering
- Chemical thin film depositions – Atmospheric and Low-Pressure Chemical Vapour Deposition (APCVD, LPCVD, LTO), thermal and plasma enhanced Atomic Layer Deposition (ALD)
- Liquid Phase Epitaxy of III-V compound semiconductors (LED manufacturing)
- Wafer bonding – Si-glass, glass-glass, polymer-glass anodic and thermal bonding
- Chip dicing, wire bonding especially for sensor applications
- Special packaging techniques and methods, 3D printing and CNC milling for application-specific polymer packages or microfluidic structures
- Close-to-industrial polymer structuring technologies (hot embossing) for manufacturing microfluidic systems

The **Micro- and Nanotechnology Research Laboratory** is recognised as one of the **strategic research infrastructures** (RIs) by the National Research, Development and Innovation Office with an excellent rating in its survey entitled "National Research Infrastructures 2023-2024".

R&D topics and research group structure and in the Microsystems Laboratory

The development of MEMS devices requires solid design capacity and advanced cooperation among the research and technical staffs for precise operation of the full micromachining fabrication line. 10 researchers, 5 PhD students, 4 engineers and 4 technicians work for the Laboratory with close and flexible cooperation with the colleagues of the Nanosensors Laboratory.

- **MEMS & 3D micromachining technology (Csaba Dücső,** Ferenc Bíró, János M. Bozorádi**):** Development specific MEMS (mechanical and gas) sensors for driving and environmental safety applications – with special emphasis on the advanced technology of 3D microstructuring and functional nanomaterials.
- **BioMEMS, integrated systems for biomedical applications (Péter Fürjes,** Barbara Beiler, Zsófia Sztyéhlikné Bérces, János Márk Bozorádi, Csaba Dücső**):** Development MEMS sensors and microsystems specifically for medical applications, considering their complex electro-mechanical integration, biocompatible packaging and signal acquisition. The topic includes the manufacturing Si and flexible implantable and wearable microstructures.
- **Microfludics, Lab-on-a-Chip & Organ-on-a-Chip devices (Péter Fürjes,** Anita Bányai, Lilia Bató, Dóra Bereczki, András Füredi, Orsolya Hakkel, Zsuzsanna Brigitta Sik, Zsombor Szomor**):** These are essential building blocks of Point-of-Care diagnostic and drug analytical tools in the medical field. Research of micro- and nanofluidic systems enable the development of sample preparation, molecular detection and cell analytical functions for LoC and OoC devices. The group works in active collaboration with companies, research institutes and universities in this field (77 Elektronika Ltd., Aedus Space Ltd., Budapest University of Technology and Economics, Microfluidic ChipShop GmbH, Micronit B.V., University of Pécs).
- **IRLED development and spectroscopy (Zoltán Szabó,** Barbara Beiler, Dóra Bereczki, András Füredi, Péter Fürjes, Orsolya Hakkel**):** Development and fabrication wavelength specific infrared LEDs (thousands per year for our partners: Anton Paar GmbH, Senop OY). We envisaged a larger scope development of broadband IRLEDs for OoC based pharmaceutical, environmental and food safety applications.
- **Technology and FEM Modelling (Eszter Leelőssyné Tóth,** Zoltán Szabó, Zsombor Szomor**):** Modelling, such as digital twin, is a widely applied method in engineering practice to speed up development and manufacturing of prototypes. These methods also effectively support the comprehension of physical and chemical processes in the microscale.

Cooperation

According to the large number of European and domestic R&D projects wide cooperative and knowledge network was established with universities (BME, DE, ÓE, PPKE, PTE, SE, TU Delft, TU Eindhoven), research centres (HUN-REN ATOMKI, HUN-REN SZBK, HUN-REN WIGNER, HUN-REN TTK, HUN-REN SZTAKI, IMEC, CSEM) or research groups and companies (77 Elektronika Ltd., Aedus Space Ltd., Microfluidic ChipShop GmbH, Micronit B.V., Philips Research) to perform interdisciplinary research. The Laboratory is supporting the National Laboratory Programmes (Quantum Technology, Brain Research or Human Reproduction) by our technology and expertise. Besides the scientific projects, the Lab offers technology development and manufacturing services for several industrial partners as SEMILAB, 77 Elektronika Ltd., Mirrotron, Bay Zoltán Appl. Res., Senop (Finland) to achieve higher technology readiness levels (TRL 2 → 6).

Major research projects

The researchers of the Laboratories are involved in development, fabrication and integration micro- and nanosystems, sensor structures to open new perspectives in the field of medical diagnostics, Minimal Invasive Surgery techniques, energy-efficient autonomous systems. Moreover, our interest covers the topics of optical analytics (spectroscopy), environmental and safety (gas detectors) sensors.

- Development of a point-of-care microfluidic device for Therapeutic Drug Monitoring in cancer treatment (POC-TDM), Marie Skłodowska-Curie Actions - Postdoctoral Fellowships (HE MSCA PF) – András Füredi, Péter Fürjes
- Unlocking data content of Organ-On-Chips - UNLOOC, Horizon-KDT-JU-2023-1-IA-Topic-1-Global call according to SRIA 2023(IA) 101140192
- Monitoring sensors deployed in emergency situations and in harsh environment, Thematic Excellence Programme - TKP2021 National Defence and Security, TKP2021-NVA-03
- Innovative biosensing technologies for medical applications – INBIOM, Thematic Excellence Programme - TKP2021 Health, TKP2021-EGA-04
- Hungarian Centre for Heterogeneous Integration and Packaging - HCHiP – Chips JU, DIGITAL Simple Grant (DIGITAL-Chips-2024-SG-CCC-1), Chips Competence Centres under the Digital Europe programme
- Participation in the work of professional organizations related to the CHIPS for EUROPE mission - CHIPS-PART, NKFIH 2024-1.2.9-NETWORKING
- Thin film integrity check by capillary bridge test – OTKA FK 128901 (participant)
- Atomic layer deposition and applications of functional sulfide nanolayers – OTKA-FK_139075 (participant)
- Manipulation and characterization of interfaces by the combination of optical and electrochemical methods for sensor development, OTKA-K_146181 (participant)
- Preventing cancer by selectively eliminating senescent cells, NKFIH NKKP STARTING 149496 (participant)
- Temperature-controlled droplet microfluidic systems in parallel bioanalytical applications - EKÖP 2025-2.1.1 EKÖP-2025-00019-D-77, Zsombor Szomor
- Development of microfluidic impedance tomography for cellular application - EKÖP-24-D-11, Lilia Bató
- Investigation of the photon recycling mechanism in InGaAsP/InP multilayers, Bolyai scholarship –2025-2028, Zoltán Szabó

Scientific and industrial cooperations

- Providing optrode devices and their characterisation background for Implantable Microsystems Research Group of Pámány Péter Catholic University
- Development Lab-on-a-Chip technology for detection nucleic acid content in extracellular vesicles for University of Pécs (cooperative partner: BME SZAKT)
- Development and optimisation polymer based autonomous microfluidic cartridge, its production technology and measurement methodology for high sensitive Point-of-Care detection of bacteria and blood biomarkers for 77 ELEKTRONIKA Ltd.
- Development, manufacturing and characterisation microfluidic systems for the HUNOR Programme in cooperation with AEDUS SPACE Ltd.
- Development and manufacturing specific calibration test samples for characterisation methods of semiconductor industry for the SEMILAB Inc.
- Development and manufacturing Near InfraRed LED devices for spectroscopic applications for SENOP Ltd. (Finland)

Scientific media appearances:

- Radio interview – InfoRádió – Szigma, a holnap világa, https://hun-ren.hu/podcast-szigma/interjut-hallhatnak-a-mesterseges-szoveteket-kezelo-mikrochipekrol-furjes-peterrel-a-hun-ren-ek-mikrorendszerek-laborvezetojevel-108905
- Radio interview – Klubrádió – Utópia, https://www.klubradio.hu/adas?hanganyag_id=50036
- TV interview – TV2 – Innovátor, https://nava.hu/id/4394905/
- TV interview: M5 – Multiverzum: https://mediaklikk.hu/ismeretterjeszto/video/2025/11/06/ismeretterjeszto/multiverzum-2025-11-07-i-adas/

Education

The Microsystems Laboratory also have an important mission to provide university students with access to micromechanical technologies and related qualification procedures, and to familiarize future engineers, physicists, chemists, and biologists with this field of science. Accordingly, the laboratory staff actively participate in higher education training as lecturers, practice leaders, and provide students with opportunities to do internships, TDK, BSc., MSc., and Ph.D. work. We have significant relationships with the Faculties of Natural Sciences, Electrical Engineering and Informatics, Chemical Technology and Biotechnology, as well as Mechanical Engineering of BME, the Faculty of Information Technology and Bionics of PPKE, the University of Óbuda, the University of Pannonia, the University of Debrecen, and several faculties and research groups of the University of Szeged.

Wearable gas sensors for emergency and extreme conditions

TKP2021-NVA-03

A. Király, K. Pankász, F. Braun, J. Bozorádi, Z. Szabó, F. Bíró, Cs. Dücső

Chemoresistive gas sensor chip-set for wearable devices

Continuous monitoring of the air in natural, built and industrial environments has become essential to identify the presence and source of toxic and hazardous gases originated dominantly from human activity and take measures to eliminate pollution. Accurate measurements of gases, which are typically present in low concentrations, requires expensive instruments, however, there is high need for inexpensive small sensors that are primarily used for alarm purposes. This requirement can be met by measuring the various physical and chemical properties of the gases.

Two families of gas sensors are considered:

1) **low cost solid-state catalytic and chemoresistive sensors** for demo applications target gases: H_2S, HCN, NH_3, Cl_2 or HCl (1-10-100ppm - TLV level or above)
2) **moderate cost optical sensor for more accurate concentration measurements** target gases: CH_4, LPG, PB 1—5 %v/v (possibly CH_4 ~ 100 ppm)

The most widely investigated devices are solid-state conductivity sensors, which operate on the principle of chemisorption-controlled resistance change. As part of the project, we developed a universally applicable system consisting of a conductivity-type gas sensor chip based on measuring changes in the conductivity of thin layers of metal oxides with semiconductor properties, and a small portable device of evaluation electronics that supports low-power Bluetooth Low Energy (BLE) communication. Due to its low power consumption and size, the implemented system is suitable for wearing on clothing during emergency interventions or for mounting on drones to continuously measure gas concentrations and provide standard-compliant alarms.

The device is based on a 3.5x3.5mm^2 chip containing three microheaters and measuring electrodes on their top. The three independently operable elements provide the 50-400 ^{o}C temperature required for detection with a power of 2-26 mW each.

The critical component of conductive gas sensors is the sensor layer; its composition, 3D micro- or nanostucture essentially determines the sensing characteristics. Therefore, the development of the sensing material requires a variety of synthesis processes and many qualification measurements. With our modified test system, we can test 3-3 elements of 5 chips at the same time.

For the demonstration, we prepared **vanadium oxides** with a nanofibrous structure using hydrothermal synthesis and deposited nanoscale particles of various precious metal catalysts onto their surfaces. We examined its gas detection properties for NH_3, H_2S, and NO in ranges around the maximum allowable workplace concentration (MAK or TLV) values. The series of measurements showed that, of the three gases, the gold-sensitized sensor operated at 250 °C provided good sensitivity and reproducible signals for H_2S in the range of 0.3 ppm-10 ppm with a response time (t90) of 5-15 s and an acceptable recovery time of a few minutes. The sensitivity of the system can be further improved by modifying the composition of the material system and its characteristic geometric dimensions. (Figure 52)

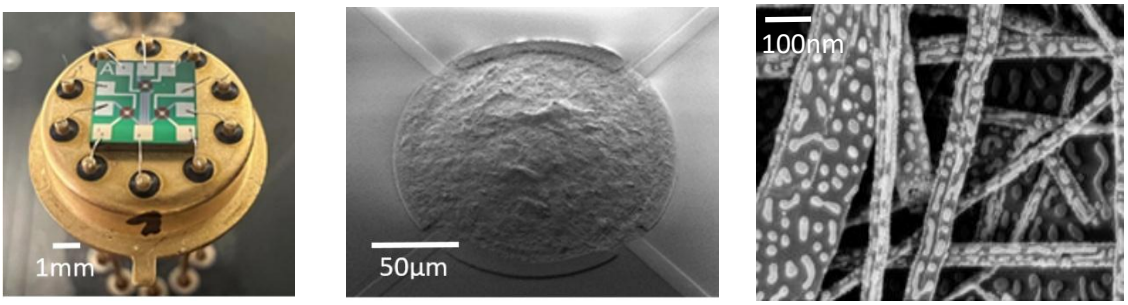

Figure 52. The chip containing the three sensor elements (left) and one of its heaters as covered with a nanofiber VOx sensor layer (middle), and VOx nanofibers sensitized with gold particles (right).

Another element of the development was the implementation of a portable instrument. The device was designed by focusing on low energy consumption, wireless data transmission, and on-site visual feedback. The electronics operates by 1.5 V supply voltage and capable of reading a single sensor chip. The chip contains three independent sensor channels, each with individually controllable heating power. The system measures the conductivity of the sensor channels in the range between 1 kΩ and 10 MΩ. The average power consumption of the electronics is 5 mA. A conventional AA (pencil) battery has a nominal capacity of approximately 2000 mAh, which allows for 8-20 hours of continuous operation, or even several days of operation with intermittent measurements.

The developed chip and BLE-based evaluation electronics, using appropriate sensor materials, offer an autonomous, small-sized, portable, and low-power solution for environmental monitoring, hazardous concentration detection, and even detection of multi-component gas mixture. The ongoing activity focuses on synthesis of nanostructured vanadium-oxide phases and investigation of their gas sensing properties.

Compact optical gas detector for portable applications

Gas sensors play an important role in environmental monitoring, healthcare applications and safety technology, not only in installed systems, but also in portable or drone-mounted forms. In addition to detectors operate with chemoresistive or electrochemical transduction principle, optical gas detectors are becoming increasingly popular. These detectors use the non-dispersive infrared (Non-Dispersive Infrared – NDIR) absorption to detect certain gas components in the middle infrared region (Middle Infrared Region – MIR) and, less frequently, in the near infrared region (Near Infrared Region – NIR). The term "non-dispersive" refers to the fact that the optical system does not contain a dispersive element, i.e., an optical grating or prism. Instead, an optical bandpass filter tuned to the optical absorption band of the target molecule in the infrared range and/or a monochromatic light source are used.

Although NDIR gas detectors have been used since the 1940s to reliably measure the concentration of certain gas components, the progress of microelectronics and MEMS industry made it possible to reduce the size of these devices and enable their rapid spread. With the use of increasingly complex integrated circuits (e.g., microcontrollers, front-end stages, etc.) and miniature light sources (LEDs, microheaters), a commercial NDIR gas detector can now be reduced to a volume of 3–4 cm^3. The minimum required electronics is placed on a circuit board with an area of approximately 2–3 cm^2, so the optical system still accounts for a significant part of the detector's volume.

To demonstrate one possible way of reducing the size, we have developed a 300 µm wide optical channel for the NDIR methane detector in this project, which was formed by photolithography in a thick SU8 polymer (Figure 53). The inner surface of the channel is coated with an optical reflective layer to reduce optical scattering and crosstalk. The transmitter side of the sensor consists of NIR/MIR LEDs and reference photodiodes placed in a common housing, while at the channel output (receiver side), a photodiode of the same type as the reference converts light pulses with a minimum frequency of 100

Hz and a width of 400 μs into electrical signals. In the presence of the target gas, the infrared LED light tuned to the absorption bands of the gas passes through the microchannel with an effective optical path length of 4.5 cm with attenuation proportional to the concentration according to the Beer–Lambert's law of absorption. The microcontroller calculates the concentration of the target gas from the decrease in intensity detected on the receiver side, the absorption coefficient of the target gas, and the optical path length. The device is powered by a 3.7 V, 190 mAh lithium battery, which allows for approximately 8–9 hours of continuous operation. [Ref.56.]

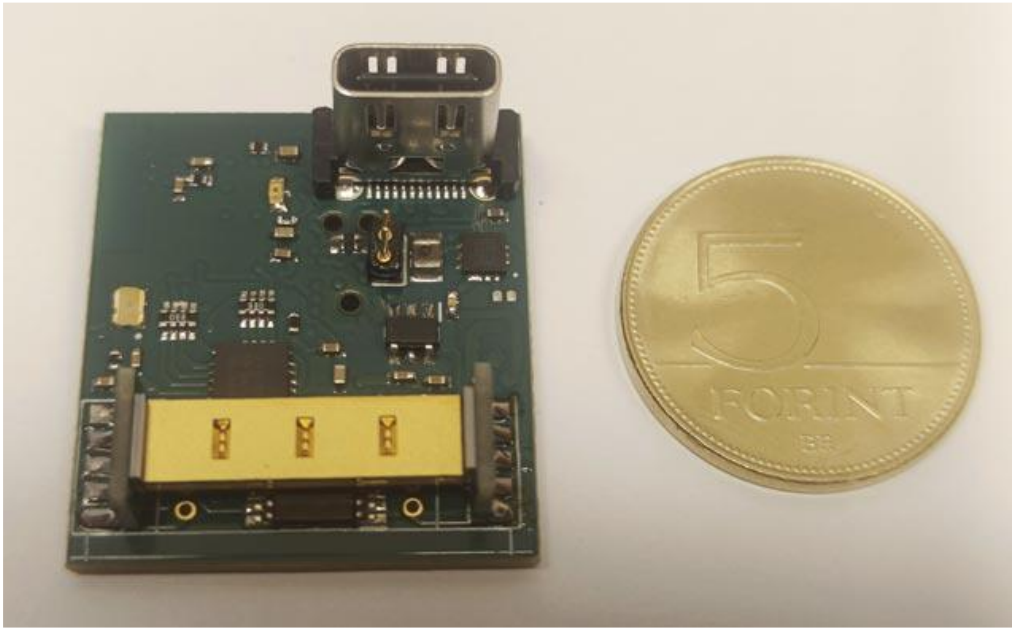

Figure 53. Prototype of an NDIR methane detector with an optical microchannel for portable applications. The god surface optical channel covered with a gas-permeable reflector is visible on the lower half of the 25×25mm^2 circuit board.

3D MEMS force sensor for tissue recognition

H2020-ECSEL-2017-2-783132 "POSITION-II, 2018-2.1.6-NEMZ-ECSEL-2018-00001

J. M. Bozorádi, K. Gáspár, Zs. Bérces, G. Pap (Uzsoki Hospital), P. Fürjes

Laparoscopic devices have been widely used in the past decades during surgical procedures. Currently they are the golden standard in minimal invasive surgery. Minimally invasive (possibly robotic) surgery (MIS) offers several advantages for the patients, although the lack of sensory feedback for the surgeon is also a barrier in its progress. Gathering immediate multi-parametric information about the physical and anatomic conditions of tissues is crucial for the operator to support the tissue recognition and pathologic characterization. Smart devices with integrated MEMS force sensors can provide such feedback and improve the safety of these interventions or help in on-site pathologic decisions.

At the Uzsoki Hospital in Budapest (Dr. Géza Pap) there is a growing interest in these sensors since these were already integrated in a laparoscope head in the previous INCITE project. Even with the existence of surgical robots there's still a great need for **handheld devices** with the addition of a „smart element" embedded in them to help the work of the surgeon by providing information regarding tissue thickness, stiffness, composition and the effect of the surgeon's current action. Our first goal was to develop a novel device with integrated micromachined 3D force sensors to provide tactile information about the different organs and tissues touched. Our developed 3D piezoresistive force sensors were designed and manufactured by silicon micromachining technology and mechanically integrated in the appropriate biocompatible packaging and elastic coverage. Application specific readout electronics were designed to solve the analog-to-digital signal conversion, initialization, noise filtering and the communication with a LabVIEW data acquisition user interface.

In our joint project with Uzsoki Hospital in Budapest, our research group has been developing a 3D MEMS force sensor-based system for biomechanical characterization of human gastrointestinal tissues. The long-term goal is to provide feedback during minimally invasive surgical procedures regarding tissue properties such as thickness and stiffness. Previous work focused on a tabletop measurement platform capable of implementing in vitro mechanical tissue characterization by recording force-displacement characteristics of resected tissue samples and providing elastomeric and pathological data. Building on these results, the current period focused on redesigning the existing tabletop system into a more compact, instrument-integrated form.

As a first step a "sensor cartridge" was designed, which is capable of housing the MEMS sensor and its flexible electronics. The cartridge is designed to be compatible with the standard laparoscopic devices, already used in clinical practice. A series of measurements were made as proof-of-concept on a resected stomach sample. In parallel, reference measurements were also made with the already existing tabletop system. While the tabletop system provides position-controlled force-displacement data, the cartridge currently yields force-time measurements due to the lack of direct position sensing. Despite this current limitation, the shape of the resulting force curve shows the same characteristic behavior and stiffening effect of soft tissues under high compression observed in tabletop measurements (Figure 54). An important new finding of this experiment is that the maximum load applied on the tissue upon closing the laparoscopic stapler device might be significantly higher than previously expected, which may influence the decision-support information provided to surgeons. These results were presented at the EUROSENSORS XXXVII conference in Wroclaw. Our hope is that information regarding the patient's status before and after surgical procedures can be correlated with the tissue elasticity curves so an optimal stapler height can be determined by a neural network based AI supported data processing system in the future. [Ref.57.]

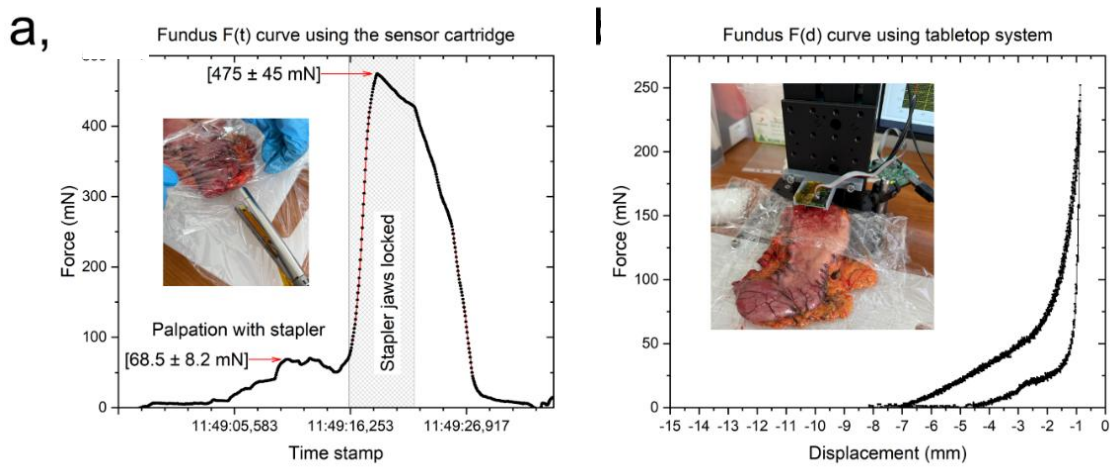

Figure 54. Force-time curve of a simulated laproscope jaws closed on a healthy stomach section (left). Force-displacement curve obtained with the tabletop measurement system (right). The compression of the same tissue section is similar to the time dependent force measurement.

Characterisation of materials for bioMEMS applications

Moore4Medical, ECSEL Innovation Actions (IA), Call ECSEL-2019-1-IA

B. Beiler, Cs. Dücső, P. Fürjes

Nanoindentation Analysis of SU-8 Coated Wafers at Different Baking Phases

This study systematically characterizes the mechanical behaviour of SU-8 thin coatings on silicon wafers through static and time-dependent nanoindentation at different baking stages in cooperation with the Semilab Zrt. The results demonstrate a strong correlation between the degree of thermal curing and both the instantaneous and viscoelastic properties of the polymer. The post-bake process produces a marked increase in hardness and elastic modulus, while the creep and relaxation tests reveal a concurrent rise in the retarded modulus and viscosities of the Burgers model, indicating a substantial reduction in long-term viscoelastic flow. The mechanical behaviour of SU-8 is primarily governed by the extent of cross-linking rather than by strain rate or size effects. The increase in modulus and viscosity with baking temperature reflects the transition from a partially polymerized resist to a highly cross-linked, glassy network.

These findings underline the importance of optimized post-bake or hard-bake conditions to achieve mechanically stable SU-8 layers for MEMS and microfluidic applications. Furthermore, the nanoindentation-based evaluation of both instantaneous and creep responses provides a rapid and nondestructive method for monitoring polymerization.

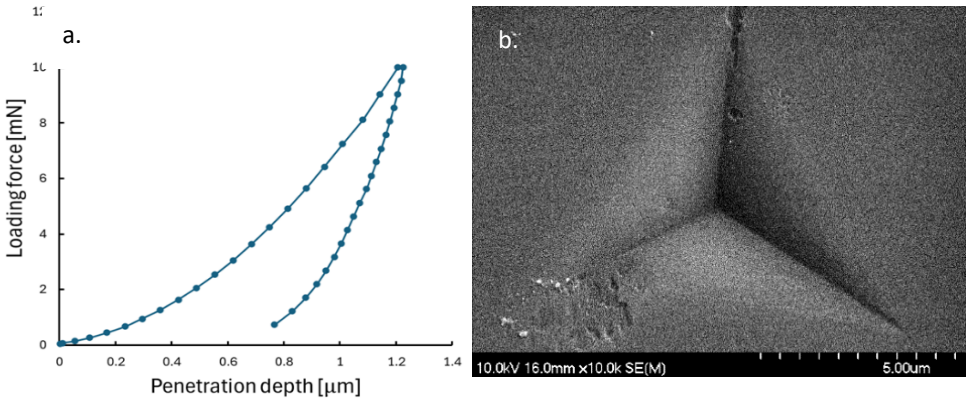

Figure 55. A representative force-displacement curve obtained from the nanoindentation measurement on the soft-baked SU-8 coated silicon wafer (a). SEM images of the SU-8 coated wafer surfaces show the indentation at a higher magnification, also showing the interfacial slipping (b).

Biocompatible coating of silicon integrated circuits

Silicon integrated circuits (ICs) are essential for the next-generation miniaturised active neural implantable devices, whether packaged in soft polymers for flexible bioelectronics or implanted as bare die for neural probes. In these applications the integrated circuits are exposed to the corrosive body environment, raising reliability concerns, particularly for chronic use. In this study the inherent hermeticity of bare die ICs was characterised, and the potential of polydimethylsiloxane (PDMS), a moisture-permeable elastomer was evaluated, as a standalone encapsulation material. The one-year accelerated in vitro and in vivo analysis proved that the PDMS coating serves as an effective, long-term protective barrier for miniature neural implant ICs, maintaining both structural and electrical stability

against bodily fluids, while uncoated areas suffer degradation. This study confirms that PDMS-covered regions prevent the failure typically seen in uncovered IC surfaces.

Results revealed stable electrical performance, indicating the unaffected operation of ICs even when directly exposed to physiological fluids. Despite this, material analysis revealed IC degradation in the bare regions. PDMS-coated regions, however, revealed limited degradation, making PDMS a suitable IC encapsulant for years-long implantation. Based on the new insights, guidelines are proposed that may enhance the longevity of implantable ICs, broadening their applications in the biomedical field.

Tailoring porous properties of polymer monoliths through the composition of the binary solvent mixture

Porous polymer monoliths with controlled porosity are critical materials for advanced separation technologies. Gamma-radiation initiated polymerization offers a straightforward and robust approach to their synthesis, employing a monomer mixture composed solely of monomers and solvents. Achieving precise control over the pore structure for a given monomer primarily depends on the careful selection of the porogenic solvent. This study presents a comprehensive investigation into how solvent composition affects both the structural characteristics and functional flow performance of diethylene glycol dimethacrylate (DEGDMA) monoliths prepared using binary solvent mixtures via gamma-radiation polymerization. Three binary solvent systems—ethyl acetate/alcohols, acetonitrile/alcohols, and acetone/alcohols—were examined, with alcohol concentrations varying from 0 to 70 vol.% in a monomer solution containing 30 vol.% DEGDMA.

The addition of 20-30 vol.% of the good solvent (ethyl acetate, acetonitrile, acetone) to the poor solvent (alcohols) initially enhances pore formation, creating larger aggregated globules and increased pore sizes compared to the pure alcohol systems. While all three good solvents follow similar trends, they exhibit distinct characteristics: acetonitrile systems show the most pronounced surface area maxima (up to 60 m^2/g), acetone systems provide intermediate behavior, and ethyl acetate systems demonstrate the most gradual transitions with sustained performance at higher concentrations. Among the alcohols, methanol consistently produces the highest flow rates and largest pore sizes, followed by ethanol and 2-propanol. This hierarchy reflects the different solubility parameters and their interaction with the DEGDMA monomer during polymerization. Maximum flow-through performance is consistently achieved at 20-30 vol.% concentrations of the good solvent across all three systems, with peak flux values ranging from 0.17 to 0.38 $mL/(min \cdot mm^2)$. This optimal range represents a balance between maintaining macroporous structure and preserving pore connectivity. The complete loss of permeability at high good solvent concentrations (>30 vol.%) indicates the formation of microporous or bulk structures without interconnected pores. [Ref.58.]-[Ref.60.]

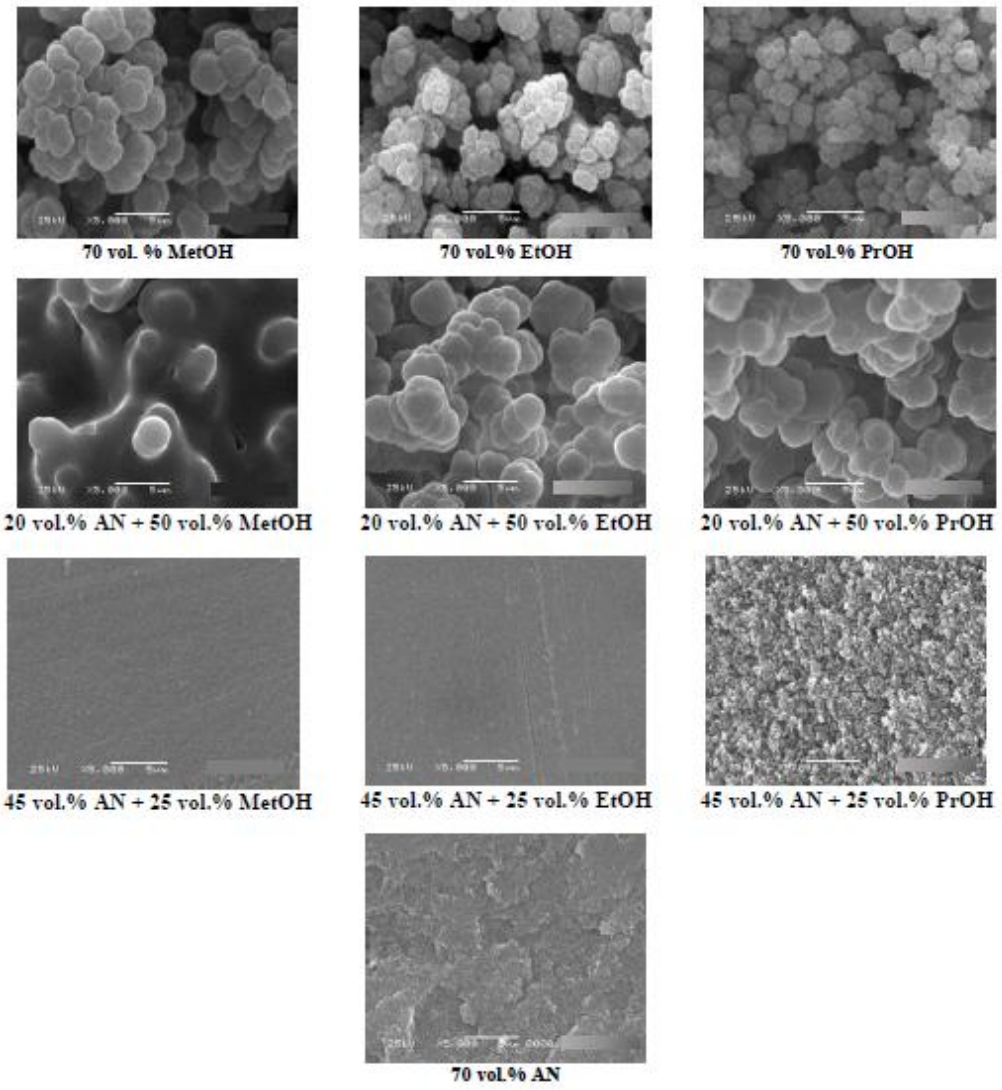

Figure 56. Morphology of DEGDMA monoliths prepared with different acetonitrile (ACN)/alcohol (MetOH, EtOH, PrOH) solvent ratios. The monomer mixture contained 30 vol.% DEGDMA and 70 vol.% of the solvent. The irradiation was performed with 30 kGy dose and 11 kGy/h dose rate.

Microfluidic methods for particle and cell manipulation and analysis

TKP2021-EGA-04

A. Bányai, M. Varga (77E Ltd.), L. Bató, Zs. Szomor, E. Leelőssyné Tóth, B. Beiler, M. Veres (HUN-REN Wigner), P. Fürjes

In the field of microfluidics, the development of medical diagnostic applications with the spread of Lab-on-a-chip (LOC) or miniaturized total analytical systems (μ-TAS), Point-of-Care (POC) diagnostic platforms, which can be used at the patient's bedside, ambulances or medical offices, has received great emphasis in recent decades. The use of Micro-Physiological Systems (MPS) or Organ-on-Chip (OoC) devices, the in-vitro study of cell populations or even individual cells in a controlled chemical environment, can be a significant step in the development of active pharmaceutical ingredients. Our goal is to develop application-specific devices that, by using integrated microfluidic and sensor systems, simultaneously solve the maintenance of artificial cell populations or even tissues, their treatment with chemical agents, and the real-time monitoring of their physiological behavior. Our long-term goal is to develop microsystems that, due to their size, can accelerate the study of the effects of active pharmaceutical ingredients, which can be an important step forward the rapid screening of antibiotic resistance or the personal chemtherapeutic treatments.

Impedance study of localized cells in a microscopic chemical environment

In vitro testing of cell populations or individual cells in artificial systems that model their real environment is highly prospective from a biomedical and environmental point of view. Cell trapping and in-vitro analysis are powerful tools that enable the investigation of cell viability and proliferation in microfluidic structures. Impedance spectroscopy is a suitable method for studying various properties of cells and cell cultures, as it allows non-invasive and real-time measurements. By integrating microelectrodes, the microfluidic structure can be suitable for impedance-based cell analytical (ECIS and TEER) measurements. Our research aims to develop a fully electrical, non-invasive microfluidic measurement system that can be broadly applied in biological research. To achieve this, a microfluidic device (Figure 57Figure 57) with integrated microelectrodes were developed to be capable of trapping cell populations or individual cells between the sensing electrodes. Using a dedicated printed circuit board (PCB) designed for measurements and a channel-switching matrix integrated into the microscope, the optical and electrical responses of the system can be investigated simultaneously.

Impedance spectroscopy-based measurements were carried out using gold and platinum electrodes integrated into the microfluidic structures. The impedance spectra obtained with different electrode arrangements were investigated using both two- and four-electrode configurations. The four-electrode configuration increases measurement sensitivity and minimizes contact impedance, enabling precise characterization of the electrical properties of biological samples.

During functional testing of the device and the fabricated chips, the EIS spectra of the microfluidic system filled with different media were examined, including phosphate-buffered saline, cell culture media relevant for later cellular applications (HepG2 or DMEM), and YPD yeast growth medium. For proof-of-concept validation of the system, yeast cells (*Saccharomyces cerevisiae*) were used, as their rapid division and ease of cultivation make them an ideal model system. The system enables the parallel acquisition of impedance spectra and optical measurements, which serves as an initial optical validation of the electrical measurements. This approach allows real-time, detailed characterization of the effects of localized cells on their microenvironment.individual electrodes.

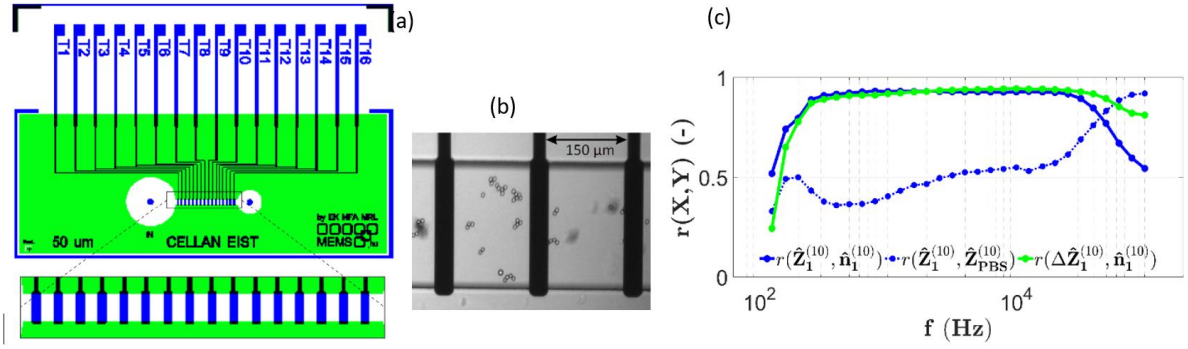

Figure 57. The layout of the microfluidically integrated EIS-based cell-analytical system (left) and Nyquist (right) plots of different numbers of trapped cells between

Electrochemical impedance tomography for morphological analysis of cell populations

EIS has numerous applications, including electrical impedance tomography (EIT), whose most widespread macroscopic uses include body composition analysis and targeted medical diagnostic applications, such as tumor detection. However, a major limitation of this approach is that it provides only qualitative, macroscopic information about tissues and does not offer cell-level resolution.

Achieving cellular-level resolution through miniaturization would significantly contribute to the in situ three-dimensional monitoring of cell culture growth, structural changes in 3D architectures, and the effects of therapeutic treatments. By combining microfluidic systems with EIS, it is possible to develop devices capable of detailed analysis of the spatially dependent properties of individual cells or cell populations, as well as high-resolution, real-time, and even three-dimensional structural investigations. Such developments represent an important step toward applications in drug testing, personalized medicine, and diagnostics. To realize such a system, our goal was to develop a device in which the placement of multiple parallel electrodes and their miniaturization enables the localization of cell distributions within a microfluidic channel, thereby paving the way for impedance tomography-based approaches. This strategy offers a new direction for overcoming the limitations of the technique and for moving toward quantitative evaluation.

In this work, the tomographic capabilities of the device and potential imaging approaches were investigated using microbeads. Two- and four-electrode measurements were taken of the bead distribution along the channel. During the experiments the effect of microbeads on the EIS spectra was observed and correlated with the size of the beads relative to the channel height. The strongest correlation was achieved when the bead size was closest to the channel height. From the two measurement methods the four-electrode one proved to be more accurate due to its more sensitive behaviour regarding the resistive part of the spectra, where the beads cause the most change.

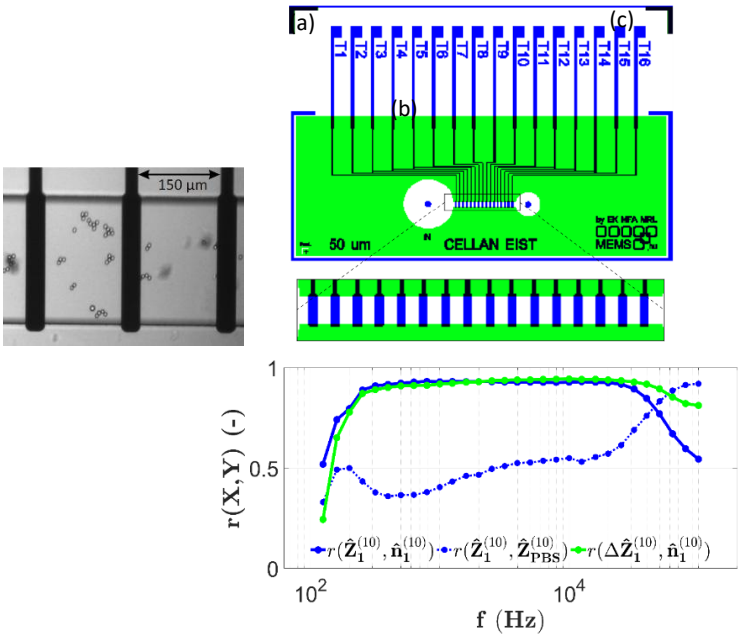

Figure 58. Microfluidic system designed for EIT measurement (a), bead distribution in the channel between two electrodes (b), and the correlation of the measurement with cell number in the case of 4-electrode configuration (c).

Investigation of flow and thermal processes in two-phase (digital) microfluidic systems

The capacity to construct intricate microfluidic architectures has empowered researchers to devise novel experimental formats for processing extremely small analytical volumes within short timeframes and with remarkable efficiency. These applications rely on generating small, separate droplets of the sample or reagent within a non-mixing carrier fluid, altering fluid behaviour. These artificial microscopic containers enable accelerated mixing of chemical primers, prevent contamination and non-specific molecular binding on channel walls, and support highly parallelized processes with the opportunity of single cell or molecule analysis.

Our goal was to develop and investigate digital microfluidic system capable of providing a stable and homogeneous chemical microenvironment for individual cells and biological samples, while supporting precise and reproducible chemical processes through targeted thermal treatment. Accordingly, our work focused on mixing phenomena and the analysis of temperature distributions within a complex microfluidic platform that enables controlled chemical and thermal treatment of individual cancer cells.

We designed and implemented two-phase flow systems, which are suitable for the reliable generation of micro-sized liquid droplets, even for the placement of cells in droplets. By appropriate modification of the microfluidic systems, we improved the reliability of the droplet generation process, and by trapping and analyzing the droplets, we investigated the course of flow (e.g. mixing) processes taking place in a closed microenvironment. We analyzed the droplet generation process, its dependence on material and hydrodynamic parameters, and the mixing phenomena taking place in closed microvolumes using 2D and 3D finite element models. Both theoretical and experimental analysis were performed to reveal the influence of various channel geometries and flow parameters, with a primary emphasis on enhancing mixing efficiency and subsequently establishing an appropriate thermal environment. The evolving temperature distribution was characterised using both single-phase and multiphase models and our results demonstrated that, due to the low thermal conductivity of the oil phase, a highly localized and well-controllable temperature field develops within the droplets.

Furthermore, Dean vortices generated in curved channel sections were shown to significantly enhance droplet homogenization, even in regions upstream of the thermal treatment zone. This work contributed to a deeper understanding of droplet-based microfluidic mixing and to the development of an integrated experimental–numerical methodology that lays the foundation for future biotechnological and Lab-on-a-Chip applications. To experimentally validate the numerical results, specific two-phase microfluidic system was designed with integrated heating elements. . [Ref.61.] - [Ref.66.]

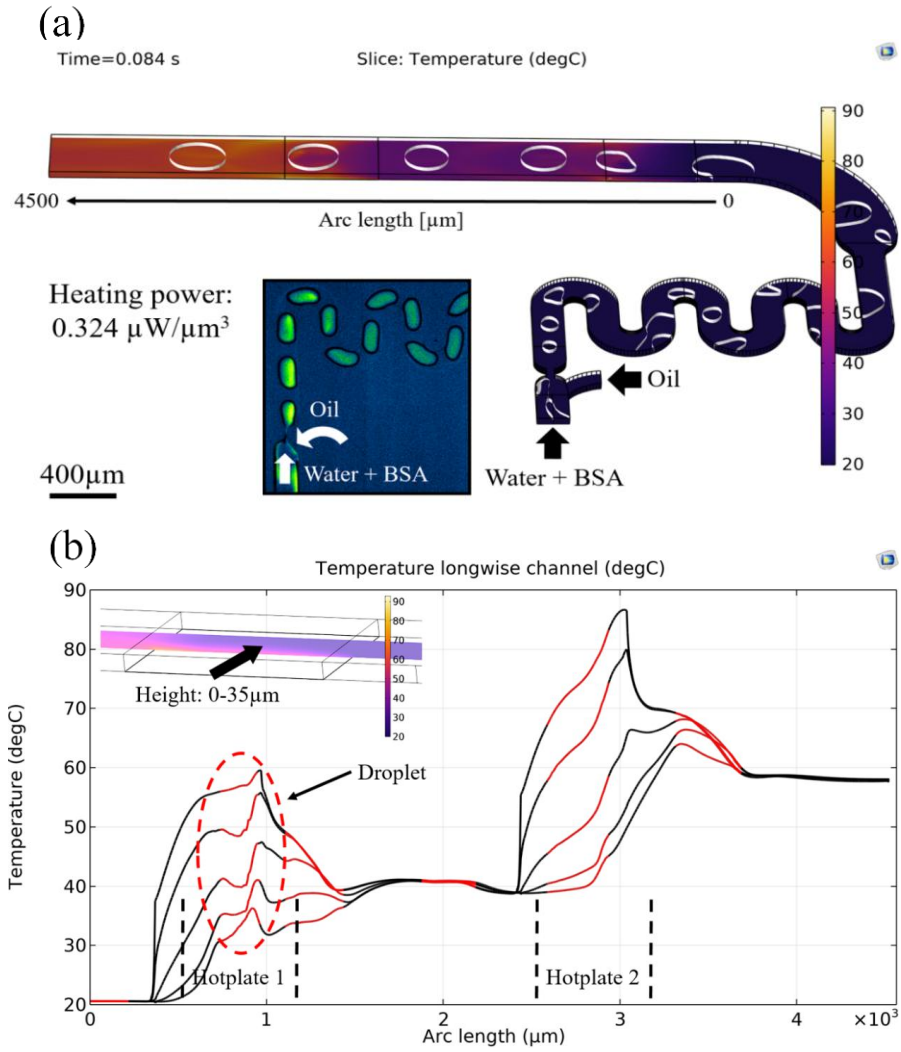

Figure 59. Simulated temperature distribution within the generated droplets (a). The longitudinal temperature distribution (b) presents the thermal isolation effect of the droplets.

Small scale production and development of near infrared LEDs

HORIZON-KDT-JU-2023-1-IA-101140192 (UNLOOC), 2024-1.2.4-KDT-2024-00001, TKP2021-EGA-04

B. Beiler, J. M. Bozorádi, Cs. Dücső, P. Fürjes, Z. Szabó

Infrared spectroscopy is a very popular measurement technique especially in food industry, pharmaceutical industry and agriculture for the detection and measurement of organic materials. GaInAsP/InP is an ideal material system for the fabrication of double heterostructure devices as the emission wavelength is easily tuneable between 950-1650 nm. As InP has higher bandgap than the lattice-matched GaInAsP active layer the absorption losses inside the device structure can be minimized. To tune the emission wavelength of the LED, the composition of the semiconductor light-emitting layer has to be properly set. Our high-quality single peak LED chips (1220nm) have a stable market. Our business partners are SENOP Oy (Fi) and Anton Paar Ltd. (At).

Wide emission-spectrum NIR LEDs

Specific InGaAsP/InP layer structures were grown by liquid phase epitaxy (LPE) to fabricate wide emission spectrum near-infrared LEDs. Multilayers structures resulting 4-wavelength emission were prepared in two consecutive LPE growth steps: by growing 2 InGaAsP photoluminescent layers, and other photo-luminescent and active layers in the second step. Preliminary results indicate that this layer configuration allows adequate control over the intensity of the longest-wavelength peak and the overall spectrum homogeneity. Samples were fabricated and characterized by optical transmittance measurements, by photo-luminescent measurements using various excitation sources in the NIR range, and by scanning electron microscopy to measure layer thicknesses and verify epitaxial crystal formation. Furthermore, ellipsometry measurements and optical modelling are underway to further understand and refine the device physics.

Various emission-distributions (Figure 60) were measured on samples prepared by varying the thicknesses of the 3 photoluminescent layers in different layer order configuration. To achieve a homogenous emission spectrum distribution, the measurement results are fed back into the planning process to refine the growth parameters. LED chips were characterized electrically and optically after dicing the wafer to 500x500 μm^2 LED chips. The shape of the emission spectra is quite stable, only slightly distorts with the increasing current due to the saturation in the thinner layers. The total emitted optical power of the wide spectrum LED compared to the emission of a standard single-wavelength LED indicates a relatively high internal photon conversion efficiency. [Ref.67.]

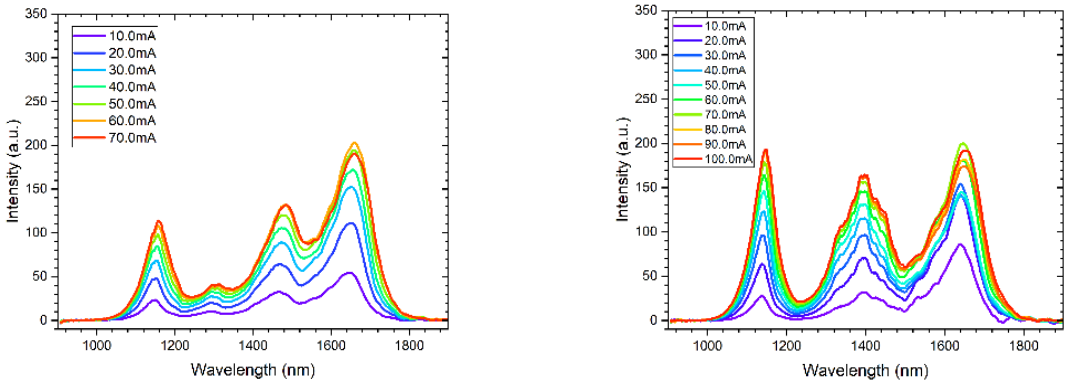

Figure 60. Emission spectrum of a 4-wavelength LEDs with different layer structures (layer order: 1650 nm, 1500 nm, 1300 nm & active 1170 nm) at forward current 10-100 mA.

Cell culture media analysis in Organ-on-Chip applications

HORIZON-KDT-JU-2023-1-IA-101140192 (UNLOOC), 2024-1.2.4-KDT-2024-00001, TKP2021-EGA-04

D. Bereczki, K. Pankász, L. Bató, Zs. Szomor, A. Füredi, Z. Szabó, O. Bálint-Hakkel, P. Fürjes

Miniaturised pH sensor for cell culture media analysis

Accurate control and real-time monitoring of biological and chemical processes in microfluidic and Lab-on-a-Chip systems critically depend on the precise measurement of local environmental parameters, among which pH is of particular importance due to its fundamental influence on enzyme activity, cellular metabolism, cell viability, and the kinetics of biochemical reactions. This is especially critical in applications involving living cells, tissue cultures, and long-term incubation experiments. Motivated by these challenges, we developed an integrable pH sensor specifically tailored for lab-on-a-chip applications. Titanium dioxide (TiO_x)-based thin films were fabricated by atomic layer deposition (ALD). ALD proved to be especially advantageous due to its ability to deliver excellent thickness control, conformality, and lateral homogeneity, even on complex or miniaturized substrates.

Electrochemical pH sensing was carried out using a PalmSens potentiostat in combination with a custom-developed extended-gate field-effect transistor (EGFET)-based readout circuit. The EGFET configuration decouples the sensing membrane from the transistor itself, enabling flexible sensor integration while maintaining excellent electrical stability. Owing to the high input impedance and well-balanced measurement bridge of the custom readout electronics, even small potential variations induced by changes in proton concentration could be detected with high accuracy and low noise. This architecture is particularly well suited for low-power and portable sensing applications, which are increasingly important in point-of-care and on-chip diagnostic systems.

Experimental results demonstrated that TiO_x thin films deposited by ALD exhibited a pH sensitivity in the range of 52–58 mV/pH, approaching the theoretical Nernst limit of 59 mV/pH at 25 °C. This near-Nernstian response confirms the excellent electrochemical performance of the fabricated films and their suitability for high-precision pH sensing. In addition to sensitivity, the sensors showed good linearity, stability, and repeatability across multiple measurement cycles, further supporting their applicability. By combining advanced thin-film fabrication, detailed materials characterization, and low-noise electrochemical readout, the developed sensing platform provides a robust foundation for real-time pH monitoring in Lab-on-a-Chip systems.

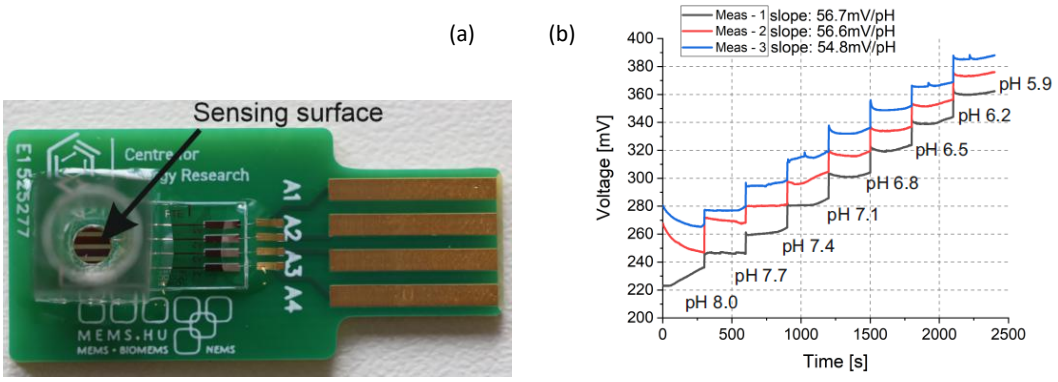

Figure 61. Perspective view of the electrochemical electrode platform highlighting the sensing surface where the functionalized TiO_x thin films are located (a) and the pH response of TiO_x layer deposited by ALD at 100 °C (b)

Therapeutic drug monitoring by fluorescent spectroscopy

Cancer claims almost 10 million lives annually, making it one of the major causes of death around the world. Chemotherapy is the most frequently used non-surgical method in clinical practice in cancer treatment to depress the growing, proliferation, or spreading of cancer cells. Detection of the anti-cancer drugs in patients' blood or standard cell culture media is the fundamental step forward in personal treatments or in vitro drug tests in Organ-on-Chip devices.

Besides the golden standard mass spectrometry, optical spectroscopy must be considered as a potential analytical method, although there is no extensively accessible database of the spectral characteristics of the widely applied chemotherapeutic drug compounds. The inherent fluorescent properties of anti-leukemic drugs offer unique advantages for real-time therapeutic tracking and optimization. In our work, we performed a systematic spectral mapping and parallel toxicity testing of several commercially available chemotherapeutic agents used in the treatment of leukemia. Our goal was to identify fluorescent molecules by creating an accurate spectrum library. The optical spectral properties of 82 different active pharmaceutical ingredients provided by Servier were investigated using a Tecan Spark Plate Reader. Accordingly, the absorption and emission spectra of these leukemia-related compounds were screened, identifying 28 autofluorescent drugs suitable for fluorescence-based optical concentration monitoring. Excitation and emission parameters were evaluated across various solvents (DMSO, fetal bovine serum, and culture media), revealing solvent-dependent spectral changes, intensity variations and effect on detection limits.

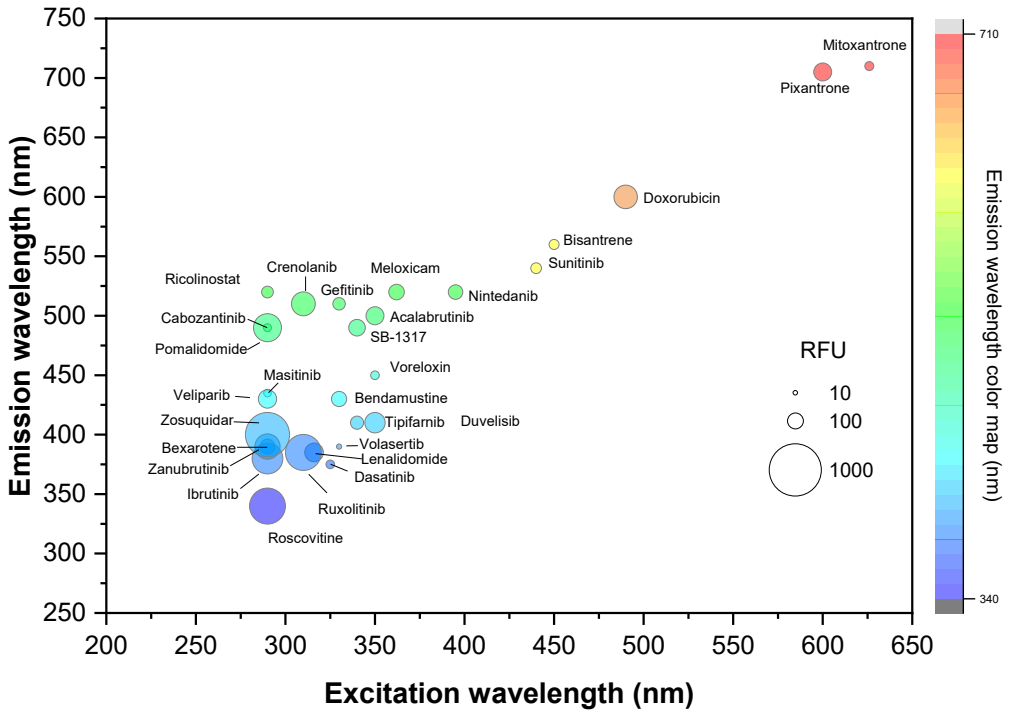

Figure 62. Spectral mapping of fluorescent FDA-approved leukemia drugs in DMSO. Excitation–emission properties are represented using wavelength-specific color coding, and emission maxima are plotted with marker size proportional to relative detected fluorescence intensity.

Therapy-induced senescence in cancer cells

Therapy-induced senescence (TIS) is considered a permanent cell cycle arrest following DNA-damaging treatments; however, its irreversibility has recently been challenged. A. Füredi and his group demonstrated that escape from TIS is universal across breast cancer cells. Moreover, TIS provides a reversible drug resistance mechanism that ensures the survival of the population and could contribute to relapses. [Ref.68.][Ref.69.][Ref.70.]

Our article “Therapy-induced senescence is a transient drug resistance mechanism in breast cancer” published in the journal Molecular Cancer was selected as the article of the month by the International Cell Senescence Association.

Solid-state nanopores for extremely sensitive nanosensors

L. Illés, P. Fürjes, R. E. Gyurcsányi (BME NanoChemSens)

Nanoporous membranes are fundamental components of the transport modulation based label free electrochemical biosensors envisioned for highly sensitive molecule detection. The sensitivity and the specificity of these sensors are significantly affected by the pore geometry what has to be fitted to the size and conformation of the target molecules. Precise tailoring of nanopore geometries and alignment to target molecule conformation and size improves the signal-to-noise level of the identification method - in our case the impedance spectroscopy. This pore geometry engineering is essential for reliable and reproducible manufacturing of integrable solid state nanopore-arrays in molecule diagnostic devices.

Chemically functionalized single gold nanopores (GNPs) have been successfully developed and fabricated that act as ultra-miniaturized, solid-state ion channels for highly selective potentiometric sensing. A single nanopore was milled by a focused ion beam (FIB) milling in a double-layered membrane consisting of a low-stress non-stoichiometric silicon nitride (SiN_x) supporting layer, a Ti adhesion layer, and a gold layer enabling surface functionalization via chemisorption of functional thiol and disulfide derivatives. By modifying a 10 nm radius nanopore with a mixed self-assembled layer, they achieved silver ion (Ag^+) selectivity exceeding that of natural biological channels. This approach bypasses the traditional requirement for subnanometer pore size control and prevents the active component loss typically seen in conventional miniaturized ion-selective electrodes.

Dehydration governs ion selectivity in both natural ion channels and synthetic ion sieves, as ions must dehydrate to traverse subnanometer pores. Because lipophilic ions experience lower dehydration energy costs, an intrinsic lipophilic selectivity pattern known as the Hofmeister series arises. This Hofmeister selectivity is modulated in natural ion channels by electrostatic and coordinative interactions between ions and nanopore surfaces. In synthetic ion channels, surface hydrophobicity is also critical for ion selectivity; however, its exact role remains undetermined.

The contribution of hydrophobicity was elucidated by comparing structurally identical hydrophilic and hydrophobic cation-exchanger surface modified gold nanopores. Zero-current potentiometry revealed that cation-exchanger nanopores do not discriminate among singly charged cations, except for a modest preference for H+. The absence of Hofmeister selectivity was confirmed in both multipore membranes and single nanopores, ruling out ensemble nonidealities as an explanation. The lack of intrinsic Hofmeister selectivity may enable unique ion-sensing applications (e.g., total ion concentration measurements, ligand-tuned ion-selective sensors). [Ref.72.][Ref.73.].

Our article “Single Solid-State Ion Channels as Potentiometric Nanosensors” published in the journal Advanced Functional Materials was selected as the publication of the month in October by the Department of Chemical Sciences of the Hungarian Academy of Sciences: https://mta.hu/vii-osztaly-a-honap-publikaciok/2025-oktoberi-kiemelt-publikaciok-114849

Nanobiosensorics Department

Head: Róbert HORVÁTH, Ph.D., Senior Scientist

Research Staff:

Robert Horvath, Ph.D.
Sándor Kurunczi, Ph.D.
Inna Székács, Ph.D.
Beatrix Péter, Ph.D.
Zoltán Szittner, Ph.D.
Enikő Farkas, Ph.D.

Ph.D. Students / Diploma Workers:

Kinga Dóra Kovács, Ph.D. student
Bálint Béres, Ph.D. student
Imola Rajmon, Ph.D. student
Anna Balogh, Ph.D. student
Igor Sallai, Ph.D. student
Péter Joó, Ph.D. student
Krisztina Borbély, Ph.D. student
Sebestyén D. Varga, Ph.D. student
Dóra Balogh, Ph.D. student
Nicolett Kanyó, Ph.D. student
Zoltán Dicső, Ph.D. student
Beatrix Magyaródi, Ph.D. student
Dorina Kiss, M.Sc. student
Szabolcs Novák, M.Sc. student
Ágoston Richárd Kiss, M.Sc. student
Bálint Legányi, M.Sc. student
Csaba Béla Váradi, M.Sc. student

The research profile of the Nanobiosensorics Department is the development and application of label-free optical biosensors, the mathematical modeling of the relevant biological and biophysical processes. Building on their broad national and international collaborative network the group conducts research in the fields of instrument development, monitoring of cell secreted extracellular vesicles, development of protein-based functional coatings, adhesion studies on human cancer and immune cells, and theoretical modeling. In 2014, the application for an ERC Consolidator Grant by the head of the research group received qualification category “A (fully meets the ERC excellence criteria and should be funded if sufficient funds are available)” after the interview in Brussels, but the funding line did not reach this proposal due to budgetary constraints. However, using this achievement the Group could successfully apply for funding from NKFIH in the framework of the ERC_HU call. In the framework of this project, they aim single cell manipulation and label-free sensing. Building on this expertise, in 2018 they won an Élvonal (NKFIH) research project for single cell biosensing. In 2020, the research group won the Tématerületi Kiválósági Program (TKP) excellence project as well in collaboration with other groups of the MFA. In 2025, they won the Lendület H (Momentum) grant of the Hungarian Academy of Sciences, the Advanced grant and the Hungarian Israeli bilateral industrial research and development co-funding grant of the NKFIH.

Kinetic monitoring of molecular interactions during surfactant-driven self-propelled droplet motion by high spatial resolution waveguide sensing

Lendület LP2025-15/2025, OTKA ERC_HU 117755, TKP2021-EGA-04, OTKA KKP 129936, KDP Programs and Bolyai Scholarship

E. Farkas, K. D. Kovács, I. Szekacs, B. Peter, I. Lagzi, H. Kitahata (Chiba University, Japan), N. J. Suematsu (Meiji University, Japan), R. Horvath

Self-driven actions, like motion, are fundamental characteristics of life. Today, intense research focuses on the kinetics of droplet motion. Quantifying macroscopic motion and exploring the underlying mechanisms are crucial in self-structuring and self-healing materials, advancements in soft robotics, innovations in self-cleaning environmental processes, and progress within the pharmaceutical industry. Usually, the driving forces inducing macroscopic motion act at the molecular scale, making their real-time and high-resolution investigation challenging. Label-free surface sensitive measurements with high lateral resolution could *in situ* measure both molecular-scale interactions and microscopic motion.

We employ surface-sensitive label-free sensors to investigate the kinetic changes in a self-assembled monolayer of the trimethyl(octadecyl)azanium chloride surfactant on a substrate surface during the self-propelled motion of nitrobenzene droplets. The adsorption–desorption of the surfactant at various concentrations, its removal due to the moving organic droplet, and rebuilding mechanisms at droplet-visited areas are all investigated with excellent time, spatial, and surface mass density resolution.

We discovered concentration dependent velocity fluctuations, estimated the adsorbed amount of surfactant molecules, and revealed multilayer coverage at high concentrations. The desorption rate of surfactant ($18.4\ s^{-1}$) during the microscopic motion of oil droplets was determined by *in situ* differentiating between droplet visited and non-visited areas [Ref.74.].

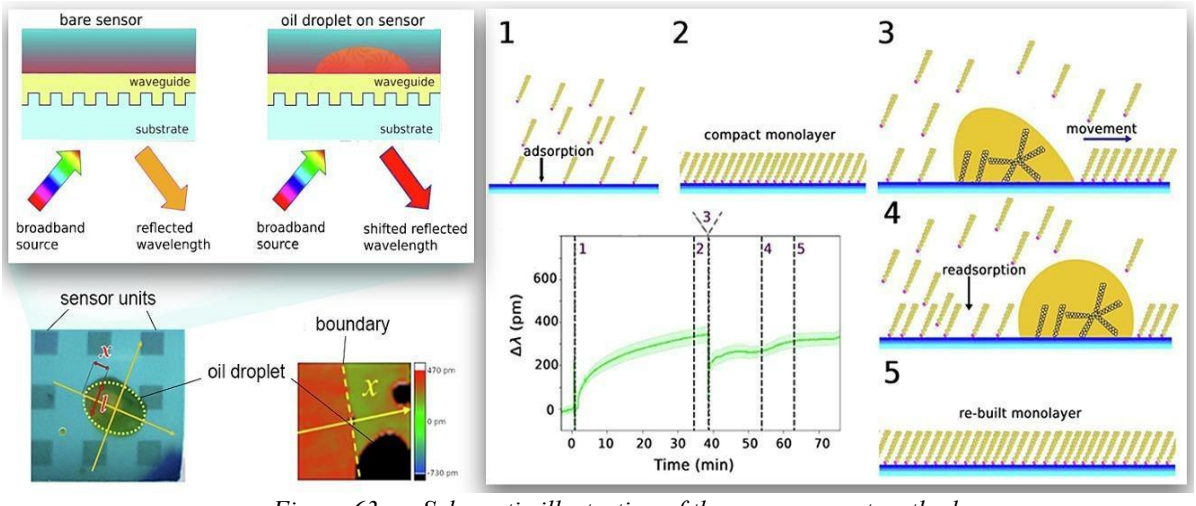

Figure 63. Schematic illustration of the measurement method.

Temporal pH waveforms generated in an enzymatic reaction network in batch and cell-sized microcompartments

Lendület LP2025-15/2025, OTKA ERC_HU 117755, TKP2021-EGA-04, OTKA KKP 129936

M. Itatani, G. Holló (University of Lausanne, Switzerland), P. Albanese (University of Siena, Italy), N. Valletti (University of Siena, Italy), S. Kurunczi, R. Horvath, F. Rossi (University of Siena, Siena, Italy), I. Lagzi (BME)

Investigating and designing reaction networks and their emergent phenomena are the backbone of systems chemistry. Designing chemical oscillators in homogeneous systems utilizing enzymatic reactions is challenging due to the consumption of the substrates over one reaction cycle. Here, we show that an antagonistic enzymatic reaction network comprising urea-urease and ester-esterase reactions can generate temporal pH variations in a batch. We developed a coupled reaction kinetic model to elucidate the mechanism that accurately captures the experimentally observed pH variation over time. To demonstrate the remarkable potential of the enzymatic reaction network, we expanded on this discovery by generating front propagation and presenting several applications by coupling this enzymatic reaction network to fuel pH-dependent processes (gelation of pH-sensitive monomers and emulsion-vesicle transformation). By employing the coupling strategy of antagonistic enzymatic reactions, we engineered a single pH pulse in cell-sized microcompartments, which could contribute to developing synthetic cells with multiple functions [Ref.75.].

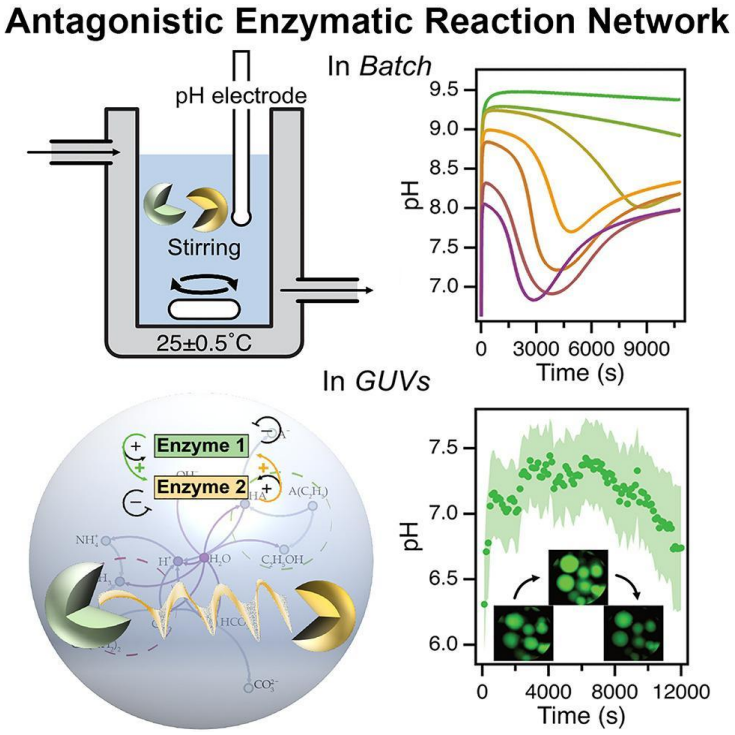

Figure 64. Schematic illustration of the antagonistic enzymatic reaction network.

Robotic manipulations of single cells using a large-volume piezoelectric micropipette with nanoliter precision

Lendület LP2025-15/2025, OTKA ERC_HU 117755, TKP2021-EGA-04, OTKA KKP 129936

B. Kovács, Sz. Novák, I. Sallai, B. Magyaródi, I. Székács, D. Selmeczi (CellSorter), B. Szabó (CellSorter, ELTE), R. Horvath

Investigating the mechanism of adhesive interactions at the individual cell level holds significant importance. We used a computer-controlled piezoelectric micropipette (NanoPick) built onto an inverted microscope, offering subnanoliter precision liquid handling in the range of 0.1–600 nanoliters with a temporal resolution of 1 millisecond. In contrast to previous pipette-based cell manipulations, in our device, phase contrast and fluorescent imaging of the microscope was not limited by the micropipette. Moreover, this compact setup efficiently enabled single-cell detection, targeting, picking, and isolation without fluidic tubes and syringes. We investigated the integrin-mediated adhesion between an RGD (Arg-Gly-Asp) motif displaying surface and the HeLa Fucci tumor cell line. Using a 70 µm inner diameter micropipette, we found that increasing the pipetting speed (voltage ramp rate applied on the piezoelectric head) improved the cell picking success rate to almost 100 %. Although the more strongly attached unmodified HeLa cells could not be picked up even at the highest flow rates. Compared to valve-controlled systems, NanoPick demonstrated higher efficiency and precision, particularly in handling THP-1 cells. Its rigid design minimized transient delays, allowing time-dependent flow profiles and enhanced detachment at lower flow rates. Our method allows adhesion measurements on hundreds of cells and offers precise control over fluid volume and timing, suitable for manipulating adherent cells or larger objects such as organoids, spheroids, oocytes, etc. [Ref.76.].

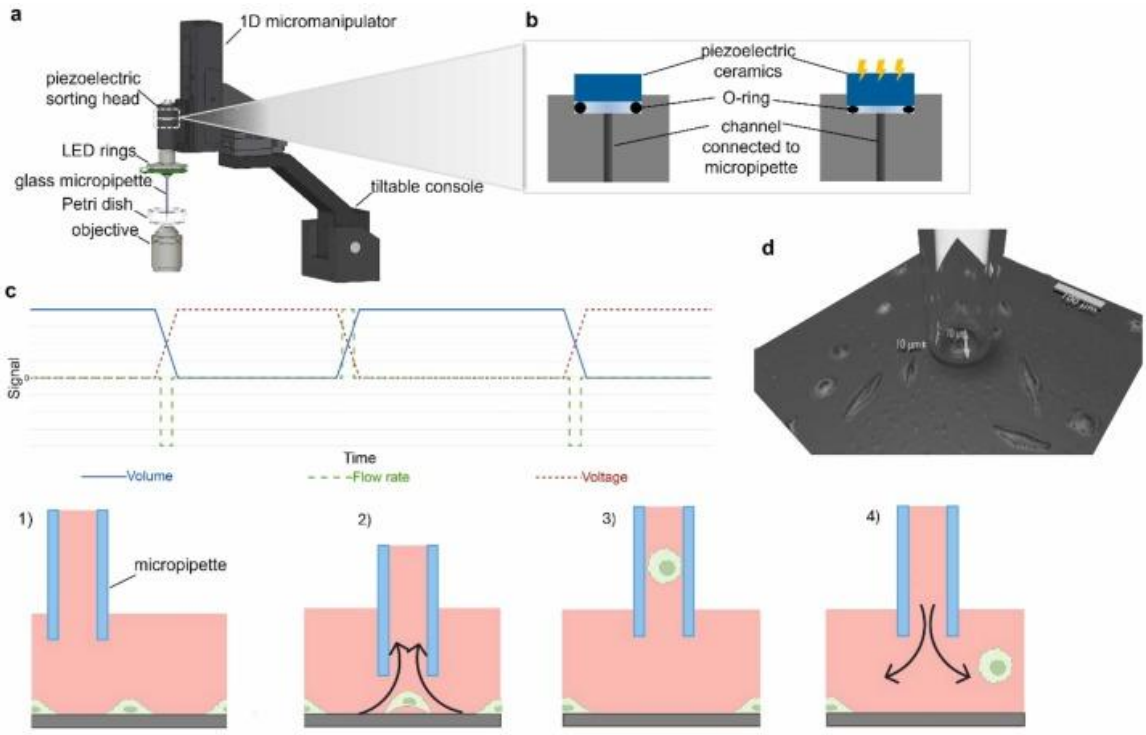

Figure 65. Configuration and working principle of the piezoelectric micropipette

Kinetic analysis of SARS-CoV-2 S1–integrin binding using live-cell, label-free optical biosensing

Lendület LP2025-15/2025, OTKA ERC_HU 117755, TKP2021-EGA-04, OTKA KKP 129936 and KDP Programs, Bolyai Scholarship

N. Kanyó, K. Borbély, B. Péter, K. D. Kovács, A. Balogh, B. Magyaródi, S. Kurunczi, I. Székács, R. Horváth

The SARS-CoV-2 spike (S1) protein facilitates viral entry through binding to angiotensin-converting enzyme 2 (ACE2), but it also contains an Arg–Gly–Asp (RGD) motif that may enable interactions with RGD-binding integrins on ACE2-negative cells. Here, we provide quantitative evidence for this alternative binding pathway using a live-cell, label-free resonant waveguide grating (RWG) biosensor. RWG technology allowed us to monitor real-time adhesion kinetics of live cells to RGD-displaying substrates, as well as cell adhesion to S1-coated surfaces. To characterize the strength of the integrin–S1 interaction, we determined the dissociation constant using two complementary approaches. First, we performed a live-cell competitive binding assay on RGD-displaying surfaces, where varying concentrations of soluble S1 were added to cell suspensions. Second, we recorded the adhesion kinetics of cells on S1-coated surfaces and fitted the data using a kinetic model based on coupled ordinary differential equations. By comparing the results from both methods, we estimate that approximately 33% of the S1 molecules immobilized on the Nb2O5 biosensor surface are capable of initiating integrin-mediated adhesion. These findings support the existence of an alternative integrin-dependent entry route for SARS-CoV-2 and highlight the effectiveness of label-free RWG biosensing for quantitatively probing virus–host interactions under physiologically relevant conditions without the need of the isolation of the interaction partners from the cells [Ref.77.].

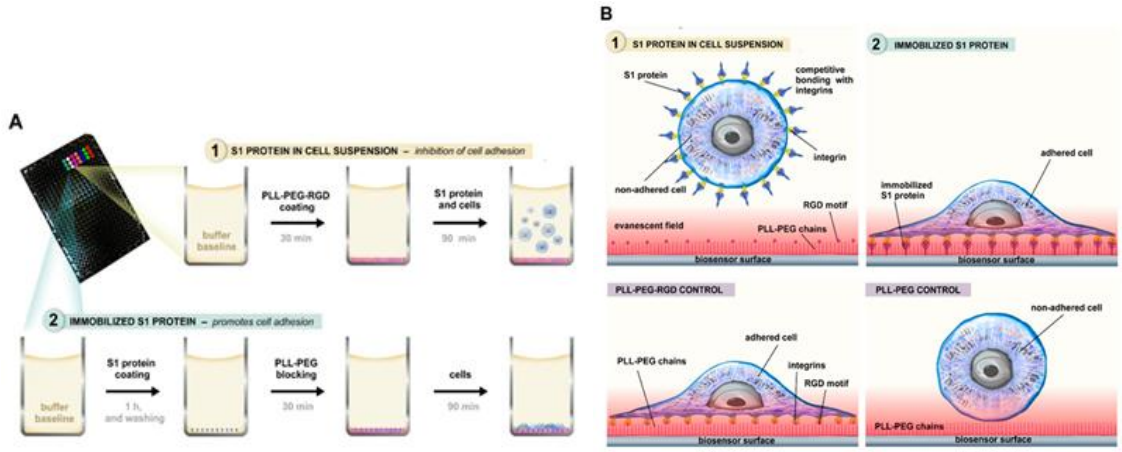

Figure 66. Experimental scheme and molecular mechanism of integrin-mediated adhesion assays. (A) Experimental workflow of the two biosensor assay setups: (1) inhibitory effect of soluble S1 protein in cell suspension and (2) adhesion to surface-immobilized S1 protein. (B) Schematic representation of molecular interactions during the assays.

In situ monitoring of cell adhesion kinetics using label-free optical biosensors: Evaluating anticancer potential and selectivity of natural compounds

Lendület LP2025-15/2025, OTKA ERC_HU 117755, TKP2021-EGA-04, OTKA KKP 129936, KDP Programs and Bolyai Scholarship

B. Péter, T. Ausbüttel (SE), N. Kanyó, P. Joó, K. Tóth, Z. Szittner, I. Székács, Sz. Bosze (ELTE), G. M. Kovács (ELTE), I. Boldizsár (ELTE, SE), R. Horváth

The limitations of conventional techniques hinder the identification of natural compounds with anticancer potential in terms of speed, throughput, sensitivity, and the capability of continuous monitoring of relevant biological effects. Novel label-free optical biosensors represent new opportunities in the discovery of drug candidates, eliminating these difficulties. Our study monitored the anti-adhesive effects of 11 isolated pure natural compounds (representing four different structural frameworks) and four crude extracts, obtained from plant and fungal sources. The resonant waveguide grating (RWG) method (using an evanescent field-based label-free optical biosensor) and a combined miniaturized holographic microscope technique were applied to investigate the effects of pure compounds and crude extracts on cancerous (HeLa) and healthy (preosteoblast) model cells in real time. The adhesion kinetics on fibronectin-coated surfaces and the morphological parameters on polystyrene surfaces were studied using these model cells in the presence and absence of compounds and extracts. The introduced biosensor method also investigated their interaction with the fibronectin surface. This methodology enables continuous, high-sensitivity parallel measurements, facilitating the identification of natural compounds with anticancer potential while also providing insights into their mechanism of action. The interaction of the aryltetralin lignans deoxypodophyllotoxin and angeloyl podophyllotoxin with fibronectin was confirmed as a key mechanism behind their non-selective anti-adhesive effects. In contrast, the selective adhesion inhibitory effects of the neolignan balanophonin and the alkaloid vermelhotin against HeLa cells were unrelated to fibronectin interaction [Ref.78.].

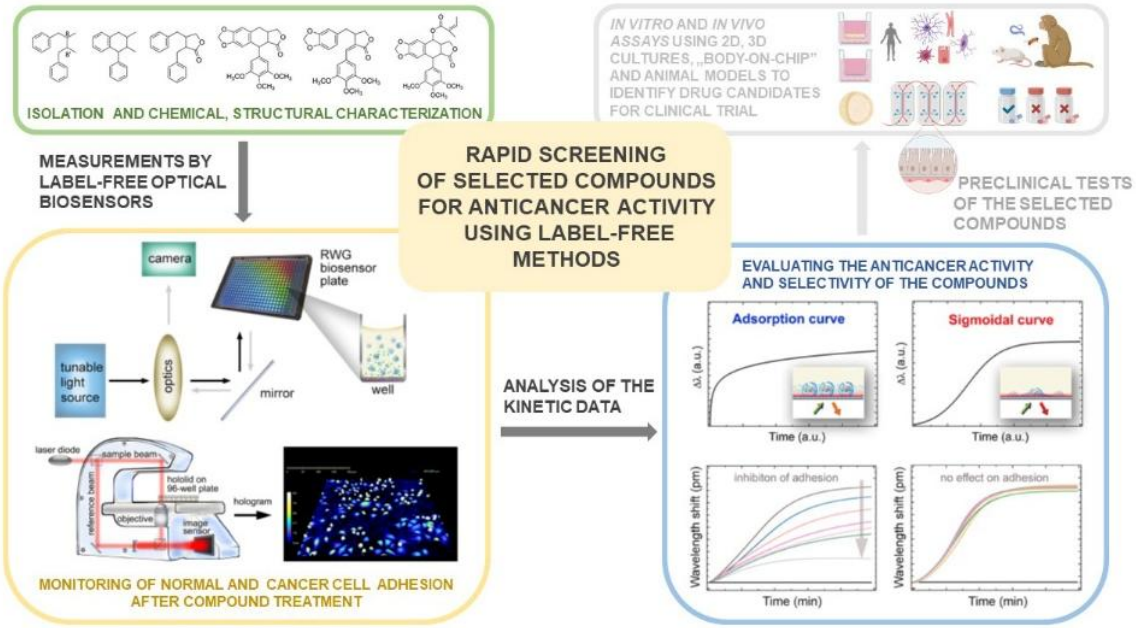

Figure 67. Schematic illustration of the measurement method.

Complex Systems Department

Head: Dr. Géza Ódor D.Sc., Scientific advisor

Research Staff:
György Szabó, D.Sc., Professor emeritus
Attila Szolnoki, D.Sc., Scientific advisor
Zoltán Juhász, Ph.D.
Balázs Király, Ph.D.
István Papp, Ph.D.
Kristóf Benedek, Ph.D. student

Diploma workers:
Gregorio Jaca, BME

The research field of the group is the investigation of complex systems by the methods of statistical physics. In 2025 they focused on advance complex systems science across social dynamics, infrastructure resilience, neuroscience, and evolutionary game theory. Common themes include:

- The importance of network structure in shaping collective outcomes.
- Emergence of cooperation, stability, and critical behavior through local interactions.
- Development of new theoretical and computational frameworks that connect microscopic interactions to large-scale system behavior.

Inter-role reciprocity in evolutionary trust game on square lattices

OTKA K 142948

C. Wang, W. Zhang, X. Wang, and A. Szolnoki

Simulating bipartite games, such as the trust game, is not straightforward due to the lack of a natural way to distinguish roles in a single population. The square lattice topology can provide a simple yet elegant solution by alternating trustors and trustees. For even lattice sizes, it creates two disjoint diagonal sub-lattices for strategy learning, while game interactions can take place on the original lattice.

This setup ensures a minimal spatial structure that allows interactions across roles and learning within roles. By simulations on this setup, we detect an inter-role spatial reciprocity mechanism, through which trust can emerge. In particular, a moderate return ratio allows investing trustors and trustworthy trustees to form inter-role clusters and thus save trust. If the return is too high, it harms the survival of trustees; if too low, it harms trustors. The proposed simulation framework is also applicable to any bipartite game to uncover potential inter-role spatial mechanisms across various scenarios. [Ref.79.]

This work was reviewed by The Science Archive: https://thesciencearchive.org/2508-06685v1/

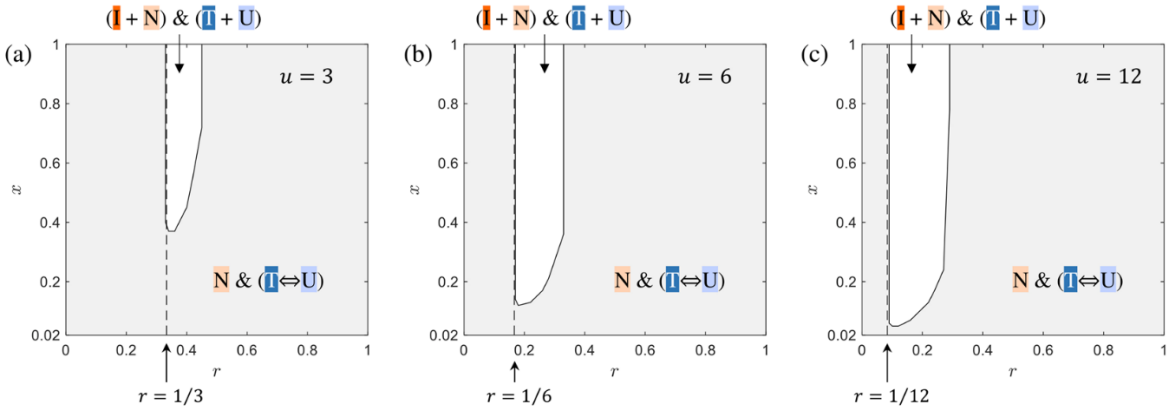

Figure 68. Phase diagrams of the system behavior with respect to return ratio r and investment ratio x for different multiplication factors u = 3, 6, 12. Trust emerges in the (I + N)&(T + U) phase (white region) with large x and moderate r, where the four strategies of the two roles coexist. Trust cannot survive in the N&(T ⇔ U) phase (gray region), where trustors do not invest, and trustworthy and untrustworthy trustees are in neutral drift. The dashed line marks r = 1/u in each panel.

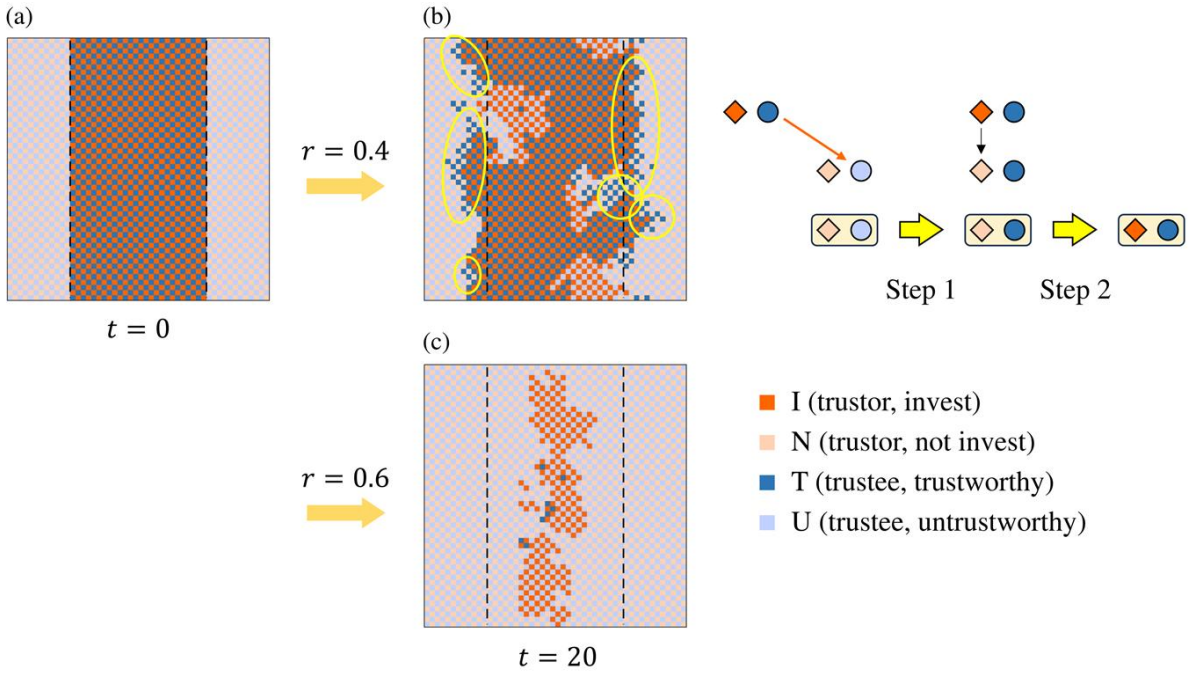

Figure 69. Inter-role spatial reciprocity in the two-step invasion I&T ⇒ I&U ⇒ N&U is key to trust emergence. (a) The initial preparation divides the lattice into two blocks, I&T and N&U, to better observe the two-step invasion. (b) At moderate return ratio (r = 0.4), trustworthy trustees are supported by neighboring investing trustors, thus invading untrustworthy trustees near non-investing trustors (Step 1, I&T ⇒ I&U, regions marked by yellow circles); near trustworthy trustees, an investing trustor has higher fitness and invades non-investing trustors (Step 2, I&U ⇒ N&U). (c) At high return ratio (r = 0.6), trustworthy trustees have low fitness due to returning too much, thus unable to make the invasion in Step 1. Other parameters: u = 3, x = 1.

Quantitative comparison of power grid reinforcements

B. Hartmann, G. Ódor, K. Benedek, I. Papp and M. T. Cirunay

This research presents a head-to-head evaluation of three grid reinforcement strategies for the Hungarian high-voltage power grid: (1) duplicating inter-community “bridge” links, (2) inserting bypasses around poorly synchronized nodes, and (3) fortifying edges identified as cascade-triggering vulnerabilities. Built from official operator data, our grid models avoid simplifications typical in prior work and show coupling distributions in close agreement with European and North American grids.

Our results show that community-based bridge duplication consistently outperforms both bypass additions and cascade-based reinforcements. It delivers the most robust increase in synchronization, frequency stability, and cascade mitigation across all tested cases. In contrast, cascade-based reinforcement is stronger under low coupling conditions, while bypass strategies present superior frequency spread control in intermediate regimes. We also discuss how Braess’ paradox is manifested in certain network configurations. As reinforcing specific lines decreases the grids stability, there is a need for topology-aware planning. Our line-cut cascade simulations show fat-tailed cascade time distributions at intermediate coupling strengths, which is indicative of Griffiths-type scaling near a hybrid phase transition. Simultaneously, edge behaviors return to exponential at extremes of the evaluated range. To our knowledge, this is the first quantitative comparison combining oscillator models with conventional power system analysis tools, offering a rigorous bridge between theoretical and operational perspectives. [Ref.80.]

Figure 70. Maps represent the first link cuts for different λ couplings for scenario #12. As we can see, several edges coincide at different values. The different number of cuts is due to the fact that for larger couplings, fewer lines are overloaded. These initial failures are typically concentrated around major power plants or large substations, surrounded by dangling ends.

Scale-free behavior of weight distributions of connectomes

M. T. Cirunay, G. Ódor, I. Papp and G. Deco

To determine the precise link between anatomical structure and function, brain studies primarily concentrate on the anatomical wiring of the brain and its topological properties. In this work, we investigate the weighted degree and connection length distributions of the KKI-113 and KKI-18 human connectomes, the fruit fly, and the mouse retina. We find that the node strength (weighted degree) distribution behavior differs depending on the considered scale. On the global scale, the distributions are found to follow power-law behavior, with a roughly universal exponent close to 3. However, this behavior breaks at the local scale as the node strength distributions of the KKI-18 follow a stretched exponential, and the fly and mouse retina follow the log-normal distribution, respectively, which are indicative of underlying random multiplicative processes and underpins nonlocality of learning in a brain close to the critical state. However, for the case of the KKI-113 and the H01 human) datasets, the local weighted degree distributions follow an exponentially truncated power law, which may hint at the fact that the critical learning mechanism may have manifested at the node level too. [Ref.81.]

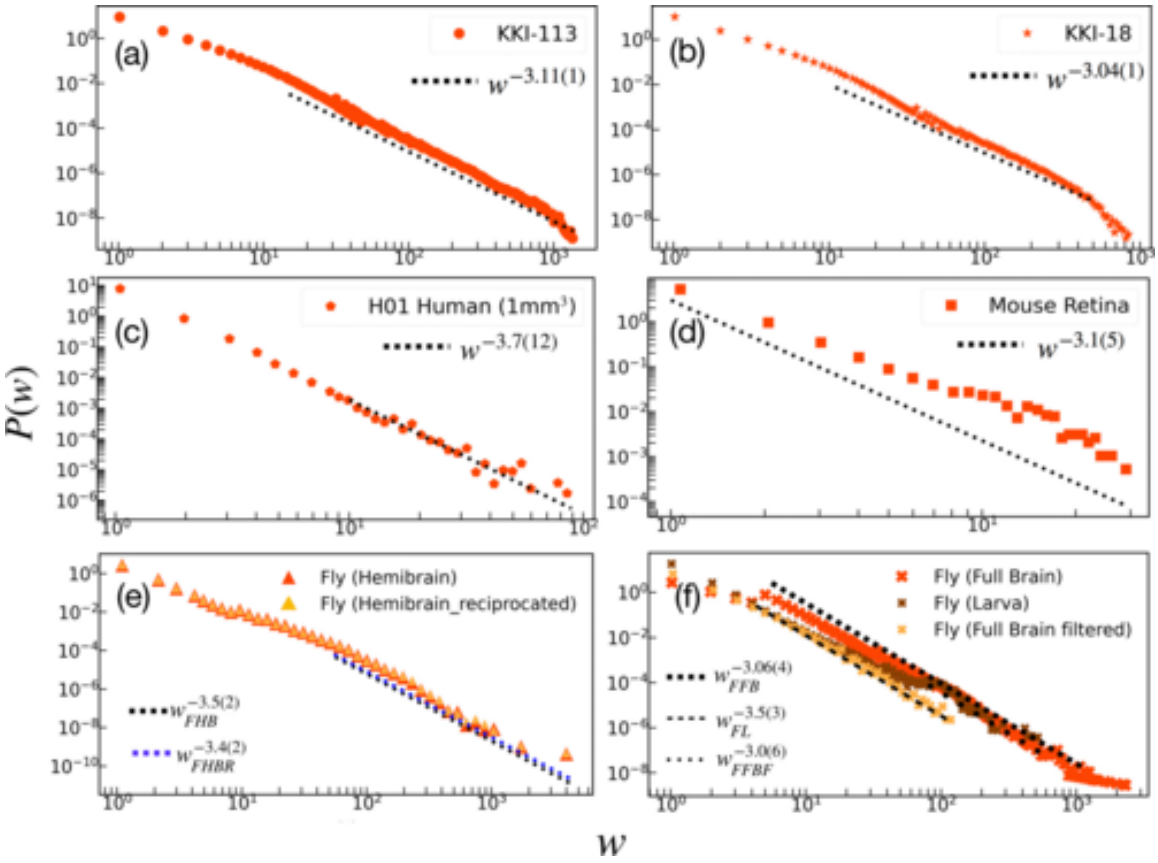

Figure 71. The weight distributions of (a) KKI-113, (b) KKI-18, (c) H01 human (1 mm3), (d) mouse retina, (e) fly (hemibrain), (f) fly (full brain, and its filtered version), and that of a larva all follow power-law behaviors in the global scale.

Derivation of potential for group interactions in evolutionary games

Gy. Szabó and B. Király

In the many-particle physical systems potentials are used to describe the sum of pair interactions. Similar potential can be introduced for the investigation of evolutionary games where two-player games define the interactions. Now we have demonstrated the existence of potential for two-strategy group interactions for which the players with identical strategies receive equal payoffs. This type of group interactions includes some extended versions of public goods and minority games that are widely used for the investigation of social dilemmas in human societies or ecological systems.

Some interesting consequences of group interactions are illustrated by a simple two-strategy model where the players are located at sites of a square lattice, and their income comes from five five-player games played with the nearest neighbors. In this model the group interactions support curious formation of strategy arrangements in the ground state representing optimal choices for the players.

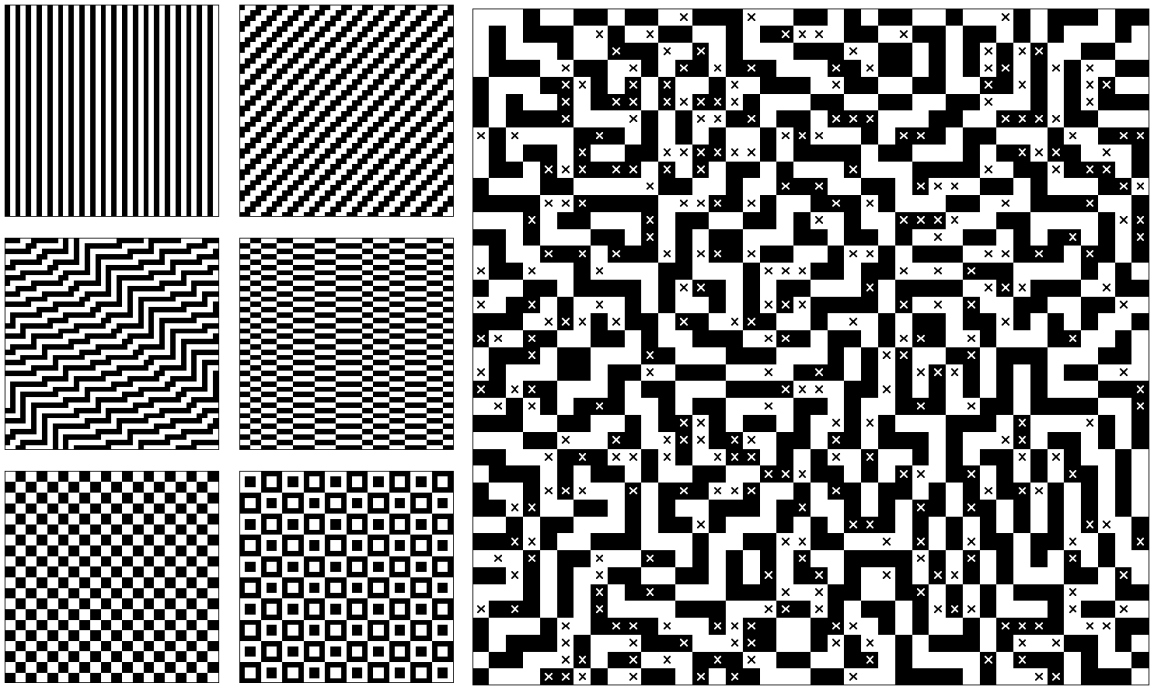

Figure 72. Optimal strategy distributions on square lattice

Six patterns (left side) show ordered or partially ordered spatial distributions of two (black and white) strategies that are found by theoretical analyses. In addition to these optimal spatial distributions the Monte Carlo simulations have indicated the existence of many other disordered labyrinth-like patterns. One of these strategy distributions is shown on the right side with enlarged boxes. Here the small x-s denote players who can reverse their strategies without decreasing the optimal payoffs. This model illustrates combinations of features that were investigated separately via Ising type models possessing ordered or disordered ground states and frustrations. [Ref.82.].

REFERENCES

[Ref.1.] Pálinkás, A., Kálvin, G., Vancsó, P. et al. The composition and structure of the ubiquitous hydrocarbon contamination on van der Waals materials. Nat Commun 13, 6770 (2022). https://doi.org/10.1038/s41467-022-34641-7

[Ref.2.] Kalvin György, Vancsó Péter, Szendrő Márton, Kandrai Konrád, Pálinkás András, Tapasztó Levente, Nemes-Incze Péter Impact of ambient molecular contamination on scanning tunneling microscopy and spectroscopy of layered materials PHYSICAL REVIEW B 113: 3 Paper: 035428, 10 p. (2026) https://doi.org/10.1103/f1vp-mlpw

[Ref.3.] Osváth Zoltán, Pálinkás András, Molnár György, Kun Péter, Koós Antal A.Strain-induced modulation of the local conductance in MoS2 layers on gold nanoparticles SURFACES AND INTERFACES 74 Paper: 107725 , 7 p. (2025) https://doi.org/10.1016/j.surfin.2025.107725

[Ref.4.] N. Nagy "Determination of solid-liquid adhesion work on flat surfaces in a direct and absolute manner" Scientific Reports, 14:29991 2024. https://doi.org/10.1038/s41598-024-81710-6

[Ref.5.] N. Nagy „Eljárás és berendezés folyadék-szilárd adhéziós munka meghatározására" Hungarian patent (231 506)

[Ref.6.] N. Nagy „Method and Apparatus for Determining Liquid-Solid Adhesion Work", WIPO PCT patent application (WO2023094846) https://patentscope.wipo.int/search/en/detail.jsf?docId=WO2023094846

[Ref.7.] Kovács, D.; Radnóczi, G. Z.; Horváth, Z. E.; Frey, K.; Sulyok, A.; Fogarassy, Z.; Pap, J. S.; Deák, A.; Zámbó, D. Photoassisted Chemical Transformation of Cu2 O Nanooctahedra into Cu2 S Quantum-Dot Superstructures: Structural and Photoelectrochemical Properties. ACS Mater. Au 2025, 5, 6, 1018–1028 https://doi.org/10.1021/acsmaterialsau.5c00106.

[Ref.8.] Kovács, D.; Deák, A.; Radnóczi, G. Z.; Horváth, Z. E.; Sulyok, A.; Schiller, R.; Czömpöly, O.; Zámbó, D. Position of Gold Dictates the Photophysical and Photocatalytic Properties of Cu2O in Cu2O/Au Multicomponent Nanoparticles. J. Mater. Chem. C 2023, 11 (26), 8796–8807. https://doi.org/10.1039/d3tc01213a

[Ref.9.] Zámbó, D.; Kovács, D.; Deák, A. Optical and Structural Properties of Cuprous Oxide Shell Coated Gold Nanoprisms. Part & Part Syst Charact 2024, 2400082. https://doi.org/10.1002/ppsc.202400082

[Ref.10.] Ganieva, Z.; Kovács, D.; Osváth, Z.; Zámbó, D.; Deák, A. Region-Selective Growth of Cu2 O Shell on Gold Nanoprisms. Adv Materials Inter 2025, 12 (16), e00512. https://doi.org/10.1002/admi.202500512 [Ref.11] M. S. Braga, R. F. V. V. Jaimes, W. Borysow, O. F. Gomes, and W. J. Salcedo, "Portable multispectral colorimeter for metallic ion detection and classification," Sensors (Basel), vol. 17, no. 8, p. 1730, Jul. 2017, doi: 10.3390/s17081730.

[Ref.11.] Z. Labadi et al., "Sensing layer for Ni detection in water created by immobilization of bioengineered flagellar nanotubes on gold surfaces," ACS Biomaterials Sci. Eng., vol. 6, no. 7, pp. 3811–3820, 2020, doi: 10.1021/acsbiomaterials.0c00280

[Ref.12.] S. Kurunczi et al., "In situ ellipsometric study of surface immobilization of flagellar filaments," Applied Surface Science, vol. 257, no. 1, pp. 319–324, 2010, doi: 10.1016/j.apsusc.2010.06.095

[Ref.13.] P. T. Kissinger and W. R. Heineman, "Cyclic voltammetry," Journal of Chemical Education, vol. 60, pp. 702–706, 1983.

[Ref.14.] N. Elgrishi, K. J. Rountree, B. D. McCarthy, E. S. Rountree, T. T. Eisenhart, and J. L. Dempsey, "A practical beginner's guide to cyclic voltammetry," Journal of Chemical Education, vol. 95, no. 2, pp. 197–206, Feb. 2018, doi: 10.1021/acs.jchemed.7b00361.

[Ref.15.] M. Fried, R. Bogar, D. Takacs, Z. Labadi, Z. E. Horvath, Z. Zolnai, Investigation of Combinatorial WO3-MoO3 Mixed Layers by Spectroscopic Ellipsometry using Different Optical Models. NANOMATERIALS 12(14) Paper: 2421 (2022); https://doi.org/10.3390/nano12142421

[Ref.16.] Z. Labadi, D. Takacs, Z. Zolnai, P. Petrik, M. Fried, Compositional Optimization of Sputtered WO3/MoO3 Films for High Coloration Efficiency. MATERIALS 17(5), 1000 (2024); https://doi.org/10.3390/ma17051000

[Ref.17.] S.P. Thompson, "Ye Magick Mirrour of Old Japan", London, private edition (1893).

[Ref.18.] F. Riesz, "The effects of the global surface curvature on Makyoh-topography imaging", Photonics Letters of Poland 11 (2019) 4. doi: 10.4302/plp.v11i1.862

[Ref.19.] F. Riesz, "Curvature, illumination conditions and imaging properties in magic mirrors", The 6th Makyoh Conversazione, 29-31 August 2025, Osaka, Abstracts, p. 25.

[Ref.20.] Lábár et al.; Nanoscale, 2026, 18, 2264–2276
[Ref.21.] AS Racz, M. Menyhard Evaluation methods for XPS depth profiling; A review, Appl. Surf. Sci. Advances, 2025, 30,100872, IF=8.7, D1
[Ref.22.] Tamás Kolonits, Szilvia Kugler, Attila Nagy, Péter Füri, Rita Ambrus, Sally Kheirandish, Attila Horváth, Árpád Farkas (2025). Effect of non-spherical shape of dry powder aerosol drugs on their airway deposition distribution. International Journal of Pharmaceutics, 671, 125209. https://doi.org/10.1016/j.ijpharm.2025.125209
[Ref.23.] A. Horváth et al.; Dramatic interference of Au TEM grid with model and supported MoNi/MgO catalysts during high temperature reduction and methane decomposition. Materials Today Nano 32 (2025) 100690. IF: 8.2
[Ref.24.] E. Dodony et al.; Structural variability of gamma Ni-silicides. Journal of Alloys and Compounds 1036 (2025) 181554. IF: 6.3
[Ref.25.] M. Gajdics et al.; A Study of HiPIMS Process Characteristics in SiO_2 Deposition. Coatings 15 (2025) 1023. IF: 2.8
[Ref.26.] M. Gajdics et al.; Assistance to Determine the Stability State of a Reactive Sputtering Process Based on the Analytical Solution of the Classical Berg Model. Coatings 15 (2025) 499. IF: 2.8
[Ref.27.] N. Q. Chinh et al.; Indentation size effects and its relevance to ultrafine-grained materials. Materials Science and Engineering A 923 (2025) 147733. IF: 7.0
[Ref.28.] D. Mukherjee et al.; Optimized sensing on gold nanoparticles created by graded-layer magnetron sputtering and annealing. Sensors and Actuators B: Chemical 425 (2025) 136875. IF: 7.7
[Ref.29.] D. Olasz et al.; Comprehensive characterisation of the Al–Cu binary thin film system: Correlation between composition, microstructure and mechanical properties. Journal of Alloys and Compounds 1051 (2026) 186114.
[Ref.30.] Sáfrán G. Ultramicroscopy, 187 (2018), p. 50
[Ref.31.] Kalas B., Sáfrán G., Serényi M., Fried M., Petrik P. Appl. Surf. Sci., 606 (2022), 154770
[Ref.32.] D. Mukherjee, K. Kertész , Zs. Zolnai, Z. Kovács , A. Deák, A. Pálinkás, Z. Osváth, D. Olasz, A. Romanenko, M. Fried, S. Burger, G. Sáfrán, P. Petrik, Sensors and Actuators: B. Chemical 425 (2025) 136875: https://doi.org/10.1016/j.snb.2024.136875
[Ref.33.] Materials Today Nano: https://www.sciencedirect.com/science/article/pii/S258884202500121X
[Ref.34.] G. Cicconi*, M. Bosi*, F. Mezzadri*, A. Ugolotti*, I. Cora*, L. Seravalli, H. Tornatzky, J. L¨ahnemann, M.R. Wagner, P. Bhatt, P.K. Thakur, T.-L. Lee, A. Regoutz, A. Baraldi, D. Bersani, L. Cademartiri, A. Parisini, B. Pecz, L. Miglio, R. Fornari, P. Mazzolini: Nucleation and faceting in (001) r-GeO2 heteroepitaxy on r-TiO2 by metalorganic vapor phase epitaxy. Applied Surface Science 725 (2026) 165788
[Ref.35.] Lukáš Vrána, Tomasz Stasiak, Matej Fekete, Vilma Buršíková, Zsolt Czigány, Katalin Balázsi, Pavel Souček Effects of Nitrogen Content on Microstructure and Mechanical Properties of DC Magnetron Sputtered CrMnMoSiY(N) High Entropy Coatings. Surface & Coatings Technology 497 (2025) 131742
[Ref.36.] Kis, V.K., Schwarcz, H.P., Nassif, N., Szekanecz, Z. Bone mineral platelets are mesocrystals formed by monoclinic nanocrystals. Communications Mater. 6, 1–8. (2025).
[Ref.37.] Tao, J., Battle, K.C., Pan, H., Salter, E.A., Chien, Y.C., Wierzbicki, A., De Yoreo, J.J. Energetic basis for the molecular-scale organization of bone. PNAS 112, 326–331 (2015).
[Ref.38.] Robin, M., Mouloungui, E., Castillo Dali, G., Wang, Y., Saffar, J-L., Pavon-Djavid, G., Divoux, T., Manneville, S., Behr, L., Cardi, D., Choudat, L., Giraud-Guille, M.M., Meddahi-Pellé, A., Baudimont, F., Colombier, M.L., Nassif, N. Mineralized collagen plywood contributes to bone autograft performance. Nature 636, 100–107 (2024).
[Ref.39.] Hegedűs, M., Kovács, Zs., Vásárhelyi, L., Kukovecz, Á., Illés, L., Szász, N., Mlinkó, É., Rózsa, N.K., Kis, V.K. Ribbon-like hypomineralization in human dental enamel. Acta Biomaterialia, 196, 281-292. (2025).
[Ref.40.] V. Domnich, S. Reynaud, R. A. Haber, and M. Chhowalla, J. Am. Ceram. Soc. 94: 3605 (2011)
[Ref.41.] G. Akselrod, M. S. Akselrod E. R. Benton, and N. Yasuda, Nucl. Intr. Meth. B 247: 295 (2006)
[Ref.42.] Z. Kis, The redesigned neutron imaging facility, NORMA at BNC, Budapest Rev. Sci. Instrum.1, 95 (7): 073702 (2024) https://doi.org/10.1063/5.0208844
[Ref.43.] https://bnc.hu/norma/
[Ref.44.] Baji, Z., Kovács, Z., Szabó, Z., Hakkel, O., Sulyok, A., Fogarassy, Z., Bérces, Z., Volk, J., 2026. Controlled nucleation of metal-sulfide layers via surface functionalization with sulfur species: Enhanced initial growth of GaSx thin films. Journal of Vacuum Science & Technology A 44, 032402. https://doi.org/10.1116/6.0005254

[Ref.45.] G. Csaba and W. Porod. Coupled oscillators for computing: A review and perspective. Applied Physics Reviews 7, 011302 (2020).
[Ref.46.] H. Liu, et al. Artificial Neuronal Devices Based on Emerging Materials: Neuronal Dynamics and Applications. Advanced Materials 35, 2205047 (2023).
[Ref.47.] E. Corti, et al. Scaled resistively-coupled VO_2 oscillators for neuromorphic computing. Solid-State Electronics 168, 107729 (2020).
[Ref.48.] S. Kumar, et al. Dynamical memristors for higher-complexity neuromorphic computing. Nature Reviews Materials 7, 575–591 (2022).
[Ref.49.] Md. Suruz Mian, et al. Self-oscillation up to 9 MHz based on voltage triggered switching in VO2/TiN point contact junctions. Journal of Applied Physics. 117, 215305 (2015)
[Ref.50.] Heungsoo Kim, Nicholas S. Bingham, Nicholas A. Charipar, Alberto Piqué; Strain effect in epitaxial VO_2 thin films grown on sapphire substrates using SnO_2 buffer layers. AIP Advances 1 October 2017; 7 (10): 105116. https://doi.org/10.1063/1.5004125
[Ref.51.] László Pósa, Péter Hornung, Tímea Nóra Török, Sebastian Werner Schmid, Sadaf Arjmandabasi, György Molnár, Zsófia Baji, Goran Dražić, András Halbritter, and János Volk: Interplay of Thermal and Electronic Effects in the Mott Transition of Nanosized VO2 Phase Change Memory Devices ACS Applied Nano Materials 2023 6 (11), 9137-9147 DOI: 10.1021/acsanm.3c00150 https://pubs.acs.org/doi/10.1021/acsanm.3c00150
[Ref.52.] S. W. Schmid, et al. Picosecond Femtojoule Resistive Switching in Nanoscale VO2 Memristors ACS Nano 18:33, 21966-21974. (2024)
[Ref.53.] Pollner, Zsigmond and Török, Tímea Nóra and Pósa, László and Csontos, Miklós and Schmid, Sebastian Werner and Balogh, Zoltán and Bükkfejes, András and Kim, Heungsoo and Piqué, Alberto and Leuthold, Juerg and Volk, János and Halbritter, András Ernő (2025) VO2 Oscillator Circuits Optimized for Ultrafast, 100 MHz-Range Operation. ADVANCED ELECTRONIC MATERIALS, in pre. No. e00433. ISSN 2199-160X https://doi.org/10.1002/aelm.202500433
[Ref.54.] Z. Scherübl et al.: Determination of the current-phase relation of an InAs 2DEG Josephson junction with a microwave resonator, Phys. Rev. Research 7(2), 023173 (2025) https://doi.org/10.1103/PhysRevResearch.7.023173
[Ref.55.] P. Révész1, J.M. Bozorádi, D. Martini, J. Volk, Estimate of the force required to transect the chorda tympani: A preliminary study using a novel measurement tool, under review.
[Ref.56.] Bíró Ferenc, Dücső Csaba, Braun Ferenc, Neumann Péter Lajos, Király Anna, Bakos Lóránt, Mészáros András Bálint, Bozorádi János Márk, Nguyen Quoc Khánh, Volk János, Vészhelyzetben és szélsőséges körülmények között alkalmazható környezetfigyelő szenzorok, ELEKTROnet, 2025. dec. 05.
[Ref.57.] János M. Bozorádi, Zsófia Bérces, Géza Papp, Maria Berkes Maros, Péter Fürjes, Force measurement in Laparoscopic Stapler for Ex-Vivo Tissue Characterization, Eurosensors 2025 Conference, Wroclaw, Poland, 2025 (poster) - AMA Proceedings of Eurosensors 2025 Conference, doi.org/10.5162/EUROSENSORS2025/TP66
[Ref.58.] Tamás Tarjányi, Gábor Gulyás, Krisztián Bali, Márton Sámi, Rebeka Anna Kiss, Barbara Beiler, Péter Fürjes and Tibor Szabó, Nanoindentation Analysis of SU-8 Coated Wafers at Different Baking Phases, Polymers, 17, 3337, 2025 (IF 4.9 / Q1) doi.org/10.3390/polym17243337
[Ref.59.] Kambiz Nanbakhsh, Ahmad Shah Idil, Callum Lamont, Csaba Dücső, Ömer Can Akgun, Domonkos Horváth, Kinga Tóth, Domokos Meszéna, István Ulbert, Federico Mazza, Timothy G. Constandinou, Wouter Serdijn, Anne Vanhoestenberghe, Nick Donaldson & Vasiliki Giagka, On the longevity and inherent hermeticity of silicon-ICs: evaluation of bare-die and PDMS-coated ICs after accelerated aging and implantation studies, NATURE COMMUNICATIONS 16 12, 2025 (IF: 15,7 / D1) doi.org/10.1038/s41467-024-55298-4
[Ref.60.] Barbara Beiler, Malik H. Mahmood, Dóra Bereczki, Ágnes Sáfrány, Péter Fürjes, Miklós Veres, Tailoring porous properties of polymer monoliths through the composition of the binary solvent mixture, Reactive and Functional Polymers 220 106614, 2026 (IF: 5.1 / Q1) doi.org/10.1016/j.reactfunctpolym.2025.106614
[Ref.61.] Lilia Bató, János M. Bozorádi, János, Zoltán Vizvári, Péter Fürjes, Real-Time Cell Viability Testing in Microfluidic System by EIS, MPS 2025 World Summit, Brussels, Belgium, 2025 (poster)
[Ref.62.] Lilia Bató, Péter Fürjes, János M. Bozorádi, Vladimir Tadić, Péter Odry, Zoltán Vizvári, Sensitivity Analysis of Localized Electrochemical Impedance Spectroscopy Towards Tomography-on-a-Chip, Sensors 25(20), 6393, 2025 (IF 3.5 / Q1) doi.org/10.3390/s25206393
[Ref.63.] Lilia Bató, János M. Bozorádi, Zoltán Vizvári, Péter Fürjes, Microfluidic System With Integrated Electrode Array for Impedance Tomography of Cell Cultures, Symposium on Design, Test,

Integration and Packaging of MEMS/MOEMS - DTIP 2025 Conference, Split, Croatia, 2025 (poster) (IEEE XPlore 11099198, doi.org/10.1109/DTIP66728.2025.11099198)

[Ref.64.] Zsombor Szomor, Nafisat Gyimah, Tamás Pardy, Péter Fürjes, Three-dimensional finite element modelling of chemical environment in droplet-based microfluidic systems for drug therapy applications, Physics of Fluids 37, 072045 2025 (IF 4.3 / Q1) https://doi.org/10.1063/5.0275809

[Ref.65.] Szomor Zsombor, Bereczki Dóra, Fürjes Péter, Cseppek mikrofluidikai rendszerekben, Fizikai Szemle 853 410-415, 2025

[Ref.66.] Zsombor Szomor, Tamás Pardy, Péter Fürjes, 3D Modelling of Mass and Heat Transport in Multi-Phase Microfluidic Systems, 31st International Workshop on Thermal Investigations of ICs and Systems – THERMINIC 2025 Conference, Naples, Italy, 2025 (poster) (IEEE XPlore 11216952, doi.org/10.1109/THERMINIC65879.2025.11216952)

[Ref.67.] Zoltán Szabó, Barbara Beiler, Zsofia Baji, Broadband InGaAsP/InP NIR LEDs based on multiple photon-recycling photoluminescent layers, Journal of Crystal Growth, Volume 652, 15 February 2025, 128045, https://doi.org/10.1016/j.jcrysgro.2024.128045 (IF 1.7 / Q2)

[Ref.68.] Zsombor Szomor, Lilia Bató, Orsolya Hakkel, Csaba Dücső, Zsófia Baji, Attila Sulyok, Erzsébet Dodony, Katalin Balázsi, János M. Bozorádi, Zoltán Szabó, Péter Fürjes, Characterisation of Titanium-Oxide Thin Films for Efficient pH Sensing in Low-Power Electrochemical Systems, Sensors 25(19), 6113, 2025 (IF 3.5 / Q1) doi.org/10.3390/s25196113

[Ref.69.] Eszter Bajtai, Csaba Kiss, Éva Bakos, Tamás Langó, Anna Lovrics, Éva Schád, Viktória Tisza, Károly Hegedűs, Péter Fürjes, Zoltán Szabó, Gábor E. Tusnády, Gergely Szakács, Ágnes Tantos, Sándor Spisák, József Tóvári & András Füredi, Therapy-induced senescence is a transient drug resistance mechanism in breast cancer, MOLECULAR CANCER 24 1 128, 2025 (IF 33.9 / D1) doi.org/10.1186/s12943-025-02310-0

[Ref.70.] András Füredi, Szilárd Tóth, Kristóf Hegedüs, Pál T. Szabó, Anikó Gaál, Gergő Barta, Lívia N. Naszályi, Krisztina Kiss, Kata Bölcskei, Zoltán Szeltner, Eszter Bajtai, Balázs Gombos, Dániel Kiss, Mihály T. Cserepes, Attila Kiss, Peter Pokreisz, Lukas Kenner, Sandra Högler, Csaba Magyar, Jamie D. Cowles, Agnes Csiszar, József Tóvári, Dávid Szüts, Zsuzsanna Helyes, Zoltán Varga, Gábor Mező & Gergely Szakács, Safe delivery of a highly toxic anthracycline derivative through liposomal nanoformulation achieves complete cancer regression, MOLECULAR CANCER 24 : 1 Paper: 269 , 18 p., 2025 (IF 33.9 / D1) doi.org/10.1186/s12943-025-02444-1

[Ref.71.] Dóra Bereczki, Ines Lidia Haffaressas, Zoltán Szabó, Szilárd Tóth, András Füredi Péter Fürjes, Fluorescent properties of FDA-approved anti-leukemia drugs, Biomedical Optics Express 17 2 963-976, 2026 (IF: 3.2 / Q1) doi.org/10.1364/BOE.580253

[Ref.72.] Gergely T. Solymosi, Gyula Jágerszki, Levente Illés, Péter Fürjes, Róbert E. Gyurcsányi, Single Solid-State Ion Channels as Potentiometric Nanosensors, Advanced Functional Materials, e19292, 2025 (IF 19 / D1) doi.org/10.1002/adfm.202519292

[Ref.73.] Gergely T. Solymosi, Tünde Kis, Péter Fürjes, Róbert E. Gyurcsányi, Absence of Hofmeister Selectivity in Hydrophobic Ion-Exchanger Nanopores, Analytical Chemistry, 97, 49, 27289−27297, 2025 (IF 6.7 / D1)

[Ref.74.] E. Farkas, K. D. Kovács, I. Szekacs, B. Peter, I. Lagzi, H. Kitahata, N. J. Suematsu, R. Horvath, „Kinetic monitoring of molecular interactions during surfactant-driven self-propelled droplet motion by high spatial resolution waveguide sensing", JOURNAL OF COLLOID AND INTERFACE SCIENCE, vol. 677, 2025.

[Ref.75.] M. Itatani, G. Holló, P. Albanese, N. Valletti S. Kurunczi, R. Horvath, F. Rossi, I. Lagzi „Temporal pH waveforms generated in an enzymatic reaction network in batch and cell-sized microcompartments", CELL REPORTS PHYSICAL SCIENCE, 102367, 2025

[Ref.76.] B. Kovacs, Sz. Novak, I. Sallai, B. Magyarodi, I. Szekacs, D. Selmeczi, B. Szabo, R. Horvath, „Robotic manipulations of single cells using a large-volume piezoelectric micropipette with nanoliter precision" COLLOIDS AND SURFACES B: BIOINTERFACES, vol. 256, 2025

[Ref.77.] N. Kanyo, K. Borbely, B. Peter, K. D. Kovacs, A. Balogh, B. Magyaródi, S. Kurunczi, I. Szekacs, R. Horvath, „Kinetic analysis of SARS-CoV-2 S1–integrin binding using live-cell, label-free optical biosensing", BIOSENSORS, vol. 15, 2025

[Ref.78.] B. Péter, T. Ausbüttel, N. Kanyo, P. Joó, K. Tóth, Z. Szittner, I. Szekacs, Sz. Bosze, G. M. Kovács, I. Boldizsár, R. Horvath, „In situ monitoring of cell adhesion kinetics using label-free optical biosensors: Evaluating anticancer potential and selectivity of natural compounds", VIEW, 20250061, 2025

[Ref.79.] Xie, Nenggang and Bai, Xi and Wang, Lu and Ye, Ye and Szolnoki, Attila (2025) Emotion-driven switching game environments facilitates general cooperation. CHAOS SOLITONS & FRACTALS,

202. No. 117524. ISSN 0960-0779 https://pubs.aip.org/aip/cha/article-abstract/35/8/083117/3358116

[Ref.80.] Hartmann, Bálint and Ódor, Géza and Benedek, Kristóf and Papp, István and Cirunay, Michelle (2025) Quantitative comparison of power grid reinforcements. CHAOS SOLITONS & FRACTALS, 200. No. 117095. ISSN 0960-0779

[Ref.81.] Cirunay, Michelle and Ódor, Géza and Papp, István and Deco, Gustavo (2025) Scale-free behavior of weight distributions of connectomes. PHYSICAL REVIEW RESEARCH, 7 (1). ISSN 2643-1564

[Ref.82.] György Szabó and Balázs Király: Derivation of potential for group interactions in evolutionary games Phys. Rev. EA 112 (2025) 064317

MFA'S FULL LIST OF PUBLICATION IN 2025

1. Ádám, B. Á., Spátay, S., Jávor, B., László, S., Illés, L., Fürjes, P., … Golcs, Á. (2025). Atmospheric air plasma pre-activation and customizable covalent functionalization of PVDF-membranes of microtiter filter plates. *SCIENTIFIC REPORTS*, *15*(1). http://doi.org/10.1038/s41598-024-85040-5
2. Al-Abassi, S. A. W., & Neumann, P. (2025). Innovative SPICE model for VO2 threshold-switching devices: Bridging insulator-metal transitions and thermal-electrical feedback for neuromorphic applications. *NEXT MATERIALS*, *9*. http://doi.org/10.1016/j.nxmate.2025.101110
3. Albert, E., Basa, P., Fodor, B., Keresztes, Z., Madarász, J., Márton, P., … Hórvölgyi, Z. (2025). Experimental and Computational Synthesis of TiO2 Sol–Gel Coatings. *LANGMUIR*, *41*(1), 704–718. http://doi.org/10.1021/acs.langmuir.4c03959
4. Alkaron, W., Almansoori, A., Balázsi, K., & Balázsi, C. (2025). Preparation and Morphology Study of Electrospun Cellulose Acetate Fibers Using Various Solvent Systems and Concentrations. *PERIODICA POLYTECHNICA-CHEMICAL ENGINEERING*, *69*(3), 427–438. http://doi.org/10.3311/PPch.41199
5. Almansoori, A., Rácz, A. S., Czigány, Z., Balázsi, K., & Balázsi, C. (2025). Effect of silicon nitride (Si3N4) powder oxidation on the microstructural and interfacial characteristics of carbon nanotube (CNT)-reinforced Si3N4 ceramics. *CERAMICS INTERNATIONAL*, *51*(30), 65592–65599. http://doi.org/10.1016/j.ceramint.2025.11.236
6. Ayyubov, I., Tálas, E., Borbáth, I., Pászti, Z., Trif, L., Szegedi, Á., … Tompos, A. (2025). Linking structure to electrocatalytic performance: Graphene nanoplatelets-derived novel mixed Oxide-Carbon composites as supports for Pt electrocatalysts with enhanced stability. *NANOMATERIALS*, *15*(23). http://doi.org/10.3390/nano15231753
7. Ayyubov, I., Berghian-Grosan, C., Dodony, E., Pászti, Z., Borbáth, I., Szegedi, A., … Tálas, E. (2025). Structure–Catalytic Behavior Relationships in TiO2-Carbon Composite Supported Pt Electrocatalysts: A Case Study. *ANALYTICAL LETTERS*, *58*(11), 1762–1783. http://doi.org/10.1080/00032719.2024.2351589
8. Baji, Z., Fogarassy, Z., Hakkel, O., & Szabó, Z. (2025). Enhancing the nucleation in atomic layer deposition: A study on vanadium sulfide and oxide layers. *JOURNAL OF VACUUM SCIENCE AND TECHNOLOGY A-VACUUM SURFACES AND FILMS*, *43*(2). http://doi.org/10.1116/6.0004247
9. Baji, Z., Fogarassy, Z., Sulyok, A., Horváth, Z. E., & Szabó, Z. (2025). Novel precursor for the preparation of vanadium sulfide layers with atomic layer deposition. *JOURNAL OF VACUUM SCIENCE AND TECHNOLOGY A-VACUUM SURFACES AND FILMS*, *43*(2). http://doi.org/10.1116/6.0004127
10. Bajtai, E., Kiss, C., Bakos, É., Langó, T., Lovrics, A., Schád, É., … Füredi, A. (2025). Therapy-induced senescence is a transient drug resistance mechanism in breast cancer. *MOLECULAR CANCER*, *24*(1). http://doi.org/10.1186/s12943-025-02310-0
11. Bálint, Z., & Piszter, G. (2025). *Lepkétől a fotonikus kristályig*. (Z. Bálint & G. Piszter, Eds.). Budapest: HUN-REN EK MFA.
12. Bálint, Z., & Biró, L. P. (2025b). A lepkeszárny kémiai és fizikai színei. In *Lepkétől a fotonikus kristályig* (pp. 7–14).
13. Bálint, Z., & Biró, L. P. (2025a). A lepkék színeváltozása. In *Lepkétől a fotonikus kristályig* (pp. 15–22).
14. Bálint, Z., Katona, G., Kertész, K., Piszter, G., Grishin, N., Neild, A. F., … Costa, M. (2025). A new sister species of Thaeides theia (Hewitson, 1870) from the Venezuelan Central Coastal Range (Lepidoptera: Lycaenidae: Theclinae). *ANNALES MUSEI HISTORICO-NATURALIS HUNGARICI*, *117*, 163–182. http://doi.org/10.53019/AnnlsMusHistNatHung.2025.117.163
15. Balogh, A., Kovács, K. D., Kanyó, N., Péter, B., Lagzi, I., Molnár, K., … Horváth, R. (2025). Real-time kinetic monitoring of gold nanoparticle uptake and adhesion in HeLa cells using label-free biophysical methods.
16. Balogh, A., Kovács, K. D., Péter, B., Molnár, K., Truszka, M., Lagzi, I., … Horváth, R. (2025). Funkcionalizált nanorészecskék és élő sejtek kölcsönhatásainak jelölésmentes vizsgálata a glikokalix enzimatikus emésztésével.
17. Balogh, D. A., Borbely, K., Kurunczi, S., Endre, G., Kondorosi, E., & Horvath, R. (2025). Quantitative analysis of plant peptide–protein interactions using GCI biosensing.
18. Balogh, D. A., Novák, S., Farkas, E., Péter, B., Domokos, H. B., Szabó, B., & Horvath, R. (2025). Technical advancements in circulating tumor cell sorting using a piezoelectric micropipette.

19. Bató, L., Bozorádi, J. M., Vizvári, Z., & Fürjes, P. (2025a). Microfluidic System With Integrated Electrode Array for Impedance Tomography of Cell Cultures. In *2025 Symposium on Design, Test, Integration and Packaging of MEMS/MOEMS (DTIP)*. http://doi.org/10.1109/DTIP66728.2025.11099198
20. Bató, L., Fürjes, P., Bozorádi, J. M., Tadić, V., Odry, P., & Vízvári, Z. (2025). Sensitivity Analysis of Localized Electrochemical Impedance Spectroscopy Towards Tomography-on-a-Chip. *SENSORS*, *25*(20). http://doi.org/10.3390/s25206393
21. Bató, L., Bozorádi, J. M., Vizvári, Z., & Fürjes, P. (2025b). Real-Time Cell Viability Testing in Microfluidic System by EIS.
22. Behrangi, S., Depla, D., Souček, P., Czigány, Z., Buršíková, V., Balázsi, K., & Vašina, P. (2025). Industrial reactive sputter deposition of TiZrN coatings: The role of nitrogen partial pressure. *SURFACE AND COATINGS TECHNOLOGY*, *499*. http://doi.org/10.1016/j.surfcoat.2025.131873
23. Beres, B., & Horvath, R. (2025). Label-Free Single-Cell Activity-Based Cell Type Classification Using Optical Resonant Waveguide Grating Biosensor Data. In *16th IEEE International Conference on Cognitive Infocommunications CogInfoCom 2025* (pp. 137–142). http://doi.org/10.1109/CogInfoCom66819.2025.11200858
24. Bíró, F., Dücső, C., Braun, F., Neumann, P. L., Király, A., Bakos, L., … Volk, J. (2025). Vészhelyzetben és szélsőséges körülmények között alkalmazható környezetfigyelő szenzorok. *ELEKTRONET*, *34*(4), 20–23.
25. Borbely, K., Balogh, D. A., Kurunczi, S., Farkas, E., Peter, B., Szekacs, I., … Horvath, R. (2025a). From protein-peptide interactions to cell adhesion: label-free biophysical insights into peptide activity.
26. Borbely, K., Balogh, D. A., Kurunczi, S., Farkas, E., Peter, B., Szekacs, I., … Horvath, R. (2025b). GCI-based profiling of protein-peptide interactions.
27. Borg, H., Zámbó, D., Bessel, P., Kranz, D., Rosebrock, M., Lübkemann-Warwas, F., … Dorfs, D. (2025). Tailoring Bimetallic Pt/Pd Cryogels for Efficient Ethanol Electro-Oxidation. *CHEMELECTROCHEM*, *12*(3). http://doi.org/10.1002/celc.202400552
28. Bors, A. M., Madarász, J., Nagy, N., Rácz, A. S., Sáfrán, G., Olasz, D., … Albert, E. (2025). Ammonia Vapor-Induced Pseudomorphic Transformation of Mesoporous TiO2 Sol-Gel Coatings. *ACS OMEGA*, *10*(31), 35029–35042. http://doi.org/10.1021/acsomega.5c04483
29. Bosio, A., Pasini, S., Spoltore, D., Foti, G., Parisini, A., Pavesi, M., … Fornari, R. (2025). Effect of Heterojunction Characteristics and Deep Electronic Levels on the Performance of (Cd,Zn)S/Sb2Se3 Solar Cells. *APPLIED SCIENCES-BASEL*, *15*(6). http://doi.org/10.3390/app15062930
30. Bozorádi, J. M., Bérces, Z. S., Fürjes, P., Maros, M. B., & Papp, G. (2025). TP66 - Force measurement in Laparoscopic Stapler for Ex-Vivo Tissue Characterization. In *AMA Proceedings of Eurosensors 2025 Conference* (pp. 486–487). http://doi.org/10.5162/EUROSENSORS2025/TP66
31. Braniste, T., Fogarassy, Z., Kovács, A., Pécz, B., & Tiginyanu, I. (2025). Formation of Zinc Oxide Buried Layers within the Walls of the Aero-GaN Microtubes. In *7th International Conference on Nanotechnologies and Biomedical Engineering* (pp. 104–111). http://doi.org/10.1007/978-3-032-06494-3_12
32. Buccheri, V., Joint, F., Amin, K. R., Elalaily, T., Kürtössy, O., Scherübl, Z., … Gasparinetti, S. (2025). Microwave dynamics of gated Al/InAs superconducting nanowires. *APPLIED PHYSICS LETTERS*, *126*(23). http://doi.org/10.1063/5.0267684
33. Bulátkó, A., Höfler, L., Kéri, M., Majzik, T. I., Mohai, M., Sáfrán, G., … László, K. (2025). Role of texture and surface chemistry in interaction of graphene oxides with water. *JOURNAL OF MOLECULAR LIQUIDS*, *438*. http://doi.org/10.1016/j.molliq.2025.128722
34. Burunkova, J. A., Tarasov, V. E., Dolgintsev, D. M., Kozyukhin, S. A., Petrik, P., Mukherjee, D., … Kökényesi, S. (2025). Photopolymerizable Composite Based on Acrylates, Arsenic Sulfide and Gold Nanoparticles for Holographic Recording. *JOURNAL OF PHOTOPOLYMER SCIENCE AND TECHNOLOGY*, *38*(5), 399–408. http://doi.org/10.2494/photopolymer.38.399
35. Chinh, N. Q., Olasz, D., Sáfrán, G., & Langdon, T. G. (2025). Indentation size effects and its relevance to ultrafine-grained materials. *MATERIALS SCIENCE AND ENGINEERING A-STRUCTURAL MATERIALS PROPERTIES MICROSTRUCTURE AND PROCESSING*, *923*. http://doi.org/10.1016/j.msea.2024.147733
36. Chouhan, H., Dobročka, E., Nádaždy, P., Ťapajna, M., Hušeková, K., Cora, I., … Gucmann, F. (2025). Rotational domains and origin of improved crystal quality in heteroepitaxial ($2\bar{}01$) β-Ga2O3 films grown on vicinal substrates by MOCVD. *JOURNAL OF ALLOYS AND COMPOUNDS*, *1044*. http://doi.org/10.1016/j.jallcom.2025.184481
37. Cirunay, M., Ódor, G., Papp, I., & Deco, G. (2025). Scale-free behavior of weight distributions of connectomes. *PHYSICAL REVIEW RESEARCH*, *7*(1). http://doi.org/10.1103/PhysRevResearch.7.013134

38. Cirunay, M. T., Batac, R. C., & Ódor, G. (2025). Learning and criticality in a self-organizing model of connectome growth. *SCIENTIFIC REPORTS*, *15*(1). http://doi.org/10.1038/s41598-025-16377-8
39. Czigány, Z., Zine, H. R. B., Balázsi, K., & Balázsi, C. (2025). Cr-Al Spinel phase formation in alumina dispersed 316 L stainless steel processed by spark plasma sintering. *SCIENTIFIC REPORTS*, *15*(1). http://doi.org/10.1038/s41598-025-87223-0
40. Daboczi, M., Eisner, F., Luke, J., Yuan, S. W., Lawati, N. A., Zhi, M., … Eslava, S. (2025). Enhanced solar water oxidation and unassisted water splitting using graphite-protected bulk heterojunction organic photoactive layers. *NATURE ENERGY*, *10*(5), 581–591. http://doi.org/10.1038/s41560-025-01736-6
41. Dodony, E., Dódony, I., Fogarassy, Z., Pekker, P., & Sáfrán, G. (2025). Structural variability of gamma Ni-silicides. *JOURNAL OF ALLOYS AND COMPOUNDS*, *1036*. http://doi.org/10.1016/j.jallcom.2025.181554
42. Dvurečenskij, A., Cigáň, A., Radnóczi, G., Škrátek, M., Majerová, M., Hájovská, Z., … Maňka, J. (2025). Magnetic Properties of Nanocolloids Based on Titanium and Ionic Liquid BMIM PF6. In *2025 15th International Conference on Measurement* (pp. 117–120). http://doi.org/10.23919/MEASUREMENT66999.2025.11078731
43. Edalati, K., Ahmed, A. Q., Akrami, S., Ameyama, K., Aptukov, V., Asfandiyarov, R. N., … Zhu, Y. T. (2025). Erratum to ' Severe plastic deformation for producing superfunctional ultrafine-grained and heterostructured materials: An interdisciplinary review' [J. Alloys Compd. 1002 (2024) 174667]. *JOURNAL OF ALLOYS AND COMPOUNDS*, *1034*. http://doi.org/10.1016/j.jallcom.2025.181313
44. Farkas, E., Kovács, K. D., Szekacs, I., Peter, B., Lagzi, I., Kitahata, H., … Horvath, R. (2025). Kinetic monitoring of molecular interactions during surfactant-driven self-propelled droplet motion by high spatial resolution waveguide sensing. *JOURNAL OF COLLOID AND INTERFACE SCIENCE*, *677*, 352–364. http://doi.org/10.1016/j.jcis.2024.07.236
45. Farkas, E., Kovacs, K. D., Szekacs, I., Peter, B., Lagzi, I., Kitahata, H., … Horvath, R. (2025b). Self-Propelled Droplet Motion with Characterization of Real-Time Kinetic Analysis of Surfactant Interactions by Label-Free Surface-Sensitive Biosensors.
46. Farkas, E., Kovacs, K. D., Szekacs, I., Peter, B., Lagzi, I., Kitahata, H., … Horvath, R. (2025a). Real time, Nanometer Scale Resolution Kinetic Detection of Self Propelled Droplet Motion by Waveguide Biosensor.
47. Frisia, S., Dietzel, M., Borsato, A., Németh, P., Pettauer, M., Hellstrom, J. C., … Augustinus, P. C. (2025). Co-precipitation of calcite and (Al)-Si-OH phases in Pleistocene subglacial environments of the East Antarctic Ice Sheet. *GEOCHIMICA ET COSMOCHIMICA ACTA*, *402*, 277–290. http://doi.org/10.1016/j.gca.2025.05.042
48. Furko, M. (2025). Bioglasses Versus Bioactive Calcium Phosphate Derivatives as Advanced Ceramics in Tissue Engineering: Comparative and Comprehensive Study, Current Trends, and Innovative Solutions. *JOURNAL OF FUNCTIONAL BIOMATERIALS*, *16*(5). http://doi.org/10.3390/jfb16050161
49. Füredi, A., Tóth, S., Hegedüs, K., Szabó, P. T., Gaál, A., Barta, G., … Szakács, G. (2025). Safe delivery of a highly toxic anthracycline derivative through liposomal nanoformulation achieves complete cancer regression. *MOLECULAR CANCER*, *24*(1). http://doi.org/10.1186/s12943-025-02444-1
50. Fürjes, P., Bereczki, D., Bató, L., Szomor, Z., Bozorádi, J. M., Hakkel, O., … Prechl, J. (2025). T6.2.1 - Impedance Spectroscopy Based Flow Rate Monitoring in Autonomous Cell Analytical Micro-Capillary Systems. In *AMA Proceedings of Eurosensors 2025 Conference* (pp. 152–153). http://doi.org/10.5162/EUROSENSORS2025/T6.2.1
51. Fürjes, P., Bereczki, D., & Füredi, A. (2025). Fluorescent molecule detection for Point-of-Care therapeutic drug monitoring and Organ-on-Chip applications.
52. Gajdics, M., Cora, I., Zámbó, D., Horváth, Z., Sulyok, A., Frey, K., & Pécz, B. (2025). Evolution of structural and photoluminescent properties of sputter-deposited Ga2O3 thin films during post-deposition heat treatment. *JOURNAL OF ALLOYS AND COMPOUNDS*, *1021*. http://doi.org/10.1016/j.jallcom.2025.179634
53. Gajdics, M., Hegedus, N., Olasz, D., & Serenyi, M. (2025). Assistance to Determine the Stability State of a Reactive Sputtering Process Based on the Analytical Solution of the Classical Berg Model. *COATINGS*, *15*(5). http://doi.org/10.3390/coatings15050499
54. Gajdics, M., Olasz, D., Sáfrán, G., & Serényi, M. (2025). A Study of HiPIMS Process Characteristics in SiO2 Deposition. *COATINGS*, *15*(9). http://doi.org/10.3390/coatings15091023
55. Ganieva, Z., Kovács, D., Osváth, Z., Zámbó, D., & Deák, A. (2025). Region-Selective Growth of Cu2O Shell on Gold Nanoprisms. *ADVANCED MATERIALS INTERFACES*, *12*(16). http://doi.org/10.1002/admi.202500512

56. Gartner, M., Chelu, M., Szekeres, A., & Petrik, P. (2025). Towards Advanced Materials: Functional Perspectives of Co-Doped ZnO Thin Films. *MICROMACHINES*, *16*(10). http://doi.org/10.3390/mi16101179
57. Greil, J., Kiechle, M., Papp, A., Neumann, P., Kovács, Z., Volk, J., … Becherer, M. (2025). The effect of Ga-ion irradiation on sub-micron-wavelength spin waves in yttrium-iron-garnet films. *NANOTECHNOLOGY*, *36*(13). http://doi.org/10.1088/1361-6528/adad7d
58. Han, J., Pi, B., Chen, X., & Szolnoki, A. (2025). Public goods cooperation via group interaction with opponent selection. *CHAOS SOLITONS & FRACTALS*, *199*. http://doi.org/10.1016/j.chaos.2025.116821
59. Hartmann, B., Ódor, G., Benedek, K., & Papp, I. (2025). Studying power-grid synchronization with incremental refinement of model heterogeneity. *CHAOS*, *35*(1). http://doi.org/10.1063/5.0237050
60. Hartmann, B., Soha, T., Cirunay, M., & Erdei, T. (2025). Inherent structural vulnerabilities in power distribution networks: a longitudinal complex network analysis. *APPLIED NETWORK SCIENCE*, *10*(1). http://doi.org/10.1007/s41109-025-00724-9
61. Hartmann, B., Ódor, G., Benedek, K., Papp, I., & Cirunay, M. T. (2025b). Quantitative comparison of power grid reinforcements. *CHAOS SOLITONS & FRACTALS*, *200*(Part 3). http://doi.org/10.1016/j.chaos.2025.117095
62. Hartmann, B., Ódor, G., Benedek, K., Papp, I., & Cirunay, M. T. (2025a). Hálózatmegerősítési módszerek kvantitatív összehasonlítása. *ELEKTROTECHNIKA*, *118*(7–8), 30–32.
63. Hartmann, B., Cirunay, M. T., Erdei, T., & Soha, T. (2025). Univerzális topológiai mintázatok a középfeszültségű elosztóhálózatokban. *ELEKTROTECHNIKA*, *118*(7–8), 33–36.
64. Hartmann, B., & Cirunay, M. T. (2025). Empirical cross-system meta-analysis of long-term transmission grid evolution. *INTERNATIONAL JOURNAL OF ELECTRICAL POWER AND ENERGY SYSTEMS*, *173*. http://doi.org/10.1016/j.ijepes.2025.111447
65. Hauert, C., & Szabó, G. (2025). Phase transitions and symmetry breaking of cooperation on lattices. *PHYSICAL REVIEW E: COVERING STATISTICAL NONLINEAR BIOLOGICAL AND SOFT MATTER PHYSICS (2016-)*, *111*(5). http://doi.org/10.1103/PhysRevE.111.054308
66. Hegedűs, M., Kovács, Z., Vasarhelyi, L., Kukovecz, A., Illés, L., Szász, N., … K.Kis, V. (2025). Ribbon-like hypomineralization in human dental enamel. *ACTA BIOMATERIALIA*, *196*, 281–292. http://doi.org/10.1016/j.actbio.2025.02.064
67. Horváth, A., Nemeth, M., Beck, A., Olasz, D., Serényi, M., & Sáfrán, G. (2025). Dramatic interference of Au TEM grid with model and supported MoNi/MgO catalysts during high temperature reduction and methane decomposition. *MATERIALS TODAY NANO*, *32*. http://doi.org/10.1016/j.mtnano.2025.100690
68. Horváth, R., Porkoláb, G., Magyaródi, B., Rajmon, I., Kovács, K., Kanyó, N., … Deli, M. (2025). LABEL-FREE BIOPHYSICAL TOOLS FOR CELLULAR ADHESION, BIOMECHANICS, AND SINGLE-CELL INJECTION.
69. Horvat, M., Kovács, K. V., & Lazar, J. M. (2025). Microstructures of feldspar crystals from Pakra Creek valley granite (Papuk Mt., Croatia). *GEOLOGIA CROATICA*, *78*(1), 45–60. http://doi.org/10.4154/gc.2025.06
70. Huang, Z.-Y., Qiu, W.-J., Wang, C.-H., Dong, Y., Daboczi, M., Shih, Y.-C., … Lin, C.-T. (2025). Reducing optical losses and enhancing charge extraction in Sn-Pb perovskite solar cells with a copolymer hole transport layer. *MATERIALS TODAY ENERGY*, *53*. http://doi.org/10.1016/j.mtener.2025.101979
71. Illés, B., Skwarek, A., Hurtony, T., Krammer, O., Medgyes, B., Szostak, K., … Pécz, B. (2025). Risk of transition to lead-free in the space sector: Sn whisker growth in thermal vacuum conditions from submicron Sn layer. *MATERIALS AND DESIGN*, *250*. http://doi.org/10.1016/j.matdes.2025.113637
72. Itatani, M., Holló, G., Albanese, P., Valletti, N., Kurunczi, S., Horvath, R., … Lagzi, I. (2025). Temporal pH waveforms generated in an enzymatic reaction network in batch and cell-sized microcompartments. *CELL REPORTS PHYSICAL SCIENCE*, *6*(1). http://doi.org/10.1016/j.xcrp.2024.102367
73. Jafer, T. A. O., Abdelbagi, H. A. A., Sulyok, A., Radnóczi, G. Z., Tőkési, K., & Malherbe, J. B. (2025). Highly oriented pyrolytic graphite chemical bonding structure after gallium implantation. *SCIENTIFIC REPORTS*, *15*(1). http://doi.org/10.1038/s41598-025-20624-3
74. Jakab, G., Dévény, Z., Vancsik, A., Sulyok, A., Frey, K., Karlik, M., … Szalai, Z. (2025). The role of minerals in fractionated soil organic matter stabilization in the subsoil. In *European Geosciences Union General Assembly 2025 (EGU25)*. http://doi.org/10.5194/egusphere-egu25-9221
75. Jiang, L.-L., Li, Y.-M., Li, W.-J., & Szolnoki, A. (2025). Combined effect of incentives and coupling in multigames in two-layer networks. *JOURNAL OF PHYSICS - COMPLEXITY*, *6*(1). http://doi.org/10.1088/2632-072X/ada844
76. Juhász, R., & Ódor, G. (2025). Finite-size scaling and dynamics in a two-dimensional lattice of identical oscillators with frustrated couplings. *CHAOS*, *35*(5). http://doi.org/10.1063/5.0247843
77. Juhász, Z. (2025). Zenei ősnyelvek nyomai a magyar népzenében. In *Sorsunk hálóiban* (pp. 401–457).

78. Kanyo, N., Borbely, K., Peter, B., Kovacs, K. D., Balogh, A., Magyaródi, B., … Horvath, R. (2025). Kinetic Analysis of SARS-CoV-2 S1-Integrin Binding Using Live-Cell, Label-Free Optical Biosensing. *BIOSENSORS*, *15*(8). http://doi.org/10.3390/bios15080534
79. Kanyó, N., Kovács, K. D., Balogh, A., Rajmon, I., Péter, B., Székács, I., … Horvath, R. (2025). Funkcionalizált arany nanorészecskék sejten belüli viselkedése FluidFM-alapú nanoinjekcióval.
80. Kanyó, N. (2025). Single-cell adhesion analysis using integrated single-cell optical biosensor and FluidFM force spectroscopy. In *Joint International Conference on Biosensors, Cancer, Women's Health, Microbiology & Advanced Medicines* (pp. 43–43).
81. Kaou, M. H., Balázsi, C., & Balázsi, K. (2025). Structural and Morphological Investigation of Calcium-Silicate-Based Bioceramics Prepared from Eggshell via Conventional Approach. *INORGANICS*, *13*(2). http://doi.org/10.3390/inorganics13020043
82. Kertész, K., Piszter, G., Vértesy, Z., Bálint, Z., & Biró, L. P. (2025). Színek harmóniája: a boglárkalepkék szerkezeti kék színének fajfelismerési szerepe. In *Lepkétől a fotonikus kristályig* (pp. 37–52).
83. Kirti, M., Sütő, M., Tóvári, E., Makk, P., Prok, T., Csonka, S., … Biasiol, G. (2025). Optimization of In-Situ Growth of Superconducting Al/InAs Hybrid Systems on GaAs for the Development of Quantum Electronic Circuits. *MATERIALS*, *18*(2). http://doi.org/10.3390/ma18020385
84. Kiss, Á. R., Sallai, I., Béres, B., Szittner, Z., Bonyár, A., & Horváth, R. (2025a). Multiplex jelöléses biofizikai módszereken és jelölésmentes bioszenzoros vizsgálatokon alapuló eljárás fejlesztése humán leukociták klasszifikációjára.
85. Kiss, Á. R., Sallai, I., Béres, B., Szittner, Z., Bonyár, A., & Horváth, R. (2025b). Multiplex jelöléses biofizikai módszereken és jelölésmentes bioszenzoros vizsgálatokon alapuló eljárás fejlesztése humán leukociták klasszifikációjára. In *XXXVIII. Neumann Kollokvium Tudományos Közlemények* (pp. 184–189).
86. Kiss, E., Bulátkó, A., Kozma, J., Krafcsik, O., Kubinyi, M., Kamarás, K., & László, K. (2025). Binding characteristics of fluorescent probes to pillararene modified graphene oxide nanosheets and their implications for indicator displacement assays. *COLLOIDS AND SURFACES A : PHYSICOCHEMICAL AND ENGINEERING ASPECTS*, *723*. http://doi.org/10.1016/j.colsurfa.2025.137341
87. Kis, V. K., Schwarcz, H. P., Nassif, N., & Szekanecz, Z. (2025). Bone mineral platelets are mesocrystals formed by monoclinic nanocrystals. *COMMUNICATIONS MATERIALS*, *6*(1). http://doi.org/10.1038/s43246-025-00890-4
88. Kolonits, T., Kugler, S., Nagy, A., Furi, P., Ambrus, R., Kheirandish, S., … Farkas, A. (2025). Effect of non-spherical shape of dry powder aerosol drugs on their airway deposition distribution. *INTERNATIONAL JOURNAL OF PHARMACEUTICS*, *671*. http://doi.org/10.1016/j.ijpharm.2025.125209
89. Kong, D., Kovács, A., Charilaou, M., Altthaler, M., Prodan, L., Tsurkan, V., … Dunin-Borkowski, R. E. (2025). Strain Engineering of Magnetic Anisotropy in the Kagome Magnet Fe_3Sn_2. *ACS NANO*, *19*(8), 8142–8151. http://doi.org/10.1021/acsnano.4c16603
90. Kovacs, B., Novak, S., Sallai, I., Magyarodi, B., Szekacs, I., Selmeczi, D., … Horvath, R. (2025). Robotic manipulations of single cells using a large-volume piezoelectric micropipette with nanoliter precision. *COLLOIDS AND SURFACES B: BIOINTERFACES*, *256*. http://doi.org/10.1016/j.colsurfb.2025.114972
91. Kovács, D., Deák, A., & Zámbó, D. (2025). Spatial distribution of photoexcited electrons and holes in Cu2O/Au multicomponent nanoparticles. In *Symposium on Materials Science 2024* (pp. 16–20).
92. Kovács, D., Radnóczi, G. Z., Horváth, Z. E., Frey, K., Sulyok, A., Fogarassy, Z., … Zámbó, D. (2025). Photoassisted Chemical Transformation of Cu2O Nanooctahedra into Cu2S Quantum-Dot Superstructures: Structural and Photoelectrochemical Properties. *ACS MATERIALS AU*, *5*(6), 1018–1028. http://doi.org/10.1021/acsmaterialsau.5c00106
93. Kovács, K. D., Visnovitz, T., Gerecsei, T., Peter, B., Kurunczi, S., Koncz, A., … Horvath, R. (2025). Nanoinjection of extracellular vesicles to single live cells by robotic fluidic force microscopy.
94. Kovacs, K. D., Beres, B., Kanyo, N., Szabó, B., Peter, B., Bősze, S., … Horvath, R. (2025). Single-cell classification based on label-free high-resolution optical data of cell adhesion kinetics.
95. Kurbonov, S., Pisárčik, M., Lukáč, M., Czigány, Z., Kovács, Z., Tolnai, I., … Almásy, L. (2025). Ordered Mesoporous Silica Prepared with Biodegradable Gemini Surfactants as Templates for Environmental Applications. *MATERIALS*, *18*(4). http://doi.org/10.3390/ma18040773
96. Kurbonov, S., Czigàny, Z., Kovács, Z., Péter, L., Pisárčik, M., Lukáč, M., … Almásy, L. (2025). Structural Characterization of Ordered Mesoporous Silica Prepared by a Sol–Gel Process Using Urea-Based Cationic Gemini Surfactants. *GELS (BASEL)*, *11*(10). http://doi.org/10.3390/gels11100804
97. Lábadi, Z., Taha Ismaeel, N., Petrik, P., & Fried, M. (2025b). Perspective Chapter: Electrochromic Efficiency in TixMe(1-x)Oy Type Mixed Metal-Oxide Alloys. In *Titanium Dioxide - Uses, Applications, and Advances*. http://doi.org/10.5772/intechopen.1008197

98. Lábadi, Z., Ismaeel, N. T., Petrik, P., & Fried, M. (2025). Optimization of SnO2/ZnO Films for Electrochromic Coloration Efficiency. In *Symposium on Materials Science 2024* (pp. 7–10).
99. Lábadi, Z., Taha Ismaeel, N., Petrik, P., & Fried, M. (2025a). Electrochromic Efficiency in AxB(1−x)Oy-Type Mixed Metal Oxide Alloys. *INTERNATIONAL JOURNAL OF MOLECULAR SCIENCES*, *26*(8). http://doi.org/10.3390/ijms26083547
100. Lengyel, A., Gracheva, M. A., Chumakov, A. I., Bessas, D., Sajti, S., Deák, A., … Merkel, D. G. (2025). Investigation of metamagnetic transition in nanosized FeRh structures. *VACUUM*, *240*. http://doi.org/10.1016/j.vacuum.2025.114533
101. Ling, T., Li, Z., Feng, M., & Szolnoki, A. (2025). Supervised cooperation on interdependent public goods games. *APPLIED MATHEMATICS AND COMPUTATION*, *492*. http://doi.org/10.1016/j.amc.2024.129249
102. Luo, J., Lin, D., Chen, X., & Szolnoki, A. (2025). Evolutionary dynamics of continuous public goods games in structured populations. *CHAOS*, *35*(4). http://doi.org/10.1063/5.0262821
103. Magyaródi, B., Kovács, K. D., Balogh, A., Szabó, I., Bősze, S., Vonderviszt, F., … Horváth, R. (2025). A PHSRN szinergiapeptid sejtadhézióra gyakorolt hatásának valós idejű vizsgálata jelölésmentes optikai bioszenzorral.
104. Magyaródi, B., Kovács, K. D., Balogh, A., Szabó, I., Vonderviszt, F., Székács, I., … Horváth, R. (2025). Investigation of the effect of the PHSRN synergy peptide on cell adhesion using real-time label-free technologies.
105. Maidebura, Y. E., Mansurov, V. G., Malin, T. V., Aleksandrov, I. A., Zhuravlev, K. S., & Pecz, B. (2025). Polytypism phenomenon in GaN nanocrystals grown on a van der Waals surface. *CRYSTENGCOMM*, *27*(15), 2307–2316. http://doi.org/10.1039/d4ce01154f
106. Márk, G. I., Szendrő, M., Mayer, A., Simon, Z., & Vancsó, P. (2025). Robust reflection asymmetry across rhombohedral—Bernal stacking boundaries in trilayer graphene. *CARBON TRENDS*, *21*. http://doi.org/10.1016/j.cartre.2025.100589
107. Márk, G. I., Bálint, Z., Kertész, K., Vértesy, Z., & Biró, L. P. (2025). A biológiai eredetű fotonikus kristályok csodái. In *Lepkétől a fotonikus kristályig* (pp. 23–32).
108. Mukherjee, D., Kertész, K., Zolnai, Z., Kovács, Z., Deák, A., Pálinkás, A., … Petrik, P. (2025). Optimized Sensing on Gold Nanoparticles Created by Graded-Layer Magnetron Sputtering and Annealing. In *Symposium on Materials Science 2024* (pp. 36–39).
109. Mukherjee, D., Kertész, K., Zolnai, Z., Kovács, Z., Deák, A., Pálinkás, A., … Petrik, P. (2025). Optimized Sensing on Gold Nanoparticles Created by Graded-Layer Magnetron Sputtering and Annealing. *SENSORS AND ACTUATORS B-CHEMICAL*, *425*. http://doi.org/10.1016/j.snb.2024.136875
110. Mukherjee, D., Burger, S., Siefke, T., Gour, J., Bodermann, B., & Petrik, P. (2025). Spectroscopic Ellipsometry of Plasmonic Gratings-Ideal Parameters for Sensing and Subpicometer Measurement Uncertainty. *ACS OMEGA*, *10*(14), 14466–14473. http://doi.org/10.1021/acsomega.5c00951
111. Mukherjee, D. (2025). *Low-Dimensional Nanostructures for the Optical Sensing of Biomolecules and Gases*. Óbudai Egyetem.
112. Nagy, N. (2025). Determination of solid-liquid adhesion work in a direct and absolute manner by the Capillary Bridge Probe. In *Symposium on Materials Science 2024* (pp. 33–35).
113. Nanbakhsh, K., Shah, I. A., Lamont, C., Dücső, C., Akgun, Ö. C., Horváth, D., … Giagka, V. (2025). Author Correction: On the longevity and inherent hermeticity of silicon-ICs: evaluation of bare-die and PDMS-coated ICs after accelerated aging and implantation studies (Nature Communications, (2025), 16, 1, (12), 10.1038/s41467-024-55298-4). *NATURE COMMUNICATIONS*, *16*(1). http://doi.org/10.1038/s41467-025-57175-0
114. Nanbakhsh, K., Shah Idil, A., Lamont, C., Dücső, C., Akgun, Ö. C., Horváth, D., … Giagka, V. (2025). On the longevity and inherent hermeticity of silicon-ICs: evaluation of bare-die and PDMS-coated ICs after accelerated aging and implantation studies. *NATURE COMMUNICATIONS*, *16*(1). http://doi.org/10.1038/s41467-024-55298-4
115. Nemes-Incze, P. (2025). Electron correlation strengthened in multilayer rhombohedral graphite. *NATURE NANOTECHNOLOGY*, *20*(2), 187–188. http://doi.org/10.1038/s41565-024-01839-3
116. Nouri, M., Olivero, P., Kroker, S., Käseberg, T., Ruo-Berchera, I., Bodermann, B., … Petrik, P. (2025). Resolution enhancement methods in optical microscopy for dimensional optical metrology. *JOURNAL OF THE EUROPEAN OPTICAL SOCIETY-RAPID PUBLICATIONS*, *21*(1). http://doi.org/10.1051/jeos/2025002
117. Novák, S., Sallai, I., Szittner, Z., Bonyár, A., & Horváth, R. (2025). Ellenanyag-közvetített immunsejt-adhézió vizsgálata különböző biofizikai módszerekkel.

118. Nugusse, B., Juhász, G., Major, C., Petrik, P., Kálvin, S., Horváth, G. Z., & Fried, M. (2025). Optical calibration of the ellipsometric mapping tool from cheap parts. In *Symposium on Materials Science 2024* (pp. 26–32).
119. Olasz, D., Sáfrán, G., & Serényi, M. (2025). A guide to the reactive HiPIMS co-sputtering of Y and Ti. In *Symposium on Materials Science 2024* (pp. 11–15).
120. Ollár, T., Vancsó, P., Kun, P., Koós, A., Dobrik, G., Sukhanova, E., … Tapasztó, L. (2025). Semiconducting Pt Structures Stabilized on 2D MoS2 Crystals Enable Ultrafast Hydrogen Evolution. *ADVANCED MATERIALS*, *37*(37). http://doi.org/10.1002/adma.202504113
121. Omondi, A. S., Kovács, D., Deák, A., & Zámbó, D. (2025). On the inevitable role of shape in engineering porous multimetallic nanoparticles for catalytic applications. In *Symposium on Materials Science 2024* (pp. 21–25).
122. Omondi, A., Kovacs, D., Radnoczi, G., Horvath, Z., Tolnai, I., Deak, A., & Zambo, D. (2025). Symmetry breaking enhances the catalytic and electrocatalytic performance of core/shell tetrametallic porous nanoparticles. *NANOSCALE*, *17*(1), 261–275. http://doi.org/10.1039/d4nr03589e
123. Osváth, Z., Pálinkás, A., Molnár, G., Kun, P., & Koós, A. A. (2025). Strain-induced modulation of the local conductance in MoS2 layers on gold nanoparticles. *SURFACES AND INTERFACES*, *74*. http://doi.org/10.1016/j.surfin.2025.107725
124. Panasci, S. E., Schilirò, E., Koos, A., Kutlu, T., Sahin, H., Roccaforte, F., … Giannazzo, F. (2025). Scalable growth of optically uniform MoWS2 alloys by sulfurization of ultrathin Mo/W stacks. *MATERIALS SCIENCE IN SEMICONDUCTOR PROCESSING*, *196*. http://doi.org/10.1016/j.mssp.2025.109648
125. Papp, I., & Zsukovszki, K. (2025). Particle simulation of various gold nanoantennas in laser-irradiated matter for fusion production. *EUROPEAN PHYSICAL JOURNAL-SPECIAL TOPICS*, *234*, 2993–2998. http://doi.org/10.1140/epjs/s11734-025-01563-6
126. Péter, B., Kurunczi, S., Szekacs, I., Bősze, S., M. Kovács, G., Boldizsár, I., & Horvath, R. (2025a). Label-free biosensing of lignan compounds applying engineered model surfaces.
127. Péter, B., Kurunczi, S., Szekacs, I., Bősze, S., M. Kovács, G., Boldizsár, I., & Horvath, R. (2025b). Label-free biosensing of lignan compounds for therapeutics.
128. Piszter, G., Kertész, K., Vértesy, Z., Jakab, E., Bálint, Z., & Biró, L. P. (2025). Lepkeszárnyakon található fotonikus nanoarchitektúrák gőzérzékelési tulajdonságai. In *Lepkétől a fotonikus kristályig* (pp. 53–60).
129. Piszter, G., Kertész, K., Bálint, Z., & Biró, L. P. (2025). Matematikai pontossággal látnak a lepkék. In *Lepkétől a fotonikus kristályig* (pp. 61–70).
130. Piszter, G., Kertész, K., Horváth, Z. E., Bálint, Z., & Biró, L. P. (2025). Ikarusz boglárka lepkék szerkezeti és pigment eredetű színeinek stresszállósága. In *Lepkétől a fotonikus kristályig* (pp. 71–80).
131. PYRCZ, T. W., BOYER, P., GARLACZ, R., FÅHRAEUS, C., ANDRADE-C., M. G., BÁLINT, Z., & MAHECHA-J., O. (2025). Out of the blue: a new blue Lymanopoda butterfly from the páramo of northern Colombia raises questions about disjunct distributions (Lepidoptera: Nymphalidae, Satyrinae). *ZOOTAXA*, *5659*(4), 547–564. http://doi.org/10.11646/zootaxa.5659.4.5
132. Racz, A. S., & Menyhard, M. (2025). Evaluation methods for XPS depth profiling; A review. *APPLIED SURFACE SCIENCE ADVANCES*, *30*. http://doi.org/10.1016/j.apsadv.2025.100872
133. Rahman, A., Raza, M. H., Hodovány, S., Ashfaq, R. K., Shah, J. S., Nyerges, B., … Ajtai, T. (2025). Photoacoustic-Driven Retrieval of Complex Refractive Indices for Absorbing Aerosols. *ANALYTICAL CHEMISTRY*, *97*(49), 27220–27227. http://doi.org/10.1021/acs.analchem.5c04788
134. Rajmon, I., Székács, I., Kovács, K. D., Porkoláb, G., Deli, M. A., & Horváth, R. (2025). Modulation and measurement of endothelial and epithelial barrier integrity by FluidFM.
135. Riesz, F. (2025a). Ancient magic mirrors: inspirations for modern science and technology. In *The 6th Makyoh Conversazione, 29-31 August, Osaka, Abstracts* (p. 8).
136. Riesz, F. (2025b). Curvature, illumination conditions and imaging properties in magic mirrors. In *The 6th Makyoh Conversazione, 29-31 August, Osaka, Abstracts* (p. 25).
137. Roccaforte, F., Vivona, M., Ethan Panasci, S., di Franco, S., Greco, G., Fiorenza, P., … Giannazzo, F. (2025). Effects of Sulfurization on the Properties of 4H-SiC Schottky Contacts. *MATERIALS SCIENCE FORUM*, *1159*, 1–7. http://doi.org/10.4028/p-j9hda2
138. Romanenko, A., Gharaibeh, A., Medgyes, B., & Petrik, P. (2025). Nanoscale monitoring of the initial stage of water condensation on a printed circuit board. *HELIYON*, *11*(2). http://doi.org/10.1016/j.heliyon.2025.e42117
139. Rózsa, P., Krafcsik, O., Czigány, Z., Lenk, S., Beke, D., & Gali, A. (2025). Thiolation and PEGylation of silicon carbide nanoparticles. *RESULTS IN CHEMISTRY*, *16*. http://doi.org/10.1016/j.rechem.2025.102337

140. Sallai, I., Szittner, Z., Béres, B., Novák, S., & Varga, S. (2025). Single live cell assays with label-free optical biosensor for the development of diagnostic methods. In *48th International Spring Seminar on Electronics Technology : Sustainable electronics for a circular economy* (pp. 170–171).
141. Sallai, I. (2025a). Az elektronikán túl, avagy modern technológiák az egyedi sejt szintű vizsgálatok szolgálatában – módosított atomierő mikroszkópia, a FluidFM nyújtotta lehetőségek.
142. Sallai, I., Szittner, Z., Béres, B., Kiss, Á., Plegányi, B., Székács, I., & Horvath, R. (2025). Development of advanced biophysical methods based on the use of label-free optical biosensors for immunodiagnostic and single cell level processes.
143. Sallai, I. (2025b). Single Live Cell Assays with Label-free Optical Biosensor for the Development of Diagnostic Methods. In *2025 International Spring Seminar on Electronics Technology (ISSE)*. http://doi.org/10.1109/ISSE65583.2025.11121062
144. Sallai, I. (2025c). Single live cell assays with label-free optical biosensor for the development of diagnostic methods.
145. Sallai, I., Novák, S., Szittner, Z., Bonyár, A., & Horváth, R. (2025). Humán leukocita aktiváció vizsgálata jelölésmentes bioszenzor alapú komplex biofizikai módszerekkel.
146. Sallai, I., Szittner, Z., Béres, B., Kiss, Á., Plegányi, B., Székács, I., … Horvath, R. (2025). Label-free single-cell profiling of antibody-induced leukocyte effector mechanisms via resonant waveguide grating biosensors.
147. Sallai, I., Váradi, C. B., Bonyár, A., & Horváth, R. (2025a). Egyedi sejtszintű vizsgálatok felületi plazmon rezonancia bioszenzorral.
148. Sallai, I., Váradi, C. B., Bonyár, A., & Horváth, R. (2025b). Egyedi sejtszintű vizsgálatok felületi plazmon rezonancia bioszenzorral. In *XXXVIII. Neumann Kollokvium Tudományos Közlemények* (pp. 200–206).
149. Sangiorgi, E., Madonia, A., Laurella, G., Panasci, S. E., Schilirò, E., Giannazzo, F., … Agnello, S. (2025). Mild Temperature Thermal Treatments of Gold-Exfoliated Monolayer MoS2. *NANOMATERIALS*, *15*(3). http://doi.org/10.3390/nano15030160
150. Scherübl, Z., Sütő, M., Kóti, D., Tóvári, E., Horváth, C., Kalmár, T., … Fülöp, G. (2025). Determination of the current-phase relation of an InAs 2DEG Josephson junction with a microwave resonator. *PHYSICAL REVIEW RESEARCH*, *7*(2). http://doi.org/10.1103/PhysRevResearch.7.023173
151. Scherübl, Z., Kocsis, M., Elalaily, T., Kupás, L., Berke, M., Fülöp, G., … Makk, P. (2025). Multimode Operation of a Superconducting Nanowire Switch in the Nanosecond Regime. *ACS NANO*, *19*(32), 29207–29215. http://doi.org/10.1021/acsnano.5c03718
152. Seravalli, L., Ugolotti, A., Bergamaschini, R., Bosi, M., Cora, I., Mezzadri, F., … Fornari, R. (2025). Supersaturation-Dependent Competition between β and κ Phases in the MOVPE Growth of Ga 2 O 3 on Al 2 O 3 (0001) and GaN (0001) Substrates. *ACS APPLIED MATERIALS & INTERFACES*, *17*(45), 62261–62276. http://doi.org/10.1021/acsami.5c13401
153. Shankar, L. S., Samaniego Andrade, S. K., László, K., Pászti, Z., Balázsi, K., Czigány, Z., … Kun, R. (2025). Corrigendum to "A fresh perspective to synthesizing and designing carbon/sulfur composite cathodes using supercritical CO2 technology for advanced Li-S battery cathodes" [J. Alloy. Compd. 1008 (2024) 176691] (Journal of Alloys and Compounds (2024) 1008, (S092583882403278X), (10.1016/j.jallcom.2024.176691)). *JOURNAL OF ALLOYS AND COMPOUNDS*, *1010*. http://doi.org/10.1016/j.jallcom.2024.177436
154. Shi, Z., Qin, W., Hu, Z., Ma, M., Liu, H., Shu, Z., … He, Y. (2025). Sub-2-nm-droplet-driven growth of amorphous metal chalcogenides approaching the single-layer limit. *NATURE MATERIALS*, *24*(8), 1186–1194. http://doi.org/10.1038/s41563-025-02273-z
155. Silva, C., Borbáth, I., Dodony, E., Olasz, D., Sáfrán, G., Szegedi, Á., … Pászti, Z. (2025). Stability enhancement of molybdenum modified rutile – carbon composite supported platinum electrocatalysts by reductive pretreatment: Surface characteristics and advanced electrocatalytic properties. *MATERIALS RESEARCH BULLETIN*, *182*. http://doi.org/10.1016/j.materresbull.2024.113114
156. Silva, C., Pászti, Z., Salmanzade, K., Olasz, D., Dodony, E., Sáfrán, G., … Borbáth, I. (2025). Advanced Pt/Ti(1−x)SnxO2–C Composite Supported Electrocatalyst with Functionalized Carbon for Sustainable Energy Conversion Technologies. *NANOMATERIALS*, *15*(5). http://doi.org/10.3390/nano15050342
157. Solymosi, G. T., Kis, T., Fürjes, P., & Gyurcsányi, R. E. (2025). Absence of Hofmeister Selectivity in Hydrophobic Ion-Exchanger Nanopores. *ANALYTICAL CHEMISTRY*, *97*(49), 27289–27297. http://doi.org/10.1021/acs.analchem.5c05239
158. Stift, M. K., Bonyár, A., Lábadi, Z., Jankovics, H., Vonderviszt, F., & Petrik, P. (2025c). Optical and Electrochemical Sensing with Gold Nanoparticles. In *2025 International Spring Seminar on Electronics Technology (ISSE)*. http://doi.org/10.1109/ISSE65583.2025.11121059
159. Stift, M. K., Bonyár, A., Lábadi, Z., & Petrik, P. (2025). Optical and Electrochemical Sensing with Gold Nanoparticles.

160. Stift, M. K., Bonyár, A., Lábadi, Z., Jankovics, H., Vondervisztt, F., & Petrik, P. (2025b). Heavy Metal Sensing Based on Electrochemically Grown Gold Nanostructure and Genetically Modified Flagellar Filaments. In *48th International Semiconductor Conference, CAS 2025* (pp. 363–366). http://doi.org/10.1109/CAS66707.2025.11222253
161. Stift, M. K., Bonyár, A., Lábadi, Z., Jankovics, H., Vondervisztt, F., & Petrik, P. (2025a). Genetikailag módosított fehérjéken alapuló nehézfémion-érzékelés. In *XXXVIII. Neumann Kollokvium Tudományos Közlemények* (pp. 72–77).
162. Szabó, G. (2025). Az evolúciós játékelmélet és a statisztikus fizika összefonódása. *FIZIKAI SZEMLE*, *75*(4), 135–140.
163. Szabó, G., & Király, B. (2025b). Orthogonal elementary interactions for bimatrix games. *PHYSICA A - STATISTICAL MECHANICS AND ITS APPLICATIONS*, *677*. http://doi.org/10.1016/j.physa.2025.130920
164. Szabó, G., & Király, B. (2025a). Derivation of potential for group interactions in evolutionary games. *PHYSICAL REVIEW E: COVERING STATISTICAL NONLINEAR BIOLOGICAL AND SOFT MATTER PHYSICS (2016-)*, *112*(6). http://doi.org/10.1103/nhxn-6zqf
165. Szabó, Z., Beiler, B., & Baji, Z. (2025). Broadband InGaAsP/InP NIR LEDs based on multiple photon-recycling photoluminescent layers. *JOURNAL OF CRYSTAL GROWTH*, *652*. http://doi.org/10.1016/j.jcrysgro.2024.128045
166. Szakolczai, K. (2025). *EK MFA Yearbook 2024*. (K. Szakolczai, Ed.). Budapest: HUN-REN EK MFA.
167. Szathmári, B., Hessz, D., Zámbó, D., Bruhn, C., Pietschnig, R., Udvardy, A., … Kelemen, Z. (2025). Carborane-Decorated Siloles with Highly Efficient Solid-State Emissions – What Drives the Photophysical Properties? *CHEMISTRY-A EUROPEAN JOURNAL*, *31*(16). http://doi.org/10.1002/chem.202404462
168. Szentpéteri, B., Márffy, A., Kedves, M., Tóvári, E., Fülöp, B., Kükemezey, I., … Makk, P. (2025). Increasing the proximity-induced spin-orbit coupling in bilayer graphene / WSe 2 heterostructures with pressure. *PHYSICAL REVIEW B*, *111*(20). http://doi.org/10.1103/PhysRevB.111.205415
169. Szilágyi, V., Furholt, K., Kovács, Z., Harsányi, I., Osztás, A., & Szakmány, G. (2025). “Whitestone”—A Specific Polished Stone Tool Raw Material in the Late Neolithic of Southern Hungary. *HERITAGE*, *8*(3). http://doi.org/10.3390/heritage8030112
170. Szomor, Z., Gyimah, N., Pardy, T., & Fürjes, P. (2025). Three-dimensional finite element modelling of chemical environment in droplet-based microfluidic systems for drug therapy applications. *PHYSICS OF FLUIDS*, *37*(7). http://doi.org/10.1063/5.0275809
171. Szomor, Z., Bató, L., Hakkel, O., Dücső, C., Baji, Z., Sulyok, A., … Fürjes, P. (2025). Characterisation of Titanium-Oxide Thin Films for Efficient pH Sensing in Low-Power Electrochemical Systems. *SENSORS*, *25*(19). http://doi.org/10.3390/s25196113
172. Szomor, Z., Pardy, T., & Fürjes, P. (2025). 3D Modelling of Mass and Heat Transport in Multi-Phase Microfluidic Systems. In *2025 31st International Workshop on Thermal Investigations of ICs and Systems (THERMINIC)*. http://doi.org/10.1109/THERMINIC65879.2025.11216952
173. Szomor, Z., Bereczki, D., & Fürjes, P. (2025). Cseppek mikrofluidikai rendszerben. *FIZIKAI SZEMLE*, *75*(12), 410–415.
174. Taaev, T. A., Komlev, A. S., Merkel, D. G., Radnoczi, G. Z., Chirkova, A., Wu, Y., … Schäfer, R. (2025). Surface properties of ferromagnetic phase nuclei in the Fe48Rh52 alloy. *JOURNAL OF ALLOYS AND COMPOUNDS*, *1040*. http://doi.org/10.1016/j.jallcom.2025.183425
175. Tapasztó, L. (2025). Grafénba zárt fény. *FIZIKAI SZEMLE*, *75*(3), 100–103.
176. Tarjányi, T., Gulyás, G., Bali, K., Sámi, M., Kiss, R. A., Beiler, B., … Szabó, T. (2025). Nanoindentation Analysis of SU-8 Coated Wafers at Different Baking Phases. *POLYMERS*, *17*(24). http://doi.org/10.3390/polym17243337
177. Tóbi, C., Khánh, N. Q., Homonnay, Z., & Széles, É. (2025). Applicability of atomic force microscopy for nuclear forensic examination. *JOURNAL OF RADIOANALYTICAL AND NUCLEAR CHEMISTRY*, *334*(1), 753–761. http://doi.org/10.1007/s10967-024-09803-0
178. Tolnai, I., Osan, J., Jovari, P., Pinakidou, F., Sulyok, A., & Fabian, M. (2025). Structural characterization of uranium and lanthanide loaded borosilicate glass matrix. *SCIENTIFIC REPORTS*, *15*(1). http://doi.org/10.1038/s41598-025-13166-1
179. Varga, D. S., Sallai, I., Csippa, B., Bonyár, A., Dér, A., & Horváth, R. (2025). OPTICAL BIOSENSOR-BASED INVESTIGATION OF CANCER CELL ADHESION UNDER SHEAR STRESS AND GLYCOCALYX DIGESTION.
180. Varga, D. S., Sallai, I., Vigh, J., Kocsis, A., Kincses, A., Csippa, B., … Dér, A. (2025a). The interface role of the glycocalyx.

181. Varga, D. S., Sallai, I., Vigh, J., Kocsis, A., Kincses, A., Csippa, B., … Dér, A. (2025b). The interface role of the glycocalyx in barrier integrity and cell adhesion.
182. Varga, D. S., Sallai, I., Vigh, J., Kocsis, A., Csippa, B., Székács, I., … Dér, A. (2025). Combining microfluidics, spectroscopy, and dynamic biosensing to decode glycocalyx function.
183. Vrána, L., Stasiak, T., Fekete, M., Buršíková, V., Czigány, Z., Balázsi, K., & Souček, P. (2025). Effects of nitrogen content on microstructure and mechanical properties of DC magnetron sputtered Cr-Mn-Mo-Si-Y-(N) high entropy coatings. *SURFACE AND COATINGS TECHNOLOGY*, *497*. http://doi.org/10.1016/j.surfcoat.2025.131742
184. Wang, C., Zhang, W., Wang, X., & Szolnoki, A. (2025). Inter-role reciprocity in evolutionary trust game on square lattices. *CHAOS*, *35*(8). http://doi.org/10.1063/5.0285064
185. Wang, L., Hua, S., Liu, Y., Lu, Z., Zhang, L., Liu, L., & Szolnoki, A. (2025). Strategic competition in informal risk-sharing mechanisms versus collective index insurance. *JOURNAL OF THE ROYAL SOCIETY INTERFACE*, *22*(228). http://doi.org/10.1098/rsif.2025.0163
186. Wang, Q., Chen, X., He, N., & Szolnoki, A. (2025). Evolutionary Dynamics of Population Games With an Aspiration-Based Learning Rule. *IEEE TRANSACTIONS ON NEURAL NETWORKS AND LEARNING SYSTEMS*, *36*(5), 8387–8400. http://doi.org/10.1109/TNNLS.2024.3439372
187. Wang, Q., Chen, X., & Szolnoki, A. (2025a). Coevolutionary dynamics of feedback-evolving games in structured populations. *CHAOS SOLITONS & FRACTALS*, *193*. http://doi.org/10.1016/j.chaos.2025.116070
188. Wang, Q., Chen, X., & Szolnoki, A. (2025b). Evolutionary dynamics in state-feedback public goods games with peer punishment. *CHAOS*, *35*(4). http://doi.org/10.1063/5.0268194
189. Wójcicka, A., Fogarassy, Z., Kravchuk, T., Kamińska, E., Perlin, P., Grzanka, S., & Borysiewicz, M. A. (2025). A new approach to N-polar n-GaN surface treatment for room-temperature transparent ohmic contact formation. *MATERIALS SCIENCE IN SEMICONDUCTOR PROCESSING*, *187*. http://doi.org/10.1016/j.mssp.2024.109135
190. Xie, K., & Szolnoki, A. (2025). Reputation in public goods cooperation under double Q -learning protocol. *CHAOS SOLITONS & FRACTALS*, *196*. http://doi.org/10.1016/j.chaos.2025.116398
191. Yue, H., Xiong, X., Feng, M., & Szolnoki, A. (2025a). Coevolution of relationship-driven cooperation under recommendation protocol on multiplex networks. *CHAOS SOLITONS & FRACTALS*, *190*. http://doi.org/10.1016/j.chaos.2024.115753
192. Yue, H., Xiong, X., Feng, M., & Szolnoki, A. (2025b). Dynamic evolution of cooperation based on adaptive reputation threshold and game transition. *CHAOS SOLITONS & FRACTALS*, *199*. http://doi.org/10.1016/j.chaos.2025.116693
193. Zhang, Y., Feng, M., Kurths, J., & Szolnoki, A. (2025). Evolutionary Dynamics Based on Reputation in Networked Populations with Game Transitions. *IEEE Transactions on Signal and Information Processing over Networks*, *11*, 1557–1568. http://doi.org/10.1109/TSIPN.2025.3636748
194. Zhou, X. H., Gong, J. M., Li, Z., Sulyok, A., Menyhard, M., Harada, Y., … Ding, Z. J. (2025). Optical Properties of Terbium, Gadolinium, and Samarium Extracted from Reflection Electron Energy Loss Spectroscopy Spectra. *JOURNAL OF PHYSICAL CHEMISTRY C*, *129*(13), 6524–6534. http://doi.org/10.1021/acs.jpcc.5c00770
195. Zsukovszki, K., & Papp, I. (2025). Numerical analysis of ionization and plasmonic phenomena on gold nanodopes upon laser pulse irradiation. *RESULTS IN PHYSICS*, *72*. http://doi.org/10.1016/j.rinp.2025.108198
196. Zsukovszki, K., & Papp, I. (2025a). Comparative analysis of optical absorption and resonating dynamics of nanoantenna dopes at intense laser shots. *EUROPEAN PHYSICAL JOURNAL-SPECIAL TOPICS*, *234*, 3021–3028. http://doi.org/10.1140/epjs/s11734-025-01521-2
197. Zsukovszki, K., & Papp, I. (2025b). Ionization Dynamics in Matter with Gold Nanoparticles upon Laser Irradiation of Various Intensities, Numerical Analysis. *PARTICLES*, *8*(1). http://doi.org/10.3390/particles8010027
198. Zsukovszki, K., & Papp, I. (2025c). Ionization of matter with resonating nanoantennas under intense laser irradiation — Numerical study. *RADIATION PHYSICS AND CHEMISTRY: THE JOURNAL FOR RADIATION PHYSICS RADIATION CHEMISTRY AND RADIATION PROCESSING*, *237*. http://doi.org/10.1016/j.radphyschem.2025.113111
199. Zsukovszki, K., & Papp, I. (2025). Enhanced Energy Transfer in Resonating Gold Doped Matter Irradiated by Infrared Laser. *PARTICLES*, *8*(4). http://doi.org/10.3390/particles8040104

LIST OF FIGURES

Figure 1. (a) Schematic image of the n-alkane self-assembled monolayer stemming from ambient air contamination. When measuring the surface by scanning tunnelling microscopy (STM) the tip can either scan above the layer or penetrate it. (b) STM image at the largest tip – sample separation showing the structure of the alkane overlayer. (c-d) Atomic resolution images of the contaminated surface (penetrating the alkane layer), show consistently larger current noise. (e) Comparison of the contaminated and clear graphite surface tunnelling conductance. The clean surface displays a clear phonon-gap. (f) Examples of I(z) curves on clean, contaminated graphite and gold samples, by measuring the tunnelling current as the tip is retracted. The contaminated samples systematically show an anomalously low decay rate of the tunnelling current. 23

Figure 2. Topographic STM images of a) a reconstructed TBG superlattice of ~65 nm periodicity, corresponding to twist angle of ~0.21º, fabricated by the conventional tear-and-stack method and b) an unreconstructed giant (65 nm) TBG superlattice formed through the graphene auto-kirigami process. Tunneling spectra recorded on the bright (AA) and dark (AB/BA) regions of the reconstructed (c), and unreconstructed (d) 0.21º MATBG superlattices, the latter displaying sharper (FWHM ~ 90 meV) LDOS peak near the Fermi level on both AA and AB/BA regions, while a less intense and much broader (FWHM ~ 180 meV) peak ias observed only in the AA regions of the reconstructed superlattice. 25

Figure 3. Center panel shows the AFM topography of a 0.7º twisted bilayer graphene sample prepared by the tear-and-stack method with alkane intercalant layer, displaying a large (5x5 μm^2) bubble-free area near the center of the image, next to areas showing the presence of bubbles. Conductive AFM images of the areas with bubbles (right) display a reconstructed superlattice of 20 nm periodicity. By contrast, the bubble-free area preserving the alkane intercalant layer, displays and unreconstructed 20 nm superlattice (left). We have also found that intercalated TBG superlattices are not only free of structural reconstructions but are also characterized by reduced twist-angle inhomogeneity, enabling the fabrication of uniform moiré superlattices on device-scale, a critical step toward reproducible twistronic devices. 26

Figure 4. (a) Schematic illustration of the STM measurement on RG – hexagonal junctions. The hexagonal side of the sample is a 6-layer RG, with a hexagonal stacking fault at the top, denoted by the "-1" layer orientation of the top layer. (b, c) Measured and calculated LDOS of the RG and hexagonal side of the sample. The sample features hexagonal nanoribbon regions of a few 10 nm widths. One example is shown in panels (d - i), where we show the tunnelling conductance of the same area at various sample bias voltages. Ripples in the local tunnelling conductance can be observed in the hexagonal region bordered by two domain walls. The tunnelling conductance is a measure of the local density of states (LDOS) at the surface. The LDOS ripples shown by $\Delta\lambda$ are only present in the middle hexagonal region. 27

Figure 5. (a) dI/dV measurement across a RG – hexagonal – RG nanoribbon. The tunnelling conductance (dI/dV) is numerically differentiated along the bias voltage coordinate for better visibility of the intravalley scattering pattern. (b) Calculated local density of states (LDOS) of the top surface of the same nanoribbon geometry as in the measurement in (a). (c) Zoom into the dI/dV spectra in panel (b), highlighting the interference pattern arising in the hexagonal part of the sample. The scattering wavelength ($\Delta\lambda$) can be measured as the distance between peaks of the dI/dV signal across the sample surface. (d) From the bias voltage dependent $\Delta\lambda$ values we can obtain the scattering wave vector (Δk), which we overlay onto the surface Dirac band of the hexagonal |1, 1, 1, 1, -1| structure. 28

Figure 6. (a) Raman spectra of MoS_2 grown by CVD on G7 and G15 graphite layers. (b) Mapping of Raman peak intensity at 408 cm^{-1} for the G15/MoS_2 sample. (c) Current density–voltage scans of MoS_2 grown on different graphite substrates, recorded in an electrochemical cell in aqueous 0.5 M H_2SO_4 electrolyte. (d) Current density–voltage scans of G15/MoS_2 samples loaded by commercial Pt/C and ultralow amount of electrodeposited Pt (2L-Pt), recorded in aqueous 1 M NaOH electrolyte. 29

Figure 7. (a) Current density–voltage scans recorded in three-electrode PEC setup for perovskite photocathodes with device design changing from larger (red) towards optimised, smaller active area (yellow and green). (b) Chronoamperometric measurement of a perovskite photocathode at 0 V_{RHE} applied. Shaded areas indicate switching off illumination. (c) Current density–voltage scans recorded in two-electrode PEC setup for a perovskite photocathode. (d) Bias-free operation of the perovskite photocathode for simultaneous hydrogen evolution and glycerol oxidation. All measurements were performed in dark (dashed lines) or under 1 sun illumination (solid lines) in aqueous 2 M NaOH electrolyte containing 20 wt% glycerol. 30

Figure 8. (a) TUNA AFM topography and (**b**)–(**d**) tunneling current images of monolayer MoS_2 covering Au NPs. The current maps overlap with the topographic images. The dashed white line marks the few-layer/monolayer MoS_2 boundary. The tunneling current maps were measured at bias voltages (U) of 2 V (b), 4 V (c) and 6 V (d). 31

Figure 9. TUNA AFM tunneling current maps (overlapped with the topography) measured on a multilayer MoS_2, using bias voltages (U) of 1 V (**a**), 1.5 V (**b**), 3 V (**c**), and 4 V (**d**). 32

Figure 10. Scanning electron microscopy images of bioinspired ZnO nanostructures: (a) unmodified, pure ZnO; (b) ZnO-based sample doped with 10 wt% graphite nanoparticles. 33
Figure 11. Photocatalytic performance of bioinspired ZnO nanostructures. The photodegradation rate of methyl orange dye was measured as a function of different additives and their concentrations. 34
Figure 12. (left) Directly measured adhesion work values as a function of contact angles determined during the same capillary bridge probe (CBP) measurement. The inset shows the result of the fit of a general cosine function to all measurement points. The fitted purple curve is in excellent agreement with the theoretical dashed green curve corresponding to the Young–Dupré equation. For this validation, metal, semiconductor, dielectric, and polymer surfaces were measured in clean, contaminated, acid-, and plasma-treated condition using ultrapure water as test liquid. (right) Work of adhesion values measured by capillary bridge probe (CBP) as a function of water contact angles determined by the sessile drop (SD) method. The purple dashed line represents the theoretical prediction of the Young–Dupré equation. 38
Figure 13. Schematics on the synthesis of Cu2O nanooctahedra and their photoassisted chemical transformation to Cu2S quantum-dot superstructures. [1] 39
Figure 14. Evolution of the extinction spectrum upon increasing the concentration of BME (a). SEM image and TEM elemental map of the Cu2S particles (b). [Ref.7] 40
Figure 15. Phase identification (a-e) and electrochemical investigations (d-f) on the synthesized nanoparticles. [Ref.7] 41
Figure 16. Proposed mechanism of the Cu2O-Cu2S photoassisted transformation process. 41
Figure 17. Scanning probe microscopy derived topography of the indium tin oxide supported nanoprisms overlain with the adhesion force maps: no AMBI treatment a) and surface modification at 1 μm b), and 190.5 μm AMBI c). [Ref.10] 42
Figure 18. TEM images of the Cu2O/Au nanoparticles prepared without (upper row) and in the presence of AMBI (lower row). [Ref.10] 43
Figure 19. Au-evaporated silicon substrate (15 x 15 mm) before the electrochemical deposition treatments. 44
Figure 20. SEM image of the surface after electrochemical AuNP deposition and immobilization of engineered protein filaments. 45
Figure 21. Experimental arrangement for in-situ SE measurements in the electrochemical liquid cell. 46
Figure 22. Calculated CE data as a function of MoO3 fraction—3D graphical representation. 47
Figure 23. Amplitude of the k (extinction) parameter as a function of the position. 47
Figure 24. Dependence of the image contrast on local and global curvatures 48
Figure 25. Optical equivalence of a globally convex mirror and a flat mirror with point-source illumination 49
Figure 26. Ternary diagrams showing (a) the compositional variation, (b) refractive index (at 632.8 nm) and (c) optical gap of the four combinatorial samples with different N_2/Ar partial pressure ratios. The arrow in (a) represents decreasing oxygen flow rate during deposition, i.e. the direction from 0 mm to 20 mm. The dotted lines in (b) are the “iso refractive index” lines, while the black line is perpendicular to them. The (d) refractive index plotted as a function of the S parameter. 53
Figure 27. Depth distribution of measured changes in d-values together with changes in d-values of the Model. Blue=Normal component. Red=Lateral component. (α=0.24 mrad and L=264 mm). (a) as-impl $[110]^{\gamma}$; (b) 300C $[110]^{\gamma}$; (c) 700C $[110]^{\gamma}$; (d) as-impl $[001]^{\gamma}$. Deviations of the measured values (symbols) from the Model (lines) indicate presence of strain. Notice that the orientations are orthogonal in (a) and (d). 55
Figure 28. Variation of depth distribution of strain in samples with different heat treatment. (α=0.24 mrad and L=264 mm. Beam direction=sample orientation $[110]^{\gamma}$). Black square=as implanted. Blue circle=heat treated at 300 C. Red triangle=heat treated at 700 C. (a) Normal strain (in direction of $(020)^{\beta}||(440)^{\gamma}$). (b) Lateral strain (in direction of $(600)^{\beta}||(400)^{\gamma}$). Three spatial sections are identified: Substrate region (from -460 nm to -328 nm), interface region (from -324 nm to -292 nm) and far from interface (close to surface) region (from -288 nm to 0 nm). Strain is close to zero at the substrate region, as expected. Steep change is observed in the interface region. Strain curves for the as-impl and the 300 C samples coincide within the statistical scatter, while the 700 C sample shows a much slower variation of strain in the far from interface region. 56
Figure 29. Left: quasi-spherical and fiber-like particles found in Trelegy® Ellipta® Right: bronchial deposition fractions of the fibres with and without considering the diameter correction with the shape factor. 58
Figure 30. (a) Set-up for micro-combinatorial deposition (1) magnetron sputtering source, (2) moving slit, (3) substrate, and (4) graded-thickness gold layer. (b) Optical transmission cell with (1) light source, (2) glass chamber, (3) substrate with annealed nanoparticles and (4) spectrometer. (c) Thickness vs. position (red circles), effective thickness (also called ’mass thickness’ corresponding to the deposited amount of material (dotted line), and error of fit for the as-deposited graded Au sample ‘B’ measured by spectroscopic ellipsometry (SE). (d) Change of measured thickness by SE as a function of temperature during annealing at the position at 8 mm on sample ’B.’ (e) Schematic, (f) scanning electron micrograph (at a position of 8 mm), and (g) optical image of the sample after annealing. (h) and (i) show m33 spectra on sample ‘B’ over the range of positions from 0 to 12 mm for the as-deposited and 300 °C annealed state, respectively. 61

Figure 31. TEM micrographs of the supported MoNi/MgO powder catalyst deposited on a C/Au grid and subjected to reduction and reaction treatment at 800 °C: a) TEM overview image; b) high-magnification image, with dark-contrast Au particles indicated by arrows; c) selected area for further STEM–EDS analysis, Au particles marked by arrows; d) STEM–EDS Mg map; e) Mo map; f) Ni map; g) Au map of the same area. 63
Figure 32. Geometric phase analysis (GPA) was performed from HRTEM images of the intermixing region, obtaining ε_{xx}, ε_{yy} deformation maps. The HRTEM image with the corresponding FFT, ε strain/deformation maps and integrated EDS line-profiles of Ti and Ge signed on the HAADF image in [110] projection (sample #212). ε_{xx} and ε_{yy} strain/deformation maps were calculated using periodicities signed on the FFT. TiO_2 was selected as the reference. The integrated and averaged deformation values inside the white rectangles are presented below the maps. The average out-of-plane deformation values calculated inside the blue rectangles are the following; r-TiO_2: ε_{yy} =0.0004(50), and r-GeO_2: ε_{yy} =-0.027(14) in the mixing area at the interface, ε_{yy} =-0.040(7) and ε_{yy} =-0.040(7) above. ε_{xx} =-0.035(10) is more homogeneous in the root part of the r-GeO_2 crystal and above. 64
Figure 33. Line profile in the EDS elemental map indicating the concentration correlation of Cr with Mo and Si with Mn. 65
Figure 34. Bright and dark field images of the Cr-Mn-Mo-Si-Y-(N) high entropy nitride coating deposited at 580C and 100V bias. The bright contrast in the DF image indicates the location of the crystalline fcc phase. 66
Figure 35. Edge view (left) and plane view (right) HRTEM of individual bone mineral platelets with their corresponding FFTs. Features deviating from hexagonal symmetry are indicated in the plane-view FFT. 67
Figure 36. (a) Diagnostic appearance of RLH enamel and density change shown by micro-CT. b) HAADF and HRTEM of hollow nanocrystals characteristic of RLH enamel. (c) Simulated SAED shows that asymmetric contrast gradient around the core of the crystals, observed on HAADF is due to small tilt. (d) Raman spectral parameters of RLH enamel allow clear distinction from MIH enamel. 68
Figure 37. Scanning electron microscope image (a) low-magnification TEM image (b), and the corresponding EDS of PCL-mCaP composite. 69
Figure 38. FE-SEM images on CA-mCP (a) and PCL-mCP (c) composites, as well as CA-mCP (b) and PCL-mCP (d) composites, after two weeks of immersion in saline solution. 70
Figure 39. SEM micrographs of the HAp sample obtained at different magnifications. The high magnification images reveal well-defined crystalline particles with faceted surfaces. Pores can be observed between the agglomerated particles, while the lower magnification image provides an overview of the porous architecture of the material. The presence of an interconnected pore network is important for bone-related applications. It can support tissue ingrowth and osseointegration. 71
Figure 40. Structure of HCHiP competence centre (www.hchip.eu) 72
Figure 41. Left: Schematics of a scintillation-based planar neutron detector structure. Right: 1.6 MeV proton-EBS spectra of 10B5C layers with varying thickness deposited on Si substrate. Arrows represent spectral edge positions for different components. 74
Figure 42. Left: Neutron absorption as a function of $^{10}B_5C$ layer thickness. Dots represent experimental data recorded at 0° and 60° sample tilt angle, while the solid (dotted) line shows calculated values with (without) taking into account beam hardening for neutrons. Right: Calculated normalized light (ionoluminescence, IL) yield of the scintillator vs. $^{10}B_5C$ layer thickness for a planar neutron detector structure shown in Figure 41. 75
Figure 43. The surfaces of the different oxides: (a) native Si-oxide, (b) CVD oxide and (c) thermal oxide; and their morphologies after 15 deposition cycles: (d) deposition on native oxide, (e) deposition on CVD oxide, and (f) deposition on thermal oxide. 76
Figure 44. Schematic illustration of the three surface functionalisation approaches applied to silicon oxide substrates prior to GaS_x deposition: (a) silane-based thiolation using mercaptopropyl-trimethoxysilane, yielding an organic spacer layer terminated with –SH groups; (b) gas-phase treatment with DMDS (c) or DTBDS producing sulphur-containing surface species The grey line represents the native Si-oxide surface covered by surface hydroxyl groups. 77
Figure 45. AFM micrographs of (a) 5 cycles of GaSx on native oxide covered Si, (b) the same with piranha pretreatment, (c) DMDS pretreatment, (d) di-tert-butyl-disulfide pretreatment, (e) piranha+dmds pretreatment, and (f) thiolation with mercaptopropyl-trimethoxysilane 78
Figure 46. Device characteristics and comparison of high and low frequency oscillations. (a) Low frequency oscillator setup. (b) High frequency oscillation setup. (c) Low frequency oscillation waveforms showing the measured current (black) and voltage drop on the memristor (blue). (d) Measured current waveform of the highest frequency oscillation with 167 MHz. (e) Schematic of the memristor device highlighting the small device size. (f) Scanning electron micrograph of a representative VO2 memristor, scale bar: 1 µm. (g) Low frequency I(V) graph of a VO2 device as a function of driving voltage (red) and as a function of the bias voltage measured on the memristor (grey). 79
Figure 47. In-depth experimental results concerning distance limitation. (a) Circuit schematics used for achieving ultrafast oscillations, and to study distance limitation. (b) Drive voltage and distance dependence of the achieved

oscillation frequency. Different colors show different memristor-serial resistance cable lengths, as shown in the legend. (c) Cable length scaling of the oscillation frequency. 80
Figure 48. (a) Schematics of the novel Andreev qubit formed by coupling a traditional transmon to a minimal Kitaev chain (source: QUKIT Proposal Part B). (b) Our platform for the realization of the Kitaev qubit: near-surface InAs 2DEG contacted by an epitaxial Al layer. 82
Figure 49. (a–b) Optical micrographs of a λ/4 coplanar waveguide resonator patterned from the epitaxial Al layer and the inductively coupled double-loop structure. (c) Scanning electron micrograph of the double Josephson junction device. Electrostatic gate electrodes are used to tune the charge carrier density in the junctions. (d) Resonance frequency of the resonator as a function of the magnetic flux applied to the two superconducting loops. The crossing of resonance-frequency dips indicates a nontrivial, mutually dependent response of the two loops. 83
Figure 50. (a) Cooper-pair splitting device. The trapezoidal electrodes deplete the electrons in the 2DEG, forming a quasi-one-dimensional channel. Beneath this channel lies the end of the superconducting aluminum contact, which acts as the Cooper-pair source. Finger gates deposited on top define and control the quantum dots. (b) Single quantum dot measurement. Coulomb diamonds are visible in the transport data; however, the device exhibits instability during operation. 83
Figure 51. Handheld tissue tester with the sensor assembly before transection of the chorda tympani nerve. 84
Figure 52. The chip containing the three sensor elements (left) and one of its heaters as covered with a nanofiber VOx sensor layer (middle), and VOx nanofibers sensitized with gold particles (right). 91
Figure 53. Prototype of an NDIR methane detector with an optical microchannel for portable applications. The god surface optical channel covered with a gas-permeable reflector is visible on the lower half of the 25×25mm^2 circuit board. 92
Figure 54. Force-time curve of a simulated laproscope jaws closed on a healthy stomach section (left). Force-displacement curve obtained with the tabletop measurement system (right). The compression of the same tissue section is similar to the time dependent force measurement. 94
Figure 55. A representative force-displacement curve obtained from the nanoindentation measurement on the soft-baked SU-8 coated silicon wafer (a). SEM images of the SU-8 coated wafer surfaces show the indentation at a higher magnification, also showing the interfacial slipping (b). 95
Figure 56. Morphology of DEGDMA monoliths prepared with different acetonitrile (ACN)/alcohol (MetOH, EtOH, PrOH) solvent ratios. The monomer mixture contained 30 vol.% DEGDMA and 70 vol.% of the solvent. The irradiation was performed with 30 kGy dose and 11 kGy/h dose rate. 97
Figure 57. Schematic illustration of the measurement method. 108
Figure 58. Schematic illustration of the antagonistic enzymatic reaction network. 109
Figure 59. Configuration and working principle of the piezoelectric micropipette 110
Figure 60. Experimental scheme and molecular mechanism of integrin-mediated adhesion assays. (A) Experimental workflow of the two biosensor assay setups: (1) inhibitory effect of soluble S1 protein in cell suspension and (2) adhesion to surface-immobilized S1 protein. (B) Schematic representation of molecular interactions during the assays. 111
Figure 61. Schematic illustration of the measurement method. 112
Figure 62. Phase diagrams of the system behavior with respect to return ratio r and investment ratio x for different multiplication factors u = 3, 6, 12. Trust emerges in the (I + N)&(T + U) phase (white region) with large x and moderate r, where the four strategies of the two roles coexist. Trust cannot survive in the N&(T ⇔ U) phase (gray region), where trustors do not invest, and trustworthy and untrustworthy trustees are in neutral drift. The dashed line marks r = 1/u in each panel. 114
Figure 63. Inter-role spatial reciprocity in the two-step invasion I&T ⇒ I&U ⇒ N&U is key to trust emergence. (a) The initial preparation divides the lattice into two blocks, I&T and N&U, to better observe the two-step invasion. (b) At moderate return ratio (r = 0.4), trustworthy trustees are supported by neighboring investing trustors, thus invading untrustworthy trustees near non-investing trustors (Step 1, I&T ⇒ I&U, regions marked by yellow circles); near trustworthy trustees, an investing trustor has higher fitness and invades non-investing trustors (Step 2, I&U ⇒ N&U). (c) At high return ratio (r = 0.6), trustworthy trustees have low fitness due to returning too much, thus unable to make the invasion in Step 1. Other parameters: u = 3, x = 1. 115
Figure 64. Maps represent the first link cuts for different λ couplings for scenario #12. As we can see, several edges coincide at different values. The different number of cuts is due to the fact that for larger couplings, fewer lines are overloaded. These initial failures are typically concentrated around major power plants or large substations, surrounded by dangling ends. 117
Figure 65. The weight distributions of (a) KKI-113, (b) KKI-18, (c) H01 human (1 mm3), (d) mouse retina, (e) fly (hemibrain), (f) fly (full brain, and its filtered version), and that of a larva all follow power-law behaviors in the global scale. 118
Figure 66. Optimal strategy distributions on square lattice 119